University of Cambridge

Cavendish Laboratory

Unconventional Fermi surface in insulating SmB$_6$ and superconducting YBa$_2$Cu$_3$O$_{6+x}$ probed by high magnetic fields

---

PhD Dissertation

Author: Yu-Te Hsu

College: Girton

Date of submission: September 2018

This dissertation is submitted for the degree of Doctor of Philosophy

Abstract

Unconventional Fermi surface in insulating SmB_6 and superconducting $YBa_2Cu_3O_{6+x}$ probed by high magnetic fields

by Yu-Te Hsu

Fermi surface, the locus in momentum space of gapless low-energy excitations, is a concept of fundamental importance in solid state physics. Electronic properties of a material are determined by the long-lived low-energy excitations near the Fermi surface. Conventionally, Fermi surface is understood as a property exclusive to a metallic state, contoured by electronic bands crossed by the Fermi level, although there has been a continuing effort in searching for Fermi surface outside the conventional description. In this thesis, techniques developed to prepare high-quality single crystals of SmB_6 and $YBa_2Cu_3O_{6+x}$ (abbreviated as $YBCO_{6+x}$ hereinafter) are described. By utilising measurement techniques of exceptional sensitivity and exploring a wide range of temperatures, magnetic fields, and electrical currents, we found signatures of unconventional Fermi surfaces beyond the traditional description in these strongly correlated electronic systems.

SmB_6 is a classic example of Kondo insulators whose insulating behaviour arises due to strong correlation between the itinerant d-electrons and localised f-electrons. The peculiar resistivity plateau onsets below 4 K has been a decades-long puzzle whose origin has been recently proposed as the manifestation of topological conducting surface states. We found that the insulating behaviour in electrical transport is robust against magnetic fields up to 45 T, while prominent quantum oscillations in magnetisation are observed above 10 T. Angular dependence of the quantum oscillations revealed a three-dimensional characteristics with an absolute amplitude consistent with a bulk origin, and temperature dependence showed a surprising departure from the conventional Lifshitz-Kosevich formalism. Complementary thermodynamic measurements showed results consistent with a Fermi surface originating from neutral itinerant low-energy excitations at low temperatures. Theoretical proposals of the unconventional ground state uncovered by our measurements in SmB_6 are discussed.

$YBCO_{6+x}$ is a high-temperature superconductor with a maximum T_c of 93.5 K and the cleanest member in the family of copper-oxide, or *cuprate*, superconductors. The correct de-

scription of electronic ground state in the enigmatic pseudogap regime, where the antinodal density of states are suppressed below a characteristic temperature T^* above T_c, has been a subject of active debates. While the quantum oscillations observed in underdoped YBCO_{6+x} have been predominately interpreted as a property of the normal state where the superconducting parameter is completely suppressed at ≈ 23 T, we made the discovery that $\mathrm{YBCO}_{6.55}$ exhibits zero resistivity up to 45 T when a low electrical current is used, consistent with the observation of a hysteresis loop in magnetisation. Quantum oscillations in the underdoped YBCO_{6+x} are thus seen to coexist with d-wave superconductivity. Characteristics of the quantum oscillations are consistent with an isolated Fermi pocket reconstructed by a charge density wave order parameter and unaccompanied by significant background density of states, suggesting the antinodal density of states is completely gapped out by a strong order parameter involving pairing correlations, potentially in addition to the other order parameters. Transport measurements performed over a wide doping range show signatures consistent with pairing correlations that persist up to the pseudogap temperature T^*.

The surprising observation of quantum oscillations in insulating SmB_6 and superconducting YBCO_{6+x} demonstrates a possible new paradigm of a Fermi surface without a conventional Fermi liquid. A new theoretical framework outside the realm of Fermi liquid theory may be needed to discuss the physics in these strongly correlated materials with enticing electronic properties.

Preface

This dissertation is the result of my own work and includes nothing which is the outcome of work done in collaboration except declared in the Preface and specified in the text. The research projects are performed under supervision of Dr Suchitra E. Sebastian in the Quantum Matter (QM) group at the Cavendish Laboratory. Single crystals of $\mathrm{SmB_6}$ and YBCO_{6+x} are primarily prepared and characterised by myself using methods described in Chapter 3. High magnetic field measurements are performed in a group setting with colleagues from QM and supporting staffs at high-field facilities. Experimental data are principally analysed by myself and Máté Hartstein. The study of quantum oscillations and thermodynamic measurements on $\mathrm{SmB_6}$ presented in Chapter 5 has been published in *Science*, **349**, 287-290 (2015) and *Nature Physics*, **14**, 166-172 (2018). A number of figures are made with substantial inputs from Máté Hartstein as credited below (Figures 5.9, 5.10, 5.13-20, 6.4, 6.7-12, 6.19-22).

It is not substantially the same as any that I have submitted, or, is being concurrently submitted for a degree or diploma or other qualification at the University of Cambridge or any other University or similar institution. I further state that no substantial part of my dissertation has already been submitted, or, is being concurrently submitted for any such degree, diploma or other qualification at the University of Cambridge or any other University of similar institution.

This thesis does not exceed the prescribed word limit for the Degree Committee for the Faculty of Physics and Chemistry.

Acknowledgements

The Cambridge journey has been a dream-come-true experience for me, one that I have numerous people to thank for.

First of all, I have to thank Suchitra for the providing me the opportunity of studying in the Cavendish. I still remember how shocked I was to receiving her email, offering me a place as a postgraduate student in Cambridge, a place I would never dream of attending. Working with her has vastly broadened my horizons, both scientifically and geographically, and taught me how to adopt to the most challenging situations. ”No measurements should be performed on non-optimal samples” is a lesson I will never forget. Thank you for all the guidance and support during the course of my PhD.

Next, I would like to dedicate my gratitude to Mátá, my comrade in highly magnetic battlefield. I could not have done it without you. Your brilliance and patience are something I truly admire. It has been an adventure to kill the magnets around the world together. I also want to thank Sofia, my work wife and confidant. You make the bad days less bad and the good days much better. The mini-tea breaks at Tallahassee, the afternoon in the Miami beach, and the sleepover before I left Cambridge are memories that always make me smile.

I am also very thankful for the friendship and support from current and former members of QM: Alex, Indy, Patricia, Paromita, Hajime, Jack, Siân, Konstantin, Aleks, Jiasheng, Xiaoye, Jordan, Seb, Cheng, Hong'En, and Beng. Things are not always working, but you are always there when I needed a hand or a chat.

Getting things done in maglabs is no easy task, and for that I am indebted to our collaborators for their wonderful support: Neil Harrison, Ross McDonald, Fedor Balakirev, and Mun Chan from NHMFL at Los Alamos, Ju-Hyun Park, Bin Zeng, Luis Balicas, and Eun Sang Choi from NHMFL at Tallahassee, Zengwei Zhu, Huakun Zuo, and Jinhua Lin from WHMFC at Wuhan, and Cyril Proust and Wojciech Tabis from LNCMI at Toulouse. Special thanks goes to Neil, for your reassuring laughters and out-of-the-box thinking, and Ju-Hyun, for showing me how to appreciate the beauty of SR124's green backlit dial and the chicken magic.

This thesis will not be possible without the beautiful crystals prepared by Toshinao Loew and Juan Porras from Prof. Keimer's group at Stuttgart, and Monica Ciomaga-Hatnean from Prof. Balakrishnan's group at Warwick. Thank you for your hard work and craftsmanship.

I shall thank the Taiwanese Ministry of Education to be the primary sponsor for my course. I would also like to thank the Sidney Perry Foundation, the Leche Trust, and Cambridge Philosophical Society whose financial support have been instrumental for the completion of my course. I also have to thank my College tutor, Frances Gandy, who has been tremendously supportive throughout my time in Cambridge.

Finally, I would like to express my gratitude towards my family: Chiao, Danny, Natascha, and my loving Mom and Dad. I have become who I am today because of you, and thank you all for your unconditional support.

Contents

Chapter 1

Introduction

1.1 Strongly correlated electronic systems

The band theory of solids is a major triumph of twentieth century physics. Based on the theoretical framework of a single-particle Hamiltonian, it successfully describes a wide range of physical phenomena of solids and explains the occurrence of conductors and insulators. The simple band theory, however, works only when the interactions between electrons are weak and can be ignored. In systems where the electron-electron interactions are strong, known as *strongly correlated electronic systems*, the simple band theory ceases to apply and novel electronic states emerge due to the collective behaviour of interacting electrons. In this section, a model applicable to describe the strongly correlated systems is introduced, and discussed in relation to two strongly correlated electronic systems.

1.1.1 t-J model

A simplistic model that has been highly successful to describe many-body system is the t-J model, pioneered by John Hubbard, with the Hamiltonian

$$H = -t \sum_{<i,j>\sigma} (c^{\dagger}_{i\sigma} c_{j\sigma} + \text{h.c.}) + J \sum_{<i,j>} \mathbf{S}_i \cdot \mathbf{S}_j, \tag{1.1}$$

where t is the hopping integral, $<i,j>$ denotes the summation over the nearest-neighbour lattice sites, σ denotes the spin of the particles, $c^{\dagger}(c)$ is the creation (annihilation) operator, h.c. is the Hermitian conjugate, J is the exchange integral that describes the coupling between particles, and $\mathbf{S}$ is the spin operator [1, 2]. The t-term describes the kinetics of particles, which favours particle hopping to neighbouring sites. The J-term describes the potential energy due to nearest-neighbour interactions. The ratio t/J determines the electronic ground state of the system. Two examples that can be described by the t-J model are discussed below.

1.1.2 Mott insulator

A Mott insulator has a single, partially filled energy band, predicted to be metallic by simple band theory, but is insulating due to electron-electron interactions. Figure 1.1 illustrates the formation of such state in a two-dimensional lattice with a half-filled d-band. Each of the free d-electron occupies an atomic lattice site and can hop to the neighbouring lattice sites. The hopping of electron is favoured energetically by $-t$, but punished by Coulomb repulsion U. An antiferromagnetic configuration of the spins are formed due to Pauli exclusion principle, and an exchange of neighbouring spins can occur via two virtual hoppings of electrons with a coupling constant $J = 4t^2/U$. When $t \gg U$, electrons can tunnel through the lattice sites without hinderance and the system is metallic; when $t \ll U$, the strong Coulomb repulsion between electrons render them to be localised and the system is insulating. In such insulating state, the originally half-filled d-band is split into an upper and a lower Hubbard band, separated by a bandgap where the Fermi energy E_F lies. Mott insulators have been discovered in abundance since the first occurrence in NiO [3], many of which are transition metal oxides and two-dimensional organic salts [1, 4].

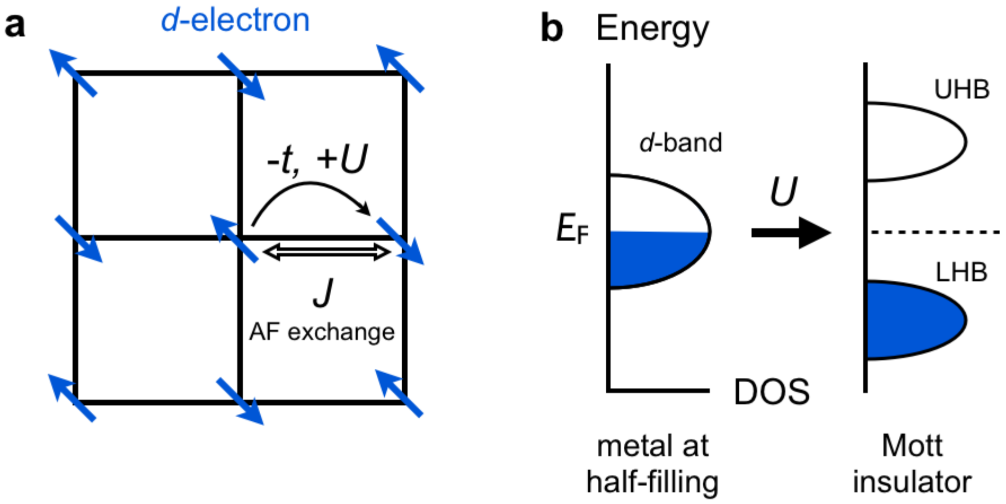

Figure 1.1: **Mott insulating state at half-filing.** (**a**) A schematic two-dimensional lattice with one d-electron occupying each lattice site, symbolised by the blue arrows with the arrow directions denoting the spins. The virtual hopping of electrons to neighbouring sites reduces the total energy by $-t$ but increases the energy by U due to Coulomb repulsion. The alternation of spin directions in the neighbouring lattice sites is a result of Pauli exclusion principle. The exchange of neighbouring spins is associated with a coupling constant $J = 4t^2/U$. (**b**) A metallic state is predicted when the Fermi energy E_F lies in the half-filled d-band by simple band theory. The d-band splits into an upper Hubbard band (UHB) and lower Hubbard band (LHB) when the Coulomb interaction between electrons is considered, leaving the Fermi energy E_F lying within the bandgap and forming a Mott insulating state.

1.1.3 Kondo hybridisation

Another example of unconventional electronic state is the Kondo system, which consists of the itinerant d-electrons and localised f-electrons. Figure 1.2 illustrates the formation of a Kondo state in a two-dimensional lattice. The f-electrons with a large magnetic moment form a lattice with an antiferromagnetic arrangement of the neighbouring spins, known as the Kondo lattice. At high temperatures, the system is metallic whose transport behaviour is dominated by the weak scattering of the itinerant d-electrons by localised f-electrons. The antiferromagnetic interaction between the d- and f-electrons grows as temperature decreases and, below a characteristic temperature known as the Kondo temperature T_{K}, the scattering becomes so strong that the d-electron is magnetically bound to the f-electron and forms a spin singlet state, known as the Kondo singlet. The formation of the Kondo singlets screens the magnetic moment of the f-electrons and disrupts the antiferromagnetic configuration of the Kondo lattice, causing the Kondo system to be paramagnetic at low temperatures.

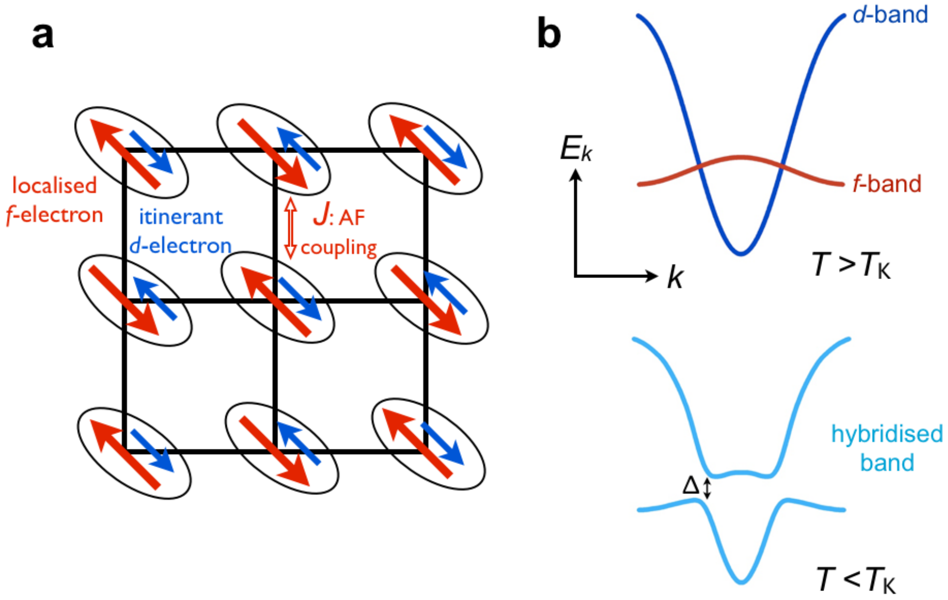

Figure 1.2: **Kondo hybridisation between d- and f-electrons.** (**a**) A schematic two-dimensional lattice with localised f-electrons (red arrows) occupying the lattice sites with a favourable antiferromagnetic coupling between the spins. Itinerant d-electrons (blue arrows) act to screen the localised magnetic moments and disrupt the antiferromangetic arrangement of the f-electrons. A spin-singlet state, illustrated by the encircled f- and d-electrons, known as the 'Kondo singlet' is formed below the Kondo temperature T_{K} when the magnetic interactions between the d- and f-electrons are sufficiently strong. (**b**) Electronic band structure before the hybridisation of d- and f-bands (top). Below T_{K}, the d- and f-bands hybridise and open up an indirect bandgap Δ (bottom). A Kondo insulating state is formed if the Fermi level lies within the bandgap.

The collective formation of Kondo singlets can be understood as the hybridisation between the electronic d- and f-bands. Below T_{K}, the dispersive d-band hybridises with the flat f-band and forms two bands that are weakly dispersive near the original f-band, with a small indirect bandgap. If the Fermi level lies within one of these flat bands, the ground state is a metal with *heavy fermions*, whose electron effective mass can be several orders of magnitude higher than that of the free electron. If the Fermi level lies within the hybridisation gap, the ground state is an insulating state known as the Kondo insulator. A dozen Kondo insulators have been discovered so far, typically consisting of elements with $4f$-electrons such as Ce and Sm [2].

1.2 $\mathrm{SmB_6}$: a Kondo insulator

1.2.1 Resistivity behaviour

$\mathrm{SmB_6}$ is the first example of a Kondo insulator discovered in 1969 [5]. It has a body-centred cubic structure with the Sm atom forming a simple cubic lattice and the $\mathrm{B_6}$ octahedron locates at the body centre. At room temperature, it is a paramagnetic metal. Upon cooling, it becomes an insulator with a small hybridisation gap of ≈ 4 meV, corresponding to a $T_{\mathrm{K}} \approx 40$ K, as shown in Figure 1.3. Intriguingly, the resistivity saturates below 4 K and reaches a plateau, suggesting that an additional conducting channel onsets at $T < 4$ K. Originally the conducting channel was attributed to impurity bands in the bulk [5], but the low-temperature resistivity plateau persists with improved sample quality, which suggests the behaviour is an intrinsic property. Until recently, the origin of the resistivity plateau in $\mathrm{SmB_6}$ had remained an unsolved puzzle for decades [2].

1.2.2 Topological insulator proposal

Recently, it has been proposed that $\mathrm{SmB_6}$ is a strongly correlated topological insulator, which provides an attractive explanation for the low-temperature transport anomaly [6]. Topological insulators are a novel electronic state of matter, in which a conducting surface state emerges from a bulk insulator.

The topological nature in these unconventional insulators is manifested by the attribution of topological order to the electronic wave functions. Insulators are characterised by a conduction band and a valence band that are separated by a bandgap. From this aspect, the physical vacuum and conventional insulators fall into the same class, characterised by the topological invariant $\mathbb{Z}_2$ index of $+1$ [7]. An analogy of this classification can be found in topology, where a donut and a mug is famously classified into the same topological class of $genus = 1$, determined by the number of holes in the manifold. In a conventional insulator, the electronic wave function can evolve smoothly from its bulk to the vacuum with the bandgap remains open throughout

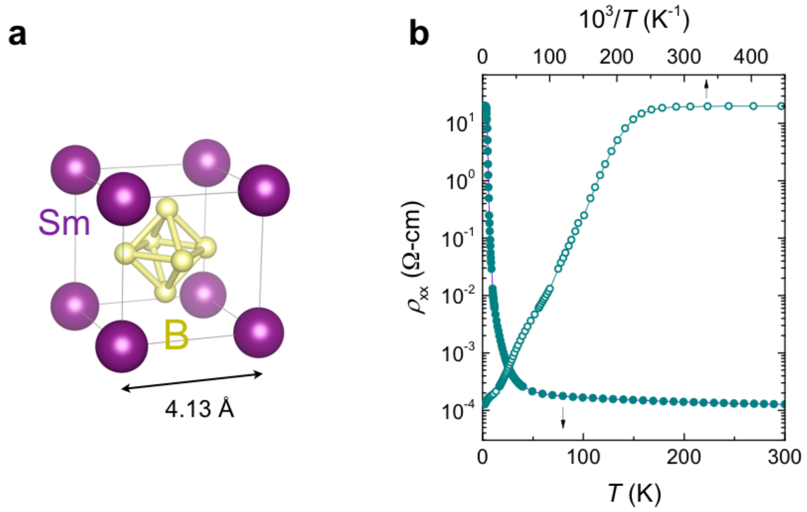

Figure 1.3: **Characteristics of the Kondo insulator SmB$_6$.** (**a**) Crystal structure of SmB$_6$. The Sm atom forms a simple cubic lattice with a lattice constant of 4.13 Å with the B$_6$ octahedron locates at the body centre. (**b**) Temperature dependence of the longitudinal resistivity ρ. The resistivity increases by orders of magnitude upon cooling below T_K = 40 K (bottom axis). However, the resistivity reaches a plateau below 4 K, corresponding to $10^3/T > 250$ (top axis).

the process, since the wave functions of the insulator and vacuum are topologically equivalent. Topological insulators, on the other hand, contain an internal twist in the electronic wave function characterised by the topological order $\mathbb{Z}_2$ = -1. This 'twist' is typically realised by *band inversion*, when the valence and conduction bands of different parities are inverted by control of chemical doping, lattice distortion, and/or spin-orbit coupling [8]. The distinct topological orders between the bulk of topological insulator and vacuum forbids the smooth evolution of the electronic wave function and the bandgap inevitably closes at the interface, giving rise to a gapless surface state with a linear dispersion near the Dirac point [7]. Figure 1.4 illustrates the band structure and transport behaviour of a topological surface state. The spin of charge carriers hosted in the Dirac surface state is locked perpendicular to their momentum, which prevents the scattering against non-magnetic impurity that would necessarily change the momentum but not the spin.

The $\mathbb{Z}_2$ order for a cubic insulator with inversion symmetry is determined by the number of crossings of bands with different parities, n, at high symmetry points [7]. Each time the band crossing occurs the $\mathbb{Z}_2$ index changes sign, i.e. $\mathbb{Z}_2 = (-1)^n$. In SmB$_6$, the 5d-band of even parity crosses three 4f-bands of odd parity at X-point [6], giving a $\mathbb{Z}_2 = (-1)^3 = -1$, hence is predicted to be a topological Kondo insulator. A simplified illustration is shown in Figure 1.5. This theoretical prediction has renewed the research interest in SmB$_6$. Recent experiments studying the nature of the low-temperature conducting state are briefly discussed in the following section.

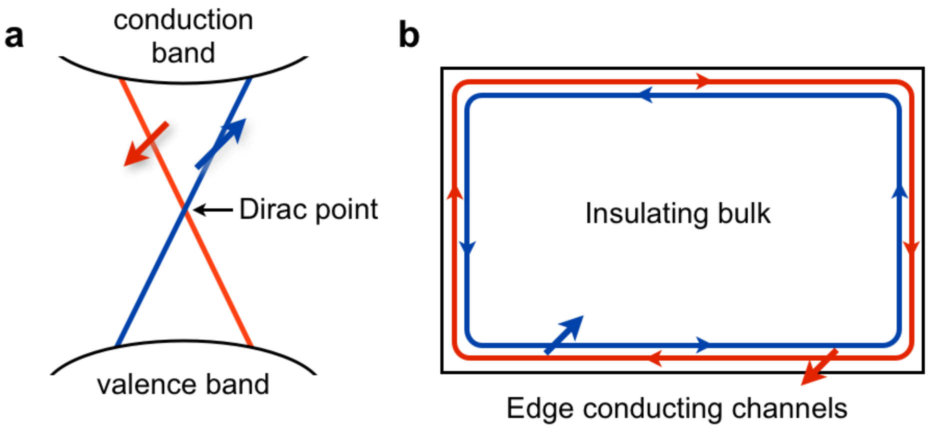

Figure 1.4: **Electronic bands and transport behaviour of a topologically insulating state.** (**a**) A topological insulator hosts gapless surface state of linearly dispersed bands within the bulk gap. The electron spins are locked to their momentum, typically via spin-orbit coupling, and spin-degeneracy of the surface bands is lifted. The crossing point of individual bands is known as the Dirac point. (**b**) In a 2D system, the electronic transport is confined to the edge of the material, whereas the interior remains insulating. Electrons with opposite spins propagate in opposite directions. Such propagation is protected against scattering from non-magnetic impurities due to spin-momentum locking.

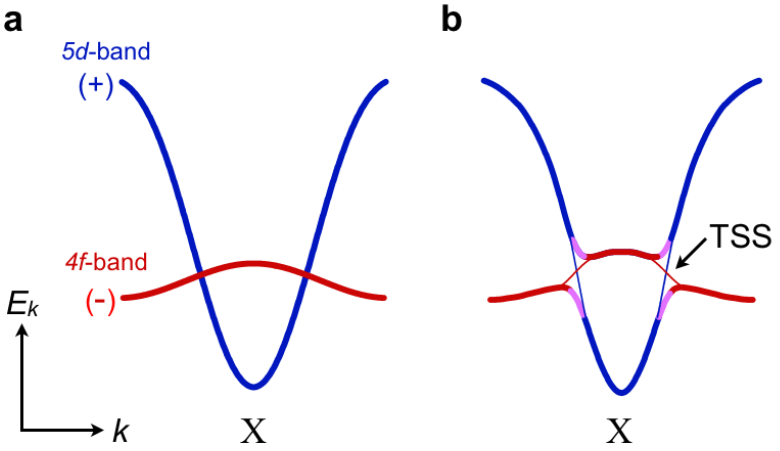

Figure 1.5: **Illustration of the topological surface states predicted in SmB_6.** (**a**) Schematics of the energy-momentum dispersion of the unhybridised $5d$- and $4f$-bands near the X-point in reciprocal space. The $5d$-band has an even parity and the $4f$-band has an odd parity. (**b**) Hybridisation of the $5d$- and $4f$-bands displaces part of the $4f$-band to the conduction band and part of the $5d$-band to the valence band, facilitating a band inversion and giving rise to topological surface states within the Kondo gap. Only one of the three $4f$-bands of SmB_6 is shown for simplicity.

1.2.3 Recent experimental progress

A number of recent transport studies of SmB_6 have demonstrated the surface nature of the conducting state at $T < 4$ K [9, 10, 11]. Figure 1.6(a) compares the ratio of resistance measured on SmB_6 doped with rare-earth impurities before and after the sample thickness is reduced. At $T > T_K \approx 40$ K, the ratio is given by the geometric factor of the sample in all cases, as expected for a bulk-dominant transport behaviour. At $T < 4$ K, where the resistance plateau is observed, the resistance ratios of SmB_6 doped with non-magnetic impurities, Y and Yb, converged to unity regardless of the thickness, indicating a surface-dominant transport behaviour. In contrast, in SmB_6 doped with highly magnetic Gd impurity, the resistance ratio is still given by the sample thickness, indicating the destruction of surface-conducting channels at low temperatures. The effect of impurity on the surface conducing channel is consistent with the behaviour expected for a topological surface state.

The most direct evidence of the existence of topological surface state is the observation of Dirac cones within the bulk insulating gap. However, due to the small bandgap of ≈ 4 meV in SmB_6, even state-of-the-art angular resolved photoelectron spectroscopy (ARPES) with a resolution of ≈ 10 meV is insufficient to resolve such Dirac surface states if existed. Most ARPES studies do report the existence of in-gap states in SmB_6 located at the X-point, also at the Γ-point as shown in Figure 1.6(b), although the origin of these states remains ambiguous [12]. With a conclusive experimental evidence of the predicted topological surface state in SmB_6 yet to be found, a complementary study of the Fermi surface geometry is warranted. Quantum oscillations, a direct probe of the Fermi surface geometry, is suited to study the Fermi surface in the Kondo insulating SmB_6 and provide new insight to the longstanding puzzle.

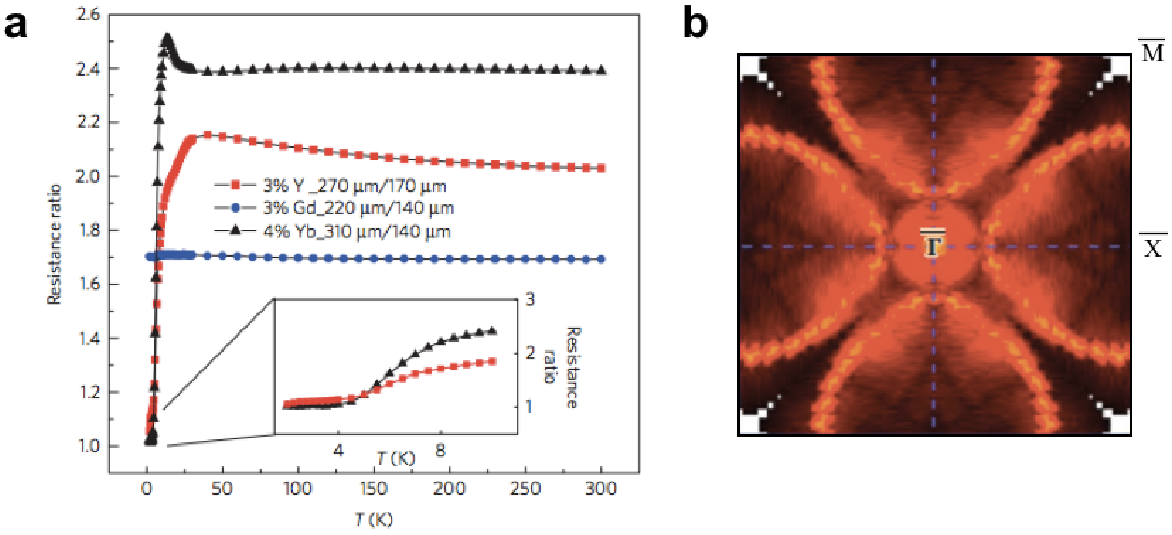

Figure 1.6: **Experimental evidence of the conducting surface state in SmB_6.** (**a**) Ratio of resistance measured before and after the sample thickness is reduced in SmB_6 doped with magnetic (Gd) and non-magnetic (Y, Yb) impurities. Measurements were performed using the same contact configuration with the thicknesses indicated. In SmB_6 samples doped with non-magnetic impurities, Y (red) and Yb (black), the resistance ratio converges to unity at $T < 4$ K, independent of the thicknesses, indicating a surface-dominant conduction. In contrast, the sample doped with magnetic Gd impurity shows a resistance ratio given by the geometric factor in the entire temperature range measured, indicating the destruction of conducting surface state at low temperatures. Figure reproduced from [10] with permission. (**b**) Angular resolved photoelectron spectroscopy measurement on SmB_6 that reports the existence of in-gap states in SmB_6. Two distinct Fermi pockets are observed, one centred at $\overline{\Gamma}$ point and one centred at $\overline{X}$ point at the surface. Figure reproduced from [13] with permission.

1.3 $\mathbf{YBCO_{6+x}}$: a doped Mott insulator

1.3.1 High temperature superconductivity

$YBa_2Cu_3O_{6+x}$, referred to as $YBCO_{6+x}$ throughout this thesis, was the first superconductor to be discovered with a critical temperature T_c above the boiling point of liquid nitrogen [14]. This breakthrough made in 1987 created the field of high-T_c superconductivity and lead to the Nobel prize awarded to Alex Müller and Georg Bednorz in the same year, who discovered the first copper oxide-based superconductor (also called *cuprate* superconductor) in 1986 [15]. $YBCO_{6+x}$ has an orthorhombic crystal structure that consists of two CuO_2 planes and one CuO_x chain in the unit cell, along with the Y and BaO layers that serve as carrier reservoirs. The amount of oxygen in the compound can be varied by adjusting the occupancy of oxygen in the CuO_x chain, which in turn varies the amount of carriers within the CuO_2 planes. The Cu^{2+} ion in the CuO_2 planes has a $3d^9$ electronic configuration, corresponding to a half-filled band at the highest energy. The formation of CuO_x chain increases the valency of Cu ions at the lattice corners from 0 to +1, as required by charge neutrality, which effectively removes electrons from the Cu^{2+} ions in the CuO_2 planes. This process, known as *hole doping*, changes the electronic properties of $YBCO_{6+x}$ dramatically. The parent compound with no oxygen chains ($x = 0$) is an antiferromagnetic Mott insulator with a Neél temperature $T_N \approx 450$ K, below which the antiferromagnetic order forms [16]. Superconductivity emerges at $x > 0.35$ and has a maximal T_c of 93.5 K at $x = 0.92$, as shown in Figure 1.7 [17].

1.3.2 Electronic structure

The building block shared by all cuprate superconductors is the CuO_2 plane, which hosts the high-T_c superconductivity. The relevant electronic orbitals are the $3d_{x^2-y^2}$ of Cu^{2+}, which has the highest energy due to crystal field splitting [18], and the $2p_x$ and $2p_x$ of O^{2-}, as illustrated in Figure 1.8. The hybridisation of the $3d_{x^2-y^2}$ and $2p_{x,y}$ orbitals gives rise to an antibonding band with a single occupancy. The corresponding Fermi surface is a large cylindrical Fermi surface centred at the Y-point in reciprocal space. However, it is a strongly correlated Mott insulator at half-filling rather than a metal as predicted by band theory. More surprisingly, the superconducting gap in the cuprates has a *d*-wave symmetry, which vanishes along the (π, π) direction, known as the *nodes*, and maximises along the (π, 0) and (0, π) directions, known as the *antinodes.* The sign of the gap function alternates across the nodes, which is described as having the *d*-wave symmetry. The superconducting gap with *d*-wave symmetry, in contrast to the *s*-wave symmetry observed in conventional BCS superconductors, demonstrates the unconventional nature of superconductivity in the cuprates. Additionally, the superfluid density in cuprates is reported to be anomalously small and scale with T_c [19, 20], whereas

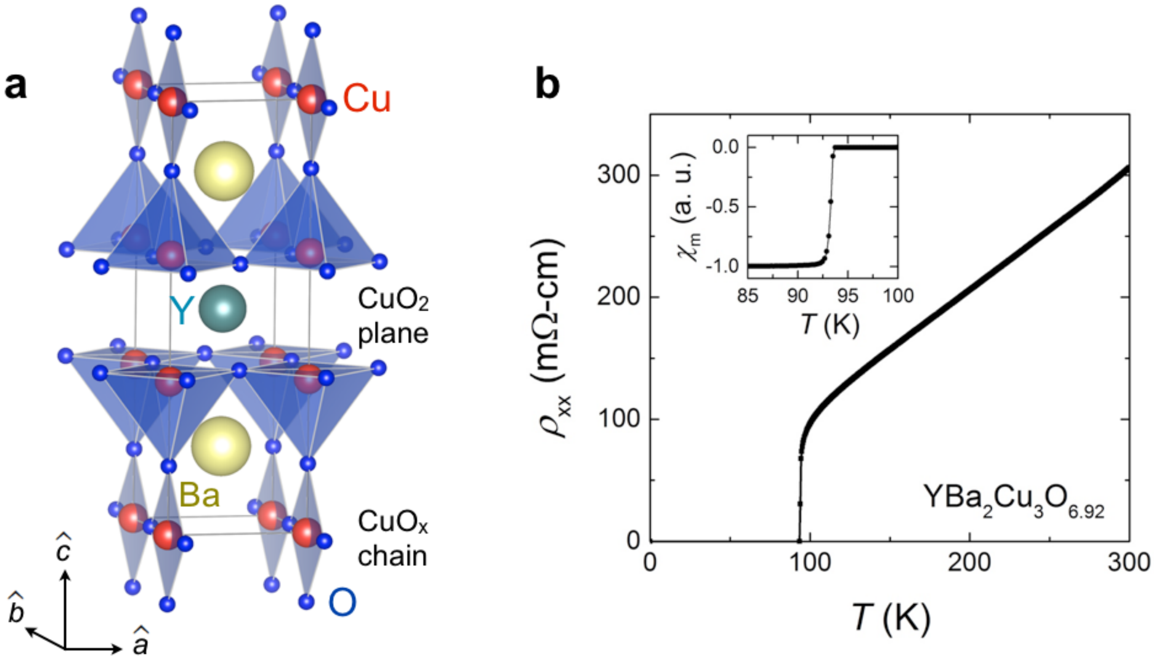

Figure 1.7: **Characteristics of the high-temperature superconductor $YBa_2Cu_3O_{6+x}$.** (**a**) Crystal structure of $YBCO_{6+x}$, which consists of two CuO_2 planes (tetrahedrons) and one CuO_x chain (squares) in the unit cell. The CuO_2 planes and CuO_x chains are separated by BaO layers. It has an orthorhombic lattice with $\hat{b}$-axis along the CuO_x chains slightly longer than the $\hat{a}$-axis. (**b**) Resistivity and magnetisation of $YBCO_{6.92}$, the stoichiometry with the maximum T_c of 93.5 K.

the BCS theory predicts the superfluidity density to be equal to the total particle density as the Cooper pairs condensate into superfluid once formed [21]. It was suggested that the phase fluctuations of the superconducting order parameter are of an energy scale comparable to the paring energy [22]. Furthermore, the conventional superconductivity emerges from a metallic state whose resistivity follows a quadratic dependence in temperature i.e. $\rho(T) = \rho_0 + aT^2$, while in the cuprates the most robust superconductivity emerges from a metallic state whose resistivity follows a T-linear dependence, as shown in Figure 1.7(b). The T-linear resistivity in LSCO near the optimal doping is observed to persist up to 800 K and shows no sign of saturation up to 1 000 K, with the resistivity corresponding to a mean free path less than the interatomic spacing [23], which violates the well-established Mott-Ioffe-Regel limit applicable to metals [24]. The regime with the T-linear resistivity is known as the 'strange metal' region and has been observed in many other unconventional superconductors and suggested to be intimately connected to the exotic superconductivity [25, 26].

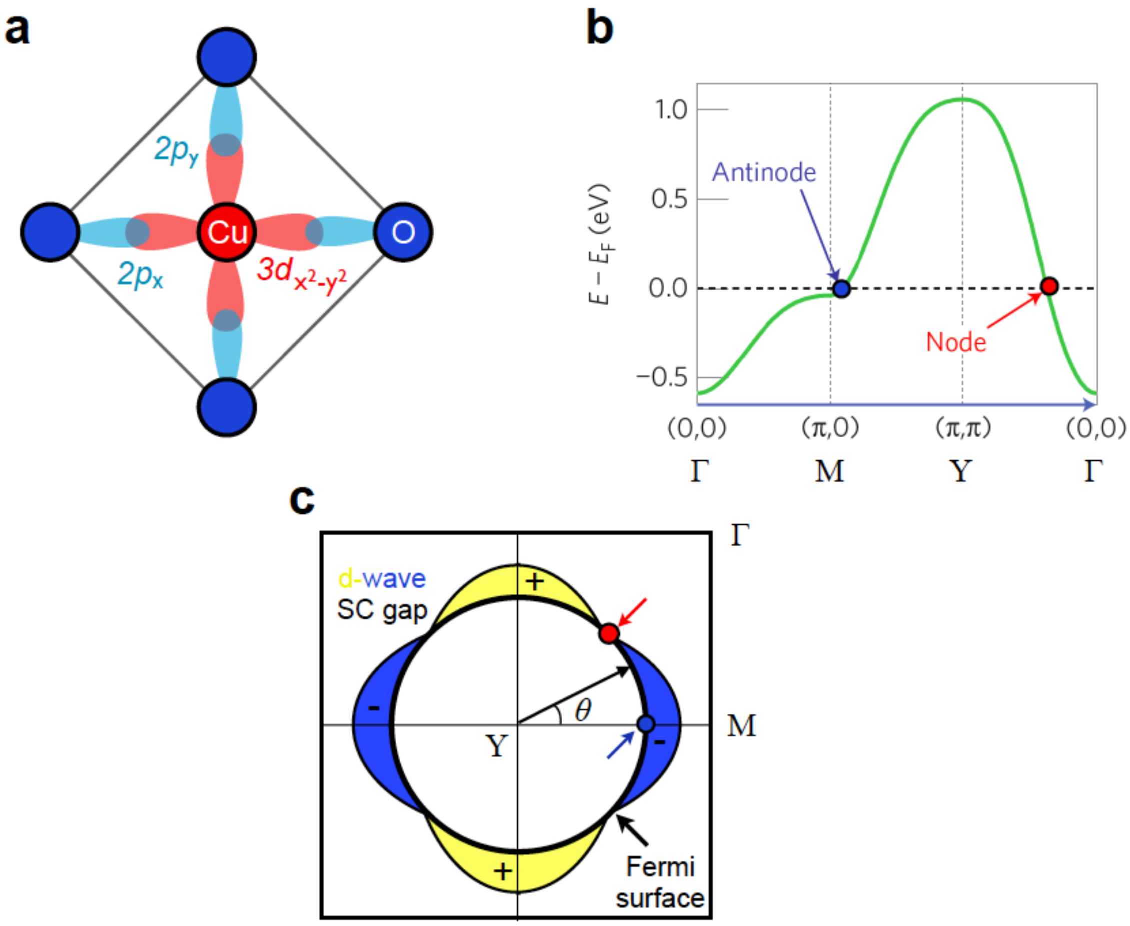

Figure 1.8: **Electronic structure and superconducting gap in cuprate superconductors.** (**a**) Schematics of the relevant orbitals for the electronic structure of the CuO_2 plane. The $3d_{x^2-y^2}$ orbital of the copper ion has the highest energy due to crystal field splitting and a single occupancy, which hybridises with the $2p_x$ and $2p_y$ orbitals of oxygen ions. (**b**) Energy dispersion of the highest electronic band calculated for the CuO_2 plane using the tight bonding model. The high symmetry points in reciprocal space (Γ, M, and Y) are labelled. (**c**) The large cylindrical Fermi surface calculated from (b) and the superconducting gap in the cuprate superconductor with a d-wave symmetry. The superconducting gap has zeros along the (π, π) direction, denoted as the nodes (red point), and maximums along the $(\pi, 0)$ and $(0, \pi)$ directions, denoted as the antinodes (blue dot). θ denotes the Fermi angle, which equals to 0° at the antinode and 45° at the node. The sign of the superconducting gap alternates between the yellow and blue regions. Figures reproduced from [27] with permission.

1.3.3 Phase diagram

In addition to the superconductivity and strange metal phases, the cuprates host a variety of symmetry-breaking electronic phases. Figure 1.9 shows the temperature-doping phase diagram of YBCO_{6+x}. As mentioned, the undoped YBCO_6 is an antiferromagnetic (AF) insulator. The rotational-symmetry-breaking AF order is strongly suppressed by doping of holes, which vanishes at $p \approx 0.05$ before the superconductivity emerges. The occurrence of superconductivity in the vicinity of antiferromagnetism has been demonstrated in many unconventional superconductors, in which p- and d-wave superconductivity has been observed [28]. Naturally, the magnetic interactions between electrons are believed to be crucial to the mechanism of unconventional superconductivity. The superconductivity has a dome-like structure with respect to p, with a maximum T_c at $p \approx 0.16$, known as the *optimal doping* p_opt. The region with doping higher than p_opt is known as the *overdoped* regime, while the region with doping lower than p_opt is known as the *underdoped* regime. Charge order, a periodic variation in the spatial charge density that breaks translational symmetry, has been recently observed in the majority of underdoped cuprates [29, 30]. The charge order is believed to compete with superconductivity and is seen to be the most robust at $p \approx 0.125$, which coincides with location where T_c is most suppressed from an empirical quadratic p-dependency. This suppression in T_c, known as the 1/8-anomaly, is naturally explained by the competition between charge order and superconductivity [17, 29].

One of the most intensely studied feature of the cuprates is the formation of the *pseudogap* state, observed below a characteristic temperature T^* that increases as p decreases [27]. For this state the density of states at E_F is suppressed around the antinodes at $T > T_\mathrm{c}$ and persists up to T^*, which exhibits the same d-wave symmetry as the superconducting gap, as illustrated in Figure 1.10. Thus far, it is yet unclear whether the antinodal density of states at E_F is rendered incoherent due to thermal and/or classical fluctuations or is completely gapped due to an unconventional order parameter [21]. Signatures of the pseudogap can be seen in various experimental probes and follow the same doping dependence [35], although the onset temperature T^* varies between experimental techniques. Whether or not the pseudogap is a distinct thermodynamic phase, or represents a regime of crossover behaviour is still under debate [36, 37]. It is widely believed that the pseudogap is closely related to the high-T_c superconductivity, while whether it signifies precursor pairing at high temperatures or a competition to the superconductivity remains unclear [36, 37]. The electronic structure of the pseudogap regime has attracted considerable interest in the field of high-T_c cuprates and is briefly discussed in the following section.

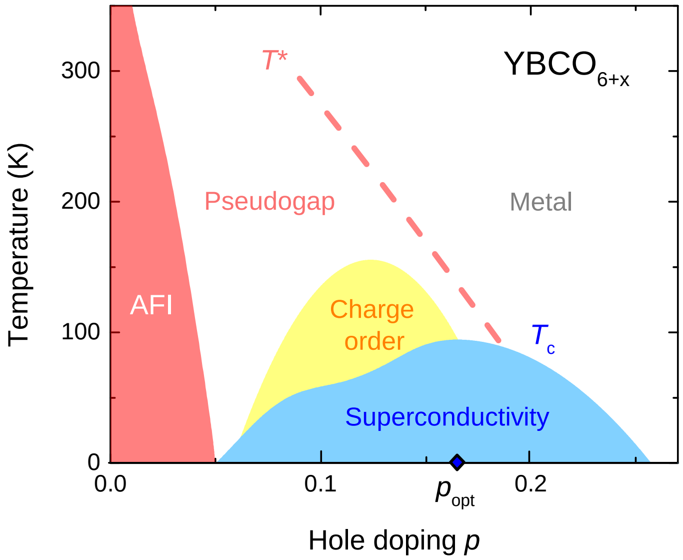

Figure 1.9: **Temperature-doping phase diagram of YBCO$_{6+x}$.** AFI refers to the antiferromagnetic insulator phase which vanished at $p \approx 0.05$. Superconductivity onsets at $p \approx 0.05$ and vanishes at $p \approx 0.27$, which can be accessed by appling pressure [31]. Diamond indicates the optimal doping level, $p_{\mathrm{opt}} \approx 0.16$, that yields the maximum T_c. Charge order has been observed in the underdoped regime ($p < 0.16$) which is the most robust at $p \approx 1/8$. The enigmatic pseudogap state is observed below an broadly-defined T^* line that increases with underdoping. Data from [17, 31, 32, 33, 34].

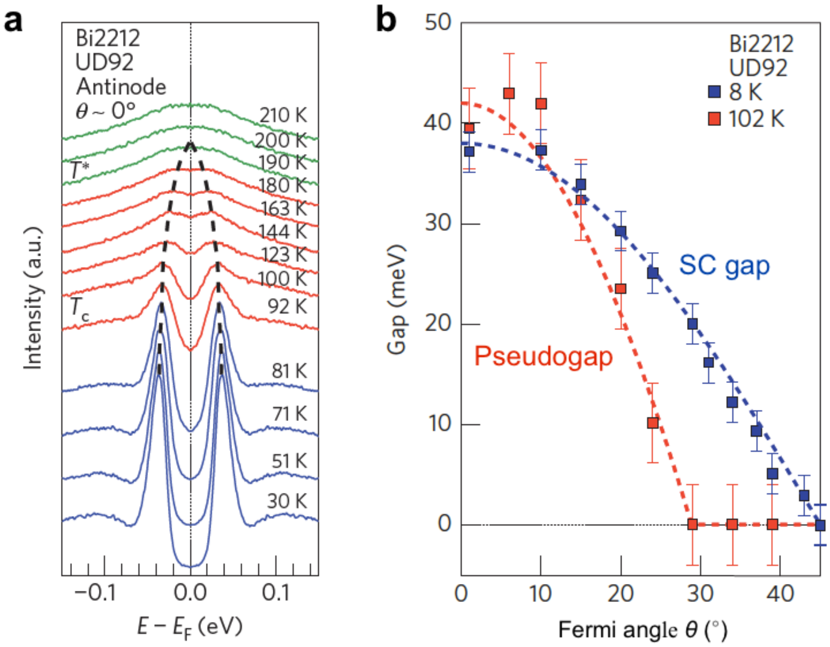

Figure 1.10: **Pseudogap in underdoped cuprate above T_c.** (**a**) Temperature evolution of photoemission intensity near the antinode in underdoped $Bi_2Sr_2CaCu_2O_{8+\delta}$ (Bi2212). Below T_c of 92 K, the density of states at E_F is gapped out by superconductivity whereas a suppression at E_F, known as the *pseudogap*, is seen to persist up to $T^* \approx 190$ K. (**b**) Angular dependence of the superconducting gap and pseudogap size. The two gaps have with similar gap size around the antinode ($\theta = 0°$) and share the same symmetry. Figures reproduced from [27] with permission.

1.3.4 Fermiology

The description of the electronic ground state from which the superconductivity emerges is of fundamental importance towards the understanding of high-T_c superconductivity. The Fermi surface in cuprates has been most extensively studied by photoemission and quantum oscillations [27, 38]. While photoemission detects predominantly the surface and directly probes the single-particle states, quantum oscillations detect the entire sample bulk and probe the collective low-energy excitations. The two techniques provide complementary information on the electronic structure and the findings are briefly reviewed here.

Photoemission

The angular resolution of photoemission technique enables a direct mapping of the Fermi surface in momentum space, as shown in Figure 1.11. In the overdoped regime, a large hole-like cylindrical Fermi surface centred at (π, π) is observed, in accordance with theoretical calculations. In stark contrast, broken Fermi arcs located near the antinodes are observed in the underdoped regime. Studies of the temperature dependence showed that the Fermi arcs grow in length as temperature increases and a full cylindrical Fermi surface is expected to restore above T^*, meanwhile the doping dependence study showed that the Fermi arcs grow as p increases [27]. The topological transition of the Fermi surface from the overdoped regime to the underdoped regime suggests a quantum phase transition occurs at low temperatures. The superconducting gap that onsets below T_c has complicated the analysis of photoemission results at $T < T_\mathrm{c}$ and the precise location of p where the Fermi surface transition occurs remains unclear.

Quantum oscillations

The existence of quasiparticles can be directly confirmed by the observation of quantum oscillations, whose frequency reflects the Fermi surface geometry. The requirement of a sufficient quasiparticle lifetime necessitates the low temperature measurement condition and minimise the effect of thermal fluctuations. Rapid quantum oscillations corresponding to a large Fermi surface occupying 60% of the first Brillouin zone, consistent with photoemission results, have been reported in the overdoped regime [40]; in contrast, slow oscillations corresponding to a small Fermi pocket occupying 2% of the Brillouin zone have been observed in underdoped YBCO$_{6+x}$ [38]. Several schemes of Fermi surface reconstruction have been proposed to yield a small Fermi pocket in the pseudogap state, where an electron pocket is likely to locate at the nodal region [38]. How to connect the zero-field Fermi arcs to the high-field Fermi pocket and whether the quantum oscillations in the underdoped regime reflects the normal-state or vortex-state behaviour remain a subject of active debate.

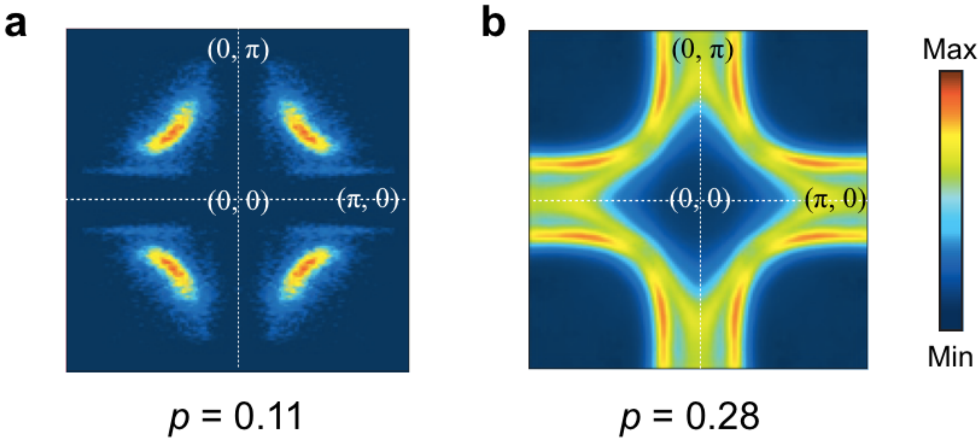

Figure 1.11: **Fermi surface in $YBCO_{6+x}$ observed by photoemission.** (**a**) At $p = 0.11$, broken 'Fermi arcs' are observed around the diagonal in reciprocal space. (**b**) At $p = 0.28$, large cylindrical Fermi surface centred at (π, π) is observed. The observed intensity is indicated by the colour scale. The high spectral intensity outside the closed cylindrical contour in (b) indicates the Fermi surface is hole-like. Figures reproduced from [39] with permission.

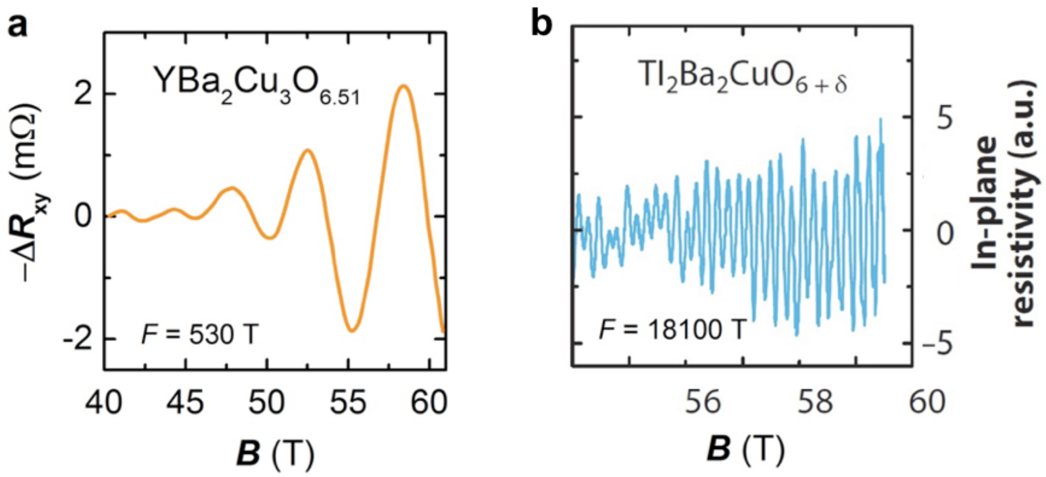

Figure 1.12: **Quantum oscillations in high-T_c cuprates.** (**a**) Quantum oscillations in the Hall resistance in underdoped $YBCO_{6.51}$, corresponding to $p = 0.10$. Slow oscillations with 530 T frequency are observed, corresponding to a surprisingly small Fermi surface. Figure reproduced from [41] with permission. (**b**) Quantum oscillations in the in-plane resistivity in overdoped $Tl_2Ba_2CuO_{6+\delta}$, corresponding to $p = 0.30$. Rapid oscillations with 18 100 T frequency are observed, in agreement with the large Fermi surface observed in photoemission. Figure reproduced from [38] with permission.

1.4 Thesis structure

The structure of the thesis is as follows. Chapter 2 discusses the concept of Fermi surface and how it can be studied using quantum oscillations. Chapter 3 describes the preparation techniques to obtain high-quality single crystals of $\mathrm{SmB_6}$ and YBCO_{6+x}. Chapter 4 discusses the measurement techniques of electrical transport and magnetisation at intense magnetic fields. Chapter 5 presents the discovery of quantum oscillations in $\mathrm{SmB_6}$ that arise from the insulating bulk, complemented by thermodynamic measurements. Chapter 6 presents the discovery of quantum oscillations in a hidden superconducting state of YBCO_{6+x} and signature of pairing correlations at high temperatures. Chapter 7 remarks on the findings of the unexpected existence of Fermi surfaces in these strongly correlated electronic materials, where energy gaps are present at Fermi energy.

Chapter 2

Fermi surface and quantum oscillations

The Fermi surface plays a decisive role in determining the electronic and thermodynamic properties of a solid. Originally conceptualised for systems of non-interacting electrons, the description of Fermi surface has been extended to interacting fermions, although it is still considered as an exclusive property of a metal. In this chapter, the conventional description of the Fermi surface and how it can be studied using quantum oscillations are briefly discussed.

2.1 Fermi surface: a conventional picture

In the free or nearly free electron models, the Fermi surface can be defined as the boundary separating the occupied and unoccupied electronic states. This definition, however, becomes meaningless when the electrons interact with each other. A more general definition for the Fermi surface is *the locus in momentum space that supports low-energy excitations*, whose prerequisite for existence in the conventional picture is discussed below.

2.1.1 Fermi-Dirac distribution

Consider an ensemble of electrons, which are fermions with spin-$\frac{1}{2}$ and obey the Fermi-Dirac distribution:

$$f_{\mathrm{FD}}(E) = \frac{1}{1 + e^{(E-\mu)/k_{\mathrm{B}}T}}, \tag{2.1}$$

where E is the particle energy, μ is the chemical potential, defined as the energy corresponding to $f_{\mathrm{FD}} = 0.5$, and k_{B} is the Boltzmann constant. f_{FD} as a function of energy and temperature is shown in Figure 2.1. At $T = 0$ K, the electrons occupy the available states from the lowest energy up to the Fermi energy E_{F}, defined as $\mu(0\text{ K})$. At finite temperatures, the distribution spreads out and the occupancy above μ becomes finite. The spread of distribution is determined by the thermal energy $k_{\mathrm{B}}T$. Due to Pauli exclusion principle, only the electrons within $k_{\mathrm{B}}T$ of μ can be excited to a state of higher energy and contribute to thermal and electrical properties of low excitation energy ϵ. Strictly speaking, E_F is only defined at 0 K and at finite temperatures one can only measure μ. However, in most metals E_F are on the order of a few eV, equivalently to a few thousands kelvin, hence $E_F \simeq \mu$ with minimal errors for most measurements.

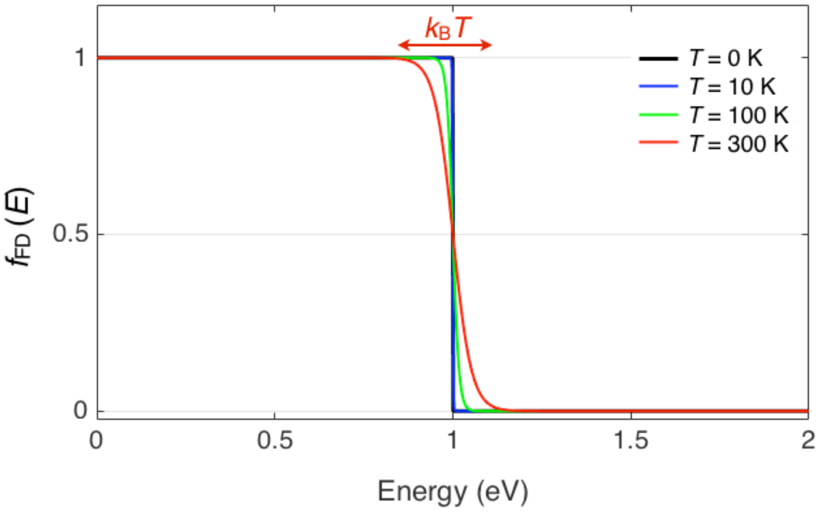

Figure 2.1: **Fermi-Dirac distribution as a function of temperature.** At $T = 0$ K, f_{FD} is a step function that equals to unity below the chemical potential μ, defined as the energy where $f_{FD} = 0.5$, and vanishes above μ. The Fermi energy E_F is defined as $\mu(0\ \text{K})$. As temperature increases, f_{FD} spreads out near μ within $k_B T$. $\mu = 1$ eV is used here.

2.1.2 Electronic band and density of states

For free electrons, the energy levels can be found by solving the Schrödinger equation with the wave function $e^{i\mathbf{k}\cdot\mathbf{r}}$, giving

$$E(\mathbf{k}) = \frac{\hbar^2 k^2}{2m_e}, \tag{2.2}$$

known as the *energy dispersion* relation where $\mathbf{k}$ is the wavevector and m_e is the rest mass of free electron. The energy dispersion in one dimension, represented in the reduced zone scheme, is shown in Figure 2.2. When the crystal lattice is taken into account, the periodic potential from the lattice leads to the opening of energy gaps Δ at the first Brillouin zone boundary, defined by $k = 0, \pm\pi/a$. The continuum of available electronic states between the bandgaps is known as the *electronic band*. The available states per unit energy, or *density of states*, have local maxima near the bandgaps. When E_F falls within the electronic bands, electrons near E_F can be excited to the nearby states with infinitesimal energy ϵ. In contrast, when E_F falls within the bandgap, excitations with energy ϵ are forbidden if $k_B T \ll \Delta$. The manifold of constant energy E_F in momentum space that support excitations at low energy is the *Fermi surface*.

Conventionally, the existence of a Fermi surface requires a finite density of states present at E_F with a sharp step at the chemical potential in f_FD so the locus remain well-defined.

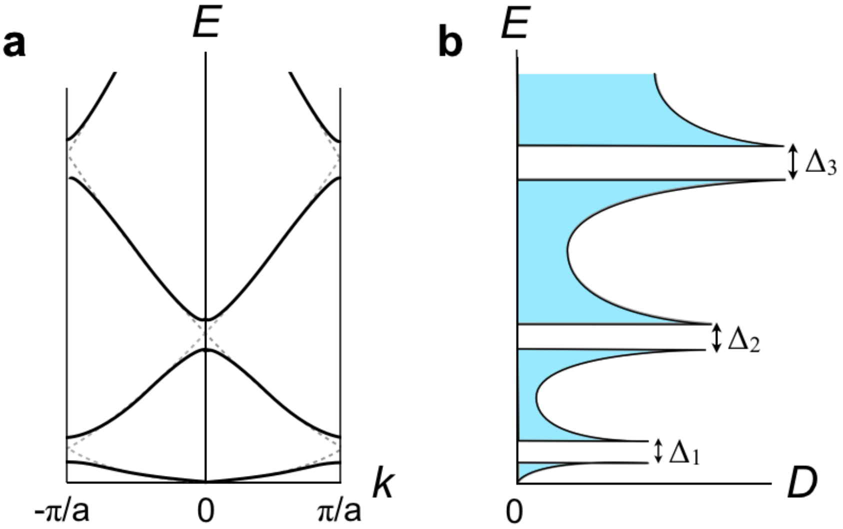

Figure 2.2: **Band structure and density of states of an 1D system in a periodic potential.** (**a**) Electronic bands within the first Brillouin zone ($k = \pm\pi/a$) in the reduced zone representation. Dashed lines illustrate the energy dispersion of free electrons, and solid lines illustrate electronic bands when the lattice potential is considered. Bandgaps open at the zone boundary ($k = 0, \pm\pi/a$). (**b**) Sketch of the corresponding density of states (D), which exhibits local maxima near the bandgaps Δ. Excitations are possible at infinitesimal energy $\epsilon \ll \Delta$ when the Fermi energy falls within the electronic bands.

2.1.3 Landau-Fermi liquid theory

The above discussion is limited to the single-particle picture where electron-electron interaction is ignored. In real materials, the interaction between electrons can have dominating effects on its physical properties. Lev Landau developed a successful theoretical framework, known as the *Fermi liquid* theory, for interacting systems where electron-electron interaction is introduced as a perturbation to the non-interacting case. When the interaction is switched on gradually on a non-interacting system, the system remains in its ground state throughout the process with an one-to-one correspondence between the old and new ground states according to the perturbation Hamiltonian, known as the *adiabatic theorem.* An important implication of the Fermi liquid theory is the concept of the quasiparticle, which is briefly discussed below.

Consider a single electron with wavevector $\mathbf{k}$ and spin σ placed at an energy ΔE above the Fermi surface. This can be expressed as $c^\dagger_{\mathbf{k},\sigma}|\Psi_0\rangle$, where $|\Psi_0\rangle$ is the non-interacting ground state of the electrons and $c^\dagger_{\mathbf{k},\sigma}$ is the creation operator of a particle with wavevector $\mathbf{k}$ and spin

σ. Considering the Coulomb interaction between electrons, the interaction Hamiltonian can be written as

$$H_{int} = \frac{1}{2V} \sum_{\mathbf{k},\mathbf{k}',\sigma,\sigma'} \sum_{\mathbf{q}\neq 0} \frac{4\pi e^2}{q^2} c^{\dagger}_{\mathbf{k}+\mathbf{q},\sigma} c^{\dagger}_{\mathbf{k}'-\mathbf{q},\sigma'} c_{\mathbf{k}',\sigma'} c_{\mathbf{k},\sigma}, \tag{2.3}$$

where V is the volume of the system, $\mathbf{q}$ is the momentum transfer between electrons, and $c_{\mathbf{k},\sigma}$ is the annihilation operator of particle with wavevector $\mathbf{k}$ and spin σ [42]. Turning on the interaction gradually can be expressed as applying a time-evolution operator

$$U = Te^{-\frac{i}{\hbar}\int\limits_{-\infty}^{0} H_{\text{int}}(t)dt}, \tag{2.4}$$

where T is the time-ordering operator. Since U is unitary, the new ground state under application of interaction, $Uc^{\dagger}_{\mathbf{k}\sigma}|\Psi_0\rangle$, can be written as

$$Uc^{\dagger}_{\mathbf{k},\sigma}U^{\dagger}U|\Psi_0\rangle. \tag{2.5}$$

Defining the *quasiparticle creation operator* as $a^{\dagger}_{\mathbf{k},\sigma} \equiv Uc^{\dagger}_{\mathbf{k},\sigma}U^{\dagger}$ and the ground state of interacting system $|\Psi\rangle \equiv U|\Psi_0\rangle$, the time-evolved state now can be expressed as $a^{\dagger}_{\mathbf{k},\sigma}|\Psi_0\rangle$. The description of the added electron is no longer a single particle since its creation operator now involves electron-hole pairs in the interaction Hamiltonian. This collection of electron accompanied by a 'cloud' of electron-hole excitation is known as the *quasiparticle.* The wavevector $\mathbf{k}$ and spin σ are still good quantum numbers hence the Pauli principle and Fermi-Dirac distribution are still obeyed. The quasiparticle behaves differently from a free electron under external excitation, which can be quantified by renormalised parameters such as the effective mass m^*.

2.1.4 Fermi surface of interacting fermions

A comparison of the Fermi surface in the non-interacting and interacting picture is shown in Figure 6.12. In the Fermi liquid picture, the scattering rate Γ between the quasiparticles is proportional to the square of the incident quasiparticle energy ϵ, since the number of available final states of both the incident and scattered quasiparticles is proportional to ϵ. Therefore, $\Gamma \to 0$ at low excitation energy $\epsilon \to 0$, i.e. the quasipartcles near the Fermi surface are long-lived. Remarkably, Luttinger has shown that the Fermi surface survives to any order of perturbation beyond the Fermi-liquid framework [43]. It has been suggested that the Fermi surface may exist beyond the realm of Fermi liquid [44] and search for such Fermi surface has been an ongoing effort.

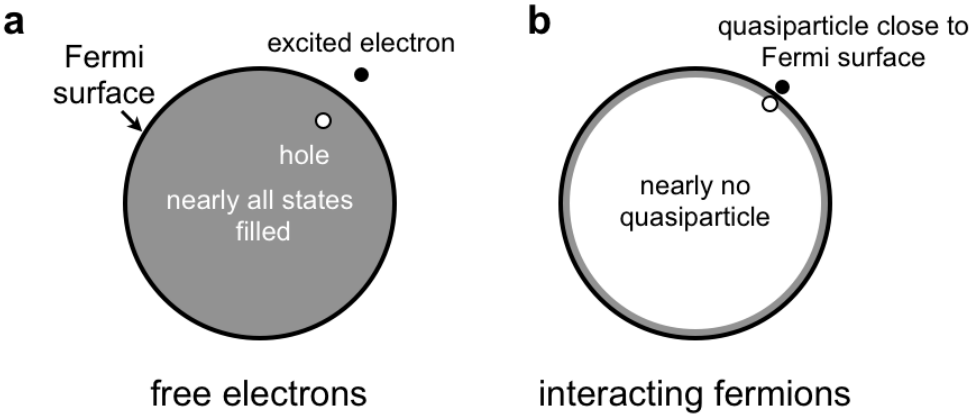

Figure 2.3: **Fermi surface in the free and interacting pictures.** (**a**) For the Fermi gas picture of (nearly) free electrons, nearly all the electronic ground states enclosed by the Fermi surface are filled by electrons. The electron can be excited by an arbitrary energy and creates a hole within the Fermi surface. (**b**) For the Fermi liquid picture of interacting fermions, long-lived quasiparticle can only be created near the Fermi surface, whose excitation creates a quasi-hole near the Fermi surface.

2.2 Basics of quantum oscillations

A powerful experimental technique to directly measure the Fermi surface is quantum oscillations, which relies on Landau quantisation of the energy levels in the presence of a magnetic field at low temperatures. The fundamental ideas and relevant theoretical tools to understand the quantum oscillation work in this thesis are discussed in this section.

2.2.1 Cyclotron motion in a magnetic field

In the presence of an external magnetic field $\mathbf{B}$, the motion of a quasiparticle is determined by the Lorentz force:

$$\hbar \frac{d\mathbf{k}}{dt} = -e(\mathbf{v} \times \mathbf{B}), \tag{2.6}$$

where the velocity of the quasiparticle is given by

$$\mathbf{v} = \frac{1}{\hbar} \nabla_{\mathbf{k}} E(\mathbf{k}). \tag{2.7}$$

The quasiparticle will exhibit cyclotron motion with an orbit along a trajectory of constant energy, as illustrated in Figure 2.4.

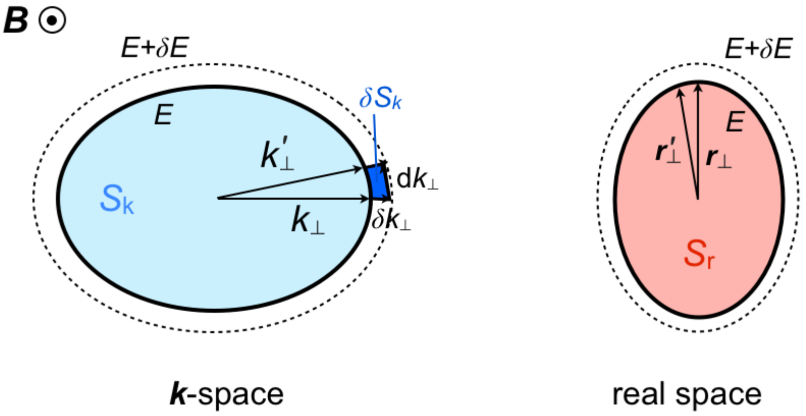

Figure 2.4: **Schematics of cyclotron motion of a quasiparticle in the presence of a magnetic field.** Left: picture in k-space. The quasiparticle with a momentum $k_\perp$ perpendicular to the magnetic field moves along a trajectory of constant energy E (solid ellipse), known as the *cyclotron orbit*, enclosing an area of S_k. The incremental area δS_k with respect to incremental energy δE and movement from $k_\perp$ to $k'_\perp$ is shown in blue. Right: picture in real space. The cyclotron orbit encloses an area of S_r and is a scaled version of that in k-space rotated by 90°.

Substituting (2.7) into (2.6) we have

$$\hbar \frac{d\mathbf{k}}{dt} = -\frac{e}{\hbar} \left(\nabla_{\mathbf{k}} E(\mathbf{k}) \times \mathbf{B} \right), \tag{2.8}$$

and after rearrangement

$$dt = \frac{\hbar^2}{e} \frac{d\mathbf{k}}{\mathbf{B} \times \nabla_{\mathbf{k}} E(\mathbf{k})}. \tag{2.9}$$

Since only the component of $\nabla_{\mathbf{k}} E(\mathbf{k})$ perpendicular to $\mathbf{B}$ will contribute to the cross product, we have

$$dt = \frac{\hbar^2}{eB} \frac{dk_\perp}{\nabla_{k_\perp} E}, \tag{2.10}$$

where $k_\perp$ is the component of $\mathbf{k}$ perpendicular to $\mathbf{B}$. Substituting $\nabla_{k_\perp} E$ by $\delta E / \delta k_\perp$ we have

$$dt = \frac{\hbar^2}{eB} \frac{\delta k_\perp dk_\perp}{\delta E}, \tag{2.11}$$

where $\delta k_\perp dk_\perp$ equals to the incremental area in the plane perpendicular to $\mathbf{B}$ in reciprocal space, denoted by δS_k, with respect to incremental energy δE. By integrating (2.11) over a complete orbital motion, the cyclotron period is given by

$$\tau_{\mathrm{c}} = \frac{\hbar^2}{eB} \frac{\partial S_k}{\partial E}, \tag{2.12}$$

where S_k is the area enclosed by the cyclotron orbit in reciprocal space. Defining the quasiparticle effective mass by

$$m^* = \frac{\hbar^2}{2\pi} \frac{\partial S_k}{\partial E}, \tag{2.13}$$

we can then define the cyclotron frequency as

$$\omega_{\mathrm{c}} = \frac{eB}{m^*}. \tag{2.14}$$

2.2.2 Landau quantisation

The Hamiltonian of a quasiparticle in a magnetic field $\mathbf{B}$ is

$$H = \frac{(\mathbf{p} - e\mathbf{A}(\mathbf{r}))^2}{2m^*}, \tag{2.15}$$

where $\mathbf{p} = -i\hbar\nabla$ is the kinetic momentum operator, $\mathbf{A}(\mathbf{r})$ is the vector potential, and an isotropic effective mass m^* is assumed for the cyclotron motion. Without loss of generality, we can choose the magnetic field $\mathbf{B}$ to be in the $\hat{z}$-direction and use the Landau gauge

$$\mathbf{A}(\mathbf{r}) = Bx\hat{y}, \tag{2.16}$$

(2.15) becomes

$$H = -\frac{\hbar^2}{2m^*}\left(\frac{\partial^2}{\partial x^2}+\frac{\partial^2}{\partial z^2}\right)+\frac{1}{2m^*}\left(-i\hbar\frac{\partial}{\partial y}-eBx\right)^2. \tag{2.17}$$

Since the Hamiltonian commutes with p_y (i.e. no y dependence), p_y can be replaced by its eigenvalue $\hbar k_y$. After rearrangement, we have

$$H = -\frac{\hbar^2}{2m^*}\left(\frac{\partial^2}{\partial x^2}+\frac{\partial^2}{\partial z^2}\right)+\frac{1}{2}m^*{\omega_c}^2\left(x-\frac{\hbar k_y}{m^*\omega_\mathrm{c}}\right)^2. \tag{2.18}$$

Now the Hamiltonian can be understood as a two-dimensional harmonic oscillator in the $\hat{x}-\hat{y}$ plane with a free electron Hamiltonian in the $\hat{z}$-direction. The energy eigenvalues are given by

$$\epsilon(n,k_z) = \hbar\omega_\mathrm{c}\left(n+\frac{1}{2}\right)+\frac{\hbar^2{k_z}^2}{2m^*}, \tag{2.19}$$

where n is the quantum number of the harmonic oscillator and k_z is the wavevector in the $\hat{z}$-direction. The energy of quasiparticle's motion in the plane perpendicular to $\mathbf{B}$ is now quantised. These quantised energy levels are known as the *Landau levels.*

Recalling the Bohr-Sommerfeld quantisation condition

$$\oint(\hbar\mathbf{k}-e\mathbf{A}(\mathbf{r}))\cdot d\mathbf{r}' = 2\pi\hbar(n+\gamma), \tag{2.20}$$

where the integral is performed around a closed path perpendicular to $\mathbf{B}$ and γ is a constant. Using the integrated form of the Lorentz force:

$$\hbar(\mathbf{k}-k_0) = -e(\mathbf{r}-r_0)\times\mathbf{B} \tag{2.21}$$

and the Stoke's theorem we arrive at

$$(n+\gamma)\frac{2\pi\hbar}{e} = \mathbf{B}\cdot\oint(\mathbf{r}\times d\mathbf{r}')-\int_{S_r}\mathbf{B}\cdot dS_r, \tag{2.22}$$

where S_r is the area enclosed by the cyclotron orbit in real space as illustrated in Figure 2.4. The first term in the right hand side is $2BS_r$ since only the $\mathbf{r}$-component perpendicular to $\mathbf{B}$ would contribute, and the second term is $-BS_r$. This remarkable result, known as the *Onsager relation*, shows that the magnetic flux passing through the area enclosed by the cyclotron orbit is quantised in units of flux quantum

$$BS_r = (n+\gamma)\frac{2\pi\hbar}{e} = (n+\gamma)\Phi_0. \tag{2.23}$$

From (2.21) it can be directly deduced that

$$S_k = \frac{e^2B^2}{\hbar^2}S_r, \tag{2.24}$$

which relates the cyclotron orbit area in real space to that in reciprocal space, S_k, which is also quantised according to

$$S_k = (n+\gamma)B\frac{2\pi e}{\hbar}. \tag{2.25}$$

This quantisation condition gives rise to a series of concentric tubes where quasiparticles motion are confined in the presence of a magnetic field, known as *Landau tubes* (see Figure 2.5). At $T = 0$ K, only the states enclosed by the Fermi surface will be occupied. It can be shown [45] that the density of states D of the Landau levels is given by

$$D = \frac{eBV}{2\pi^2\hbar c}. \tag{2.26}$$

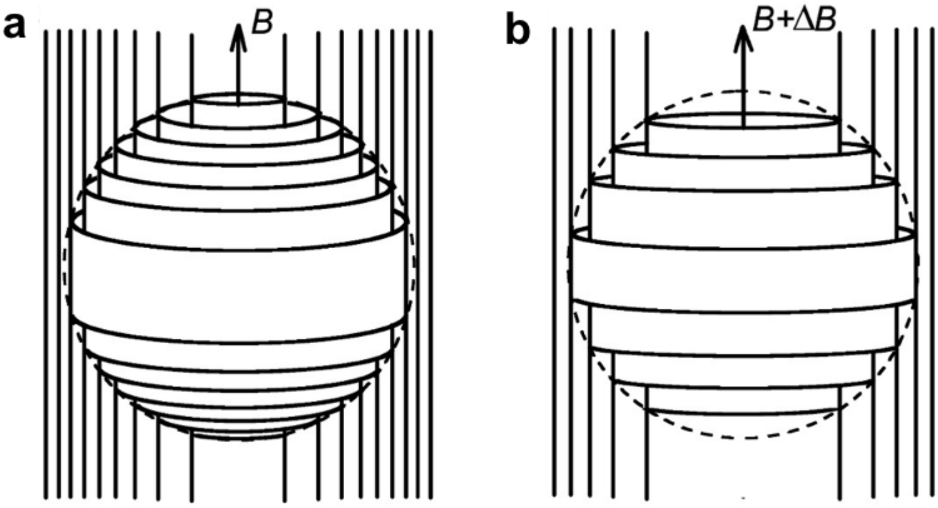

Figure 2.5: **Schematics of Landau quantisation for a spherical Fermi surface in reciprocal space.** (**a**) In the presence of a magnetic field **B**, the allowed electronic states are rearranged into concentric tubes due to Landau quantisation. Only the states enclosed by the Fermi surface are occupied at $T = 0$ K. (**b**) When **B** increases to **B** + Δ**B**, the cross-sectional area of the Landau tubes perpendicular to **B** increases, which reduces the number of Landau tubes enclosed by the Fermi surface. The outermost Landau tube exits the Fermi surface periodically as the magnetic field increases, causing the free energy and related physical quantities to oscillate periodically in $1/B$. Figure modified from [45].

As the magnetic field increases, the Landau tubes accommodated within the Fermi surface shrink in height and increase in radius until the area of the outermost Landau tube reaches the extremal Fermi surface cross-section perpendicular to **B**, before leaving the Fermi surface. Each time a Landau tube leaves the Fermi surface there is a sudden change in the free energy of the system and the density of states at E_{F}. Therefore material properties related to the total energy and density of states exhibit oscillatory behaviour with respect to magnetic field, most notably in magnetisation (de Haas-van Alphen effect) and electrical resistivity (Shubnikov-de Haas effect). Denote B_n as the field at which the n^{th} Landau tube area equals the extremal cross-sectional area of the Fermi surface, then at a higher field B_{n-1} the $(n-1)^{th}$ Landau tube will have the same area. From (2.25) we then have

$$\frac{S_k\hbar}{2\pi e B_n} - \gamma = \frac{S_k\hbar}{2\pi e B_{n-1}} - \gamma + 1. \tag{2.27}$$

We can define

$$F \equiv \frac{1}{\frac{1}{B_n} - \frac{1}{B_{n-1}}} = \frac{\hbar S_k}{2\pi e}, \tag{2.28}$$

where F is the frequency which the Landau tubes pass through the Fermi surface expressed in the units of tesla T.

2.2.3 Fermi surface geometry

Since the quantum oscillation frequency is proportional to the extremal area of the Fermi surface cross-section, one can map out the Fermi surface geometry by rotating the magnetic field, as illustrated in Figure 2.6. For a two-dimensional system, the Fermi surface is an open cylinder along the k_z direction, whereas for a three-dimensional system the Fermi surface is a sphere in the simplest case. The quantum oscillation frequency exhibits a different angular dependence for the 2D and 3D systems as shown in Figure 2.6(c). The angular dependence of quantum oscillations of a more general ellipsoidal Fermi surface is shown in Appendix A. Three-dimensional geometry of the Fermi surface can be reconstructed by band structure calculation considering the experimentally measured angular dependence of oscillation frequency. Quantum oscillations and Fermi surface of the well-studied $\mathrm{Sr_2RuO_4}$ are shown in Figure 2.7, which illustrates the oscillation waveform due to multiple Fermi surface sheets. An advantage of quantum oscillations is the capability in accessing the entire bulk of the sample, whereas spectroscopic probes such as ARPES and scanning-tunneling spectroscopy can only probe the surface. Another advantage is the resolution in the area of a a closed Fermi surface section (commonly referred to as a Fermi pocket). Laser-based ARPES with the highest energy resolution of ≈ 3 meV can achieve a momentum resolution of ≈ 0.005 Å^{-1}, correspondingly to a resolution in Fermi surface area of ≈ 100 T [27, 46]. Meanwhile, a resolution of ≈ 10 T can be commonly achieved with quantum oscillations, at least one order of magnitude better than ARPES.

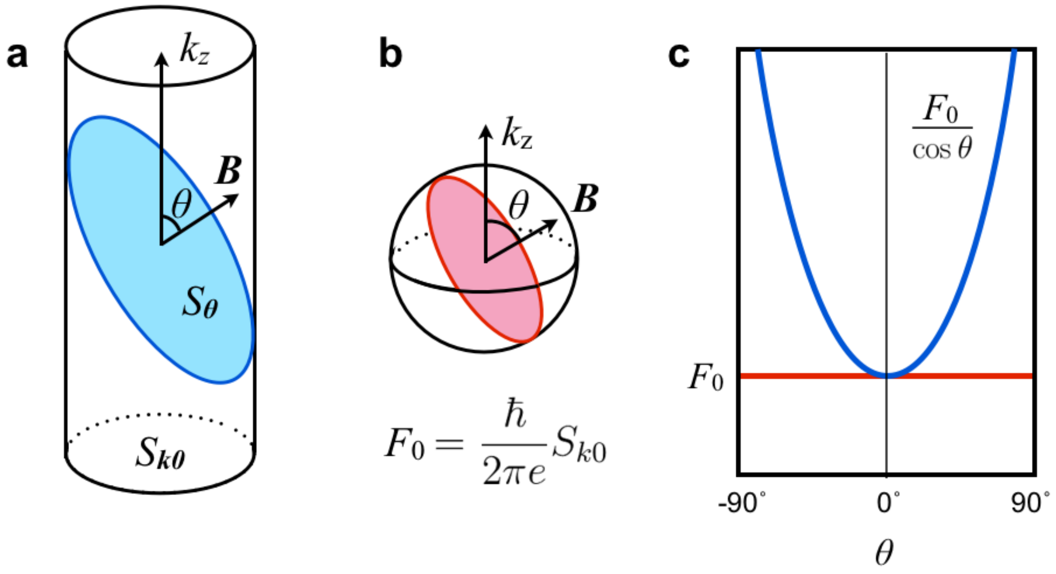

Figure 2.6: **Illustration of the angular dependence of the quantum oscillation frequency.** (**a**) Schematic of a cylindrical Fermi surface from a two-dimensional system without dispersion in k_z. (**b**) Schematic of a spherical Fermi surface from an isotropic three-dimensional system. S_{k0} denotes the Fermi surface cross-section area perpendicular to k_z, defined to be equal for both (**a**) and (**b**), and S_θ denotes the extremal Fermi surface cross-sectional area at field angle θ. (**c**) Angular dependence of the quantum oscillation frequency F. For the spherical Fermi surface (red) F is independent of θ, given by $F_0 = (\hbar/2\pi e)S_{k0}$, while it follows a $1/\cos\theta$ dependence for the two-dimensional Fermi surface and diverges as $\theta \to \pm\, 90°$ (blue).

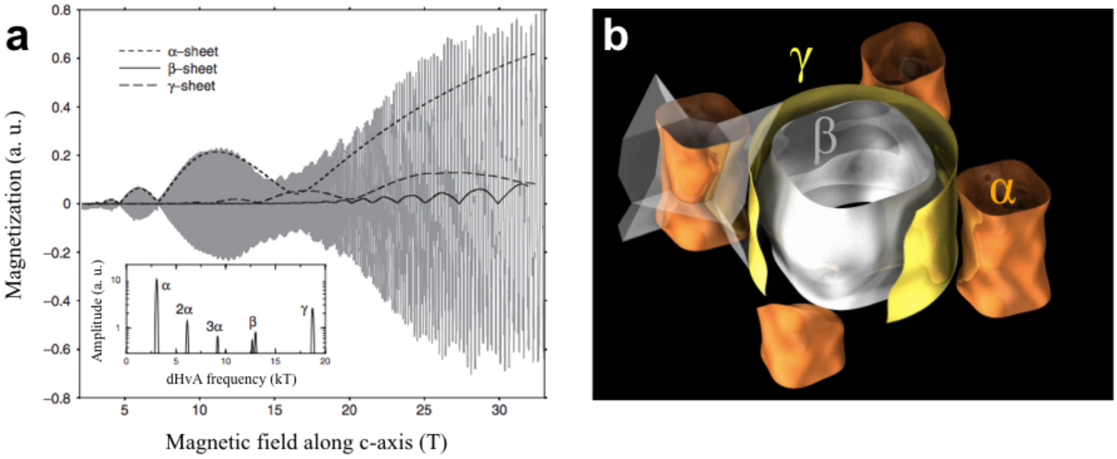

Figure 2.7: **Quantum oscillations and Fermi surface of Sr_2RuO_4.** (**a**) Quantum oscillations in magnetisation with multiple frequencies contributed by the three Fermi surface sheets. Rapid oscillations, periodic in $1/B$, that grows with magnetic field due to the three fundamental frequencies (α, β, and γ) are observed. Beat patterns of the fundamental frequencies, due to the Fermi surface corrugation along $\hat{c}$-axis, are shown in thick black lines. **Inset**: Fourier transform spectrum of the quantum oscillations revealing the α and its harmonics, β, and γ frequencies. (**b**) Calculated Fermi surface with corrugated cylindrical sheets along $\hat{c}$-axis corresponding to the observed oscillations in (a). The α sheet has a smaller cross sectional area, corresponds to a lower oscillation frequency of ≈ 300 T, compared to the β and γ sheets with larger cross-sectional area perpendicular to the $\hat{c}$-axis. Figures reproduced from [47] with permission.

2.2.4 de Haas-van Alphen oscillations

The oscillations in magnetisation, known as the de Haas-van Alphen (abbreviated as dHvA) effect, is the most well-studied type of quantum oscillations. Since magnetisation is a thermodynamic property, it provides a direct insight to the system's total energy and can be calculated from first principles. The formulae derived in reference [45] for the dHvA oscillations and the theoretical waveform and amplitude are presented here, which will be useful in understanding the results presented in the following chapters.

Calculation of bulk magnetisation

The thermodynamic potential Ω of an ensemble of N electrons is defined by

$$\Omega = A - N\mu, \tag{2.29}$$

where μ is the chemical potential and A is the Helmholtz free energy defined as

$$A = U - TS, \tag{2.30}$$

where U is the internal energy and S is the entropy of the system. For a system that obeys Fermi-Dirac statistics, the thermodynamic potential is given by

$$\Omega = -k_{\mathrm{B}}T \sum \ln\left(1 + e^{(\mu-\epsilon)/k_{\mathrm{B}}T}\right), \tag{2.31}$$

where the summation is over all the possible states with energy ϵ. Using the density of states of the Landau levels given by (2.26), the thermodynamic potential becomes

$$\Omega = -k_{\mathrm{B}}T \int_{-\infty}^{\infty} \frac{eBV}{2\pi^2 c\hbar} \sum_i \ln(1 + e^{(\mu-\epsilon_i)/k_{\mathrm{B}}T}) dk_z, \tag{2.32}$$

where i denotes the quantum number of the energy states. (2.32) in effect formulates how to calculate the thermodynamic properties of the system. Next we will present the formulae derived for the oscillating component of magnetisation.

For a two-dimensional system with a fixed number of total electrons, which is the experimentally relevant condition, the magnetisation M is given by

$$M = -\left.\frac{\partial A}{\partial B}\right|_{N,T}. \tag{2.33}$$

Considering the highest occupied Landau level has a quantum number n and the chemical potential $\mu = \epsilon_n$ given by (2.19), we have at $T = 0$ K:

$$U = D\sum_{i=0}^{n-1}\epsilon_i + (N - nD)\epsilon_n, \tag{2.34}$$

where D is the degeneracy of Landau level given by (2.26). It is convenient to define a continuous variable X_0

$$X_0 = S_{k0}c\hbar/2\pi eB = N/D, \tag{2.35}$$

which would give the quantum number n of the highest Landau level. It can be shown that δU, the varying component of (2.34), can be expressed as

$$\delta U = -\frac{1}{2}\frac{\beta B\delta N}{X_0}\left[(X_0 - n)^2 - (X_0 - n) + \frac{1}{6}\right], \tag{2.36}$$

where δN is the change in number of electrons at the highest occupied Landau level and $\beta = e\hbar/m^*c$ [45]. Correspondingly, the oscillatory magnetisation δM is given by

$$\delta M = \frac{\beta\delta N}{\pi}\sum_p \sin\frac{2\pi pX_0}{p}. \tag{2.37}$$

Figures 2.8(a) and (b) illustrate the variation of internal energy and magnetisation as a function of X_0 i.e. the number of filled Landau levels. δU reaches a minimum when X_0 reaches an integer, corresponding to the situation where the highest filled Landau tube has just left the Fermi surface. At $T = 0$ K, δM exhibits a 'sawtooth' waveform that goes backwards with respect to increasing X_0 (Figure 2.8(b)) and forwards with respect to increasing B (Figure 2.8(c)). The corresponding magnetic susceptibility, $d\delta\tilde{M}/dB$, has a 'downwards spike' waveform, which exhibits a discontinuity at integer fillings of the Landau levels. The deviation of these characteristic waveforms in δM and $d\delta M/dB$ from the sinusoidal waveform is a result of the summation of the harmonics as formulated in (2.37). At finite temperatures, the oscillation waveform in magnetisation is rounded at the vertices, due to the smeared Fermi surface (see next section), and correspondingly the susceptibility waveform has an 'inverted U'-shaped waveform.

The waveforms shown in Figure 2.8 are unique to the situation when the chemical potential can jump discontinuously between empty and filled Landau levels, a condition realised when the Fermi surface comprises of a single section. In contrast, when the Fermi surface consists of multiple sections, the chemical potential is pinned to the highest Landau level and the oscillation waveform in magnetisation is reversed compared to Figure 2.8(c), with a negative slope as the field increases, and consequently a 'U'-shaped waveform in susceptibility. The quantum oscillation waveform is a sensitive probe to identify the background of the Fermi pocket that gives rise to the quantum oscillations, which can only be used when the sample is sufficiently pure so higher-order harmonics are not damped out.

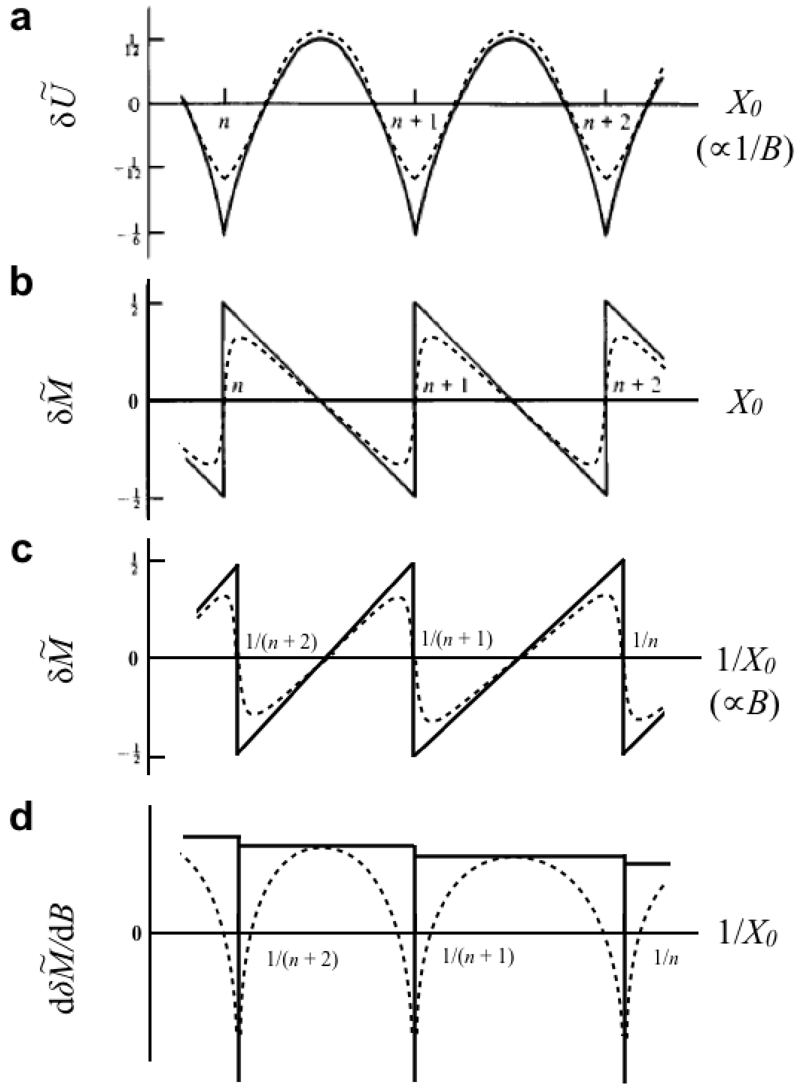

Figure 2.8: **Theoretical quantum oscillation waveforms calculated for a fixed number of total electrons.** Scaled variations in (**a**) internal energy $\delta\tilde{U} = \delta U(2X_0/\beta H\delta N)$ and (**b**) magnetisation $\delta\tilde{M} = \delta M/\beta\delta N$ plotted as a function of $X_0 = S_{k0}c\hbar/2\pi eB$. (**c**) $\delta\tilde{M}$ and (**d**) corresponding magnetic susceptibility $d\tilde{\delta M}/dB$ plotted as a function of $1/X_0$. Solid lines correspond to $T = 0$ K and dashed lines correspond to $T > 0$ K. (**a**) and (**b**) modified from [45].

2.2.5 Lifshitz-Kosevich theory

A generalised formula has been developed by I. M. Lifshitz and A. M. Kosevich to describe the magnetisation of metals at low temperatures [48]. The Lifshitz-Kosevich formula incorporates independent terms to account for various damping effects, known as *phase smearing*, due to thermal fluctuation, impurity scattering, and spin splitting. Physical properties specific to the measured sample, such as quasiparticle effective mass, lifetime, and g-factor, can be extracted by fitting to the Lifshitz-Kosevich formula. The fundamental oscillatory magnetisation ΔM is given by

$$\Delta M = D \cdot R_{\mathrm{T}} R_{\mathrm{D}} R_{\mathrm{S}} \cdot \sin(2\pi F/B + \phi), \tag{2.38}$$

where $R_{\mathrm{T}}, R_{\mathrm{D}}$, and R_{S} are the damping terms due to finite temperature, scattering, and spin-splitting, ϕ is a phase factor that relates to the Berry phase β via

$$\phi = \beta + \delta - \pi, \tag{2.39}$$

where $\delta = 0, \pm\pi/4$ for a 2D and 3D Fermi surface, respectively [49], and D is the infinite field, zero spin-splitting amplitude given by

$$D = -\frac{\mu_{\mathrm{B}} S_{k0}^{3/2} m_{\mathrm{e}}}{2\pi^4 m^*} \sqrt{\frac{B}{F|S''|}}, \tag{2.40}$$

where μ_{B} is the Bohr magneton, F is the oscillation frequency, and $|S''|$ is the second derivative of the extremal Fermi surface area with respect to the effective wavevector along B. Equation (2.40) determines the theoretical oscillation amplitude of the magnetisation without any damping. In experiments, this amplitude will be suppressed due to the various sources of damping discussed below.

Finite temperature

At finite temperature, the Fermi-Dirac distribution is no longer a step function that abruptly vanishes at the chemical potential μ, but with a finite component spreading above μ that is compensated by the loss of weight below μ, as illustrated in Figure 2.1. The corresponding Fermi surface becomes less-defined, or *blurred*, which leads to a reduced amplitude in the quantum oscillation. The reduction in the quantum oscillation amplitude due to finite temperature is given by

$$R_{\mathrm{T}} = \frac{\pi\lambda}{\sinh(\pi\lambda)}, \tag{2.41}$$

where

$$\lambda = 2\pi p \frac{m^* k_{\mathrm{B}} T}{e\hbar B} = 2\pi p \frac{k_{\mathrm{B}} T}{\hbar\omega_{\mathrm{c}}}. \tag{2.42}$$

λ can be thought of the ratio between the thermal energy, $k_{\mathrm{B}}T$, to the magnetic energy, $\hbar\omega_{\mathrm{c}}$. When the magnetic energy scale is much larger than the thermal energy scale i.e. $\pi\lambda \ll 1$, the phase smearing due to temperature is negligible i.e. $R_{\mathrm{T}} \approx 1$. When the thermal energy becomes comparable to the magnetic energy i.e. $\pi\lambda \gtrsim 1$,

$$R_{\mathrm{T}} = \frac{4\pi^2 p k_{\mathrm{B}} T}{\hbar\omega_c} e^{-\frac{2\pi^2 p k_{\mathrm{B}} T}{\hbar\omega_{\mathrm{c}}}}. \tag{2.43}$$

Therefore, an increase in T would decrease the oscillation amplitude exponentially, which affects the harmonics of higher order p even more. The quasiparticle effective mass can be inferred from the temperature dependence of the oscillation amplitude using (2.41), as illustrated in Figure 2.9.

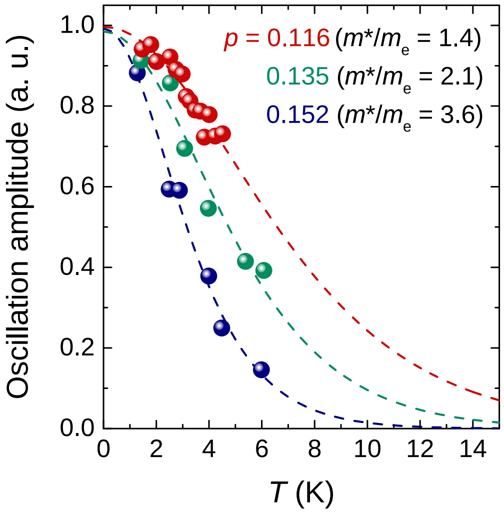

Figure 2.9: **Lifshitz-Kosevich temperature dependence of quantum oscillation amplitude and extraction of quasiparticle effective mass m^*.** Measurements performed on YBCO_{6+x} of three doping levels as indicated. Oscillation amplitudes as a function of temperature are fitted using the Lifshitz-Kosevich formula (2.41) and normalised at $T = 0$ K. The steeper increase in oscillation amplitude with decreasing temperature reflects the heavier m^* of quasiparticle. Data reproduced from [50] with permission.

Finite scattering

Another source of phase smearing is quasiparticle scattering. When the lifetime of quasiparticles becomes finite due to scattering events, the Landau levels become broadened due to the uncertainty principle. This broadening leads to a reduction in oscillation amplitude given by

$$R_{\mathrm{D}} = e^{-\frac{B_{\mathrm{c}}}{B}}, \tag{2.44}$$

and

$$\frac{B_\mathrm{c}}{B} = \frac{\pi p}{\omega_\mathrm{c}\tau} = \frac{\pi p r_\mathrm{c}}{l}, \tag{2.45}$$

where τ is the quasiparticle lifetime, l is the mean free path, and r_c is the cyclotron orbit radius. It is instructive to define the Dingle temperature $T_\mathrm{D} = \frac{\hbar}{2\pi k_\mathrm{B}\tau}$, (2.44) then becomes

$$R_\mathrm{D} = e^{-\frac{2\pi^2 p k_\mathrm{B} T_\mathrm{D}}{\hbar\omega_\mathrm{c}}} = e^{-\frac{B_0}{B}}, \tag{2.46}$$

where B_0 is related to T_D via $B_0 = \frac{2\pi^2 p k_\mathrm{B} m^*}{e\hbar} T_\mathrm{D}$. Now (2.46) is of the same form as (2.43), in which T_D can be interpreted as a temperature scale that quantifies the amount of scattering. T_D and B_0 can be obtained by fitting the oscillation amplitude as a function of magnetic field using (2.46) and be used to evaluate sample quality and infer the mean free path using

$$l = \frac{\pi p \hbar k_\mathrm{F}}{e B_0}. \tag{2.47}$$

Finite spin-splitting

The oscillation amplitude is also modulated due to the quasiparticle spins. In a magnetic field, the spin-degenerate energy levels are separated due to Zeeman splitting by

$$\Delta E = \frac{1}{2} g^* \beta B, \tag{2.48}$$

where g^* is the spin-splitting factor ($g = 2.0023$ for free electron) and $\beta = e\hbar/m^*c$. The effect of this splitting is equivalent to a phase difference ϕ in the oscillations between the spin-up and spin-down quasiparticles [45], given by

$$\phi = 2\pi \Delta E/\beta B. \tag{2.49}$$

The superposition of the spin-up and spin-down oscillations will therefore lead to a modulation of the oscillation waveform given by a prefactor

$$R_\mathrm{S} = \cos\left(\frac{1}{2} p\pi g^* \frac{m^*}{m_\mathrm{e}}\right). \tag{2.50}$$

Chapter 3

Sample preparation

Samples of the highest quality possible are vital for investigating the intrinsic material property without the inclusion of measurement artefacts. I, together with my colleagues, have set up a suite of equipments to prepare SmB_6 and $YBCO_{6+x}$ single crystals of exceptional quality which enables further new discoveries in these already well-studied materials. In this chapter, the working principles and techniques of these sample preparations are described in detail.

3.1 SmB_6 preparation

3.1.1 As-grown crystals

Single crystals of SmB_6 are grown by the group of G. Balakrishnan at the University of Warwick using two different techniques: flux method and floating zone method. Details of the crystal growth can be found in [51], that are briefly described below. In the flux method, commercial SmB_6 powder is mixed with a large excess of aluminium (SmB_6:Al = 0.2:99.8 wt%) and placed in an alumina crucible. The mixture is heated at 1450 °C for four hours to form a homogeneous solution, then slowly cooled down to 650 °C at 4 °C/hr for the single crystals to spontaneously grow out of the solution. Crystals grown by the flux method have naturally exposed {100} and {110} surfaces with sub-millimetre lateral dimensions, as shown in Figure 3.1. Inclusions of aluminium flux are commonly found on the surfaces of flux-grown crystals, which can usually be removed by cleaning with 1% hydrochloric acid. In the floating zone method, commercial SmB_6 powder is firstly pressed into a rod and sintered at 1550 °C with flowing argon. The sintered rod is then heated above its melting point by focusing intense light generated by four Xenon arc lamps into a small region of the rod. Single-crystalline regions form as the melted zone travels through the length of the rod. Crystals grown by the floating zone method are exempt from the contaminations due to crucible or flux, and can be grown into large boules of several centimetres in length. However, the crystal orientation is pre-determined by the seed

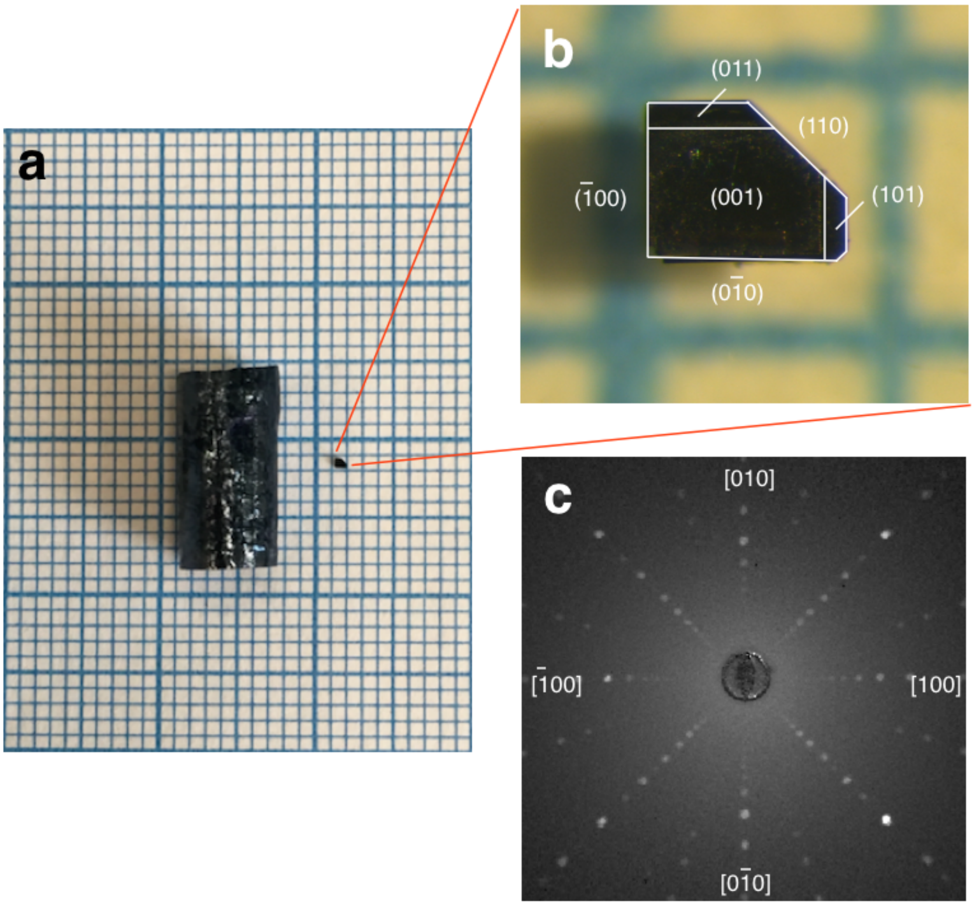

Figure 3.1: **Pristine SmB$_6$ single crystals.** (**a**) Pictures of a single-crystalline boule grown by floating zone method (left) and a small crystal grown by flux method (right). (**b**) Magnified view of the flux-grown crystal showing the high symmetry crystallographic planes {100} and {110}. (**c**) Laue pattern of SmB$_6$ with incident X-ray beam perpendicular to the (001) plane.

used for the growth and often misaligned with the boule's principal axes. Crystal orientation is identified using Laue diffractometer, then discs of $\approx$ 3 mm in diameter and $\approx$ 500 μm in thickness with dominant {100} or {110} surfaces are made using diamond cutting wheel for further preparation.

3.1.2 Sectioning

Flux-grown crystals are usually of suitable size for transport and quantum oscillation measurements without further treatment. Floating-zone crystals, on the other hand, need to be sectioned into pieces of approximately 1 mm × 1 mm × 0.4 mm for high-field measurements. This can be done by a precision wire saw with 50 μm or thinner tungsten wire or by LatticeAx 120, a device developed for wafer cleaving by LatticeGear, as shown in Figure 3.2. Cuts of arbitrary crystallographic directions can be made using the wire saw, but it usually takes sev-

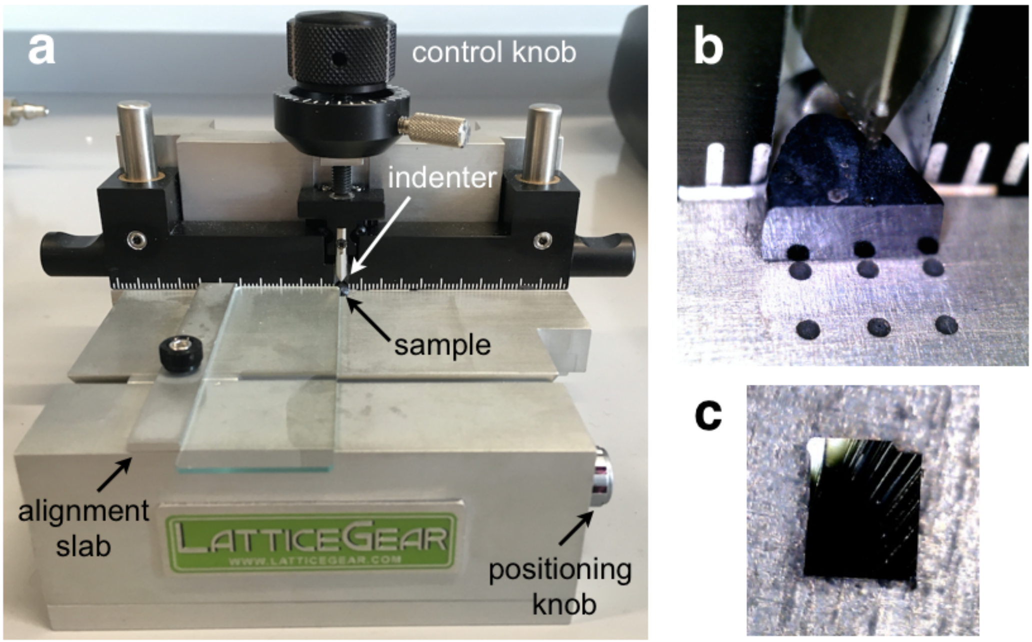

Figure 3.2: **Cleaving device and cleaved SmB_6 crystal.** (**a**) The LatticeAx 120 cleaving device. Sample is placed below the diamond indenter with <100> aligned against the alignment slab using a glass slide. The indenter can be moved horizontally using the positioning knob with one mark corresponding to ≈ 0.25 mm. Cleaving is done by lowering the indenter with the control knob until the sample breaks. (**b**) Zoom-in view of the indenter and a SmB_6 disc with cleaved surface. (**c**) A rectangular SmB_6 sample with ≈ 1 mm sides made by cleaving.

eral hours to cut through a thickness of 500 μm with considerable material loss. Well-defined cleaved surfaces can be achieved within minutes using LatticeAx 120 regardless of the sample thickness. However, SmB_6 preferentially cleaves along the <100> directions, hence the cleaved surfaces can only be made with {100} orientation, limiting the flexibility of sample preparation. Another drawback with cleaving is the yield. Cleaved edges usually terminate at surface steps or internal cracks, which often leaves incomplete cuts and sample wastes. The usage of wire saw and cleaver can be combined to section samples with maximal efficiency.

3.1.3 Electropolishing

Samples cut by a diamond wheel or a wire saw suffer from surface damage and strain that can propagate into the crystal bulk. We have developed a technique to polish the sample surface electrochemically, known as *electropolishing*, to remove the damaged surface layer and improve sample quality. The working principle of electropolishing is illustrated in Figure 3.3. The positive terminal of a DC power supply is connected to the sample that acts as anode, and the negative terminal is connected to a platinum electrode that acts as cathode. Both the sample

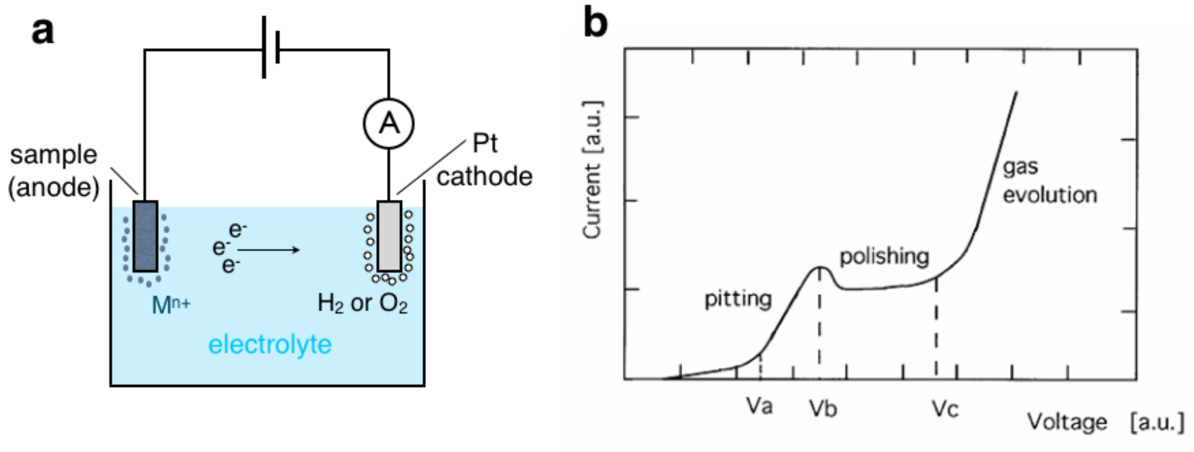

Figure 3.3: **Working principle of electropolishing.** (**a**) Schematic diagram of the electropolishing setup. Metallic sample and Pt electrode are immersed in a liquid electrolyte and connected to a DC voltage source. (**b**) Characteristic current-voltage curve of the electropolishing process adapted from [52]. The voltage range for a polishing effect is between V_b and V_c with the best result achieved at just below V_c.

and electrode are immersed in an acidic solution that serves as electrolyte. A current flows through the anode, which oxidises the sample and releases electrons which are collected at the cathode, which can be illustrated with the following equations:

$$\mathrm{M} \rightleftharpoons \mathrm{M^{n+}} + \mathrm{ne^-}(\mathrm{Anode}) \tag{3.1}$$

$$2\,\mathrm{H_2O} + 2\,\mathrm{e^-} \rightleftharpoons \mathrm{H_2} + 2\,\mathrm{OH^-}(\mathrm{Cathode}) \tag{3.2}$$

The surface layer of the metal object dissolves as a result of the oxidisation reaction. A larger electric field will be established at the protruding parts (hence a faster reaction rate) compared to the recesses parts of the surface, resulting in a polishing effect and ideally an eventual uniform surface.

Several parameters affect the electropolishing results, including temperature, acid concentration, and, mostly importantly, the applied voltage. A schematic current-voltage characteristic is shown in Figure 3.3(b). It has been established that the ideal working voltage range is the plateau between V_b and V_c [52]. Below V_a, the reaction is effectively etching rather than polishing which results in a pitted surface; above V_c, gas bubbles start to form and can be trapped at sample surface, which will also result in a pitted surface. The $I-V$ curve, in theory, provides a guidance for the ideal operating voltage; however, in practice, the fluctuation in the current reading is very large for a small sample and it is very difficult to establish the $I-V$ curve with reasonable precision. Much of the optimisation is done by trial-and-error. For $\mathrm{SmB_6}$, we have found that the operating voltage between 10 to 12 V gives consistently good results.

We use the commercial Model 451 Electrolytic Crystal Polisher from South Bay Technology,

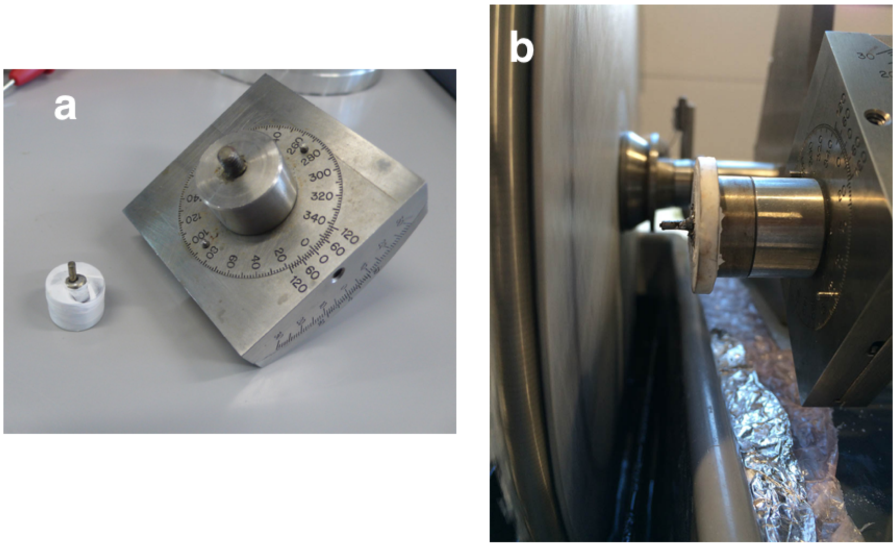

Figure 3.4: **Setup of Model 451 Electrolytic Crystal Polisher.** Pictures of (**a**) sample holder (left) and goniometer (right) and (**b**) Zoom-in view of the polishing wheel and and a mounted sample.

which requires an external DC voltage source and ammeter to complete the setup. Sample is mounted onto a homemade sample holder using a conductive wax, a mixture of CrystalBond 509 and silver powder ($>$ 80 vol.%). It is important to keep the targeted surface parallel to the base of the sample holder so the crystal orientation can be maintained. The platinum-plated polishing wheel is covered by a Teflon cloth with its lower part immersed in 1% perchloric acid-methanol solution in a PVC container. As the wheel rotates, the acid is uniformly distributed over the wheel. The acid solution is cooled by a salt-ice bath (1:3 by weight) below 12 °C to ensure the reaction proceeds in a controlled manner. A thermocouple with corrosion-resistant coating is in contact with the back of the polishing wheel for temperature monitoring.

With the parameters described above (voltage = 10 - 12 V, $T_{\text{acid}} < 12$ °C), a current $\approx$ 10 mA and polishing rate of $\approx$ 10 μm/minute is usually obtained with samples of surface area $\approx$ 1 mm^2. The optimal polishing time seems to be between 4 to 5 minutes when a smooth surface is just formed. Further polishing appears to give the crystal rounded edges and a less-defined surface orientation.

3.1.4 Wiring

Contact resistances $< 10\ \Omega$ between electrical leads can be made using conducting adhesives with electropolished or cleaved SmB$_6$ samples, while pristine flux-crystals usually give a contact resistance in the range of tens to hundreds of ohms. Spot welding with an applied voltage of 5.7 V can reduce the contact resistance to sub-ohm, if needed.

3.2 YBCO_{6+x} preparation

A significant amount of research effort in the field of high-T_c superconductivity has been dedicated to improve the sample quality and the results have been rewarding. YBCO_{6+x} is known to be the cleanest cuprate in which large quantum oscillations have been consistently observed [41], and Liang [53] and Lin [54] are known to produce YBCO_{6+x} single crystals of exceptional quality. I have combined their approaches in sample preparation and optimised the procedure in the order presented in the following sections.

3.2.1 Self-flux growth

YBCO_{6+x} single crystals grown by the self-flux technique have proven to be of exceptionally high quality [53]. In the self-flux technique, the BaO-CuO flux used contains the chemical components of YBCO_{6+x} with lower melting points, hence eliminates the contamination in the crystals from the flux. The high temperature part of the pseudo-binary phase diagram of YBCO_{6+x}-BaCuO_2 system is shown in Figure 3.5. An issue intrinsic to the self-flux method is the high reactivity of BaO-CuO flux, which reacts with most crucible materials and leads to sample contamination. Two materials have been shown to be a good choice for crucibles: yittria-stablised-zirconia ($\mathrm{Y_2O_3}$-$\mathrm{ZrO_2}$, or YSZ) and barium zirconate ($\mathrm{BaZrO_3}$).

In YSZ, 3 to 8 mol.% of $\mathrm{Y_2O_3}$ is added into $\mathrm{ZrO_2}$ to prevent a tetragonal-monoclinic structural transition occurring at 1200 °C in pristine $\mathrm{ZrO_2}$, which can crack the ceramic. BaO in the flux reacts with $\mathrm{ZrO_2}$ at high temperature, forming a thick layer of flux on the crucible wall rendering a low growth yield and crucibles that cannot be re-used after growth. $\mathrm{Y_2O_3}$ in the crucible can also be dissolved into the flux and change the stoichiometry of starting materials. Nevertheless, high-quality YBCO_{6+x} single crystals can still be obtained using YSZ crucibles. To address the issues pertinent to YSZ, Liang [53] and Erb [55] have reported that the use of homemade $\mathrm{BaZrO_3}$ crucibles can solve these issues pertinent to YSZ and claimed a superior sample quality using $\mathrm{BaZrO_3}$ crucibles. However the $\mathrm{BaZrO_3}$ powder with Ba:Zr ratio between 0.992 and 1.008, a requirement for a leak-tight ceramic, is not commercially available and difficult to make, limiting the widespread use of $\mathrm{BaZrO_3}$ crucibles for YBCO_{6+x} growth.

We have performed measurements on YBCO_{6+x} single crystals grown from both YSZ crucibles at Cambridge and Max Planck Institute for Solid State Research, and $\mathrm{BaZrO_3}$ crucibles at University of British Columbia. The best quantum oscillations with less Dingle damping were observed in crystals grown using YSZ crucibles. Single crystals studied in this thesis were grown using YSZ crucibles.

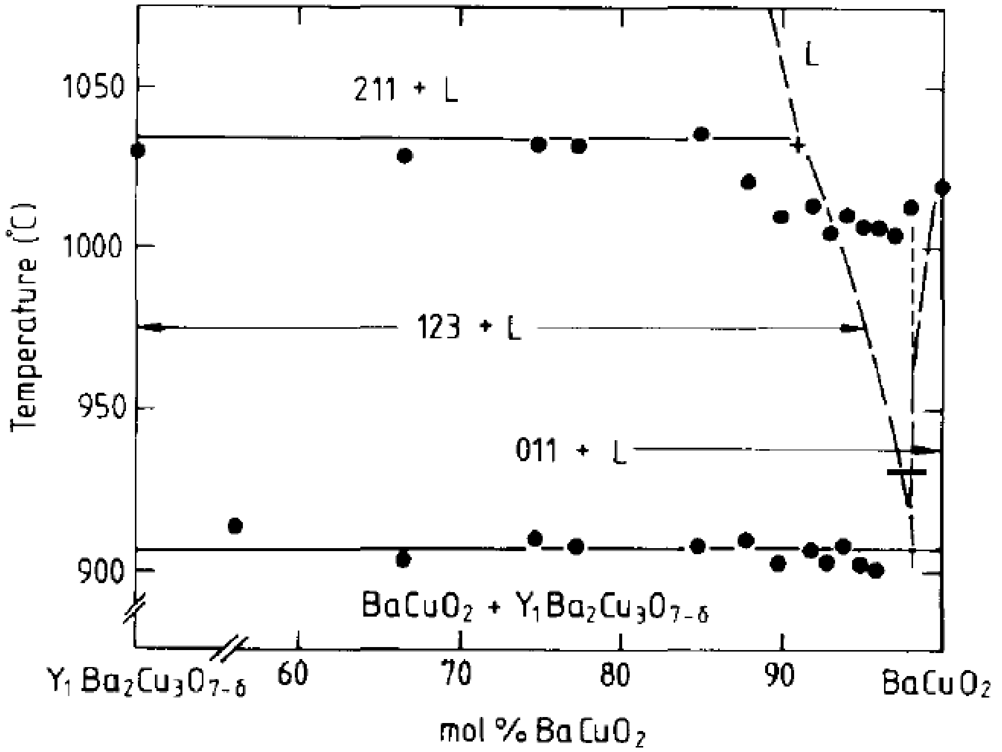

Figure 3.5: **High temperature part of the pseudo-binary phase diagram for $YBCO_{6+x}$-$BaCuO_2$ in ZrO_2 crucible.** L refers to the liquid phase, 211 refers to the parasitic phase Y_2BaCuO_5, 123 refers to the targeted phase $YBa_2Cu_3O_{6+x}$, and 011 refers to the flux phase $BaCuO_2$. The ideal starting material composition is at the peritectic point marked by the cross symbol, where the $YBCO_{6+x}$ starts to form without the presence of the parasitic Y_2BaCuO_5 phase. Figure from [56].

3.2.2 Sample selection

Typically tens to hundreds of single crystals with varying sizes and shapes can obtained in one growth. The ideal sample size and geometry depends on the experiment. For in-plane electrical transport measurements, rectangular platelets of dimensions ≈ 1.5 mm × 0.5 mm × 0.05 mm with clean, flux-free surfaces are ideal. The longitudinal resistance R_{xx} and Hall resistance R_{xy} are given by

$$R_{\mathrm{xx}} = \rho_{\mathrm{xx}}(l/wt) \tag{3.3}$$

$$R_{\mathrm{xy}} = R_{\mathrm{H}}B_{\mathrm{z}}/t, \tag{3.4}$$

where l, w, t, ρ_{xx}, R_{H}, are the length, width, thickness, longitudinal resistivity, and Hall coefficient of the sample, respectively, and B_{z} is the magnetic field applied perpendicular to the (100) plane. Since R_{xx} scales with l/wt and R_{xy} scales with $1/t$, it is important to use samples with an aspect ratio $l/w \gtrsim 3$ and thickness $t < 100$ μm to maximise the signals and ensure a uniform current distribution. Samples with $l/w \gg 3$ or $t < 20\mu$m, however, are very fragile and tend to break during the multi-stage preparation. A rectangular shape with well-defined l and w is important for ρ_{xx} calculation and twin-removal (see Section 3.2.5). Clean and flat surface without residual flux is indicative of a fully detwinnable crystal with good contact resistance. If a sample is too large or has unparallel edges, it is possible to cleave it with a sharp scalpel along the crystalline $\hat{a}$- or $\hat{b}$-axis if it is thinner than 100 μm. Alternatively, samples can be trimmed using the wire saw, with a significant loss of material.

For quantum oscillation measurements using contactless techniques, such as magnetic torque or proximity effect measurements, signals scale with sample size so dimensions of ≈ 1.5 mm × 1.5 mm × 0.15 mm are preferred. Samples of much larger size are more likely to contain impurities or defects and suffer from significant self-heating in pulsed fields.

3.2.3 Electrical contact

The outermost layer of YBCO$_{6+x}$ is insulating due to the formation of BaCO$_3$ from the BaO layer reacting with CO$_2$ in the atmosphere. The contact resistance is in the range of kΩ to MΩ when leads are made using conducting adhesives without any further treatment, rendering it unusable for reliable measurements. Good electrical contacts with sub-ohm resistances can be achieved by depositing gold pads onto the sample surface and annealing at high temperature for the gold to diffuse through the insulating layer into the bulk. Annealing at 500 °C for two days is usually sufficient to bring the contact resistance to a few ohms, if not sub-ohm.

The mask for gold deposition is made by cutting a 10 μm aluminium foil with a scalpel into the shape outlining the standard six-contact configuration, as shown in Figure 3.6. To prevent the aluminium foil from moving during the cutting, it is glued to a flat metal plate using a thin

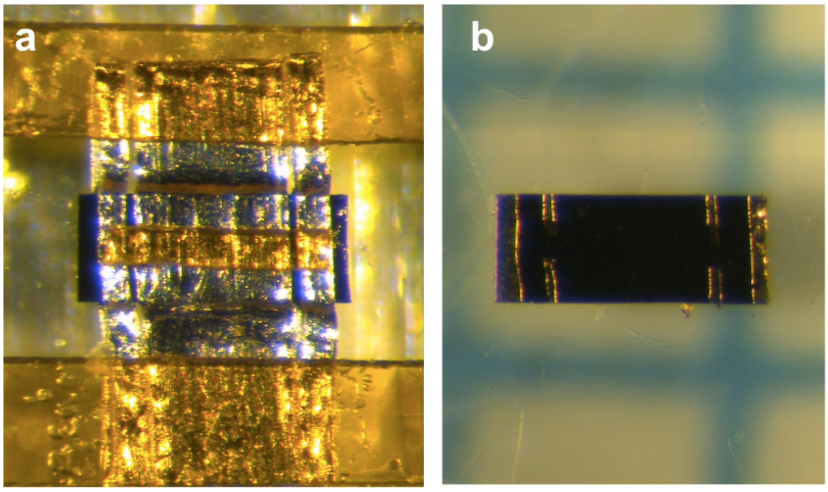

Figure 3.6: **Making electrical contact for $\mathbf{YBCO_{6+x}}$.** (**a**) A $YBCO_{6+x}$ sample masked by 10 μm-thick Al foil with six-contact configuration, then stuck down to a glass slide using Kapton tape. (**b**) The same sample after 160 nm and 80 nm of gold is deposited on the top and side surfaces, respectively, by thermal evaporation.

solution of CrystalBond 509 in acetone. Slits of 50 μm width can be made with sharp No. 11 scalpel blade. There is a compromise when preparing the mask dimensions. Wide slits would increase the error in resistivity calculation while narrow slits would increase the difficulty in sample wiring and potentially contact resistances. Distances between the voltage slits should be maximised for maximal signal without risking the voltage leads to be shorted to current leads. After a mask is cut, it is folded around the crystal tightly to expose the targeted area then stuck down to a glass slide using Kapton tape. A thin strip of Kapton tape is used to divide the parallel voltage slits into four voltage pads and prevent the relative movement between the mask and the sample.

Gold pads of 100 nm in thickness are deposited using either magnetron sputtering or thermal evaporation. The advantage of magnetron sputtering is that the entire volume enclosed by the Ar plasma will be deposited at the same time. It is important to deposit both the top surface and the sides of the sample with gold to eliminate the contribution from the $\hat{c}$-axis to the in-plane signals, as the $\hat{c}$-axis resistivity is several orders of magnitude higher than the in-plane resistivity. The sputtered film also has a better adhesion to the sample surface, and often lower contact resistances, than the evaporated film. However, the plasma often goes underneath the mask if there is a gap between the mask and the sample, which gives pads with a diffusive (rather than well-defined) boundary and can lead to shorts between the voltage and current leads. The advantage of thermal evaporation is that it is a directional technique and deposits pads with clear boundary. Two evaporation sessions, however, are needed to deposit gold on all sides of the crystal. Samples are oriented at an angle such that edges are facing towards the gold source each time.

3.2.4 Oxygen setting

A major advantage of YBCO$_{6+x}$ over other cuprates is that the doping level p can be changed by varying the oxygen content without introducing additional disorder. The equilibrated oxygen content x in YBCO$_{6+x}$ is a function of oxygen partial pressure and temperature, which has been established in [57]. The time needed to reach equilibrium can be estimated from the diffusion time constant τ given by

$$\tau = \frac{t^2}{\pi^2 D_0}\, e^{\frac{E_\mathrm{a}}{k_\mathrm{B}T}}, \tag{3.5}$$

where t is the sample thickness, D_0 is the diffusion constant of 10^{-2} cm^{2}s^{-1}, and E_a is the activation energy of 0.8 eV [58]. A duration of 10τ is sufficient to achieve a homogenous distribution of oxygen throughout the sample bulk. A continuous flow of ultra-high purity (99.9999%) oxygen is maintained throughout the annealing process. At the end of the annealing, samples are quickly quenched into liquid nitrogen to prevent oxygen escaping from sample surface and ensure sample homogeneity.

The diffusion of gold pads is done together with the oxygen setting, without the process of sealing the contacted samples with YBCO$_{6+x}$ ceramic powder of the same doping in a quartz ampoule and annealing at 570 °C as reported in [53]. I have found that samples suffer a oxygen loss from the sealing and annealing process, likely due to the voids created by the ceramic powder in the ampoule. It is also difficult to retrieve single crystals from ceramic powder. Samples with $x \approx 1$ are annealed at 520 °C for 48 hours to diffuse the gold effectively into the bulk, before the required temperature to achieve the desired oxygen content is set for an extended period.

3.2.5 Twin removal

YBCO$_{6+x}$ with x > 0.3 is orthorhombic at room temperature with the crystalline $\hat{b}$-axis longer than the $\hat{a}$-axis [59]. The random distribution of $\hat{a}$- and $\hat{b}$-axis in an oxygenated crystal leads to a random orientation of (100) and (010) planes and forms *twin* domains which can be identified using an optical microscope. The formation of twins not only makes the crystal apart from being truly single-crystalline but also causes stresses and segregation of oxygen on the twin boundaries. Application of a uniaxial stress of 100 MPa at 250 °C for 20 minutes can remove these twins, realising a homogeneous, stress-free YBCO$_{6+x}$ single crystal [53]. A de-twinning apparatus has been designed and manufactured in our lab with modification from [54]. The stress is applied through a pair of stress plates capped with 50 μm Au foil as a buffer layer. Samples are kept under vacuum during de-twinning and no loss of oxygen has been observed after the process.

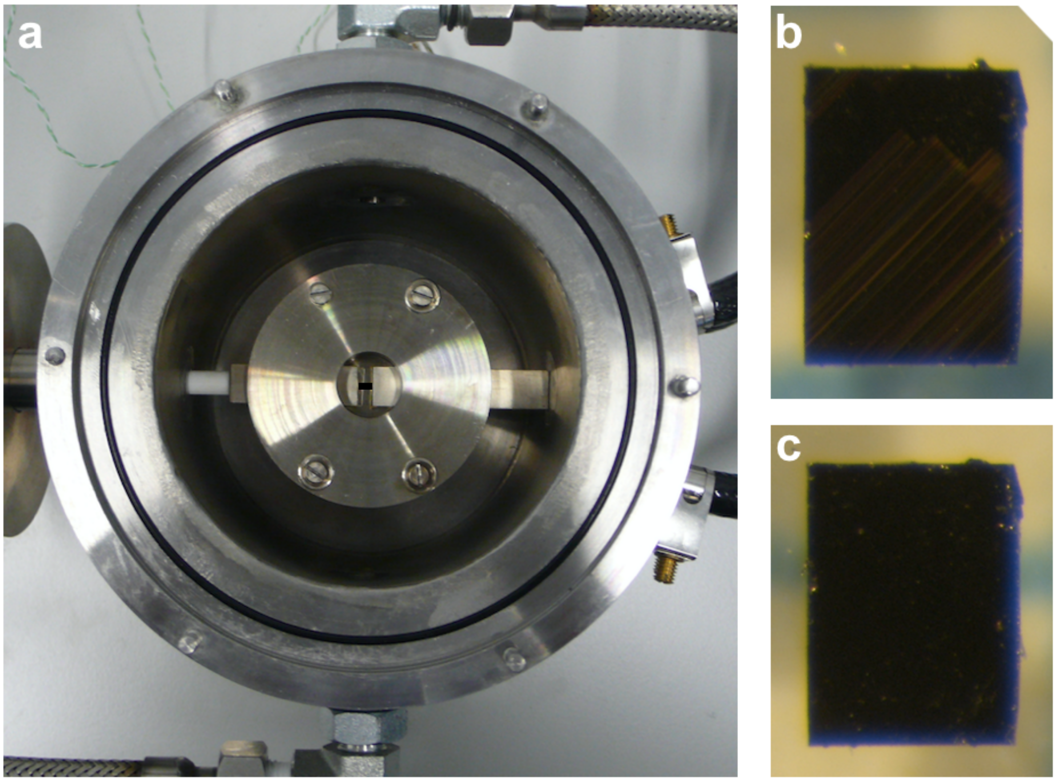

Figure 3.7: **Twin-removal of $\mathbf{YBCO_{6+x}}$ single crystal.** (**a**) Sample space of the de-twinning apparatus built in the Cavendish laboratory. Sample is placed on top of a rectangular quartz rod in the centre of the chamber. Stress of 100 MPa is applied to the crystal via a pair of stress plates capped with 50 μm-thick gold foil using a force feedthrough on the left. (**b**) A twinned $YBCO_{6+x}$ single crystal with twin boundary running along the diagonal which can be identified by the coloured-lines. (**c**) The same crystal after the twin-removal treatment. Diagonal lines in (b) are no longer visible.

3.2.6 Oxygen-chain ordering

Superstructures with a periodicity larger than the lattice parameter of $\hat{a}$-axis is known to be present in $YBCO_{6+x}$ with $0.3 < x < 0.85$ at room temperature, due to the preferential distribution of the Cu-O chains [59]. The so-called *ortho-N* order is illustrated in Figure 3.8, with N corresponding to the superstructure periodicity in the unit of $\hat{a}$-axis lattice constant. The conditions for oxygen-chain ordering, done by annealing at a temperature 10 °C below the phase boundary of the ortho-N phase for one week, are summarised in Table 3.1. Disordering of the oxygen chains, reported to affect the amplitude of quantum oscillations in $YBCO_{6+x}$ with $p \approx 0.12$ and ≈ 0.13 [50], can be done by heating at 120 °C for one hour followed by quenching into liquid nitrogen. Measurements are to be done quickly after quenching to prevent the re-ordering of oxygen chains, especially for $p \approx 0.12$ samples for its low lying phase boundary of 40 °C.

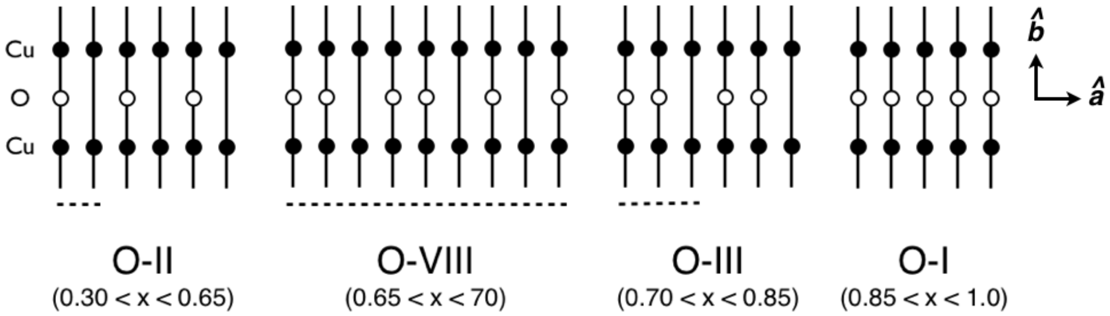

Figure 3.8: **Cu-O chain superstructure in $YBCO_{6+x}$ with $0.3 < x < 0.85$.** Schematic diagram of various superstructures present in $YBCO_{6+x}$ with the vertical lines representing the Cu-O chains along $\hat{b}$-axis. Dashed line indicate the superstructure periodicity.

Table 3.1: **Temperature profiles used for oxygen-chain ordering in $YBCO_{6+x}$.**

Ortho-order	Temperature profile
O-II	92 °C for two days, followed by 67 °C for five days
O-VIII	30 °C for one week
O-III	65 °C for one week

3.2.7 Preparation sequence

As presented, the sample preparation of $YBCO_{6+x}$ involves multiple steps and the order of steps should be optimised for maximum effectiveness. The guiding principle is that the sequence of preparations should follow in order of decreasing temperature, otherwise the process carried out at an earlier stage may be nulled. For example, annealing a de-twinned crystal above 400

°C may lead to re-twinning, and detwinning an ortho-ordered sample would disrupt the chain ordering. Magnetisation characterisation should be performed after oxygen setting so only the samples with sharp transition proceed for further treatments. I found that pre-selecting samples with sharp transition for electrical contacting is not an effective strategy, as a small variation within a single batch could lead to significantly different sample quality i.e. a good sample in one batch is not necessarily good in another batch. It is more useful to prepare several samples for a batch, choose the superior ones for further preparation, and save the inferior ones for later batches. Table 3.2 summarises the parameters used for thermal treatments of samples studied in this thesis.

Table 3.2: **Experimental parameters for thermal treatments of $\mathbf{YBCO_{6+x}}$.** p refers to the approximate hole dopings, T_{set} and t refer to the annealing temperatures and durations used for setting oxygen content under 1 bar oxygen, respectively, and O-N refers to the oxygen-chain order, if exists.

x	p	T_{set}(°C)	t (days)	O-N
0.55	0.11	723	3	II
0.67	0.12	668	3	VIII
0.75	0.13	626	3	III
0.84	0.14	580	5	III
0.87	0.15	551	5	-
0.92	0.16	520	5	-
0.97	0.17	375	20	-
Ca-doped	0.18 - 0.20	375	20	-

3.2.8 Wiring

The wires attached to the sample for transport measurements suffer from large environmental vibrations due to running cooling water and pulsed magnet movement, as well as the torque exerted on any open loop due to the intense magnetic field. A broken wire can end a measurement prematurely. I have learnt the technique to wire sample securely to survive such conditions from Dr Cyril Proust at LCNMI in Toulouse, as described below:

1. Attach 25 μm gold wires to the sample using silver paint DuPont 4929N. The amount of silver paint should be kept minimal while keeping the wires firmly attached to the sample.
2. Glue the sample down to a 2 mm × 2 mm × 0.25 mm quartz platelet using diluted GE Varnish. Enough varnish needs to be used to prevent the sample from being lift off the quartz platelet due to the torque exerted at high magnetic field. Care should be taken to avoid the varnish overflowing to the gold pads, as the varnish solvent can dissolve silver paint and weaken the contact robustness and increase contact resistances. It can be avoided by controlling the amount and consistency of the varnish.

3. Bend the gold wires towards the edge of the quartz platelet and glue them down to avoid possible wire movement. Three or more layers should be applied.
4. Connect the gold wires to twisted wire pairs leading to the probe with silver paint. Open loops should be minimised to reduce any torque exerted on the wires and voltage induced by a time-varying magnetic field. Twisted wire pairs of diameter similar to the gold wires should be used, as it is difficult to connect wires with very different diameters securely using silver paint.

All wires should be glued down to an immobile surface whenever possible to avoid any possible movement during the measurements. For $YBCO_{6+x}$ samples with x > 0.85, it can be useful to use silver epoxy such as Epo-Tek H20E to further strengthen the contacts. Baking at 120 °C for 15 minutes is needed for epoxy curing. For samples with oxygen-chain order, such thermal treatment will disrupt the superstructure and should be done before the ordering process.

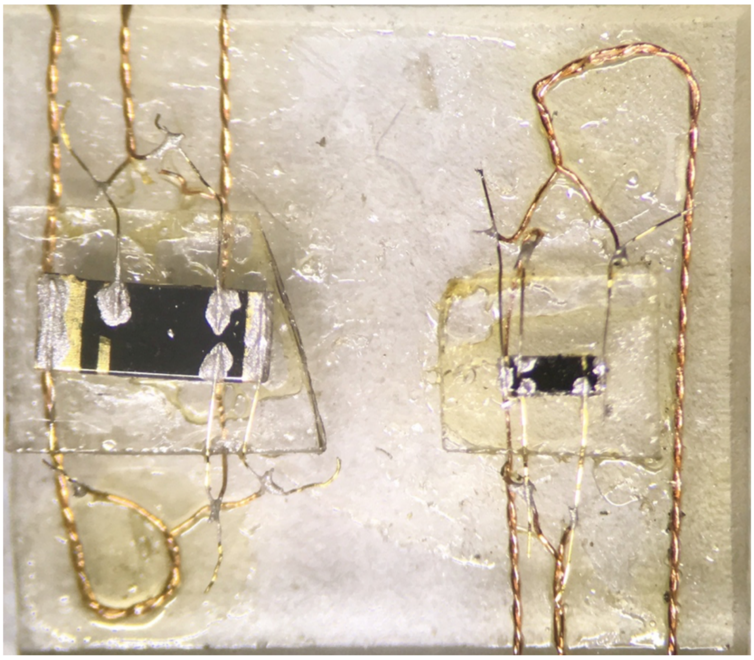

Figure 3.9: **$YBCO_{6+x}$ samples wired for high-field measurements.** Picture of two wired YBCO samples for in-plane transport measurements. 25 μm gold wires are attached to the sample using silver paint, then secured to the edges the quartz platelets using GE Varnish. Gold wires are connected using silver paint to the twisted wire pairs arranged for simultaneous measurements of longitudinal and Hall resistances.

Chapter 4

Measurement techniques

The majority of work presented in this thesis is performed in international high magnetic field facilities including the National High Magnetic Field Laboratory in the US, Wuhan High Magnetic Field Centre in China, and Laboratoire National des Champs Magnétiques Intenses in France. In this chapter, I will give a brief introduction of the high-field magnets used in this work and a detailed discussion of the experimental techniques used for electrical transport and magnetisation measurements.

4.1 High field magnets

Magnetic fields up to 5 T can be generated using a permanent magnet made of iron [60]. To generate magnetic fields well above 5 T, one can only use electromagnets. Various magnets that can produce continuous magnetic fields up to 45 T and pulsed magnetic fields up to 65 T have been used in this work. The design principles and technical limitations of these magnets are briefly discussed in this section.

4.1.1 Superconducting magnet

The electromagnet is a natural application of superconductors given its ability to carry electrical current without dissipation. A magnetic field is generated when a current, usually on the order of 100 A, is passed through a solenoid made of superconducting materials. Three material parameters set the constraints for the operation of a superconducting magnet: the critical temperature (T_c), the upper critical field ($\mu_0 H_\mathrm{c2}$), and the critical current density (j_c). T_c and $\mu_0 H_\mathrm{c2}$ are intrinsic material properties. A superconducting magnet needs to be operated at temperatures below T_c and cannot generate a magnetic field larger than $\mu_0 H_\mathrm{c2}$ above which the superconductivity is destroyed. j_c, however, depends largely on metallurgical treatments of the material. Magnetic flux vortices, whose movement leads to finite resistivity in type-II superconductors, can be pinned by crystallographic defects to maintain the zero resistivity state. These pinning centres, such as grain boundaries and impurities, can be effectively introduced by mechanical processing and increase j_c from 100 A·cm^{-2} to 100 kA·cm^{-2} in the same material [60]. As the maximum achievable magnetic field (below $\mu_0 H_{c2}$) is limited by j_c, which decreases with increasing temperature, superconducting magnets are typically operated at 4.2 K to achieve high magnetic field.

Although numerous superconductors have been found, only a few are of practical relevance for magnet application. NbTi, a low temperature superconductor with a T_c of 10.2 K and $\mu_0 H_{c2}$ of 12 T, is the universal material choice to produce magnetic fields up to 9 T, since it is a ductile, metallic material from which wires can be readily made. Nb$_3$Sn, a brittle intermetallic compound with a T_c of 18.3 K and $\mu_0 H_{c2}$ of 22 T, is only used to produce magnet fields > 9 T as it is difficult and expensive to be made into wires. Dual NbTi/Nb$_3$Sn coils are often used to produce magnetic fields up to 21 T for cost effectiveness. Although high temperature superconductors have a much higher T_c and $\mu_0 H_{c2}$, they are ceramic materials with complex structures and present a major technical challenge for coil winding. They also have a lower achievable j_c at 4.2 K than NbTi and Nb$_3$Sn at magnetic fields below 9 T and 18 T, respectively, therefore are only used to generate magnetic fields above 21 T [60].

Superconducting magnets require a minimal electricity to operate but can be seriously damaged by electrical disruption. A superconducting solenoid operating at a current of 100 A, with a typical inductance of 40 H, stores an energy of 200 kJ. If any part of the superconducting coil becomes resistive due to a transient perturbation or strain-induced underperforming of the coil, ohmic heating will occur and the resistive zone can propagate across the entire coil rapidly. Only a very small amount of energy is required to induce the resistive transition locally due to the small heat capacity of superconductors at 4.2 K. The stored energy will dissipate and evaporate the liquid helium instantly, which elevates the magnet temperature and damages the coil. This process is known as *quenching*. A protection circuit can be installed to dissipate the energy controllably. Interestingly, new superconducting magnets usually experience several quenches to release the strain built up during coil winding until the designed field strength can be reached.

4.1.2 Resistive magnet

The field strength of a resistive electromagnet, unlike the superconducting magnet, is not limited by any law of physics but by economics. It requires a power of 8 MW to generate a magnetic field of 25 T, 19 MW to generate 35 T, and over 40 MW to generate 45 T using current technology [60]. More power input means more heat dissipation, and more cooling power required to operate the magnet. Moreover, the force applied on the coil due to the produced magnetic field further limits the magnet performance. A force of ≈ 100 kN can be generated on the coil at a magnetic field of ≈ 35 T. Materials with high mechanical strength are thus needed for coil construction, accompanied by an increased electrical resistivity, more heat dissipation, and higher requirements for the cooling power. A widely employed design for a resistive magnet is the Florida-Bitter magnet, an improved version of Bitter's original invention in 1939, developed at the National High Magnetic Field Laboratory (NHMFL) in Tallahassee, Florida. Schematic diagrams of the Bitter magnet and Florida-Bitter plate are shown in Figure 4.1. The Bitter magnet consists of stacked conducting Bitter plates separated by insulating spacers, which serves to guarantee the desired flow of electrical current, with a distribution of holes for flowing cooling water. The Florida-Bitter plate has elongated slits, rather than circular holes used in Bitter plate, distributed along the polar direction to optimise the balance between cooling surface area, structural integrity, and electrical conductivity. Cu-based alloys, such as Cu-Ag and Cu-Al_2O_3, provide an enhanced mechanical strength that outweigh the sacrifice in conductivity.

The most powerful resistive magnet in the world is currently the 41.5 T magnet at the NHMFL in Tallahassee. It requires 33 MW of power at the maximum magnetic field, which in one hour uses equivalently seven years of power consumption of an average UK household.

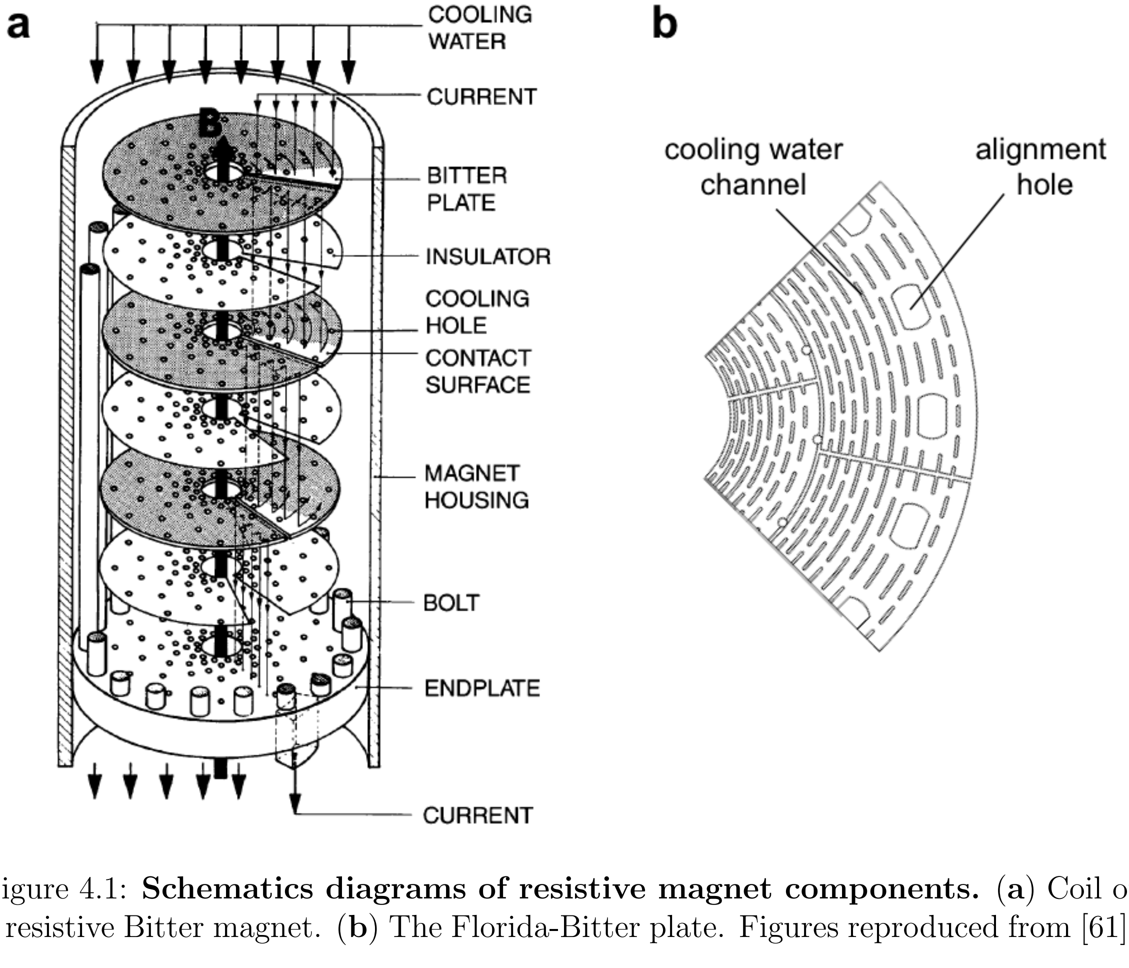

Figure 4.1: **Schematics diagrams of resistive magnet components.** (**a**) Coil of a resistive Bitter magnet. (**b**) The Florida-Bitter plate. Figures reproduced from [61].

4.1.3 Hybrid magnet

The combination of a resistive magnet (insert) with a surrounding superconducting magnet (outsert), known as a *hybrid* magnet, can boost the achievable magnetic field for a given available power. It is a technological challenge that involves many considerations in magnet design. Firstly, it requires an unusually large superconducting magnet with bore size of $\approx$ 600 mm compared to the typical bore size of $\approx$ 50 mm. Secondly, a very large cryostat needs to be installed to accommodate the superconducting magnet. As the magnetic field in the insert varies, a current will be induced in the superconducting outsert. In the event of the insert tripping from the maximal field, over 20 kJ of energy can be stored in the outsert and quench it. Superfluid helium produced at 1.8 K has a very high thermal conductivity and low viscosity, which can be used to increase the reliability of the superconducting magnet considerably and prevent quenching. Thirdly, a magnetic force up to 3 MN can be generated on the resistive coil when the insert operates in a background magnetic field of $\approx$ 10 T [60]. Special Cu-alloy with unusually high mechanical strength and lower electrical conductivity is required to construct the insert coil, which leads to a lower power efficiency than a standalone coil. The 45 T hybrid magnet at NHMFL in Tallahassee, currently the record-holder of the highest continuous field, uses 33 MW of power and 15 000 litres of cooling water per minute for the 34 T insert and 2 800 litres of superfluid helium circulating at 1.8 K for the superconducting outsert.

4.1.4 Pulsed magnet

Magnetic fields of even higher magnitude can be generated at the expense of field duration. This technology is known as the *pulsed magnet*. A pulse of magnetic field can be created by sending a large transient current through a resistive coil. This approach circumvents the issue of a limited cooling power for a continuous resistive magnet. The coil sits in liquid nitrogen and is cooled sufficiently between each pulse. The pulsed magnet is typically charged by a capacitor bank with energy capacity of $\approx$ 1 MJ at a voltage of $\approx$ 10 kV. The duration of magnetic pulses is typically of the order of 10 ms, with the rising part being shorter than the falling part. Field profiles of pulsed magnets used in this work are shown in Figure 4.3.

Magnetic fields of 60 T can now be routinely generated at pulsed field facilities worldwide, with a few having the ability to generate fields over 80 T using multiple coils. Key parameters of selected pulsed magnets worldwide are summarised in Table 4.1. Currently the highest magnetic field generated by non-destructive pulsed magnet is 101.3 T achieved at the NHMFL in Los Alamos using an immense energy of 150 MJ per pulse. The majority of pulsed field measurements on YBCO_{6+x} were performed at Wuhan High Magnetic Field Center in China.

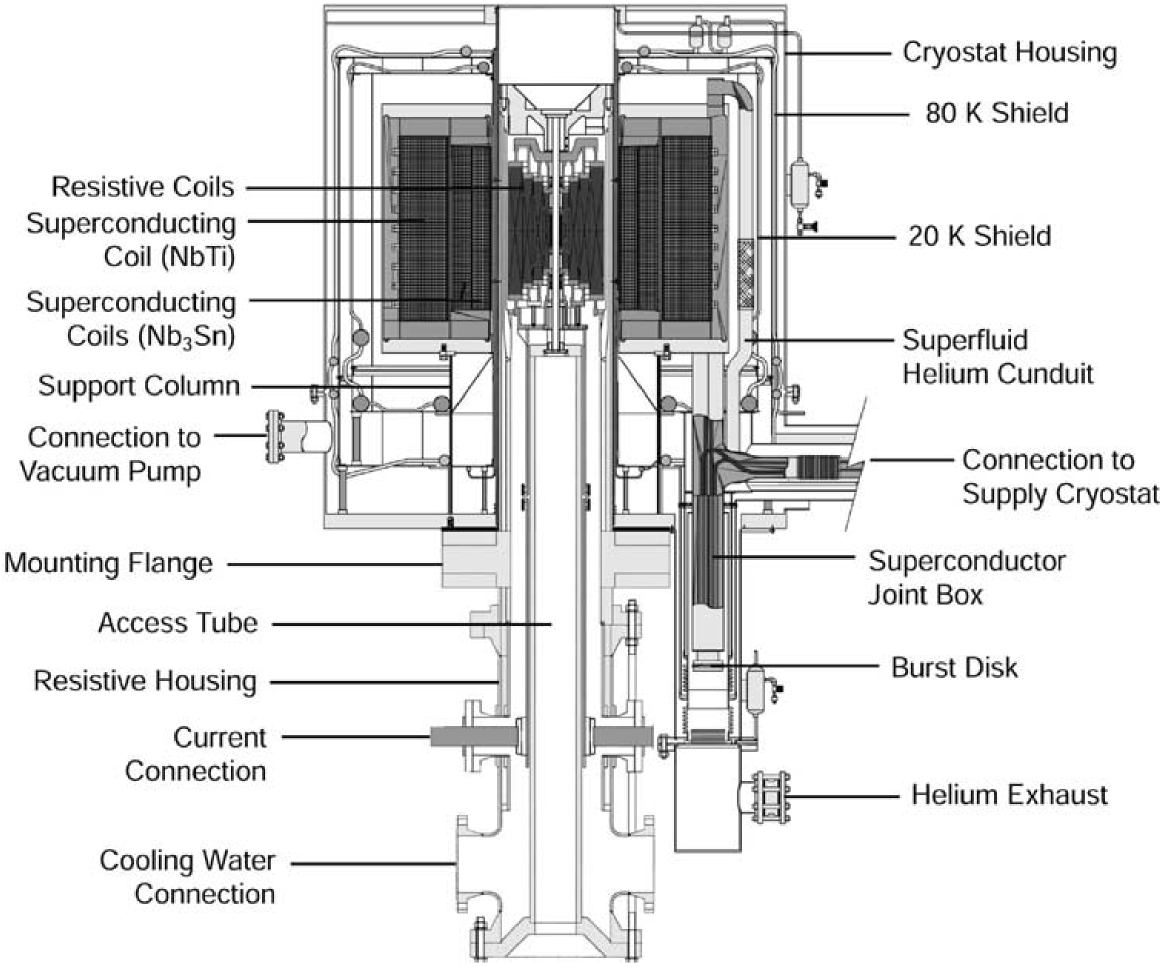

Figure 4.2: **Sketch of the 45 T hybrid magnet at the NHMFL in Tallahassee**. It consists a 34 T resistive insert and an 11 T superconducting outsert. Figure reproduced from [61].

Table 4.1: **Key parameters of selected magnets from pulsed field facilities worldwide.** HLD refers to the Dresden High Magnetic Field Laboratory in Germany. NHMFL-PFF refers to the National High Magnetic Field Laboratory's Pulsed Field Facility at Los Alamos, New Mexico. LNCMI-T refers to the Laboratorie National des Champs Magnétiques Pulsés at Toulouse, France. WHMFC refers to the Wuhan High Magnetic Field Center in Wuhan, China. Values in the parenthesis indicate the durations of the peak field pulses.

Facility	B (T)	Number of coils	Energy (MJ)	Pulse duration (ms)	Bore size (mm)	Time between pulses (hr)
HLD	65	1	1	25	20	1
	95	2	9.5	100(10)	16	4
NHMFL-PFF	65	1	1	25	15	0.75
	100	2	150	2500(25)	10	3
LNCMI-T	60	4	5	300	28	1.25
	90	2	13	1200(40)	8	1.5
WHMFC	65	1	3	60	22	1
	90	2	12.6	200(8)	12	3.5

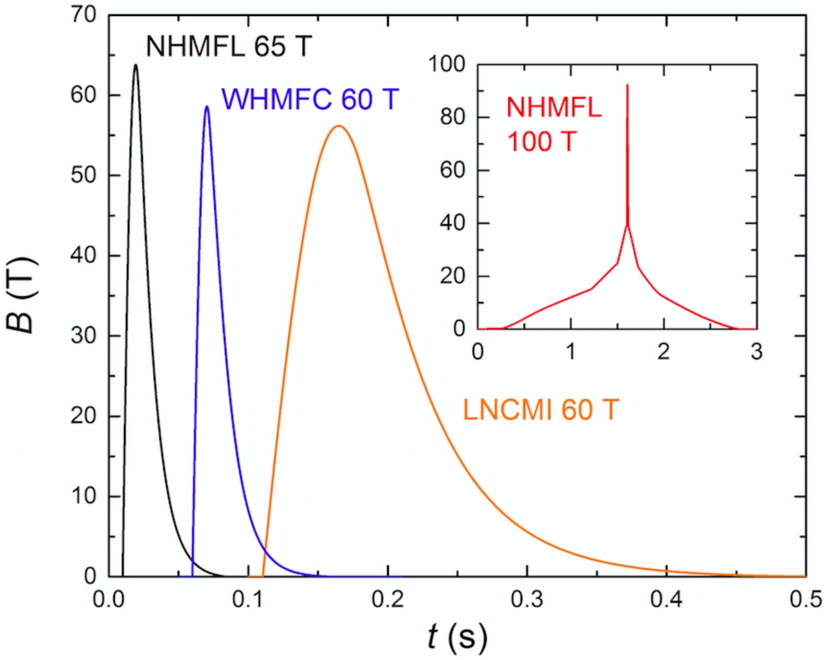

Figure 4.3: **Magnetic field-time profiles of pulsed magnets used in this work.**

4.2 Electrical transport

The electrical transport properties of a material are often the first properties to be studied but the last to be understood. The principle of the measurement is simple, yet it can be challenging to perform successfully. In this section, methods used to measure electrical resistivity in both continuous and pulsed fields are discussed in detail.

4.2.1 Continuous field measurement

Resistivity measurements on YBCO$_{6+x}$ for studying the superconductivity down to 40 mK and temperature dependence up to 300 K under fixed magnetic fields were performed at the NHMFL in Tallahassee using the experimental setup described in Figure 4.4. Four electrical leads are attached to the sample, with one pair of leads sending an electrical current I and the other pair measuring the potential difference V_{xx} (or V_{xy}). An AC current with a frequency of 10 to 40 Hz is applied using the Keithley 6221 current source in order to use a lock-in amplifier to measure the signal of a chosen measurement frequency and filter out the background noise. The measurement frequencies are adjusted individually for each sample in a magnetic field above 11 T to minimise the noise level at higher fields. A pre-amplifier is used to further enhance the signal-to-noise ratio (S/N). We find that the specialised preamplifier SA-400F3 from NF Corporation, which amplifies the signal but not the noise, gives a superior noise performance than the commonly-used SR551 from Stanford Research Systems. Noise level of $\approx$ 10 nV can be achieved at fields below 35 T, similar to the noise level measured in the commercial Physical Property Measurement System from Quantum Design Inc. The noise increases significantly at the maximum field of 45 T to $\approx$ 100 nV due to the increased mechanical vibrations and magnetic force acting on the sample.

R_{xx} and R_{xy} of YBCO$_{6+x}$ are of the order of 50 mΩ and 5 mΩ, respectively. When a voltage lead is shorted to a current lead, the measured resistance will increase by at least one order of magnitude. This issue cannot be circumvented by re-arranging the leads on the instruments' or probe's end, and the voltage leads on the sample have to be re-made. A diagonal arrangement of the voltage leads, as shown in Figure 4.5, can be used to extract ρ_{xx} and ρ_{xy} simultaneously. The diagonal signal consists of both longitudinal (V_{xx}) and transverse (V_{xy}) components, which can be extracted using

$$V_{\mathrm{xx}} = (V^{+}_{\mathrm{diagonal}} + V^{-}_{\mathrm{diagonal}})/2 \tag{4.1}$$

$$V_{\mathrm{xy}} = (V^{+}_{\mathrm{diagonal}} - V^{-}_{\mathrm{diagonal}})/2, \tag{4.2}$$

where $V^{+}_{\mathrm{diagonal}}$ and $V^{-}_{\mathrm{diagonal}}$ are the voltages measured when the magnetic field is applied with positive and negative polarity, respectively. The V_{xy} component can only be reliably extracted when it is sufficiently large compared to V_{xx}, usually on the order of 5%; otherwise it will be

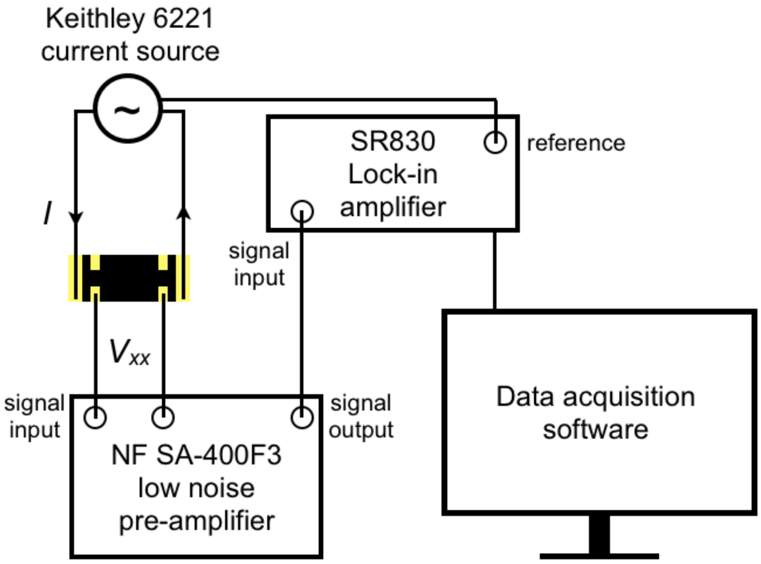

Figure 4.4: **Block diagram of the four-probe resistivity measurement setup used in continuous fields.** An electrical current I is supplied by Keithley 6221 current source and the voltage signal V_{xx} is amplified by NF SA-400F3 pre-amplifiers and measured via SR830 Lock-in amplifier.

dominated by the uncertainty in V_{xx}.

A current of 3 mA gives a good signal-to-noise ratio without risking the wires to be damaged due to magnetic force. A low current below 1 mA, however, should be used for measurements taken at temperatures below 1 K to minimise the effect of ohmic heating. After signal optimisation, a noise level of $\approx 10\ \mu\Omega$ (i.e. S/N $\gtrsim 10^3$) can be achieved using $I = 3$ mA, and ≈ 3 mΩ can be achieved using $I = 10\ \mu$A (i.e. S/N $\gtrsim 3$), a necessary condition to access the superconducting state in the underdoped YBCO$_{6+x}$ below 1 K.

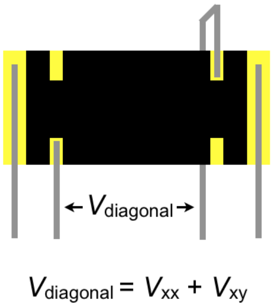

Figure 4.5: **Schematic diagram of the diagonal arrangement of voltage leads.** The measured signal V_{diagonal} consists of both longitudinal (V_{xx}) and transverse (V_{xy}) components. In the absence of a magnetic field, $V_{\mathrm{xy}} = 0$ and $V_{\mathrm{diagonal}} = V_{\mathrm{xx}}$.

4.2.2 Pulsed field measurement

Resistivity measurements on YBCO_{6+x} to establish the vortex-state boundary over a broad range of doping were performed at WHMFC. It is considerably more challenging to measure electrical resistivity using the four-probe technique in pulsed fields compared to that in continuous fields. The intense magnetic pulse is accompanied by a large energy release and vibrational noises. A successful resistivity measurement relies on achieving a satisfactory signal-to-noise ratio. A measurement frequency of 30 to 100 kHz, much higher than that used in continuous field, is used to effectively filter out the vibrational noises that are more prominent at low frequencies. An AC current is applied by sending an AC voltage across a shunt resistance. Data is recorded at ≈ 1 MHz sampling rate to collect enough data points during the transient magnetic pulse. The major challenge of high-frequency resistivity measurements is to reduce the contribution of reactive components to the impedance signal, whose contribution increases with frequency. As the resistivity signal, which is in phase with the AC current, is the only quantity of interest, the out-of-phase signal comprised of the capacitive and inductive components should be minimised. The signal optimisation relies on choosing a frequency that gives a high signal-to-noise ratio without a significant out-of-phase component. The strategy used to achieve successful four-probe resistivity measurements in pulsed fields is outlined below.

Contact resistance

First and foremost, the contact resistance between the voltage leads of the sample has to be as low as possible. A large contact resistance indicates a high capacitance between the lead and the sample. The two-point resistance measured between the voltage leads should be below 5 Ω, and ideally below 2 Ω. Note that the absolute value of the out-of-phase signal is sensitive to the exact circuit configuration and varies significantly when a test lead is removed and reconnected. It is the change in the out-of-phase signal with magnetic field that defines the signal quality, which should be < 2 mΩ over the entire field range.

Probe

A well-maintained probe gives a good signal. One should consult the local user support about the probe condition before mounting the sample. There are usually over 16 wires running along the probe and some of them may be damaged. The wire resistances should be checked without the sample and the wires with unusual resistances need to be fixed or avoided. Coax cables should be avoided for voltage leads due to the complexity for instrument connection. Probes with a glue-on sample space and soldering pads for lead connections are preferred to ones that use a standard DIP chip. The latter option uses a spring mechanism to secure the chip to the probe, which vibrates during the pulse and amplifies the noise at high fields. A stabilising piece, if available, should be used to prevent the probe tail from touching the cryostat wall, which would cause very large noises.

Crosstalk

High-frequency AC signals can propagate outside the transmitting cable and leak into the adjacent wires, causing the signal from one sample to appear in the other sample's signal. This phenomenon is known as *crosstalk*. The most effective way to eliminate the crosstalk is to keep the leads from different samples physically apart. It should be done on the sample platform and at the breakout box where the leads are connected to the instruments.

Frequency choice

The frequency chosen for the measurement should be high enough to effectively eliminate the background noise while maintaining a minimal, field-independent out-of-phase contribution. Frequency that lies in close proximity to another measurement frequency and/or background noise with high intensity should be avoided. It is useful to study the background noise present in the circuit using a spectrum analyser. The presence of high-intensity noise at high frequency often leads to a large, field-dependent out-of-phase signal that needs to be eliminated. Note that a shift in measurement frequency as small as 4 kHz could reduce the noise by 50%. Extensive efforts should be made before deciding the measurement frequency.

Temperature control

The temperature of the sample space is determined by the heater's power output and the dewar's cooling power, moderated by the amount of exchange gas within the probe. For the best temperature stability, low heater power with low exchange gas pressure should be used. A pressure of 10^{-3} mbar and heater power below 10% using the Lakeshore 335 temperature controller gives a good temperature stability. The temperature reading can sometimes be misleading, due to self-heating from the vortex motion and eddy currents, and the field values of the resistive transition can provide a calibration for the sample temperature.

A noise level of $\approx 100\ \mu\Omega$ at $B = 60$ T can be achieved with a current of 10 mA after signal optimisation. However, it is still at least one order of magnitude higher than that in continuous fields using similar measurement current. Therefore, the thinnest samples with lowest contact resistances should be used for optimal signal-to-noise ratio in pulsed fields, especially for ρ_{xy} measurements.

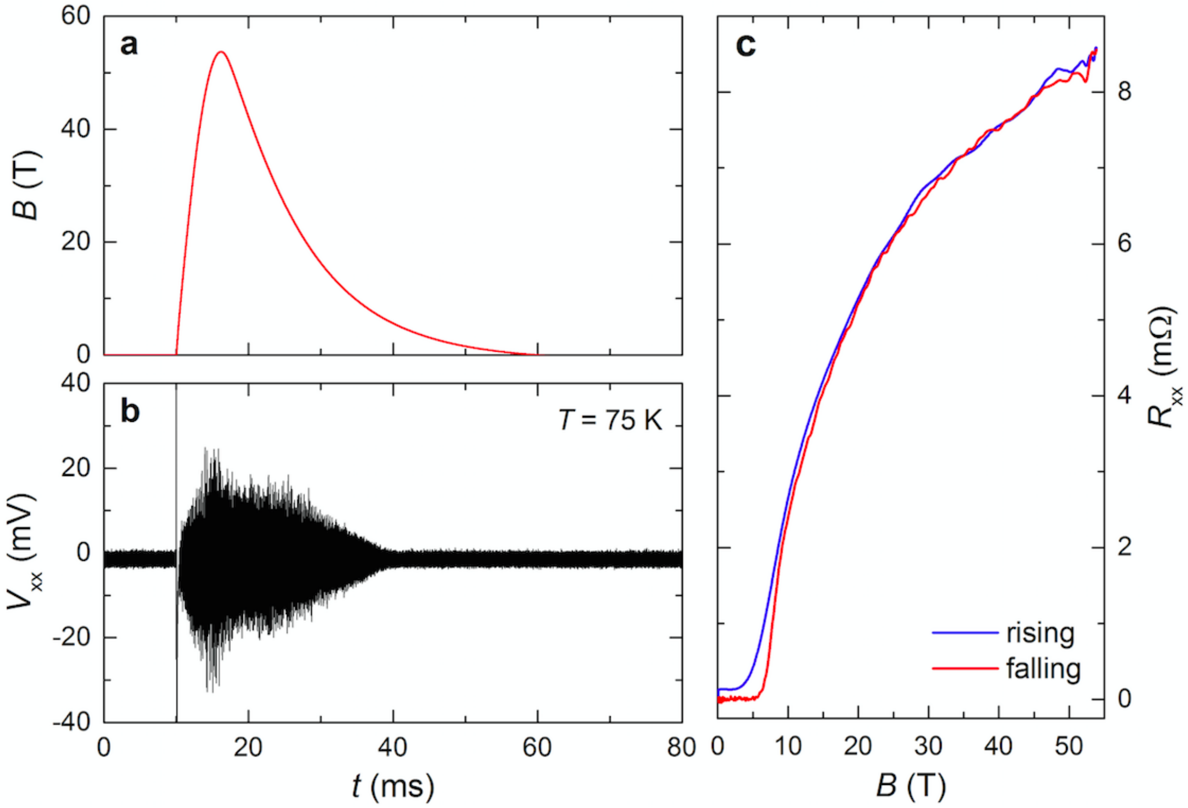

Figure 4.6: **Typical ρ_{xx} signal measured in pulsed fields.** (**a**) Field-time profile of a 54 T pulse made in WHMFC. (**b**) Raw voltage signal measured using a frequency of 83 kHz at $T = 75$ K in a YBCO$_{6+x}$ sample ($T_{\mathrm{c}} = 85$ K). The sample became resistive between $t = 10$ ms and 40 ms with voltage signal exceeds the noise floor in the superconducting state. (**c**) R_{xx} as a function of field after signal processing. A slight mismatch between rising and falling parts can be seen, possibly due to insufficient data collection in the rising part or self-heating due to eddy currents.

4.2.3 Proximity detector oscillator

A complementary technique to measure electrical resistivity is the proximity detector oscillator (PDO) method. It is a contactless technique which has proven to be very successful for quantum oscillation studies on superconductors with high sensitivity [62]. Studies of the quantum oscillation waveform in contactless resistivity of YBCO$_{6+x}$ were performed at the NHMFL in Los Alamos and WHMFC. PDO consists of a resonant LC circuit with the sample placed on an inductive coil, as illustrated in Figure 4.7. A change in the sample resistivity induces a change in the effective inductance L_{eff} of the coil given by

$$L_{\text{eff}} = L_1\left[1 - \frac{M^2}{L_1(L_2 + L_0 + L_{\text{coax}})}\right], \tag{4.3}$$

where M is the coupling factor, L_{coax} is the inductance of the coax cable, and L_1 and L_2 are the inductors as shown in Figure 4.7(a) [63]. As a result, the resonant frequency f_0 shifts according to

$$\frac{\Delta f}{f_0} = -\frac{\Delta L}{2L_{\text{eff}}}, \tag{4.4}$$

where Δf and ΔL are the change in resonance frequency and effective inductance, respectively [63]. The signal is amplified, down-converted, and filtered twice for noise reduction before being analysed in the oscilloscope. The PDO sensitivity is sensitive to the resonance frequency, which can be altered by changing the capacitors C_1 and C_2, and/or the inductors L_1 and L_2. We have found that the resonance frequency of $\approx$ 32 MHz gives the highest sensitivity.

The sample coil is made by hand-winding enamelled AWG50 copper wire. Picture of a coil without a sample is shown in Figure 4.7(b). Thin GE Varnish is used to glue the coil down to a sapphire platform. The number of turns is determined by the sample size, which should fully cover the coil. It usually take five to six turns, followed by a counter-wound circle with contour area matching the area of the spiral. The counter-circle cancels the induced *emf* from the spiral. After the coil is made, the sample is glued to the coil using GE Varnish. Prominent quantum oscillations in underdoped YBCO$_{6.55}$ measured using the PDO technique are shown in Figure 4.7(c). The noise level is $\approx$ 100 Hz, or 100 ppm.

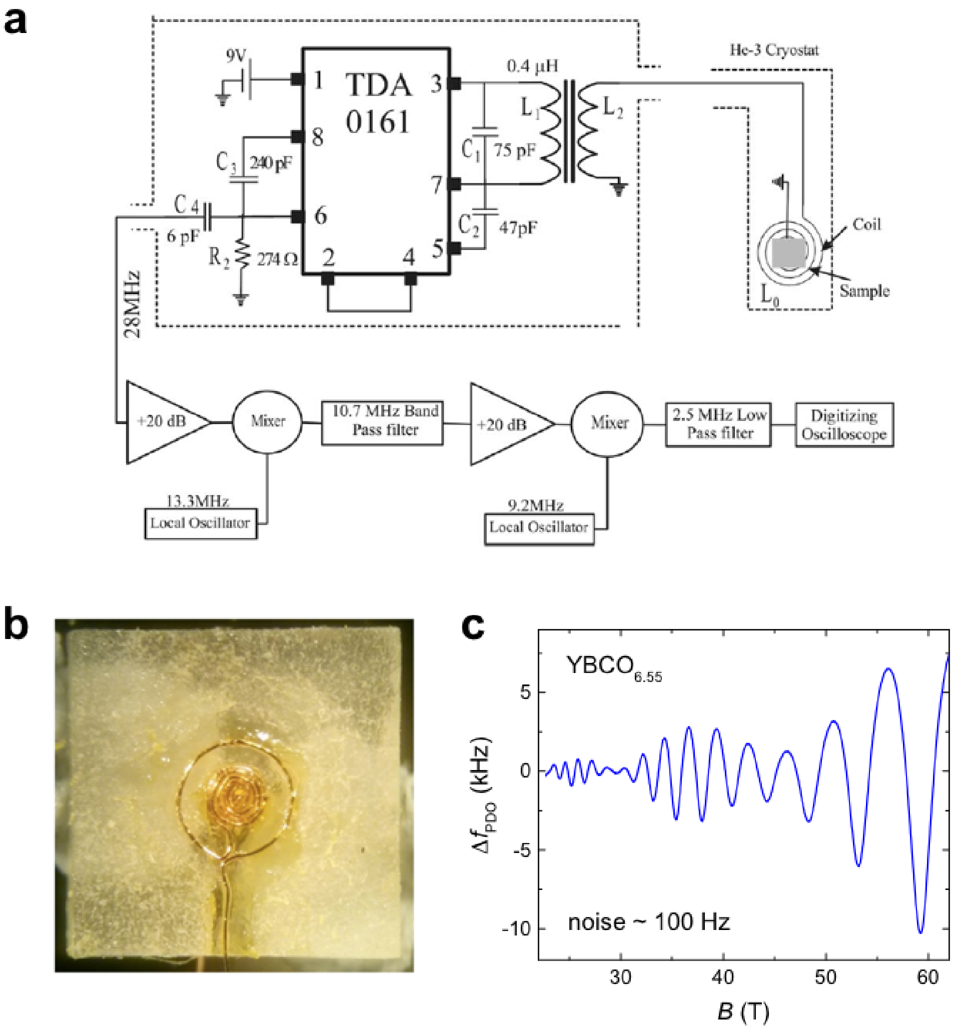

Figure 4.7: **Proximity diode oscillator (PDO) technique for contactless resistivity measurement.** (**a**) Schematic diagram of the PDO circuit from [63]. TDA0161 is a commercial integrated circuit commonly used for proximity detector. The output signal is amplified by 100 times (+20 dB) and filtered twice before reaching the oscilloscope. (**b**) Picture of the sample coil on a sapphire platform. (**c**) Quantum oscillations in $\mathrm{YBCO}_{6.55}$ measured by PDO technique at the NHMFL in Los Alamos. The change in resistivity is expressed as the shift in the resonance frequency Δf_{PDO}.

4.3 Torque magnetometry

A powerful technique for magnetisation measurement is torque magnetometry, which is particularly suited for high field conditions for its compactness and sensitivity. In this section, the principle and experimental setups of torque magnetometry measurements are discussed.

4.3.1 Basic principles

Torque magnetometry measures the anisotropy of magnetic susceptibility along different crystallographic axes. As illustrated in Figure 4.8, a torque τ is exerted on a sample with magnetic moment $\mathbf{m}$ in magnetic field $\mathbf{B}$ given by

$$\begin{aligned}\tau &= |\mathbf{m} \times \mathbf{B}| \\ &= \mu_0 V(M_c H_x - M_a H_z),\end{aligned} \tag{4.5}$$

where μ_0, V, and $M_{a,c}$ are the vacuum permeability, sample volume, and magnetisation along $\hat{a}$- and $\hat{c}$-axis of the sample, respectively. For convenience the $\hat{a}$- and $\hat{c}$-axis of the sample coincide with the $\hat{x}$- and $\hat{z}$-axis of the coordinate frame. We can substitute $M_c = \chi_c H_z = \chi_c H \cos\theta$ and $M_a = \chi_a H_x = \chi_a H \sin\theta$ into equation (4.5) and get

$$\begin{aligned}\tau &= \mu_0 V(\chi_c H \cos\theta \sin\theta - \chi_a H \sin\theta \cos\theta) \\ &= \frac{1}{2}\mu_0 V H \Delta\chi \sin 2\theta,\end{aligned} \tag{4.6}$$

where $\Delta\chi = \chi_{\mathrm{c}} - \chi_{\mathrm{a}}$.

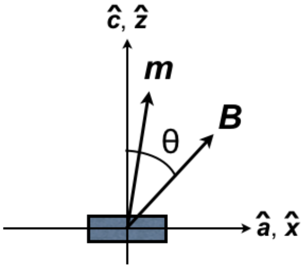

Figure 4.8: **Illustration of a sample with magnetisation m in a magnetic field B.** The $\hat{x}$- and $\hat{z}$-axis of the coordinate frame coincide with the $\hat{a}$- and $\hat{c}$-axis of the sample. θ is the angle between the magnetic field and $\hat{z}$-axis.

Very high sensitivity of 3×10^{-11} emu at $B = 10$ T has been achieved using torque magnetometry [64], three orders of magnitudes better than the commercial magnetometers. Two types of torque magnetometry techniques used in this work, the capacitive and piezo methods, are described below.

4.3.2 Capacitive method

Quantum oscillation measurements on SmB_6 and $YBCO_{6+x}$ down to 40 mK were performed at the NHMFL in Tallahassee using the capacitive technique, the most sensitive technique of torque magnetometry. A capacitor is formed between a thin cantilever, where the sample is mounted, and a metallic plate at the bottom, spaced by a small gap, as shown in Figure 4.9. In an applied magnetic field, the cantilever beam deflects due to the magnetic torque exerted on the sample and the capacitance changes accordingly. Cantilevers are made of beryllium copper, a highly elastic and non-magnetic material. The bottom plate is made of copper/G10 composite with lead pattern made by chemical etching. Miniature coax cables should be used for lead connections, which eliminates the parasitic capacitance when enamelled copper wires are used instead.

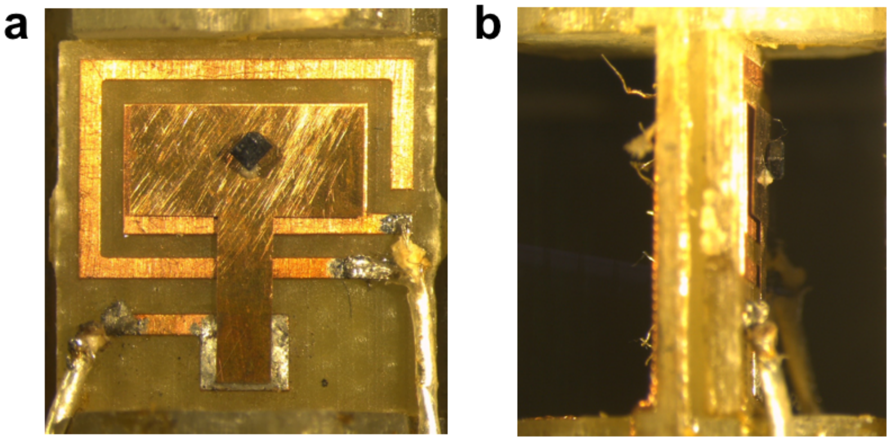

Figure 4.9: **Magnetometer used in the capacitive torque measurements.** (**a**) Top view and (**b**) side view of the magnetometer. A SmB_6 single crystal is mounted to the 20 μm Be-Cu cantilever, spaced by a 100 μm gap to the patterned circuit board underneath. The capacitance between the cantilever and the bottom plate is measured via two miniature coax cables on the edges of the magnetometer.

At intense magnetic fields, a highly magnetised sample can come off the cantilever due to the magnetic force exerted; thus it is crucial to mount the sample securely. The protocol used is described below.

1. Firstly, the cantilever is roughly sanded using fine sandpaper to increase the contact area with the adhesive. The use of inert solvents such as ethanol or isopropanol helps to keep the cantilever stationary while sanding. Care should be taken to maintain the flatness of the cantilever while sanding. The sanded cantilever is then cleaned with acetone to remove dust residues.

2. Next, the sample is glued onto the cantilever by adhesives. GE Varnish is used for samples that are not sensitive to thermal cycling such as $YBCO_{6+x}$. A piece of cigarette

paper with size slightly larger than the sample is glued down to the cantilever, followed by placing the sample onto the paper and coated with numerous layers of GE Varnish. Cigarette paper absorbs the varnish very well and improves the adhesion between the sample and cantilever. For samples that are sensitive to thermal cycling such as SmB_6, a two-part epoxy with exceptionally low thermal expansion coefficient (EP30LTE-LO from MasterBond Inc.) is used. Small droplets of well-mixed epoxy, aligned with the sample corners, are applied onto the cantilever using a fine needle. The epoxy needs to be cured at room temperature for 24 hours or under intense illumination for minimum of 6 hours.

3. After the adhesive is set, the sample is covered by short segments of Teflon tape for protection in case the sample falls off the cantilever. GE Varnish is used for YBCO_{6+x} and Loctite 304 is used for SmB_6 to glue the tapes, respectively. Solution of methanol-toluene (50:50 vol.%) and dichloromethane can be used to remove GE Varnish and EP30LTE-LO epoxy, respectively, if needed.

4. The bottom plate should be cleaned using acetone and/or air-duster before the cantilever is mounted to the magnetometer. A flat spacer of desired thickness, usually of 100 μm, is placed between the bottom plate and cantilever. The cantilever is soldered to the bottom plate at the joint point using a soldering iron with fine tip for minimal heating of the cantilever. The spacer is removed after the cantilever is soldered and the gaps on both sides should be checked to ensure a uniform spacing.

The capacitance at room temperature is typically around 1 pF, which can be tested using the Andeen-Hagerling 2700A digital capacitance bridge (referred as AH bridge hereinafter). The setup for the electronics is shown in Figure 4.10. The General Radio 1616 analogue capacitance bridge (referred as GR bridge hereinafter) requires additional electronics for digital data processing, but provides a superior signal-to-noise ratio than the AH bridge. An AC voltage of 30 to 100 V, powered by a General Radio audio oscillator at frequency $\approx$ 5 kHz, is applied across the sample capacitor via the GR bridge. The output signal is sent to two analogue SR124 lock-in amplifiers (Stanford Research Systems) to measure the in-phase and out-of-phase signals simultaneously. The amplified signals are measured using the Keithley 2000-series multimeters for data collection. A comparison of data measured using the AH and GR bridges is shown in Figure 4.11.

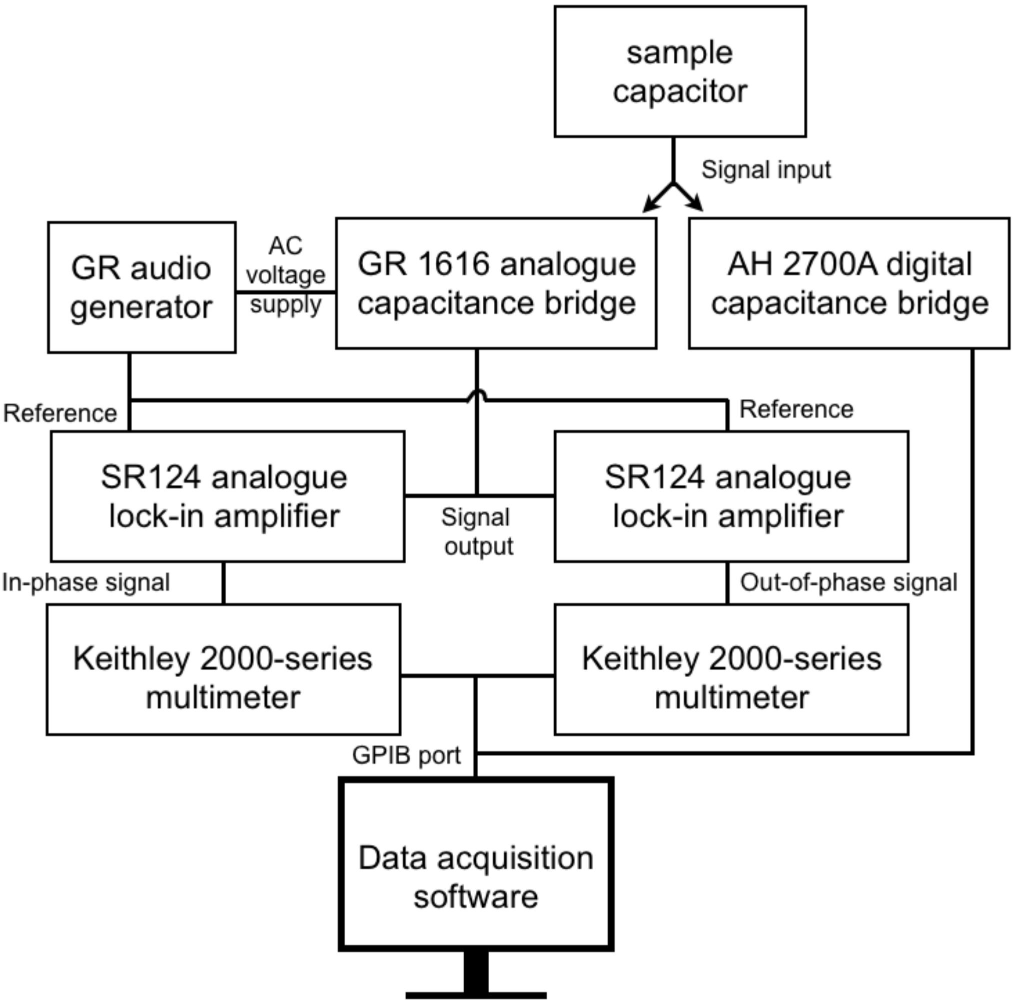

Figure 4.10: **Block diagram of a capacitive torque measurement setup.**

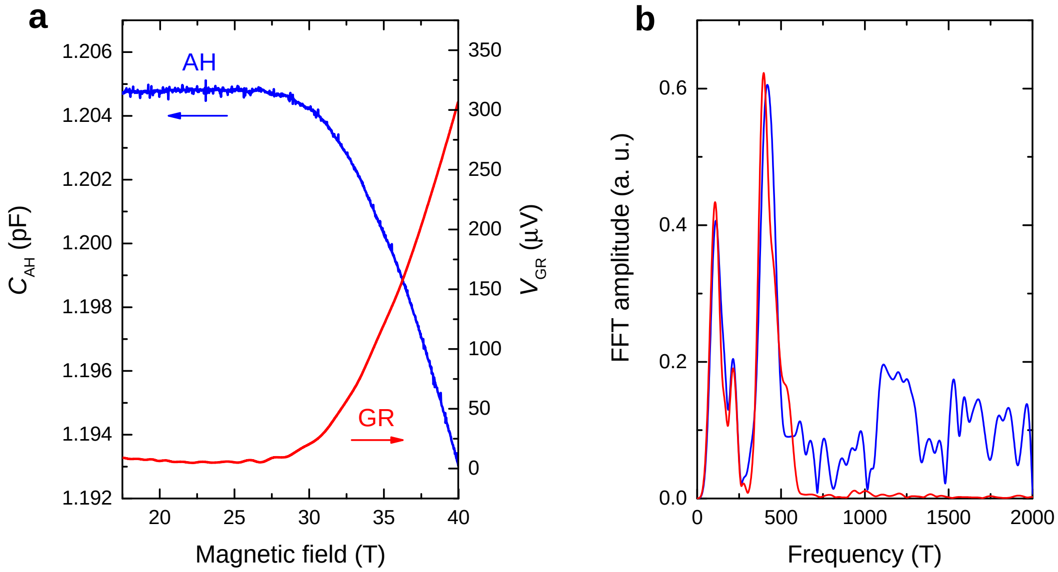

Figure 4.11: **Comparison of capacitance signals measured by the AH and GR capacitance bridges.** (**a**) Measurements were performed on a SmB_6 crystal with a fast sweeping rate in which the low frequency oscillations are prominent. The data collected using the analogue GR1616 bridge is has a lower noise than that using the digital AH2700A bridge. (**b**) FFT spectrum of quantum oscillations after background subtraction in (a). The noise floor obtained using the GR bridge is significantly better than that using the AH bridge.

The measured capacitance signal can be converted into magnetisation using the expression derived below. The torque τ exerted on the cantilever is proportional to its deflection given by $\tau = lk\delta$, where l is the length, k is the spring constant, and δ is the deflection of the cantilever. δ is proportional to the change in capacitance given by $\delta = d_0 \cdot \Delta C/C_0$, where d_0 is the distance between the cantilever and the bottom plate, and C_0 is the capacitance at zero magnetic field. Using the relation between and torque and magnetic moment of $\tau = mB\sin\theta$ and the expressions of τ and δ, one finds

$$\Delta m = \frac{lkd_0}{BC_0 \sin\theta}\Delta C. \tag{4.7}$$

By substituting k into equation (4.7) using

$$k = \frac{Ewt^3}{4l^3}, \tag{4.8}$$

where E, w, t are the Young's modulus, width, and thickness of the cantilever, respectively, one finds the sensitivity in magnetic moment δm given by

$$\delta m = \frac{Ed_0}{BC_0 \sin\theta} \frac{wt^3}{l^2} \delta C, \tag{4.9}$$

where δC is the sensitivity in the capacitance. Equation (4.9) shows that the use of a long, narrow, and thin cantilever, and a small gap between the capacitor plates increases the sensitivity. Using the typical values of $l = 3.8$ mm, $k = 28$ N·m^{-1}, and $d_0 = 0.1$ mm in our setup, we have a sensitivity of 10^{-7} emu using the AH bridge and 3×10^{-10} emu using the GR bridge at $B = 40$ T.

4.3.3 Piezo method

Although it is a powerful technique in continuous fields, the capacitive method is not suitable for pulsed field measurements because (1) the capacitance signal is compromised by the mechanical vibrations associated with magnetic pulse and (2) the cantilever response is too slow for transient data collection. An alternative technique is the piezo method, which measures the change in resistance of a piezoresistive cantilever induced by the magnetic torque. Studies of the quantum oscillation waveform in the magnetic torque of YBCO$_{6+x}$ were performed at the NHMFL in Los Alamos. An illustration of the experimental setup for piezo-torque measurement is shown in Figure 4.12. Commercial piezocantilevers from Seiko Instruments of dimensions 120 μm × 50 μm × 4 μm with a resonance frequency of 250 to 300 kHz are used. The high resonance frequency ensures a fast response of the piezocantilever to the magnetic pulse. A small, sub-μg sample is mounted onto the measurement cantilever using vacuum grease. A second cantilever on the platform acts as a reference to eliminate the background signal from the piezocantilever due to the change in temperature and magnetic field. The change in resistance of the piezoresistor is measured by a Wheastone bridge with the induced *emf* signal eliminated by a compensation coil.

The resistance-torque relationship is approximated by

$$\frac{\Delta R}{R} = \pi_L \frac{6\tau}{(2a)t^2}, \tag{4.10}$$

where ΔR, π_L, a, and t are the change in resistance, piezoresistive coefficient, width, and thickness of the cantilever, respectively [65]. The resistance through the path is $\approx 700\ \Omega$ at room temperature and $\approx 500\ \Omega$ at 4.2 K, which can achieve a sensitivity of 5×10^{-11} emu at $B \approx 50$ T. A drawback of the piezo method is the fragility of the piezocantilever, which can break under an excessive torque and end the measurement prematurely.

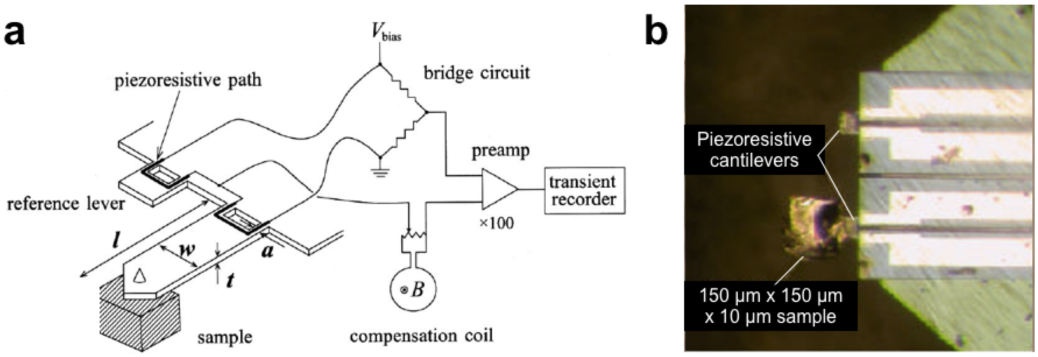

Figure 4.12: **Experimental setup of a piezo-torque measurement.** (**a**) Schematic diagram of the piezo-torque magnetometry setup taken from [65]. (**b**) Picture of a piezocantilever platform with one cantilever mounted with a sample and a reference cantilever. Picture taken from webpage of the NHMFL in Los Alamos.

Chapter 5

Fermi surface in SmB_6

In this chapter, a comprehensive study of the transport, quantum oscillations, and thermodynamic properties of SmB_6 is presented. While the transport measurements revealed the insulating behaviour persists at magnetic fields up to 45 T, quantum oscillations with a three-dimensional characteristic are observed in the magnetic torque above 10 T, with an absolute amplitude consistent with a bulk origin. The surprising observation of de Haas-van Alphen oscillations in the Kondo insulating SmB_6, taken together with complementary thermodynamic evidence, points to a new electronic ground state in SmB_6 with an in-gap state of itinerant low energy excitations.

5.1 Electrical transport of SmB_6

The formation of a bulk charge gap in SmB_6 at low temperature has been verified by a variety of experimental probes, including optical absorption and conductivity, neutron scattering, specific heat, and electrical resistivity [66]. The majority of these measurements were performed on flux-grown crystals; meanwhile, the hallmarks of Kondo insulating behaviour have also been observed in floating-zone crystals with subtle differences [51, 67]. In this section, the effect of sample preparation and magnetic field on the transport properties is discussed, revealing that the insulating behaviour is robust against magnetic field up to the highest available field.

5.1.1 Effects of sample preparation

We first performed resistivity measurements on SmB_6 single crystals prepared by different growth methods and surface treatments to investigate how the sample quality is affected by preparation technique. Figure 5.1 shows the surface image of crystals prepared by different techniques. The floating-zone (FZ) crystals were prepared either by cutting with a diamond wheel (cut), cleaving (CL), or electropolishing (EP). Cutting a floating-zone crystal with a diamond wheel introduces severe damage, several microns deep into the sample surface, as shown in Figure 5.1(a), which can be minimised by cleaving or electropolishing. The surface of pristine flux-grown crystals, while having high-symmetry crystallographic planes, is rougher than the electropolished or cleaved floating-zone crystals.

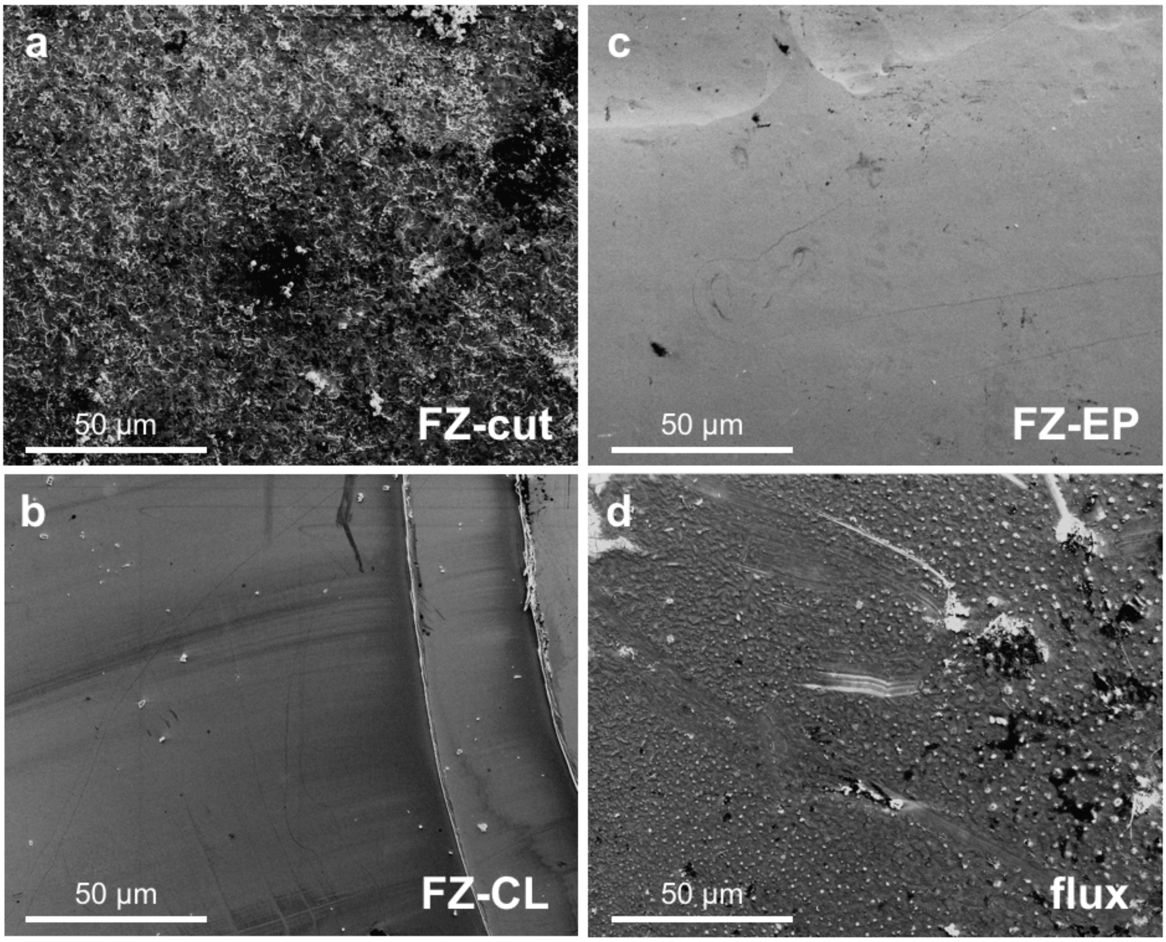

Figure 5.1: **Surface image of SmB_6 crystals with different surfaces.** Surfaces are prepared by (**a**) cutting with diamond wheel, (**b**) cleaving, (**c**) electropolishing of floating-zone crystals, (**d**) a pristine flux-grown crystal. Cleaved or electropolished floating-zone crystals have surfaces much smoother than that made by cutting wheel. Flux-grown crystals, while having pristine high-symmetry surfaces, has many particulates present on the surface.

Figure 5.2 compares the temperature dependence of the longitudinal resistivity $\rho_{\mathrm{xx}}(T)$ of the various SmB_6 single crystals shown in Figure 5.1. The resistivity of all samples is seen to diverge below the Kondo temperature T_{K} of 40 K, which signifies the opening of the hybridisation gap. The diverging behaviour stops at 4 K when the resistivity starts to reach a plateau. The plateau itself occurs at varying values, ranging from 5 to 30 Ω·cm, while the resistivity at 300 K only varies within a factor of two. It is known that impurities and defects can give rise to conducting states within the insulating gap thus reducing the resistivity of an insulator. The inverse resistance ratio (IRR), defined as $R_{\mathrm{xx}}(2\ \mathrm{K})/R_{\mathrm{xx}}(300\ \mathrm{K})$, is thus used as an indicator of the sample quality. The IRRs of our SmB$_6$ crystals are of the order of 10^5, higher than many previous reports [68, 69], indicating an improved sample quality. The IRRs of electropolished or cleaved floating-zone crystals are typically better than that of cut floating-zone or pristine flux-grown crystals. It should be noted that the resistivity defined here is a bulk property, $\rho_{\mathrm{xx}} = R_{\mathrm{xx}}(wt/l)$, where R_{xx} is the measured resistance, and l, w, t are the sample length, width, and thickness, respectively. At 2 K, the electrical transport is dominated by the surface and the inclusion of t in the calculation is not appropriate to reflect the surface resistivity. Therefore, we found that the IRR normalised by sample thickness, IRR$/t$, should be used to assess the sample quality of SmB$_6$. Having characterised over sixty samples, the crystals with the highest IRR$/t$ were selected for measurements at high magnetic fields.

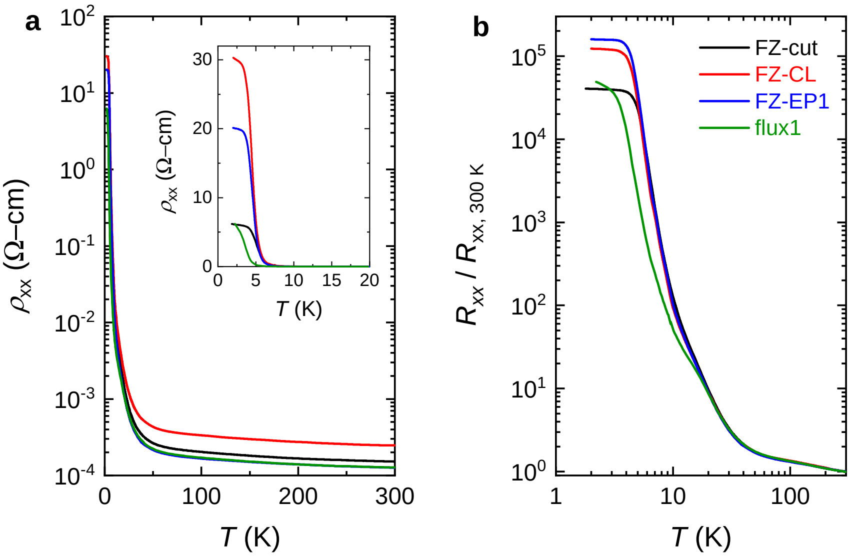

Figure 5.2: **Longitudinal electrical resistivity of SmB$_6$ crystals prepared by different techniques**. (**a**) $\rho_{\mathrm{xx}}(T)$ of three floating-zone SmB$_6$ crystals with surfaces prepared by cutting with diamond wheel (cut), cleaving (CL), and electropolishing (EP), and one pristine flux-grown crystal. ρ_{xx} increases by over five orders of magnitude between 300 and 2 K in all samples. **Inset**: An expanded view at $T < 20$ K to illustrate the resistivity plateau below 4 K. (**b**) Resistance normalised by the value at 300 K of the data shown in (a). At $T > 20$ K, all traces collapse into a single curve, indicating a bulk-dominant behaviour independent of surface conditions. The ratios at 2 K are seen to correlate with the sample surface quality as shown in Figure 5.1.

5.1.2 Effects of magnetic field

We next investigated how the Kondo gap in SmB_6 responds to a magnetic field. Figure 5.3 shows the longitudinal resistance R_{xx} of an electropolished floating-zone crystal, FZ-EP2, measured at $T < T_K$ in magnetic fields up to 45 T. The temperature dependence of the resistance is qualitatively the same under different field intensities, with the resistance reducing only slightly as the magnetic field increases. The reduction is expected for an insulator as the energy gap for charge transport is reduced via the Zeeman effect. R_{xx} reduces by 40 Ω with a magnetic field of 14 T, 2.5% of its zero field value. The sample remains insulating at the highest available field of 45 T.

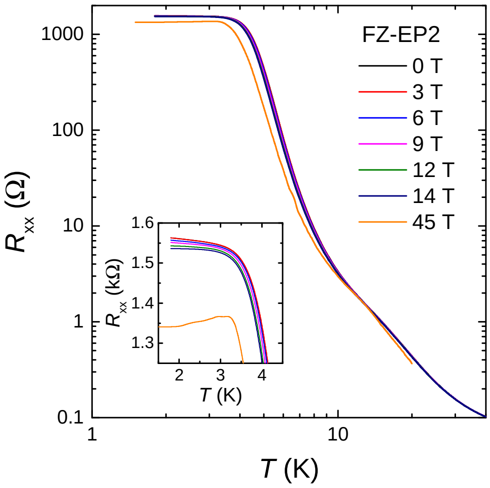

Figure 5.3: **Effect of a magnetic field on the longitudinal resistance R_{xx}.** The temperature dependence of R_{xx} remains qualitatively the same at varying field intensities. **Inset**: expanded view at low temperatures to illustrate the effect of magnetic field on the resistance plateau. The sample remains insulating at $B = 45$ T.

The size of the energy gap for charge transport is extracted using the Arrhenius-type equation:

$$R_{xx} = R_0 e^{\Delta/k_B T}, \tag{5.1}$$

where Δ is the activation energy [70]. Fits made to two SmB_6 crystals, one floating-zone and one flux-grown, are shown in Figure 5.4. The temperature range fitted is between 5 and 15 K, before the resistance plateaus. The magnetic field has only a minor effect on the slopes and gap sizes. The extracted Δ as a function of magnetic field for the two samples is shown in Figure 5.5. At zero magnetic field, Δ for the floating-zone and flux-grown crystals are 3.8 and 2.9 meV, respectively. Δ decreases monotonically with magnetic field and is reduced by 21% for EZ-EP2 at 45 T. Recent measurements on flux-grown SmB_6 crystal show Δ reduced by 50% at 60 T with the gap estimated to close at ≈ 120 T [70]. The insulating behaviour of SmB_6 is thus found to be robust against magnetic fields of 45 T from electrical transport.

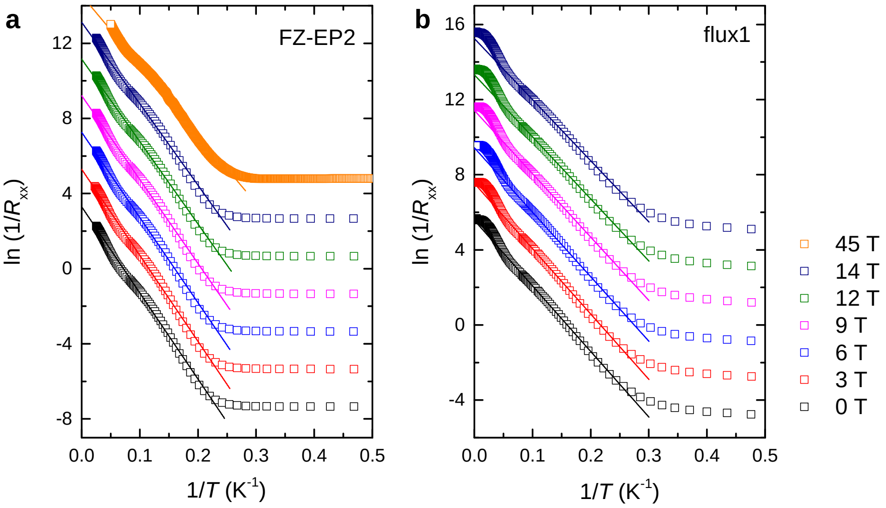

Figure 5.4: **Extraction of energy gap Δ for charge transport in SmB$_6$.** Measurements were performed on (**a**) an electropolished floating-zone crystal and (**b**) a pristine flux-grown crystal at fixed magnetic fields as indicated. $R_{\mathrm{xx}} = R_0 e^{\Delta/k_{\mathrm{B}}T}$ is used for linear fits between $T = 5$ and 15 K. Data are shifted vertically for clarity.

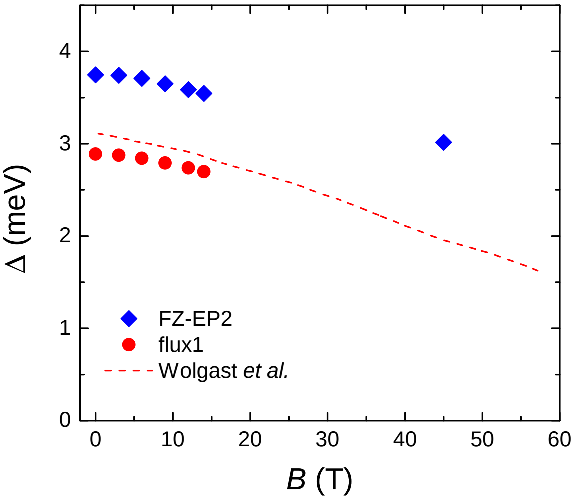

Figure 5.5: **Transport energy gap Δ as a function of magnetic field in SmB$_6$.** Good quantitative agreement in the field dependence of Δ is found between our measurements on the flux-grown crystal and recent measurements reported in [70].

5.2 Quantum oscillations in SmB_6

The theoretical proposal of a topological surface state in SmB_6 offers an attractive explanation for the low temperature resistivity plateau [6] and prompts searches for experimental evidence of the predicted two-dimensional Fermi surface. Recently, Li *et al.* have reported quantum oscillations in magnetic torque measured on flux-grown SmB_6 [71] and attributed its origin to the predicted topological surface states with a two-dimensional Fermi surface. However, the interpretation requires arbitrary grouping of the observed oscillation frequencies and the large oscillation amplitude, dominating over the background bulk signal, is difficult to be reconciled with the surface model. Here, we have measured the magnetic torque in both floating-zone and flux-grown SmB_6 crystals over an extended angular and temperature range, and found that the observed quantum oscillations are consistent with a three-dimensional Fermi surface geometry that is shared by the metallic rare-earth hexaborides and a bulk origin, despite the insulating behaviour in the electrical transport.

5.2.1 de Haas-van Alphen oscillations

Raw data from capacitive torque measurements on an electropolished floating-zone crystal and a flux-grown SmB_6 crystal are shown in Figure 5.6. Measurements were done in magnetic fields up to 40 T and down to $T = 0.4$ K, in magnetic fields up to 33.5 T and down to $T = 0.04$ K, and in magnetic fields up to 18 T and down to $T = 0.018$ K. Quantum oscillations periodic in inverse magnetic field are observed against a quadratic background. Dominant oscillations with frequency ≈ 410 T can be seen in both samples, with a larger oscillation amplitude in the flux-grown crystal than the floating-zone crystal. Fast oscillations on top of the dominant oscillations can be clearly seen above 30 T in the floating-zone crystal, while not prominent in the flux-grown crystal even at the highest field of 33.5 T before background subtraction. The components of the oscillatory signals are revealed by taking the Fourier transform of the quantum oscillations after background subtraction, as shown in Figure 5.7. Frequencies ranging from 30 T to 16 000 T are observed in both samples, with the frequencies below 1 000 T more prominent in the flux-grown crystal and the frequencies above 4 000 T more prominent in the floating-zone crystal. The observation of rapid quantum oscillations with frequencies higher than 10 kT is surprising. This very high oscillation frequency corresponds to nearly half the volume of the first Brillouin zone in SmB_6 and is typically characteristic of a highly conductive metal [72], in direct contrast to the insulating behaviour of SmB_6.

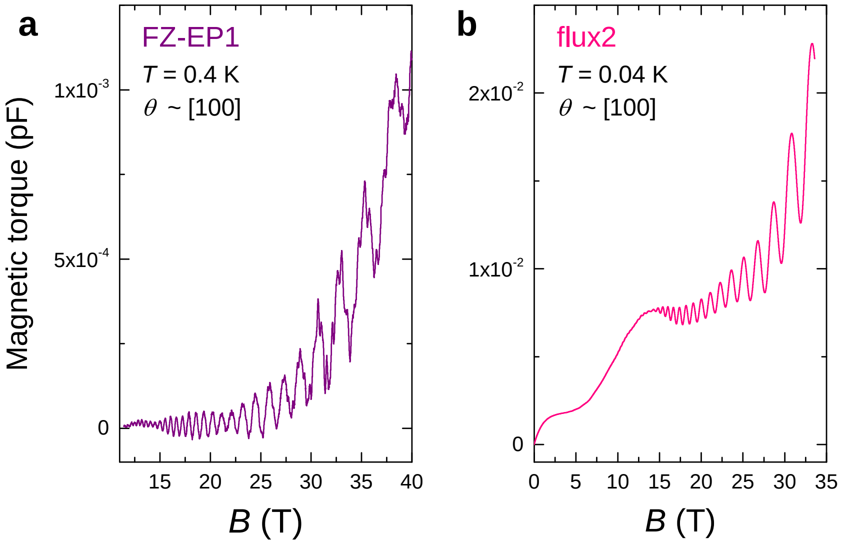

Figure 5.6: **Quantum oscillations in magnetic torque in SmB$_6$.** Measurements were performed on single crystals grown by the (**a**) floating-zone and (**b**) flux method, with magnetic field lies close to the [100] axis of the crystals. Dominant oscillations with frequency ≈ 410 T can be seen against a quadratic background in both samples, with the additional rapid oscillations above 30 T visible in (a). Large-amplitude slow oscillations with a frequency of 31 T are seen in the flux-grown crystal over the entire field range.

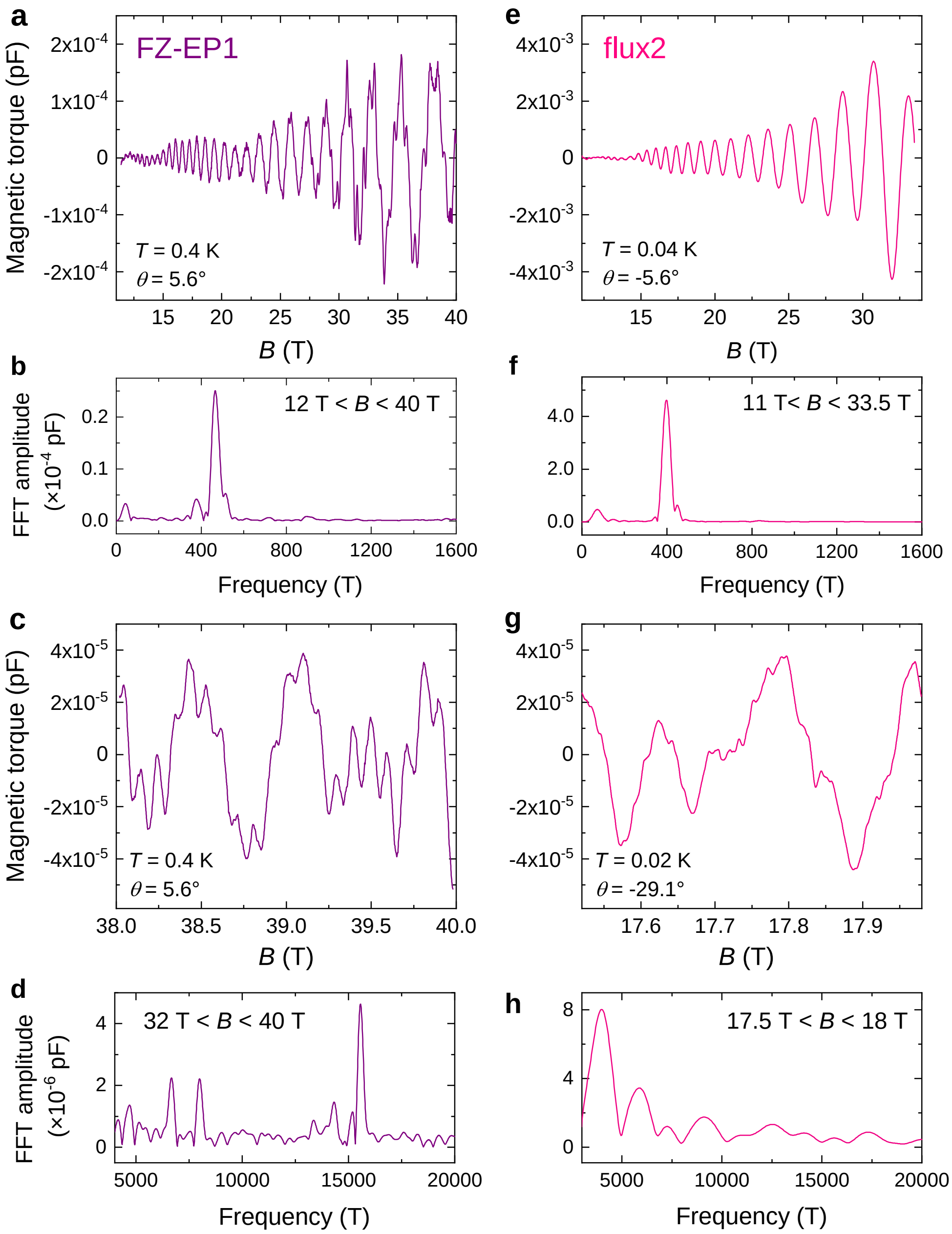

Figure 5.7: **Analysis of the dHvA oscillations in SmB$_6$.** (**a, e**) Quantum oscillations in the (a) floating-zone and (e) flux-grown crystals after background subtraction of a sixth order polynomial over 12 T $< B <$ 40 T and 11 T $< B <$ 33.5 T, respectively. (**b, f**) Fast Fourier transform (FFT) spectra of dHvA oscillations shown in (a, e) as a function of inverse magnetic field, revealing the low quantum oscillatory frequencies ranging from 30 T to 1 000 T. (**c, g**) Quantum oscillations over the field range of 38 T $< B <$ 40 T in the floating-zone crystal and 17.5 T $< B <$ 18 T in the flux-grown crystal, showing the rapid oscillations after background subtraction. (**d, h**) FFT spectra of magnetic torque shown in (c, g) revealing the high quantum oscillatory frequencies ranging from 2 000 T to 16 000 T. Field ranges for analysis have been chosen to best capture the observed oscillations, with the highest frequencies only appearing in the higher field ranges.

5.2.2 Angular dependence of oscillation frequency

To establish the origin of the observed quantum oscillations, we studied the angular dependence of the oscillation frequency in detail, covering both the [100]-[111]-[011] rotation plane (denoted as positive field angle θ) and [100]-[110] rotation plane (denoted as negative θ). Figure 5.8 shows the fast Fourier transform (FFT) spectrum of the dominant quantum oscillations measured on two flux-grown SmB$_6$ crystals with magnetic field rotating along different crystallographic planes. Three peaks are visible in the FFT spectrum at most angles, leading to the well-defined ρ-branch between 200 T and 1 000 T as shown in Figure 5.9(a). The observation of multiple FFT peaks over a wide range of angles, with a modest change in frequency, does not support the model of a two-dimensional Fermi surface confined to the crystal surfaces, for which a diverging behaviour in oscillation frequency near the [100] or [110] directions is expected. Instead, we find a strong resemblance in the angular dependence of the oscillation frequencies seen in insulating SmB$_6$ to those observed in the metallic rare-earth hexaborides (RB$_6$, R = La, Ce, Pr), as compared in Figure 5.9. The three-dimensional Fermi surface geometry common to the metallic RB$_6$ family is shown in Figure 5.10, which consists of three large ellipsoidal electron pockets along the $\langle 100 \rangle$ directions, corresponding to the α-branch with oscillation frequencies $\approx$ 9 kT, and twelve small ellipsoidal electron pockets along the $\langle 110 \rangle$ directions, corresponding to the ρ-branch with oscillation frequencies between 450 T and 900 T in PrB$_6$ [73]. The ellipsoidal Fermi pockets can be parameterised by their semi-principal axes ak_0, bk_0, and ck_0, and the extreme cross-sectional area F_{min}. The ρ-pockets are ellipsoids with $c > a \approx b$, and the α-pockets are prolate spheroids with $c \gtrsim a = b$. We fitted the observed ρ- and α-branches in SmB$_6$ using the formulae shown in Appendix A and the fitted parameters are summarised in Table 5.1. Good agreement is found between the experimental data and the fits for the ρ- and α-branch. The angular dependence of the oscillations with the lowest frequencies below 200 T construct a branch that is analogous to the ρ'-branch found in PrB$_6$ [73], which can be reasonably fitted to the ellipsoidal model as shown in Figure 5.11. However, there is a large error in the frequencies since very few oscillations are observed within the accessed field range and the branches are not as well-defined as with the ρ-branch.

The fact that the characteristics of the angular dependence of quantum oscillation frequencies in the metallic rare-earth hexaborides are reproduced in the Kondo insulating SmB$_6$ is striking. This observation suggests that a three-dimensional Fermi surface arises from an insulating bulk, contradictory to the conventional description of a Fermi surface being exclusive to a metallic ground state. The insulating behaviour at 45 T excludes the possibility of the quantum oscillations originating from a high-field state in which the charge gap is closed by the magnetic field. The possibility of spatially disconnected metallic patches in SmB$_6$ that gives the observed quantum oscillations has been explored. The presence of rare-earth elements other than Sm has been ruled out to within 0.01% by x-ray spectroscopy.

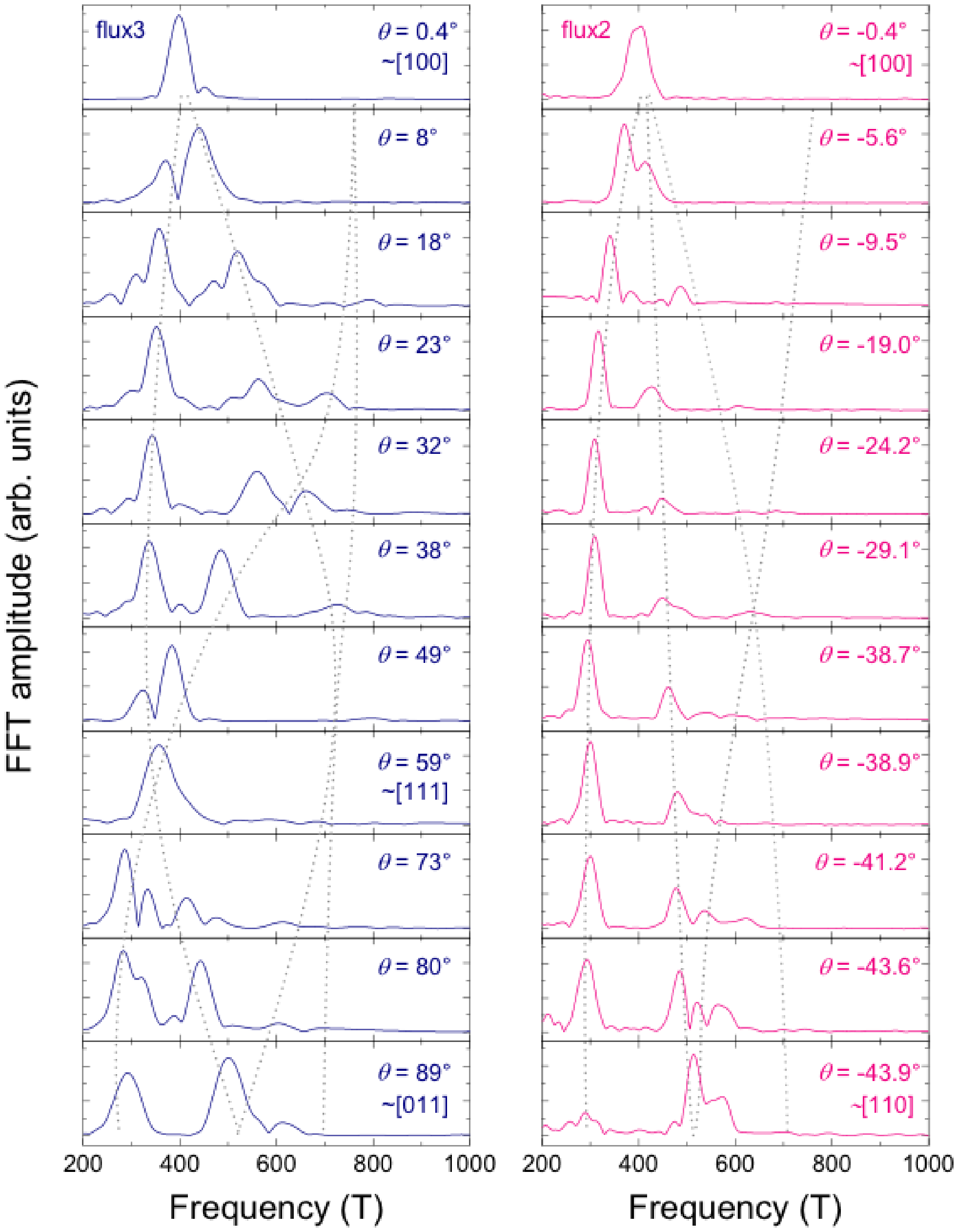

Figure 5.8: **Angular dependence of the dominant oscillation frequencies in SmB$_6$.** θ denotes the angle of the magnetic field **B** with respect to the [100] axis. Measurements are taken on two flux-grown SmB$_6$ crystals. Left: measurements performed with **B** rotating along the [100]-[111]-[110] plane, denoted as positive θ. Right: measurements performed with **B** rotating along the [100]-[110] rotation plane, denoted as negative θ. Dotted lines are guides to the eye illustrating the ρ-branch shown in Figure 5.9.

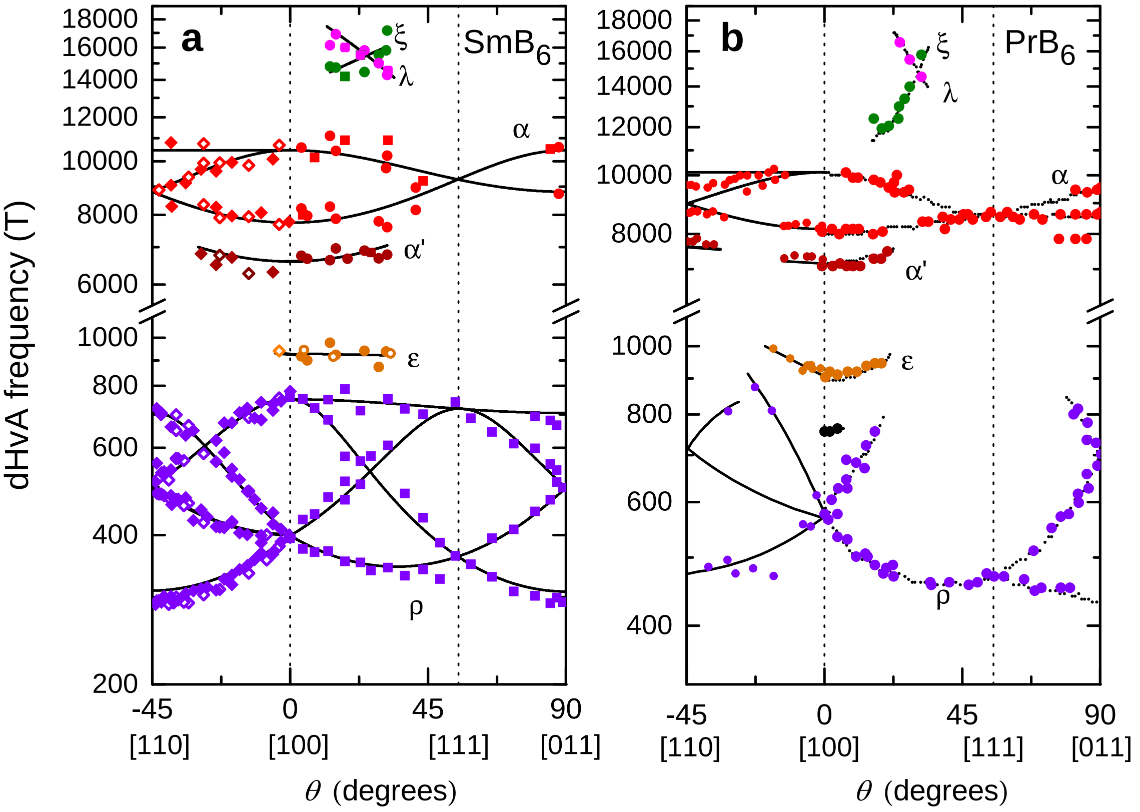

Figure 5.9: **Comparison of the angular dependence of the quantum oscillation frequencies in insulating SmB_6 and metallic PrB_6.** (**a**) Angular dependent quantum oscillations measurements in the [100]-[110] rotation plane performed on two flux-grown crystals (open and solid diamonds), and in the [100]-[111]-[011] rotation plane performed on two floating-zone crystals (open and closed circles) and one flux-grown crystal (close squares). (**b**) Angular dependence of quantum oscillations frequencies in the metallic PrB_6 [73]. Strong resemblance is found between (a) and (b). The α-branch in red is fitted to three large ellipsoidal electron pockets along the $\langle 100 \rangle$ directions and the ρ-branch is fitted to twelve ellipsoidal electron pockets along the $\langle 110 \rangle$ directions as shown in Figure 5.10.

The impact of off-stoichiometry is found to be minimal as atomic emission spectroscopy shows the bulk B:Sm ratio to be 6.02(3) and x-ray spectroscopy shows a surface Sm homogeneity within 1% over multiple scans of 500 μm × 500 μm area. The large amplitude of the dominant oscillations, consistent with the theoretical estimation assuming a contribution from the entire bulk (see Section 5.2.5), makes the contribution from finite metallic patches undetectable by chemical analysis unlikely. The identical quantum oscillation frequencies observed in floating-zone and flux-grown crystals at the same field angle excludes the contribution of aluminium inclusion pertinent to the flux growth. SmB$_6$ is known to become metallic under applied pressure of 4 GPa [69]. The fact that the electropolished floating-zone crystals exhibit the same oscillations as the electropolished and pristine flux-grown crystals shows the quantum oscillations are intrinsic to SmB$_6$ rather than due to surface effect such as strain. However, we observed a significant decrease in oscillation amplitude after thermal cycling in all the samples measured, suggesting the amplitudes of quantum oscillations in SmB$_6$ are sensitive to strain.

The possibility of the quantum oscillations originating from the quantum interference of electron waves between alternative trajectories of an open orbit [74] is found to be inconsistent with our observations. Firstly, it is generally understood that such effect would only manifest in resistivity, but not in thermodynamic properties [45, 75]. Additionally, the oscillation amplitude due to quantum interference is expected to exhibit a very weak, if any, temperature dependence [45], in contrast to our temperature-dependent study (see next Section). Lastly, in the scenario where the largest cyclotron orbits originating from tunnelling through the neighbouring orbits, the magnetic breakdown field is estimated using

$$H_{\mathrm{breakdown}} = \frac{\pi\hbar}{e}\left(\frac{k_g^3}{a_r + b_r}\right)^{1/2}, \tag{5.2}$$

where $1/a_{\mathrm{r}}$ and $1/b_{\mathrm{r}}$ are the radii of curvature of the two closest Fermi surface sections, and k_g is their separation in reciprocal space [45]. In SmB$_6$, $k_g \approx 3.8\ \mathrm{nm}^{-1}$ for the ρ-ellipsoids which are separated by one quarter of the Brillouin zone, $1/a_{\mathrm{r}} = 1/b_{\mathrm{r}} = 1$ nm (see Table 5.1), and we find $H_{\mathrm{breakdown}} \approx 11\ 000$ T. This giant breakdown field, well beyond the access field range, excludes the possibility of a magnetic breakdown occurring in SmB$_6$.

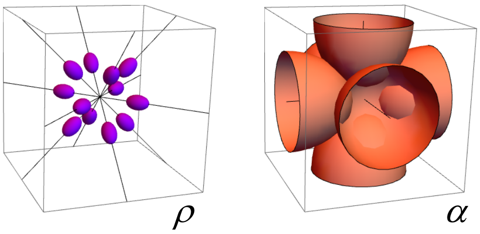

Figure 5.10: **Fermi surface models shared by insulating SmB$_6$ and metallic rare-earth hexaborides.** A density functional theory with a downward shift of the Fermi energy from its calculated position within the gap is used to yields pocket sizes similar to that observed in SmB$_6$.

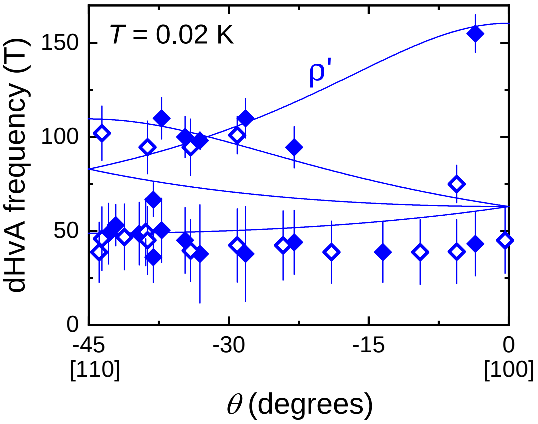

Figure 5.11: **Angular dependence of the lowest dHvA frequencies in SmB$_6$.** Measurements were performed with **B** rotating along the [100]-[110] plane. Errors are given by the full width at half maximum of the peaks in the Fourier transform spectra.

Table 5.1: **Parameters of the observed dHvA frequency branches in SmB$_6$.** Quasiparticle effective mass m^*, in units of free electron mass m_e, are extracted by fitting the temperature dependence of the oscillation amplitude using the Lifshitz-Kosevich formula down to 1 K (section 5.3). The relative ratio of the semi-principal axes of the ellipsoidal Fermi pockets (a, b, and c) are obtained by fitting to the angular dependence of the quantum oscillation frequencies.

Sheet	F_min(T)	m^*/m_e	ak_0 (nm^{-1})	b/a	c/a
α	7750(90)	0.70(4)	4.85(3)	1	1.36(2)
ρ	309(14)	0.18(1)	1.00(2)	0.94(4)	2.3(1)
ρ'	31(6)	0.12(1)	0.23(2)	1.2(2)	3.9(5)

5.2.3 Temperature dependence and effective mass

We next studied the temperature dependence of the observed dHvA oscillations to investigate the low-energy excitations associated with the Fermi surface observed in SmB$_6$. Figure 5.12 shows the quantum oscillations of the floating-zone crystal, FZ-EP1, measured at selected temperatures between 0.4 K and 27 K during the same thermal cycle. Prominent oscillations with a dominant frequency $F = 330$ T can be observed at all temperatures, while the fast oscillations with $F > 1\ 000$ T are rapidly suppressed above 10 K. The more pronounced suppression in amplitude of the high-frequency oscillations suggests a higher effective mass m^* of the associated Fermi pockets. Figure 5.13 shows m^* as a function of oscillation frequency observed in SmB$_6$, extracted by fitting the oscillation amplitude as a function of temperature between $1\text{ K} \leq T \leq 27$ K using the Lifshitz-Kosevich formula of the temperature-damping factor

$$\frac{A_\mathrm{T}}{T} = \frac{A_0}{\sinh X}\ ,\ X = 14.69\frac{m^*T}{B}, \tag{5.3}$$

shown in Figure 5.14. We found that m^*/m_e observed in SmB$_6$ above 1 K lies in the range of 0.12 to 0.90, a surprising low value considering the Kondo effect would typically give rise to heavy fermions. However, m^* as a function of oscillation frequency is found to track closely to that observed in the metallic hexaborides, especially LaB$_6$, as shown in Figure 5.13, which supports a common Fermi surface geometry shared by SmB$_6$ and the metallic rare-earth hexaborides.

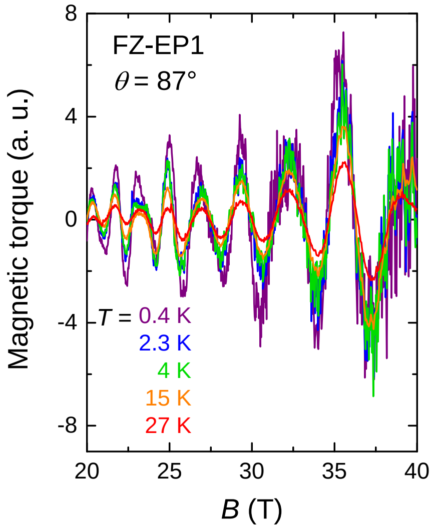

Figure 5.12: **Temperature dependence of the quantum oscillations in SmB$_6$.** Magnetic torque measured on the floating-zone crystal FZ-EP1 with magnetic field applied along $\approx$ [011] ($\theta = 87°$) at temperatures as indicated. The signals are subtracted with a polynomial background of 8th order. High-frequency oscillations can be seen at $B > 28$ T, which are suppressed rapidly with increasing temperature.

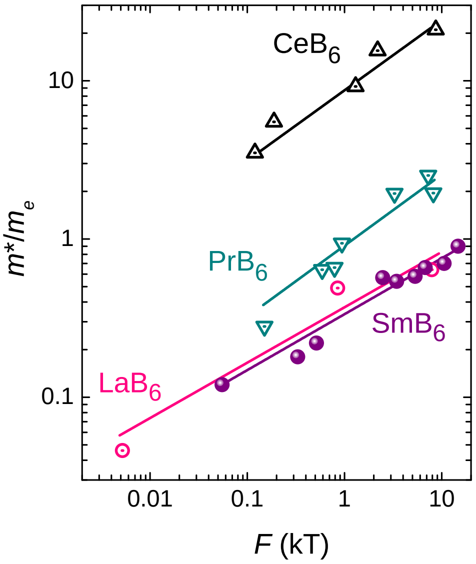

Figure 5.13: **Comparison of m^* in various rare-earth hexaborides.** m^* of multiple frequency branches of SmB_6 is seen to be very similar to the metallic rare-earth hexaborides, especially the non-magnetic LaB_6. Data for the RB_6 (R = La, Ce, Pr) are from [76, 77, 78, 79].

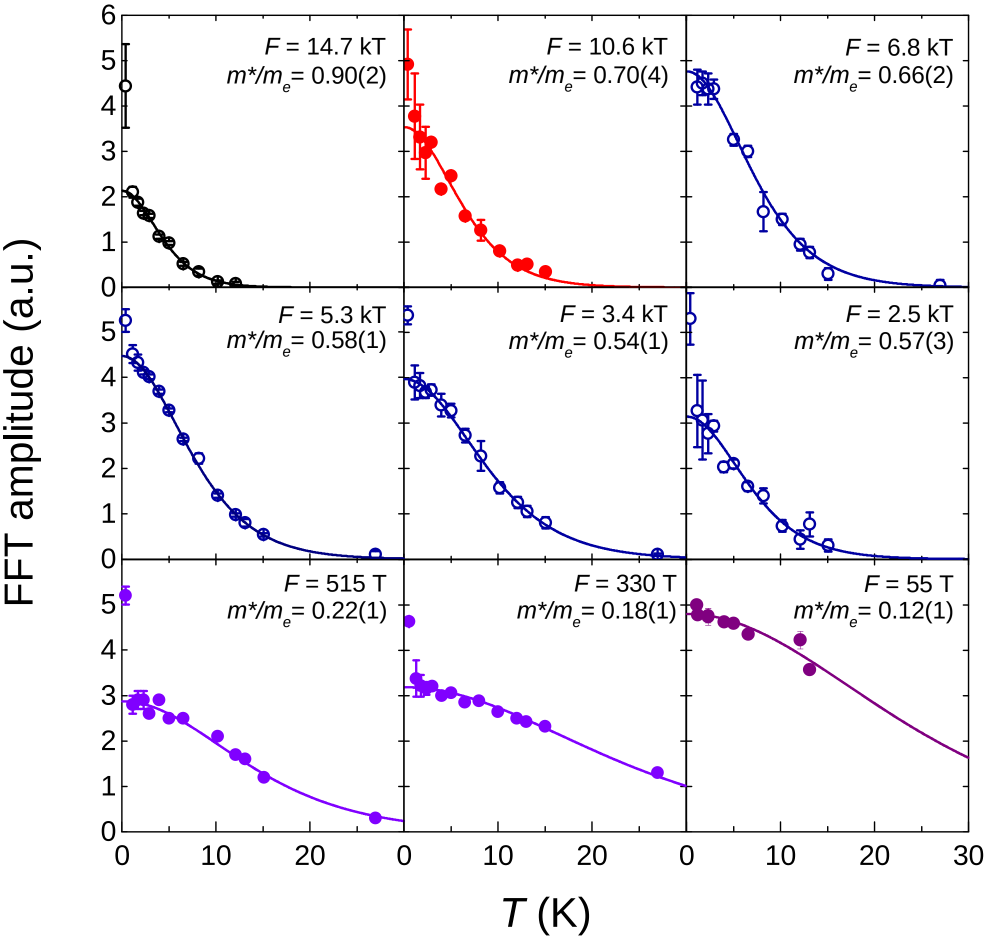

Figure 5.14: **Extraction of effective masses m^* of the observed Fermi pockets in SmB$_6$.** The oscillation amplitude of the frequencies observed at $\theta = 87°$ plotted as a function of temperature. Solid lines are fits to the Lifshitz-Kosevich formula down to $\approx$ 1 K. The error in the amplitude corresponds to the noise floor of the Fourier transform. Below 1 K the oscillation amplitude is considerably higher than the Lifshitz-Kosevich fit for most observed frequencies.

5.2.4 Non-Lifshitz Kosevich behaviour

Given the lightness of the observed m^*, the quantum oscillation amplitude is expected to saturate as temperature decreases below 1 K. However, an unexpected increase in the oscillation amplitude is observed below 1 K across most frequencies, as shown in Figures 5.12 and 5.14, suggesting a deviation from the Lifshitz-Kosevich description. The Lifshitz-Kosevich formalism has been known to be very robust in most strongly correlated electronic systems, most notably the cuprate and heavy fermion superconductors [80, 81]. The departure from the Lifshitz-Kosevich formula indicates the unconventional character of the Fermi surface in SmB$_6$. The increase in oscillation amplitude below 1 K is further investigated by extending the measurement temperature range down to $\approx$ 30 mK. Figure 5.15 shows the amplitude of the dominant F = 330 T oscillations as a function of temperature measured on two floating-zone SmB$_6$ crystals. In both samples the oscillation amplitude exhibits a steep upturn as the temperature decreases from 1 K and shows no sign of saturation down to 33 mK. In contrast, the upturn in the oscillation amplitudes of the same frequency is absent in the flux-grown crystals. This observation further illustrates the subtle difference between the two types of SmB$_6$ crystals. Such diverging behaviour is often associated with quantum criticality, and possibly points to the floating-zone crystals being in close proximity to a postulated quantum critical point, potentially associated with the pressure-induced insulator-metal transition [69].

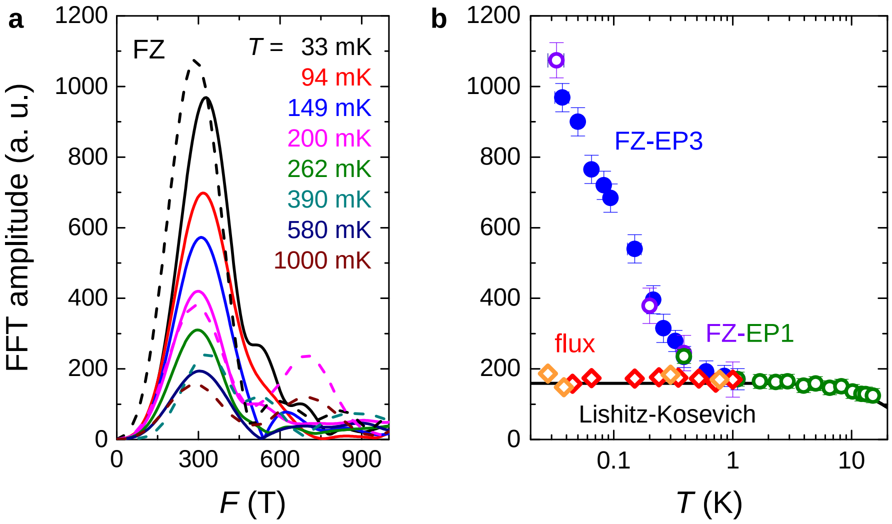

Figure 5.15: **Departure from the Lifshitz-Kosevich behaviour in SmB$_6$.** (**a**) Fourier transform of the dominant oscillation frequency F = 330 T in two floating-zone SmB$_6$ crystals, FZ-EP1 (dashed) and FZ-EP3 (solid), measured at temperatures as indicated. (**b**) Amplitude of the F = 330 T oscillations in floating-zone crystals (open and close circles) shows a steep upturn deviating from the Lifshitz-Kosevich fit below 1 K, while the deviation is absent in the flux-grown crystals (open diamonds).

5.2.5 Evidence of a bulk origin

The surprising observation of quantum oscillations originating from the insulating bulk of SmB$_6$ is further supported by comparing the experimental oscillation amplitude with theoretical calculations. Figure 5.16 compares the amplitudes of quantum oscillations with the lowest frequencies measured in the metallic LaB$_6$ and insulating SmB$_6$, with the theoretical calculations assuming either a bulk or surface origin. The lowest frequency oscillations are chosen since they are closest to the zero phase, infinite field limit. The LaB$_6$ and SmB$_6$ measurements are performed using an identical setup, and the measured capacitance ΔC is converted into magnetic moment using

$$\Delta p_s = \frac{d_0 L k a^3}{s^3 \mu_\mathrm{B} B \sin\theta_\mathrm{M}} \frac{\Delta C}{C_0} \tag{5.4}$$

as derived in Section 4.3, where $p_s = m(a^3/s^3)/\mu_\mathrm{B}$ is the magnetic moment in units of Bohr magneton per unit cell, θ_M is the angle between the magnetic field B and the total magnetic moment, and s^3 is the sample volume. Using the experimental parameters of $d_0 = 0.1$ (0.1) mm, $L = 3.8$ (3.8) mm, $k = 17$ (28) N$\cdot m^{-1}$, $a = 0.413$ (0.416) nm, and $s^3 = 0.16$ (0.25) mm^3 for the LaB$_6$ (SmB$_6$) crystal, the quantum oscillation amplitudes are estimated to be $\approx \frac{1.3\cdot 10^{-5}}{\sin\theta_\mathrm{M}}$ for LaB$_6$ at 9 T and $\approx \frac{1.1\cdot 10^{-5}}{\sin\theta_\mathrm{M}}$ for SmB$_6$ at 18 T.

The infinite field, zero spin-splitting amplitude in the oscillatory magnetisation M assuming a bulk origin in the Lifshitz-Kosevich theory is given by

$$D = -\frac{\mu_\mathrm{B} S_{k0}^{3/2} m_\mathrm{e}}{2\pi^4 m^*} \sqrt{\frac{B}{F|A''|}}, \tag{5.5}$$

where S_{k0} is the Fermi surface area normal to the magnetic field, m^* is the effective mass in absolute units, F is the oscillation frequency, and $|A''|$ is the second derivative of the Fermi surface area with respect to the effective wave vector along B [45]. We define the magnetic moment per unit cell in units of Bohr magnetons as Dv/μ_B, where $v = a^3$ is the volume of the unit cell, and the theoretical amplitude in the infinite field, zero spin-splitting limit becomes

$$p_s = \frac{|D|v}{\mu_\mathrm{B}} = \sqrt{\frac{2\pi}{|A''|}} \frac{m_\mathrm{e}}{m^*} \left(\frac{a k_\mathrm{F}}{\pi}\right)^3 \sqrt{\frac{B}{8F}}, \tag{5.6}$$

where we define the effective Fermi wavevector k_F via $S_{k0} = \pi k_\mathrm{F}^2$. The anisotropy term, $\sqrt{2\pi/|A''|}$, is dependent on the eccentricity r of the ellipsoidal Fermi surface, and hereafter will be written as $f(r)$.

A comparison of the measurements with the expected theoretical amplitudes for oscillations from the bulk is shown in Figure 5.16(a,b). For LaB$_6$, using the experimentally measured values of $F = 5.9$ T, $m^*/m_\mathrm{e} = 0.05$, $a = 0.416$ nm, and considering the damping terms $R_\mathrm{D} = $ exp(-1

T/B), $R_{\mathrm{S}} = 0.5 - 1$, an estimated $f(r) \approx 1 - 2$, and a degeneracy factor of 2, we find the theoretical amplitude of the $F = 5.9$ T oscillations to be of the order $\approx 10^{-4}$ μ_{B} per unit cell at $B = 6.2$ T. This calculated amplitude is consistent with the measured value within an order of magnitude, since $\sin\theta_{\mathrm{M}}$ is of the order 0.1 to 1. Similarly for SmB$_6$, using the experimentally measured values of $F = 31$ T, $m^*/m_{\mathrm{e}} = 0.12$, $a = 0.413$ nm, and $R_{\mathrm{D}} = \exp(\text{-}30\ \mathrm{T/B})$, and an estimated $f(r) \approx 1 - 2$, $R_{\mathrm{S}} = 0.5 - 1$, and a degeneracy factor of $2 - 8$, we find the theoretical amplitude is of the order $\approx 10^{-5}$–10^{-4} μ_{B} per unit cell at $B = 16.7$ T. This calculated amplitude is again consistent with the measured value within an order of magnitude.

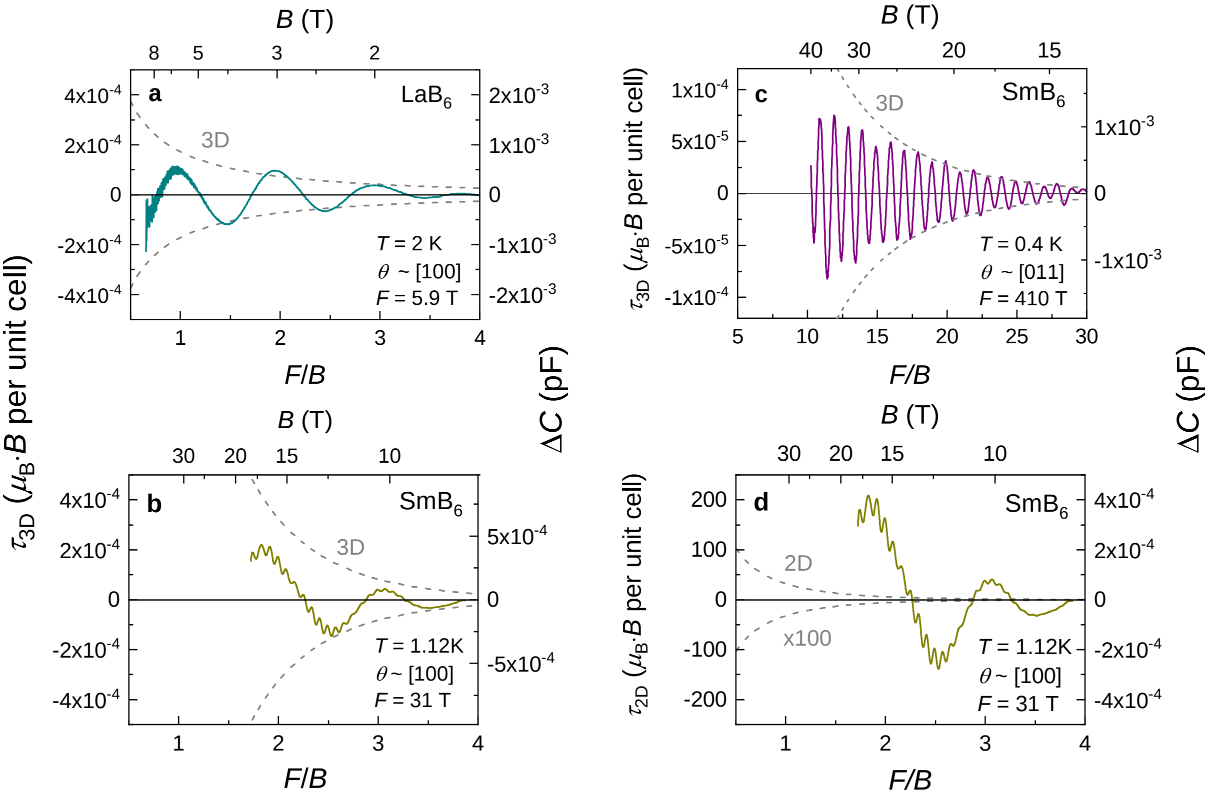

Figure 5.16: **Comparison of the observed quantum oscillations to theoretical values assuming a 3D and 2D Fermi surface model.** (**a, b**) Amplitude of the lowest frequency quantum oscillations in units of $\mu_{\mathrm{B}} \cdot B$ per unit cell assuming a bulk origin measured using the same setup in (**a**) metallic LaB$_6$ and (**b**) insulating SmB$_6$. The theoretical estimates using the Lifshitz-Kosevich formalism and assuming that the quantum oscillations originate from the bulk using the Lifshitz-Kosevich formulation are shown in grey dashed lines. (**c**) Amplitude of the dominant quantum oscillations in SmB$_6$ assuming a bulk origin. The lowest frequency oscillations are subtracted away. (**d**) Amplitude of the lowest frequency quantum oscillations in SmB$_6$ assuming a surface origin with the same data shown in (b). Experimental amplitude is at least an order of magnitude larger than the theoretical values assuming a surface origin.

A theoretical estimation of the quantum oscillation amplitude is made for the dominant quantum oscillations with $F = 410$ T in $\mathrm{SmB_6}$, using $m^*/m_e = 0.18$, $R_{\mathrm{D}} = \exp(\text{-}51\ \mathrm{T}/B)$, and similar estimates for $f(r), R_{\mathrm{S}}$, and degeneracy factor, as previously discussed. This calculated amplitude is again found to be consistent with the measurement within an order of magnitude, as shown in Figure 5.16(c).

In the two-dimensional limit, the carrier density per unit surface area is given by

$$n = \frac{2}{(2\pi)^2}\pi k_{\mathrm{F}}^2, \tag{5.7}$$

including a factor of 2 for spin degeneracy. For the lowest observed quantum oscillation frequency of $F = 31$ T, we find $n = 1.5\times10^{16}\ m^{-2}$. We define the magnetic moment per unit cell in units of Bohr magneton, which yields the peak amplitude in the infinite field, zero spin-splitting limit given by

$$p_s = na^2\frac{2m_{\mathrm{e}}}{\pi m^*} = \frac{4m_{\mathrm{e}}}{m^*}\Big(\frac{k_{\mathrm{F}}}{k_{\mathrm{BZ}}}\Big)^2, \tag{5.8}$$

where $k_{\mathrm{BZ}} = 2\pi/a$. Using the measured parameters for the $F = 31$ T oscillations in $\mathrm{SmB_6}$, we find the theoretical maximum value of the peak amplitude to be $\approx 10^{-2}\ \mu_{\mathrm{B}}$ per surface unit cell before considering the damping terms R_{D} and R_{S}, which would reduce the theoretically predicted value to $\approx 10^{-3}\ \mu_{\mathrm{B}}$ per surface unit cell at $B = 18$ T. Considering the ratio of surface unit cells to all unit cells of $\approx 10^{-6}$, calculated using the sample dimensions, the magnetic moment is at least $\approx 10\ \mu_{\mathrm{B}}$ per surface unit cell at $B = 18$ T (Figure 5.16(d)), without accounting for the orientation of the magnetic moment $\sin\theta_{\mathrm{M}}$ that would further increase p_s. This magnetic moment associated per surface unit cell is an unphysically large value for the non-magnetic $\mathrm{SmB_6}$ and several orders of magnitude larger than the theoretical calculation. The quantum oscillations associated with a surface origin is thus not supported.

The absence of quantum oscillations in the resistivity of $\mathrm{SmB_6}$ in magnetic fields up to 93 T [70], and the presence of large bulk quantum oscillations in the torque magnetisation from magnetic fields as low as 10 T is striking. One possibility to resolve the different responses of $\mathrm{SmB_6}$ to magnetic field in electrical transport and in magnetisation is to invoke a neutral low-energy itinerant excitation within the charge Kondo gap. Such itinerant neutral low-energy excitations could exhibit quantum oscillations by Landau quantisation of the density of states within the charge gap. Experimental evidence from specific heat and thermal conductivity supporting this scenario is presented in the following section.

5.3 Evidence of neutral itinerant in-gap excitations

The measurements described in this section were performed in collaboration. The specific heat measurements were performed by A. Padgett and Y. Yakano at the University of Florida, and S. Yamashita from Osaka University. The thermal conductivity measurements were performed by W. Toews and R. Hill from the University of Waterloo, and X. Chen and M. Sutherland from the University of Cambridge.

5.3.1 Specific heat

The available electronic density of states near the Fermi level contributes directly to the specific heat of a material, making it a direct probe of low-energy excitations within the charge gap at the Fermi energy E_F. The specific heat of a solid can be expressed as

$$\begin{aligned} C_\mathrm{V} &= \frac{\pi^2}{2} N k_\mathrm{B} \frac{k_\mathrm{B} T}{E_\mathrm{F}} + \frac{12\pi^4}{5} \frac{k_\mathrm{B}}{a^3} \left(\frac{T}{\Theta_\mathrm{D}}\right)^3 \\ &= \gamma T + A T^3, \end{aligned} \tag{5.9}$$

where N is the number of electrons, a is the lattice constant, and Θ_D is the Debye temperature. Since the compressibility of a solid is negligible, $C_\mathrm{V} \approx C_\mathrm{P}$ under experimental conditions. The T-linear term is the electronic contribution with the proportionality factor γ, known as the Sommerfeld coefficient, and the T^3-term is the phonon contribution. C_P/T is expected to vanish at zero temperature for an insulator while a residual term is expected for a metal due to the finite electronic contribution. Figure 5.17 shows the specific heat and Sommerfeld coefficient of a floating-zone $\mathrm{SmB_6}$ crystal measured between 0.06 K and 10 K. The phonon contribution is calculated using $\Theta_\mathrm{D} = 373$ K [82]. A finite γ is observed down to the lowest temperature, in contrast to what is expected for an insulator.

Known effects that can contribute to a finite specific heat, such as the electronic and nuclear Schottky anomaly, are found to be insufficient to account for the observed γ within the probed temperature range. The electronic Schottky anomaly, due to the opening of a charge gap, is known to occur in $\mathrm{SmB_6}$ at $T \approx 40$ K with an estimated $\Delta \approx 10$ meV [83], in good agreement with the transport measurements. The nuclear contribution due to splitting of the nuclear energy levels, by either an effective magnetic field (from electron orbital motion) or an electric field gradient (acting on nuclear quadrupole moment), are found to be negligible. A finite time-average of the effective magnetic field is required for an observable nuclear contribution to specific heat. The absence of a static magnetic order in $\mathrm{SmB_6}$ down to 19 mK [84] excludes of a magnetic origin of the measured γ down to 63 mK. The nuclear quadrupole contribution is estimated to be $\approx 0.02\ \mathrm{mJ{\cdot}mol^{-1}{\cdot}K^{-2}}$, two orders of magnitudes smaller than the observed γ [85]. Rather, this observation of a finite γ down to the lowest temperature suggests that a sizeable additional density of states emerges at low temperatures, consistent with the observation of quantum oscillations due to the Landau quantisation of the density of states.

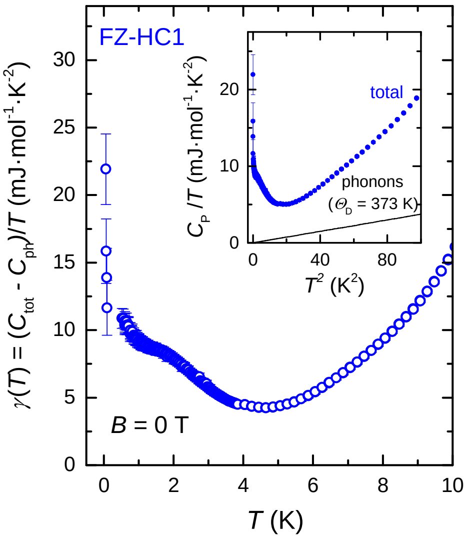

Figure 5.17: **Sommerfeld coefficient γ of floating-zone SmB$_6$ at zero magnetic field.** Measurements were performed on an electropolished floating-zone crystal, FZ-HC1, down to 63 mK. A finite γ at low temperatures is found, unexpected for an insulator. **Inset**: the measured total specific heat and calculated phonon contribution using the Debye temperature Θ_D of 373 K [82].

We calculate γ using the three-dimensional Fermi surface model obtained from the quantum oscillations, and find a good quantitative agreement with that observed in the specific heat measurement. Within conventional Fermi liquid theory [86], the linear specific heat coefficient γ is related to the density of states at the Fermi energy, $D(E_F)$, by

$$D(E_F) = \frac{3\gamma}{\pi^2 k_B^2} \tag{5.10}$$

$$= \frac{1}{4\pi^3 \hbar} \int_S \frac{dS}{|v^*|}, \tag{5.11}$$

where v^* is the quasiparticle velocity and S is the Fermi surface in k-space. We parameterise the Fermi surface of SmB$_6$ using

$$E_F = \frac{\hbar k_x^2}{2a^2 m^*} + \frac{\hbar k_y^2}{2b^2 m^*} + \frac{\hbar k_z^2}{2c^2 m^*}, \tag{5.12}$$

where $a, b,$ and c are the relative ratios of the semi-principal axes for the ellipsoidal Fermi pockets. Using $k_x = ak_0 \cos\phi \sin\theta$, $k_y = bk_0 \cos\phi \cos\theta$, and $k_z = ck_0 \sin\phi$, the area element dS

and quasiparticle velocity v^* are given by

$$dS = k_0 \cos\phi \sqrt{a^2b^2\sin^2\theta + c^2\cos^2\phi(a^2\sin^2\theta + b^2\cos^2\theta)}d\phi d\theta, \tag{5.13}$$

$$|v^*| = |1/(\hbar k_0)\nabla_k E_\mathrm{F}| = \frac{\hbar k_0}{abcm^*}\sqrt{a^2b^2\sin^2\phi + c^2\cos^2\phi(b^2\sin^2\theta + a^2\cos^2\theta)}. \tag{5.14}$$

Using the fitted parameters for a, b, c, and m^*, as summarised in Table 5.1, and integrating over $\phi = (-\pi/2, \pi/2)$ and $\theta = (0, 2\pi)$, γ is found to be 4(1) mJ·mol^{-1}· K^{-2} from the quantum oscillation measurements, with the large α sheet contributing 3 mJ·mol^{-1}· K^{-2}. This calculated γ is found to agree quantitatively with γ = 4(2) mJ·mol^{-1}· K^{-2} observed in the specific heat measurements at $\approx$ 4 K, before the further increase in γ occurs and the conventional Fermi liquid picture no longer applies. A common origin of in-gap low-energy excitations is indicated from the agreement between the specific heat and quantum oscillation measurements.

A distinction between the SmB$_6$ grown by the floating zone and flux methods is observed, as shown in Figure 5.18. The behaviour of C_P/T as a function of temperature is qualitatively similar down to 1 K between the floating-zone and flux-grown crystals, with the latter showing a higher C_P/T. Upon cooling below 1 K, a further increase in C_P/T is observed in the floating-zone crystals while absent in flux-grown crystal. The steep increase in γ at low temperatures resembles the increase of quantum oscillations amplitude in the floating-zone crystals as shown in Figure 5.15, potentially a characteristic of proximity to a quantum critical point.

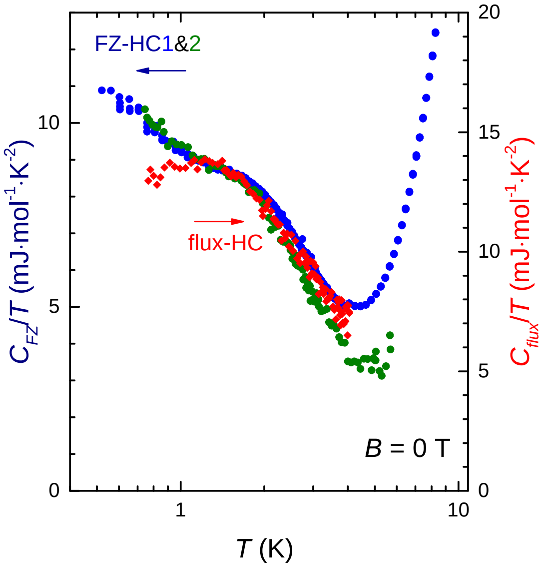

Figure 5.18: **Measured specific heat of three SmB$_6$ crystals grown by the floating zone and flux methods at zero magnetic field.** A finite specific heat at low temperature is observed in all samples. A further increase in C_P/T below 1 K is observed in floating-zone crystals but is absent in flux-grown crystal.

5.3.2 Thermal conductivity

A complementary technique to probe the itinerant excitations at E_F is the thermal conductivity measurement at low temperature where the electronic contribution is isolated. The thermal conductivity κ of a solid can be expressed as

$$\begin{aligned}\kappa &= \frac{1}{6}n\pi^2 {k_\mathrm{B}}^2 \frac{T}{E_\mathrm{F}} {v_\mathrm{F}}^2 \tau + \frac{4\pi^2}{5}\frac{k_\mathrm{B}}{a^3} d v_\mathrm{s} \left(\frac{T}{\Theta_\mathrm{D}}\right)^3 \\ &= \beta T + \alpha T^3,\end{aligned} \tag{5.15}$$

where n is the electron density, τ is the carrier lifetime, a is the cubic lattice constant, and v_s is the sound velocity. It can be rewritten as

$$\kappa / T = \beta + \alpha T^2, \tag{5.16}$$

where β is the electronic contribution and αT^2 is the phonon contribution. At zero temperature when the phonon contribution vanishes, β is expected to vanish for an insulator while remain finite for a metal.

Figure 5.19 shows the thermal conductivity measured on a floating-zone $\mathrm{SmB_6}$ crystal down to 150 mK, plotted as a function of T^2. At zero magnetic field, the temperature dependence of κ/T is well modelled with a phonon contribution calculated using sample dimensions and Θ_D = 373 K, as shown in Figure 5.19(a). The peak in κ with decreasing temperature indicates the phonon contribution transitions from being limited by the mean free path at higher temperatures (due to phonon-phonon scattering) to being limited by the number of active phonons at lower temperatures (while the mean free path is limited by sample dimensions) [87]. The fact that the low-temperature phonon contribution is limited by sample boundary reflects the high sample quality in our study. Surprisingly, κ/T is enhanced significantly with an application of magnetic field, in contrast to what is expected for an insulator. This additional κ/T arises from a phonon contribution is unlikely as the boundary-limit has already been reached. The electronic contribution of κ/T after subtracting the phonon contribution is highlighted in Figure 5.19(b). The expected contribution from the conducting surface layer is calculated using the Wiedemann-Franz relation:

$$\frac{\kappa}{\sigma} = L_0 T, \tag{5.17}$$

where L_0 is the Lorenz number = 2.44×10^{-8} W·Ω·K^{-2}. The expected surface contribution is found to be 3×10^{-6} W·m^{-1}·K^{-2}, four orders of magnitudes lower than the measurement, excluding the possibility of a surface origin of the field-enhanced thermal conductivity.

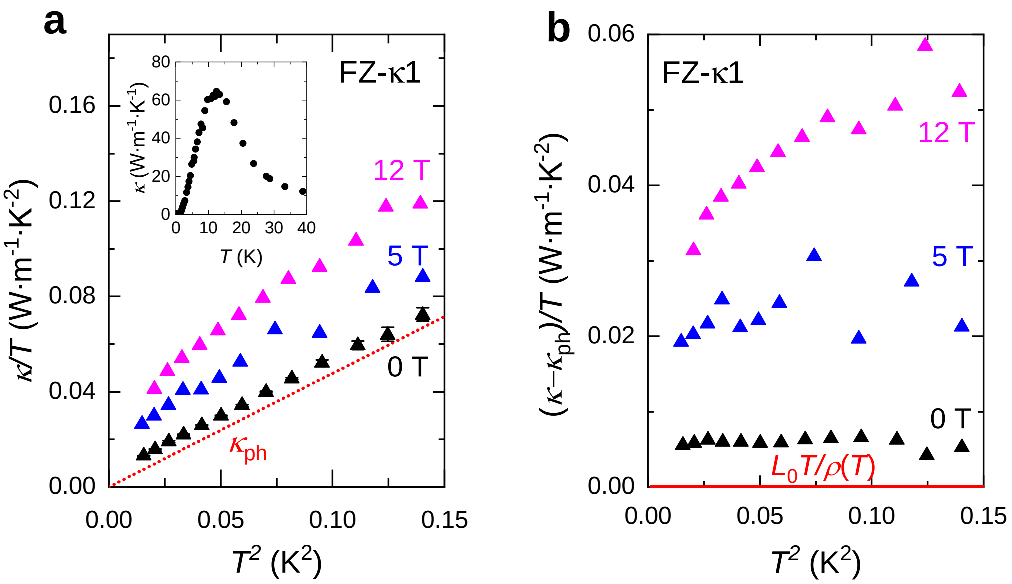

Figure 5.19: **Thermal conductivity of SmB_6 at fixed magnetic fields.** (**a**) Measured κ/T as a function of T^2 of a floating-zone crystal, FZ-κ1, down to 150 mK. The phonon contribution κ_{ph} is calculated using $\Theta_{\mathrm{D}} = 373$ K [82]. Good agreement is found between the measured κ at zero magnetic field and calculated κ_{ph}.A significant enhancement in κ/T is found with increased magnetic field, unexpected for an insulator. **Inset**: Measured κ up to 40 K at zero magnetic field. The peak at ≈ 10 K signifies the phonon mean free path is limited by sample dimensions [87]. (**b**) κ/T after subtraction of the phonon contribution κ_{ph}. The red line shows the expectation from the Wiedemann-Franz relation using the resistivity at zero magnetic field.

We estimate the carrier mean free path, l, from the measured thermal conductivity and find good agreement with that inferred from the quantum oscillations. For a spinon Fermi surface with gapless excitations, κ is related to the scattering time τ by

$$\frac{\kappa}{T} = \frac{k_{\mathrm{B}}^2 \tau}{m^* a^3}, \tag{5.18}$$

where a is the lattice constant and $\tau = \frac{l}{v_{\mathrm{F}}}$, where v_{F} is the Fermi velocity [88]. Using the relation $m^* v_{\mathrm{F}} = \hbar k_{\mathrm{F}}$, one finds

$$l = \frac{\kappa}{T} \frac{\hbar k_{\mathrm{F}} a^3}{k_{\mathrm{B}}^2}, \tag{5.19}$$

where $k_{\mathrm{F}} = \sqrt{2eF/\hbar} = 5.8 \times 10^9$ m^{-1} for the 11 kT α-pocket in SmB$_6$, and $a = 4.13$ Å. The large α-pocket is used since it contributes the most to the density of states at E_{F} and thus to the thermal conductivity. At temperature ≈ 0.2 K and magnetic field ≈ 12 T, we find $\kappa/T = 0.04$ W·m^{-1}·K^{-2} and $l \approx 10^{-8}$ m. The mean free path obtained from quantum oscillations is calculated using

$$l = \frac{\pi \hbar k_{\mathrm{F}}}{e B_0}, \tag{5.20}$$

with the exponential damping term B_0 found to be ≈ 200 T for the 11 kT α-pocket in the floating-zone crystal. l is found to be $\approx 5 \times 10^{-8}$ m from quantum oscillations, which agrees with that estimated from thermal conductivity within one order of magnitude. The agreement between the thermal conductivity and quantum oscillation measurements points to a common bulk origin of the itinerant neutral carriers.

Recent studies have reported a significant field-enhancement in κ/T in the floating-zone SmB$_6$ crystals and a less-pronounced enhancement in the flux-grown crystals [89, 90], similar to our observations. The absence of a neutral fermionic excitation, however, was concluded based on the extrapolation of $\kappa/T \to 0$ as $T \to 0$ in their measurements down to 70 mK, with the field-enhancement interpreted as an increased phonon contribution due to a scattering mechanism suppressed by magnetic field. We note that thermal conductivity measurements in the insulating SmB$_6$ are challenging due to the large contact resistances at very low temperatures. Known effects such as a long thermal equilibrium time and the phono-electron thermal decoupling [91] can lead to experimental uncertainties, hence we are careful to only report results within the low temperature limit where the κ/T can be reliably measured. The interpretation of the field-enhancement due to an increased phonon contribution appears to be inconsistent with our results as the phonon contribution has reached the boundary limit at zero field (see Figure 5.19(a)), which cannot further increase in a magnetic field. We note that the observation in [89, 90] of a non-boundary limited phonon contribution is possbly due to a difference in sample quality, as evidenced by the lower IRR in [89] and a lower height of the phonon $\kappa(T)$ peak at high temperature [90].

Intriguingly, the field enhancement of the thermal conductivity of SmB_6 in a magnetic field is reminiscent of what has been observed in the Mott insulating organic systems $EtMe_3Sb$-$[Pd(dmit)_2]_2$ and κ-$(BEDT\text{-}TTF)_2Cu_2(CN)_3$ [92, 93]. Figure 5.20 shows the field dependence of the thermal conductivity enhancement expressed as $\kappa(B)/\kappa(0)$ at $T \approx 0.3$ K in SmB_6 and in the organic compounds, which are thought to be spin liquid candidates with neutral quasiparticles within the charge gap. The remarkable similarity of the field-enhanced thermal conductivity observed in SmB_6 and the spin liquid candidates suggests the presence of in-gap itinerant neutral low-energy excitations at low temperatures in SmB_6.

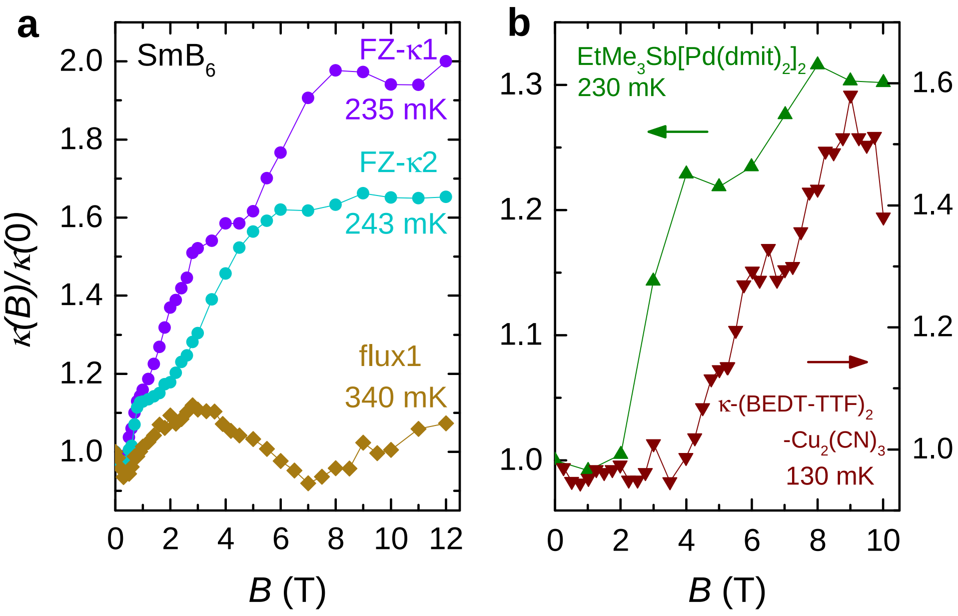

Figure 5.20: **Field dependence of field-induced enhancement in thermal conductivity $\kappa(B)/\kappa(0)$ in SmB_6 and insulating spin liquid candidates.** (**a**) Measurements from two floating-zone and one flux-grown SmB_6 crystals. (**b**) Data in the organic spin liquid candidates at low temperatures reproduced from [92, 93]. Large increase in $\kappa(B)/\kappa(0)$ in magnetic field is seen in two floating-zone SmB_6 crystals with strong similarity to those in the insulating spin liquid candidates. A subtle increase in the flux-grown SmB_6 is observed, in contrast to what is seen in the floating-zone crystals.

5.4 Proposals for the electronic ground state in SmB_6

The observation of dHvA oscillations with three-dimensional characteristics in the Kondo insulating SmB_6 is striking. The collective experimental evidence of (i) an electrically insulating behaviour at high magnetic field, (ii) a large quantum oscillation amplitude consistent with theoretical calculations assuming a bulk origin, (iii) a finite linear specific heat at low temperatures, and (iv) an electronic thermal conductivity enhanced in a magnetic field at low temperatures points to additional fermionic density of states emerging from the charge gap. This in-gap state is found to have charge-neutral and itinerant low-energy excitations that do not carry electrical charge but carry heat.

Known systems that exhibit key experimental observations similar to SmB_6 are the organic quantum spin liquid (QSL) materials $EtMe_3Sb[Pd(dmit)_2]_2$ and κ-$(BEDT\text{-}TTF)_2Cu_2(CN)_3$ [92, 93]. These QSL candidates have been associated with a theoretical model of novel neutral low-energy excitations, known as *spinons*, which carry energy but not charge. However, no quantum oscillations have been reported to date in the QSLs. A possible explanation of the absence of quantum oscillations is the large size of the charge gap $\approx$ 50 meV in the QSLs, an order of magnitude higher than $\approx$ 4 meV in SmB_6. In addition, the linear specific heat coefficients at low temperature are $\approx 30\ \mathrm{mJ{\cdot}K^{-2}{\cdot}\ mol^{-1}}$, again an order of magnitude higher than that in SmB_6. These observations implies the quasiparticle effective mass is much larger in the QSLs, making the observation of quantum oscillations more challenging. A caveat in associating SmB_6 with the QSLs is the different nature of the insulating gaps between these two systems. In the QSLs, the insulating behaviour is due to the Mott interaction in the 2D building blocks, in contrast to the Kondo gap formed by the hybridisation between the f- and d-electrons in cubic SmB_6. The theoretical framework to describe spinons in a QSL requires the virtual charge fluctuations in the 2D geometry [94], while it is not immediately clear how charge fluctuation is facilitated in a 3D lattice.

A viable theoretical model to describe the electronic ground state in SmB_6 must account for all the experimental observations. The model that invokes inter-band tunnelling to explain the occurrence of quantum oscillations in an insulating state [95] appears to be at odds with the thermodynamic evidence which indicates the existence of a substantial density of states within the Kondo gap. Alternative proposals that invoke low-energy excitations within the charge gap have been presented, including spinons [94], magnetic excitons [96], composite excitons [97], and Majorana fermions [98]. However, these models are based on the framework of conventional Fermi liquid in which novel excitations are invoked to construct a neutral quasiparticle. A central challenge in the aforementioned models would be how to reconcile the different responses of the quasiparticles to electric and magnetic fields. From the Maxwell formulation, a particle that responds to the magnetic field must also respond to the electric field due to gauge invariance of the vector potential. Unless the gauge invariance is locally broken. A proposal that SmB_6

is a 'failed' superconductor has been presented [99], with sub-Kelvin T_c and sub-Gauss H_c, making the experimental verification challenging. An outstanding possibility is to discard the conventional description of a Fermi liquid, which has shown some of its limitations in the last two decades, and explore a new route to the realisation of Fermi surface in the absence of a Fermi liquid [100].

Chapter 6

Fermi surface in YBCO$_{6+x}$

The correct description of the mysterious pseudogap regime is crucial towards a better understanding of the high-T_c cuprates. The origin of the small nodal Fermi arcs accompanied by large antinodal gaps, in stark contrast to the starting large paramagnetic Fermi surface calculated from band structure and observed in overdoped cuprates [21], and the description of the low-temperature ground state in underdoped cuprates has remained unclear [38, 101]. In this chapter, results of transport and magnetisation measurements on YBCO$_{6+x}$ over a wide range of temperature, electrical current, doping, and magnetic field are presented. We unveiled a hidden vortex solid state that constitutes the ground state of the pseudogap regime in underdoped YBCO$_{6+x}$ at millikelvin temperatures, resilient to magnetic field but fragile against thermal or electrical perturbations. A surprising coexistence of superconductivity and quantum oscillations, with signatures of a nodal Fermi pocket formed by connecting the truncated Fermi arcs, is thus found. This field-resilient vortex solid state at low temperature evolves to a state with pairing correlations up to T^*, suggesting a large pairing energy scale but suppressed phase coherence in the underdoped YBCO$_{6+x}$.

6.1 Hidden vortex solid state in underdoped YBCO$_{6+x}$

Since YBCO$_{6+x}$ is a high-T_c superconductor, previous efforts on studying the underlying electrical transport properties by suppressing superconductivity with magnetic fields have been made primarily in pulsed fields, for the higher available magnetic fields, meanwhile it limits the lowest accessible temperature to ≈ 1.5 K and requires the use of a high measurement current on the order of 10 mA for satisfactory signal-to-noise. By performing electrical transport measurements in continuous fields down to millikelvin temperature and using a vanishingly small applied current, on the order of 10 μA, we found a dramatic dependence of the onset magnetic field of finite resistivity on the applied current density, and revealed a previously hidden vortex state in underdoped YBCO$_{6+x}$ which persists to the highest accessible field of 45 T.

6.1.1 Onset magnetic field of finite resistivity

We first performed electrical resistivity measurements on YBCO$_{6.55}$, with a hole doping $p = 0.108$, where quantum oscillations and transport properties have been intensively investigated [38, 102]. Figure 6.1 shows the in-plane resistivity and magnetic torque measured as a function of magnetic field on two YBCO$_{6.55}$ samples, with an applied current I of 1 mA along the crystalline $\hat{a}$-axis and magnetic field along the crystalline $\hat{c}$-axis. Experimental setups are shown in Figures 3.9 and 4.9, respectively. The same configuration is used hereinafter unless stated otherwise. The onset magnetic field of finite resistivity, $\mu_0 H_\mathrm{r}$, defined as the magnetic field at which the resistivity exceeds the noise level, is seen to increase quickly with decreasing temperature and exceeds 35 T at 1.2 K in both YBCO$_{6.55}$ samples. This observation is complemented by the hysteresis observed in magnetic torque upon sweeping the magnetic field in different directions, which signifies the trapping of vortices in a superconductor.

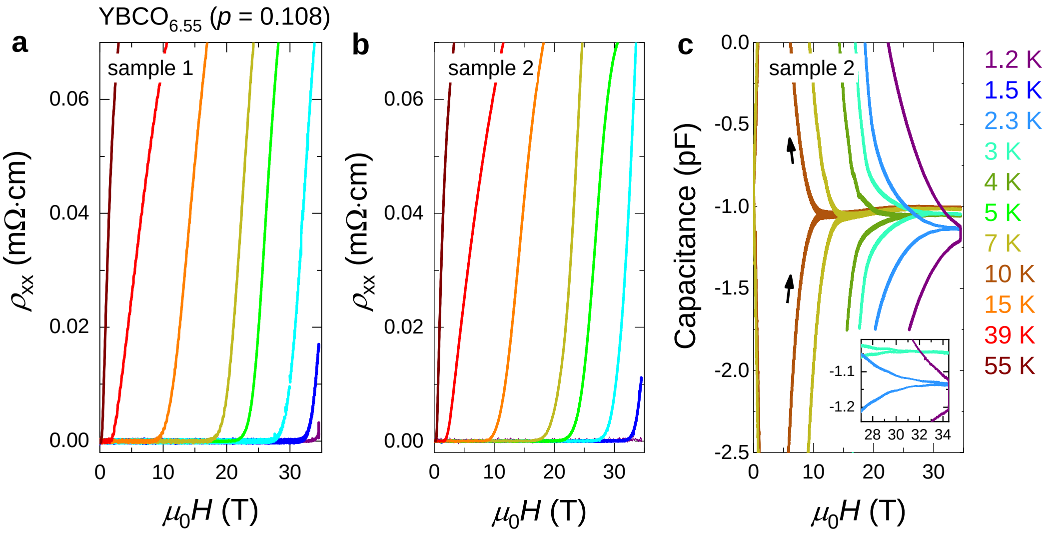

Figure 6.1: **Superconductivity in YBCO$_{6.55}$ revealed by electrical resistivity and torque magnetometry.** (**a, b**) In-plane resistivity ρ_xx as a function of magnetic field measured on two samples using an electrical current of 1 mA at temperatures as indicated. The magnetic field and electrical currents were applied along the $\hat{c}$- and $\hat{a}$-axis of the sample, respectively. The samples remain superconducting above 30 T at $T \leq 2.3$ K. (**c**) Capacitive torque measurements on sample 2, after subtraction of normal state background measured at 83 K. Black arrows indicate the direction in which the field is swept. **Inset**: Magnified view at $\mu_0 H > 27$ T to highlight the persistence of the hysteresis between the up- and down-sweep at $T \leq 2.3$ K, consistent with the observation in (a, b).

To further investigate the persistence of superconductivity at low temperature, we expanded the experimental parameters of temperature, magnetic field, and electrical current to the range that was previously unexplored. Measurements were performed on three underdoped YBCO_{6+x} samples with $p = 0.108$, 0.116, and 0.132, the doping range that has been previously reported to have the lowest $\mu_0 H_{\mathrm{c2}}$ [102]. Figure 6.2 shows the low-field magnetisation of the three samples, which shows sharp transitions in temperature and a high sample homogeneity.

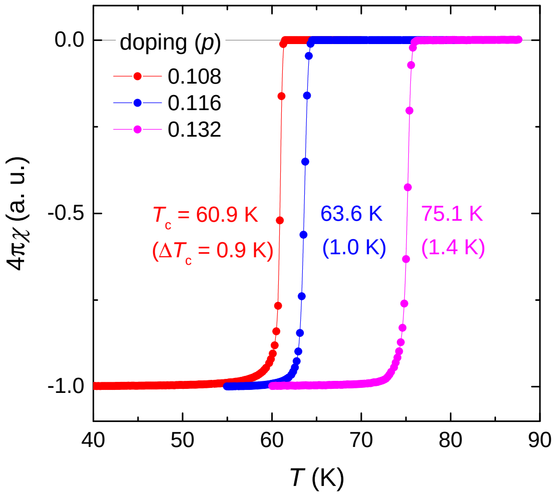

Figure 6.2: **Superconducting transitions characterised by low-field magnetic susceptibility.** Magnetisations were measured by a superconducting quantum inference device at $\mu_0 H = 0.2$ mT. T_{c} is defined by the midpoint of the transition (i.e. $4\pi\chi = -0.5$) and transition width (ΔT_{c}) is defined by the difference in temperatures corresponding to 10% and 90% of total magnetisation (i.e. $4\pi\chi = -0.1$ and -0.9).

Figure 6.3 shows the resistivity as a function of magnetic field measured at fixed temperatures and applied currents on underdoped YBCO_{6+x} samples. At 10 K, the onset of finite resistivity is independent of the applied current for all samples, as expected for an ohmic conductor. However, upon decreasing temperature, $\mu_0 H_{\mathrm{r}}$ becomes increasingly dependent on applied current, which shows a dramatic increase from ≈ 33 T to ≈ 42 T by reducing the applied current from 5 mA to 10 μA at 0.44 K, as shown in Figure 6.3(b). At 40 mK, all samples remain superconducting at the highest magnetic field of 45 T when a current < 10 μA is applied, corresponding to a current density ≈ 0.10 mA$\cdot$cm^{-2}, three orders of magnitude lower than that used in previous pulsed field measurements. The possibility of the current dependence of $\mu_0 H_{\mathrm{r}}$ caused by Ohmic heating is excluded down to 0.44 K, since the cooling power ≈ 100 μW of a He-3 refrigerator is much larger than the dissipation power of ≈ 25 μW using a current of 5 mA, considering the contact resistance ≈ 1 Ω in our samples. The substantially lower cooling power of a dilution refrigerator, on the order of $1 - 10$ μW at 40 mK, requires an applied current below 1 mA to be used.

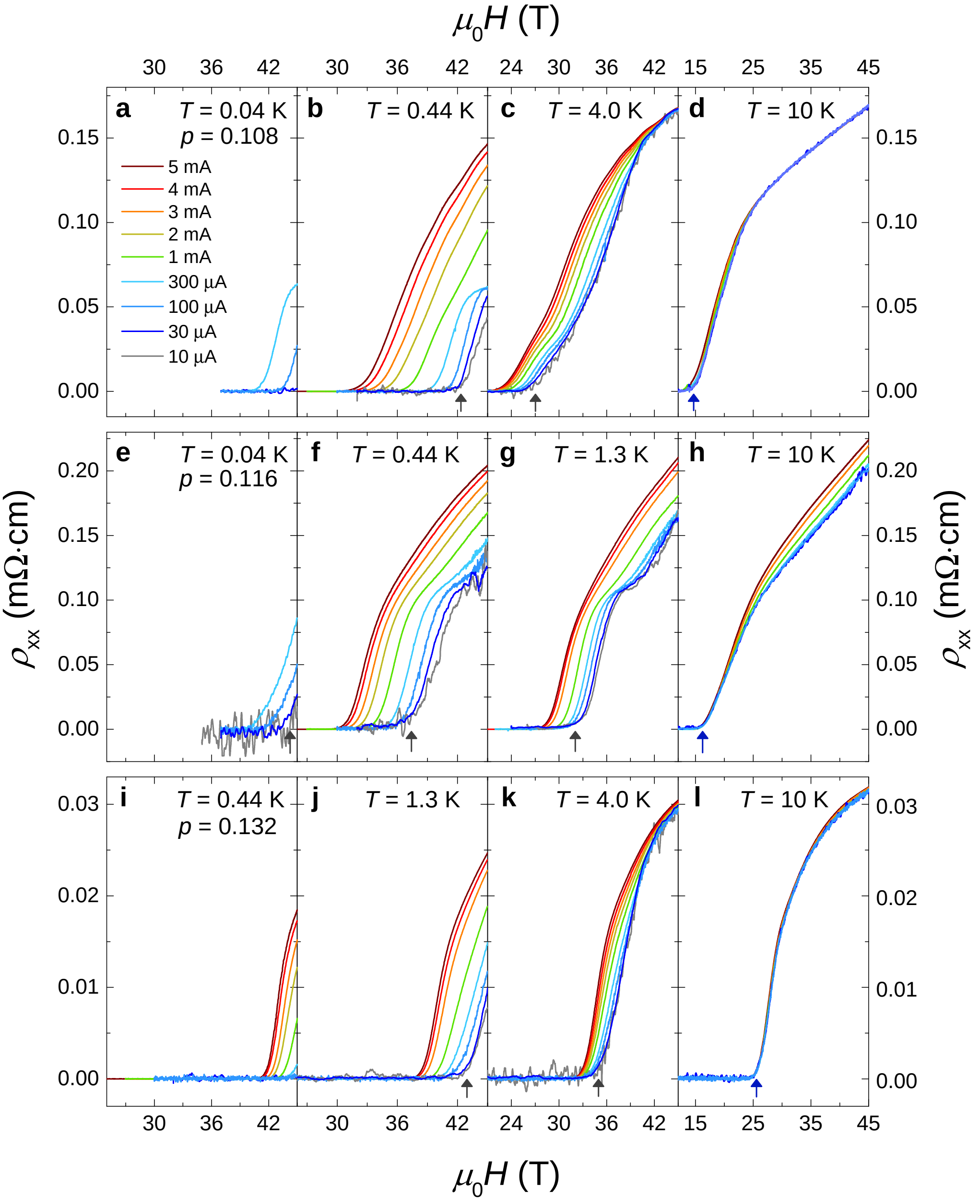

Figure 6.3: **In-plane resistivity of underdoped YBCO$_{6+x}$ as a function of magnetic field, temperature, and applied electrical currents.** Measurements were performed on samples with doping levels p of (**a-d**) 0.108, (**e-g**) 0.116, and (**h-k**) 0.132 using electrical currents as indicated. Arrows indicate the onset magnetic field of finite resistivity at the low current density limit, $\mu_0 H_\mathrm{r}(j \to 0)$. Temperature readings recorded by the thermometer are used, which accurately reflect the sample temperature down to 0.44 K. At 40 mK, significant self-heating occurs through ohmic dissipation when $I > 300\ \mu$A is used hence are not shown. The gaps between the traces measured at different applied currents become widened with decreasing temperature. Here an applied current $I = 1$ mA corresponds to a current density $j \approx 5$ A·cm^{-2}.

The extracted dependence of $\mu_0 H_\mathrm{r}$ on the applied current is shown in Figure 6.4. A steeper increase in $\mu_0 H_\mathrm{r}$ with decreasing temperature is seen with a lower measurement current. The irreversibility field ($\mu_0 H_\mathrm{irr}$) corresponding to the closure of the hysteresis loop in magnetic torque is shown for $p = 0.108$, which tracks closely to $\mu_0 H_\mathrm{r}$ at the lowest applied current, suggesting its correspondence to $\mu_0 H_\mathrm{r}(j \to 0)$.

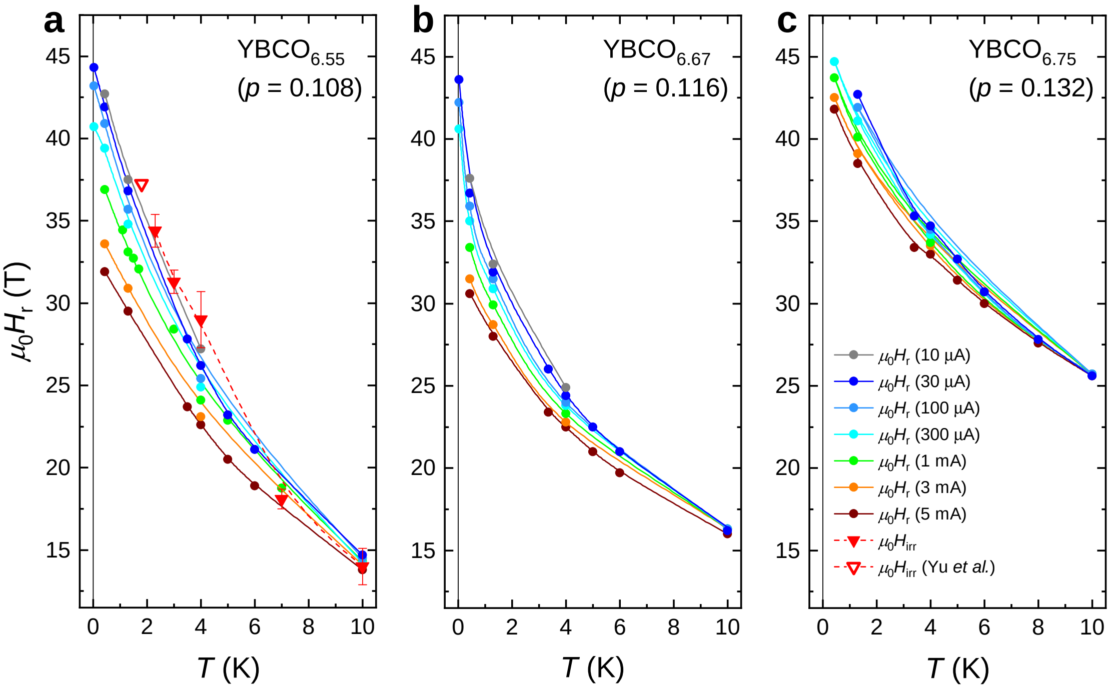

Figure 6.4: **Dependence of onset magnetic field of finite resistivity ($\mu_0 H_\mathrm{r}$) on applied current density in underdoped YBCO$_{6+x}$.** $\mu_0 H_\mathrm{r}$ as a function of temperature measured at applied current as indicated, on samples with p of (**a**) 0.108 (**b**) 0.116 and (**c**) 0.132. A steeper increase in $\mu_0 H_\mathrm{r}$ with decreasing temperature is seen when a lower measurement current is used. Downward triangles show the irreversibility field measured from hysteretic magnetic torque from Figure 6.1 and [103], reflecting the persistence of bulk pinned vortices up to $\mu_0 H_\mathrm{irr}$. Good agreement between $\mu_0 H_\mathrm{irr}$ and $\mu_0 H_\mathrm{r}$ is seen at the lowest applied current density, indicating the presence of bulk superconductivity below $\mu_0 H_\mathrm{r}(j \to 0)$.

6.1.2 Evidence of bulk superconductivity

We examined the possibility of surface-induced superconductivity in our measurements and found evidence supporting the bulk nature of the observed superconductivity rather than a surface effect. Firstly, the homogeneity of the measured samples is evidenced by the narrow transition width of ≈ 1 K in magnetisation measured at 0.2 mT, as shown in Figure 6.2, and prominent quantum oscillations (see next section), arguing against the sensitivity of $\mu_0 H_\mathrm{r}$ due to sample inhomogeneity.

Secondly, the bulk nature of the observed superconductivity is evidenced by the sharp transition from a resistive to zero-resistivity state in a magnetic field, as shown in Figure 6.5. A sharp transition is observed when a low measurement current is used, with a transition width comparable to that observed from the low-field magnetisation. The superconducting state exhibits a zero resistivity, rather than a reduced but finite resistivity, arguing against a filamentary superconductivity with a small volume contribution.

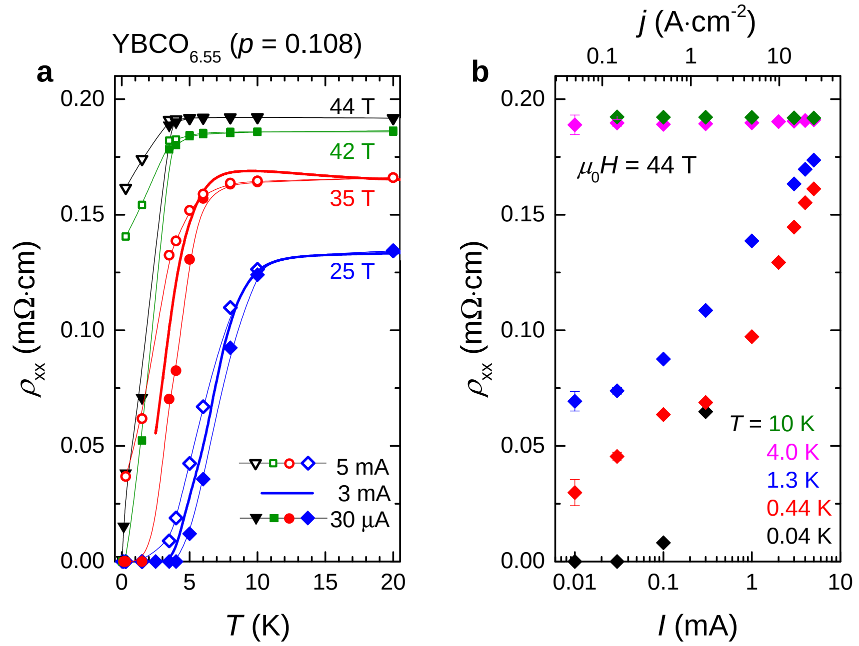

Figure 6.5: **Electrical resistivity of $\mathbf{YBCO_{6.55}}$ as a function of temperature and electrical current at fixed magnetic field**. (**a**) In-plane resistivity ρ_{xx} transition into the zero resistivity superconducting state for $p = 0.108$ at magnetic fields and currents as indicated. The corresponding current densities are ≈ 25, 15 and 0.15 A·cm^{-2}, respectively. The width of the transition is similarly narrow to that observed at zero magnetic fields. (**b**) In-plane resistivity ρ_{xx} as a function of applied current at fixed magnetic field of 44 T, measured at temperatures as indicated. The measured resistivity is strongly dependent on the applied current, indicating a vortex liquid state with non-ohmic behaviour.

Furthermore, if the observed high $\mu_0 H_\mathrm{r}$ at low temperature originates from a filamentary inclusion of superconducting volume with near-optimal doping, a high T_c and j_c are expected. Instead, we observed a very low T_c and j_c accompanied by a high $\mu_0 H_\mathrm{r}$. The observation that $\mu_0 H_\mathrm{r}$ and T_c evolve with doping, as shown in Figures 6.4 and 6.7, further argues against the observation due to filamentary superconductivity.

Lastly, we calculated the critical density, j_c, from the hysteresis loop and found a good agreement with that inferred from resistivity measurement, as shown in Figure 6.6. j_c is calculated using the Bean model, which assumes a bulk contribution of vortex pinning in a type-II superconductor [104]. For strong pinning of individual vortices, assuming a slab geometry with magnetic field perpendicular to the dominant surface, j_c is given by

$$j_\mathrm{c} = 3\frac{\Delta M}{\pi D}, \tag{6.1}$$

where ΔM is the size of the hysteresis loop and D is the sample thickness [104]. For weak pinning of collective vortices, j_c is given by

$$j_\mathrm{c} = 20\frac{\Delta M}{r}, \tag{6.2}$$

where $r = a/(1 - a/3b)$ and a, b are the long and short sample dimensions perpendicular to the magnetic field, respectively [105]. j_c inferred from the two measurements agree within one order of magnitude, indicating the bulk nature of the observed superconductivity.

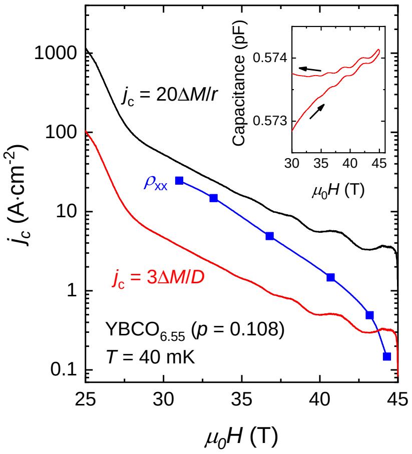

Figure 6.6: **Comparison of the critical current density inferred from resistivity and magnetic hysteresis.** In-plane resistivity and magnetic torque measurements were performed on the same YBCO$_{6.55}$ sample at 40 mK. j_c inferred from magnetic hysteresis, assuming individual and collective pinning of vortices are shown in red and black, respectively. **Inset**: Raw capacitive torque data with arrows indicating the direction at which the magnetic field is swept.

6.1.3 Phase boundary of vortex solid

Our finding of the resistivity onset dependent on applied current indicates the vortex solid regime at low temperatures can only be accessed using a vanishingly small electrical current density. Figure 6.7 shows the temperature dependence of $\mu_0 H_\mathrm{r}$ at the low current density limit, reflecting the true boundary of the vortex solid state. $\mu_0 H_\mathrm{r}$ above 10 K were measured using $I = 10$ mA in pulsed field, when $\mu_0 H_\mathrm{r}$ is independent of applied current density. Below 10 K, $\mu_0 H_\mathrm{r}(j \to 0)$ is seen to deviate strongly from the extrapolation made from high temperatures and show no sign of saturation up to the highest accessible field of 45 T. This previously hidden vortex solid state indicates the superconductivity in underdoped YBCO$_{6+x}$ is surprisingly resilient against magnetic field, while fragile against elevated temperature and electrical current. We note that the step-like feature in thermal conductivity [102], previously attributed to $\mu_0 H_{\mathrm{c}2}$, is found to be well below the $\mu_0 H_\mathrm{r}(j, T \to 0)$ and likely to be associated with density-wave order [103]. Previous studies performed in magnetic fields, including Hall resistivity [106], heat capacity [107], and quantum oscillations [41], and others, should thus be interpreted as a property of a vortex liquid state, rather than a conventional metallic state.

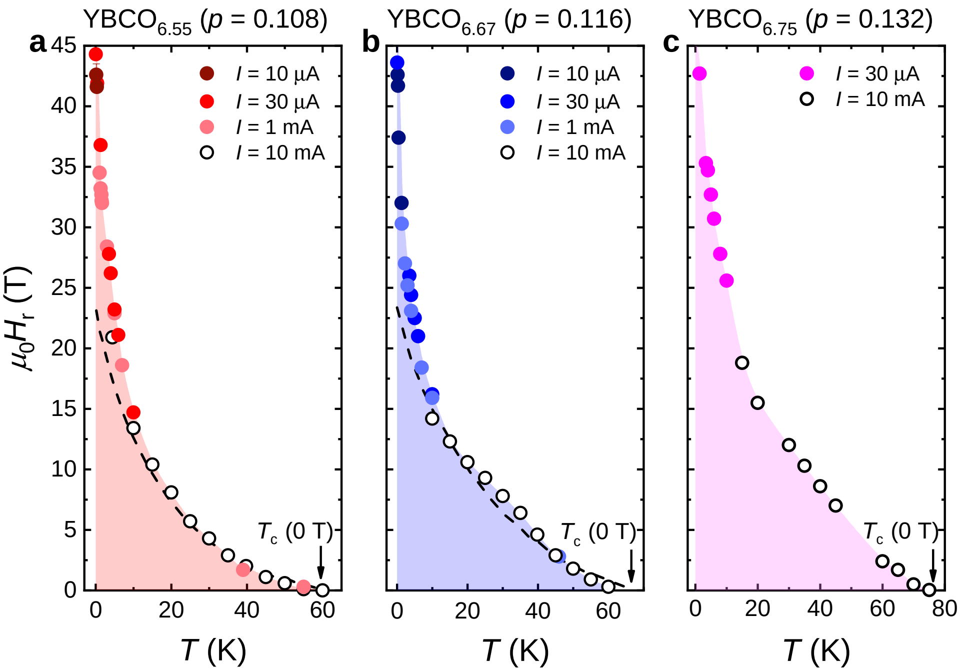

Figure 6.7: **Phase diagrams of the hidden vortex solid state in underdoped YBCO$_{6+x}$.** $\mu_0 H_\mathrm{r}$ measured at fixed temperatures and currents as indicated on samples with p of (**a**) 0.108 (**b**) 0.116 and (**c**) 0.132. A narrow steep region of magnetic field-resilient superconductivity is revealed at low temperature when a low current is used, which persists above the highest available magnetic field of 45 T. The dashed lines indicate $\mu_0 H_\mathrm{r}$ reported in [102].

6.2 Quantum oscillations in the pseudogap regime

While the Fermi surface in the underdoped cuprates has been studied in remarkable detail using quantum oscillations, the origin of the observed oscillations is still a subject of active debate. A key outstanding question is whether quantum oscillations originate from a conventional metallic state or a vortex state, and the number of sections present in the Fermi surface. Here, by performing quantum oscillation measurements with improved sample quality and measurement sensitivity, we find the high-field pseudogap ground state is characterised by the surprising coexistence of superconductivity and quantum oscillations, with signatures of an isolated nodal Fermi pocket. This observation suggests that the antinodal electronic density of states in the pseudogapped cuprates is completely gapped out at $T_\mathrm{c} < T < T^*$, rather than rendered incoherent due to scattering or thermal fluctuations, possibly due to an additional order parameter.

6.2.1 Coexistence of quantum oscillations and superconductivity

Previously, quantum oscillations in underdoped YBCO_{6+x} were predominantly thought to reflect the underlying Fermi surface of the normal metallic ground state when superconductivity is fully suppressed [41, 108]. However, considering the newly revealed vortex solid state with $\mu_0 H_\mathrm{r} > 45$ T at millikelvin temperature, the quantum oscillations that onsets at ≈ 20 T are seen to occur deeply within the superconducting state. Figure 6.8 shows the de Haas-van Alphen oscillations in magnetic torque measured in two $\mathrm{YBCO}_{6.55}$ sample at $T = 0.04$ K and 1.0 K. Prominent quantum oscillations can be seen on top of a hysteresis loop, consistent with the previous reports but with a much increased amplitude [109]. Interestingly, although the size of the hysteresis loop depends strongly on temperature, the amplitude of the oscillations is the same at 0.04 K and 1 K, indicating that quantum oscillations are relatively insensitive to the presence of a vortex solid or vortex liquid state. Quantum oscillations are also observed in in-plane resistivity as shown in Figure 6.9. Shubnikov-de Haas oscillations in ρ_xx are seen immediately after the resistivity onset at 32 T using $I = 5$ mA at $T = 0.44$ K. Meanwhile, the zero-resistivity superconducting state persists to 42 T at the same temperature using $I < 30$ μA. This observation demonstrates the surprising coexistence of quantum oscillations with zero-resistivity superconductivity, and the quantum oscillations, although exhibiting seemingly Fermi-liquid behaviour [110], occur within a vortex solid or liquid regime.

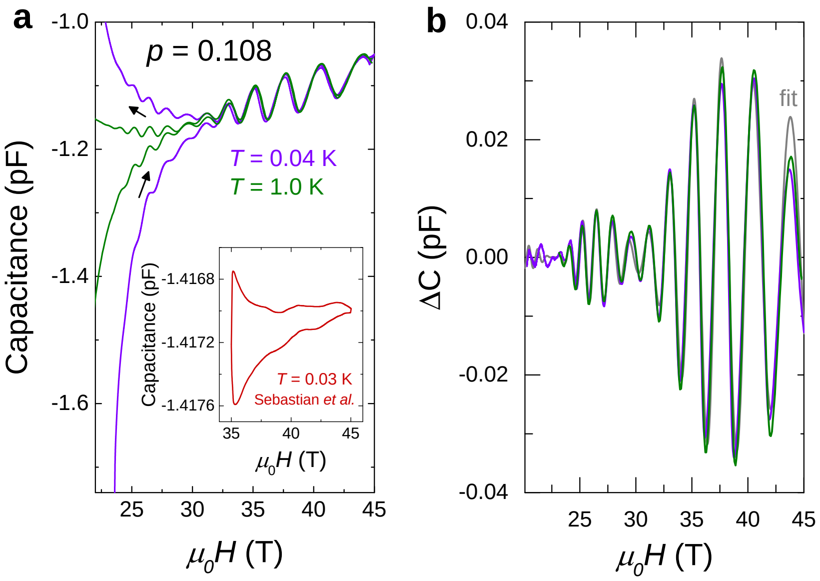

Figure 6.8: **De Haas-van Alphen oscillations in the vortex state of YBCO$_{6.55}$.** (**a**) Raw capacitive torque data measured at temperatures with considerably different $\mu_0 H_\mathrm{r}$ and $\mu_0 H_\mathrm{irr}$, as reflected by the sizes of hysteresis loops. Arrows indicated the field-sweeping direction. **Inset**: Comparison with previous results in [109]. A much increased oscillation amplitude is seen in our data. (**b**) Quantum oscillations after background subtraction. Grey line shows the Lifshitz-Kosevich fit with a single damping term. Very similar oscillation amplitudes are observed at 0.04 K and 1.0 K.

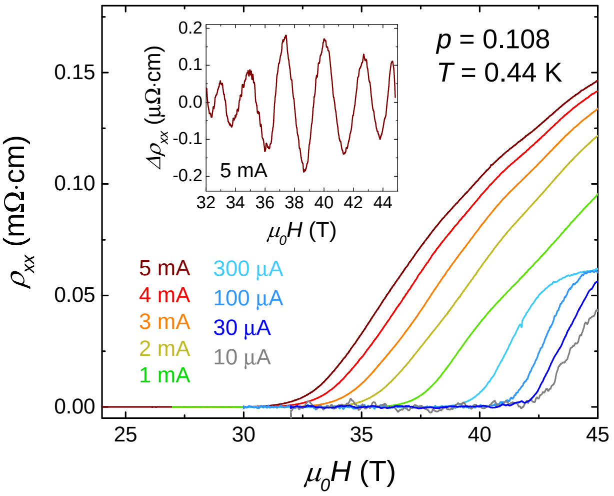

Figure 6.9: **Coexistence of Shubnikov-de Haas oscillations and superconductivity in YBCO$_{6.55}$.** In-plane resistivity as a function of magnetic field measured at 0.44 K using different applied currents as indicated. **Inset**: quantum oscillations after background subtraction. Oscillations are seen immediately after $\mu_0 H_\mathrm{r} \approx 32$ T using $I = 5$ mA, while superconductivity persists to over 42 T upon using $I < 30$ μA.

Although quantum oscillations in the vortex solid state have been observed in other type-II superconductors [111, 112], a dramatic increase in amplitude is seen when the vortex solid state is destroyed by magnetic field, unlike the observation in YBCO_{6+x}. This difference is likely to originate from the substantial vortex liquid regime that persists in cuprate superconductors, unlike other type-II superconductors. Additionally, the typical condition for quantum oscillations in a type-II superconductor requires $\hbar\omega_\mathrm{c}/\Delta \gtrsim 1$, where ω_c the cyclotron frequency and Δ is the maximum of the superconducting gap [113]. For $\mathrm{YBCO}_{6.55}$, using the onset magnetic field of the quantum oscillations of 20 T, effective mass m^* of $1.6m_\mathrm{e}$ [80], and Δ estimated by $5k_\mathrm{B}T_\mathrm{c}$ [35], we find $\hbar\omega_\mathrm{c}/\Delta = 0.06$, making the oscillations originating from the strongly gapped antinodal region very unlikely. An unusual scenario where the carriers in one CuO_2 plane in the unit cell of YBCO_{6+x} form the superconducting condensate, while carriers in the other CuO_2 plane remain uncondensed and give rise to quantum oscillations onset at fields much lower than $\mu_0 H_\mathrm{irr}$, appears to be challenging to reconcile with our observations. Firstly, the oscillation amplitude does not change dramatically when crossing the vortex solid boundary $\approx$ 38 T at 1 K (see Figure 6.8), in contrast to the expectation that the oscillation amplitude would increase abruptly when the superconducting condensate is destroyed. Furthermore, the beat pattern due to the bilayer magnetic breakdown [62] is seen to occur throughout the entire field range, which cannot occur unless both CuO_2 planes contribute to the quantum oscillations. This scenario may be further explored by measuring the superfluid density at high magnetic fields, a technically challenging experiment.

Alternatively, we consider the possibility of observing quantum oscillations that originate from the ungapped nodal region in the momentum space while the antinodal region remains strongly gapped. A Fermi surface reconstructed by the charge order wavevectors that yields an isolated nodal pocket appears to be consistent with our observations [108]. Further supporting evidence for such a Fermi surface model is presented in the following section.

6.2.2 Evidence of an isolated nodal Fermi pocket

Measurements and simulations shown in this section were performed in collaboration with Dr R. McDonald and Dr N.Harrison at NHMFL.

The small Fermi pocket observed in the underdoped cuprates [38], in sharp contrast to the large Fermi pocket observed in the overdoped regime [39, 40], indicates that the Fermi surface undergoes a reconstruction by a symmetry-breaking order parameter. The recently discovered charge density wave order in the underdoped cuprates is believed to be responsible for the Fermi surface reconstruction [29, 30], yielding a small nodal electron pocket per CuO_2 plane per unit cell, while the details of the reconstruction are still under debate [101, 108]. It is further unclear whether the antinodal electronic states in the pseudogap regime are suppressed by a complete gapping or a loss of quasiparticle coherence [22, 1]. By measuring quantum oscillations with an improved sample quality and sensitivity, we found evidence that suggests the nodal Fermi pocket is isolated in the Brillouin zone, with the antinodal states being completely gapped, in the pseudogap ground state at high magnetic field.

Figure 6.10 shows contactless resistivity measurements on a $YBCO_{6.55}$ sample at 1.5 K using the proximity detector oscillator technique. Compared to the previous report [108], we found an improved data quality in our measurements indicated by (i) an earlier onset of the prominent quantum oscillations at ≈ 22 T, (ii) a lower Dingle temperature and higher oscillation amplitude when normalised at the infinite field limit, and (iii) a richer harmonic content revealed by the Fourier transform, with the fifth harmonics also being visible. An asymmetric oscillation waveform deviating from a sinusoidal waveform, with a rounder top and sharper bottom, can be observed, as a result of the rich harmonic content present in our data.

The quantum oscillation waveform is a sensitive probe of whether the associated Fermi pocket is accompanied by additional electronic density of states at the Fermi energy [114, 115, 116], which can be only be used when the sample has an exceptional high quality with minimal scattering and minimal contribution to the density of states from the impurities. As illustrated in Chapter 2, the hallmarks of a clean two-dimensional metal with an isolated Fermi pocket unaccompanied by a background density of states include (i) a forward 'sawtooth' waveform in the oscillatory magnetisation, (ii) a subsequent inverted 'U'-shape waveform in the magnetic susceptibility and resistivity, and (iii) harmonics whose amplitudes lie on an exponential curve. Quantum oscillations in magnetic susceptibility and resistivity measured on $YBCO_{6.55}$ at field angle $\theta \approx 36°$, defined as the angle between the magnetic field and crystalline $\hat{c}$-axis, are shown in Figure 6.11, compared with that measured in a GaAs heterostructure, a known two-dimensional system with a single component of Fermi surface [115]. The forward sawtooth waveform in magnetisation and inverted 'U'-shape waveform in susceptibility can be seen in both systems, showing good agreement with simulations assuming an absence of background density of states, pointing to an isolated Fermi pocket in $YBCO_{6.55}$.

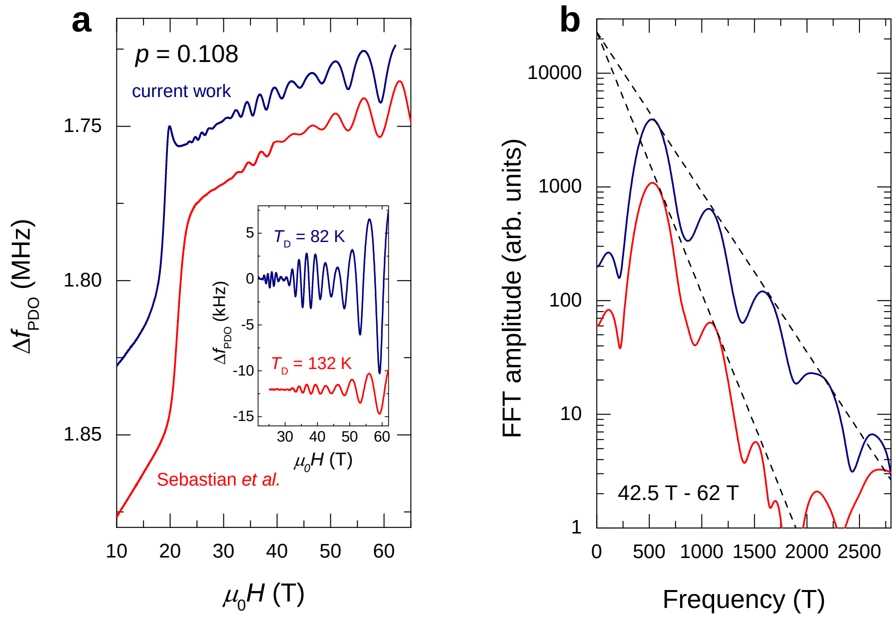

Figure 6.10: **Quantum oscillations in contactless electrical resistivity in YBCO$_{6.55}$.** (**a**) Resistivity measured by the shift in the resonant frequency of a proximity detector oscillator circuit (Δf_{PDO}) as a function of magnetic field with comparison to a previous report [108]. The beating pattern arises from the bilayer splitting of the nodal pocket due to the presence of two CuO$_2$ planes in the unit cell [62], which can be eliminated by rotated the field angle to ≈ 36° with respect to the $\hat{c}$-axis. **Inset**: Quantum oscillations after background subtraction. The extracted Dingle temperatures T_{D} are found to be significantly lower in our data. (**b**) Fourier transform of the quantum oscillations within the field range of 42.5 T to 65 T. The two datasets are scaled to have equal amplitude at the infinite field limit (dashed line).

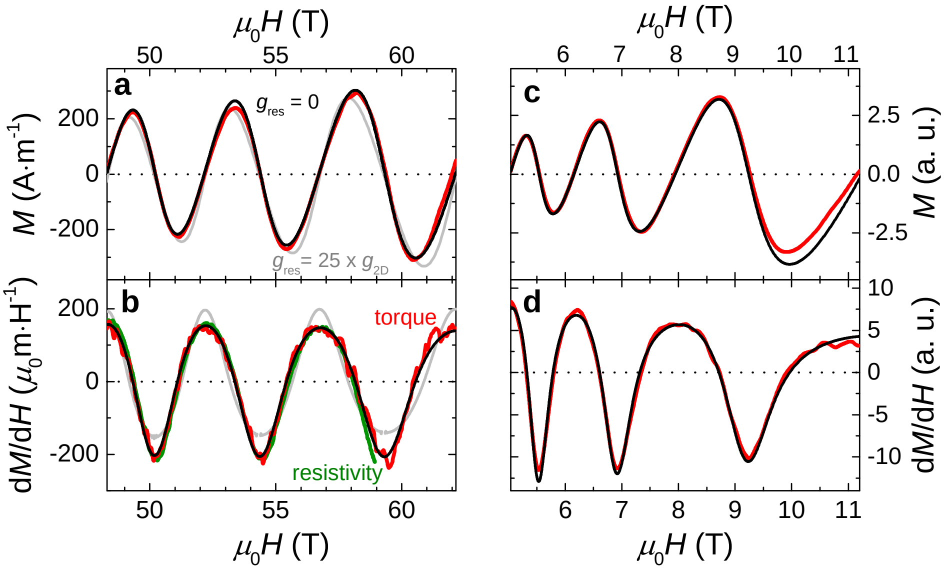

Figure 6.11: **Quantum oscillation signatures of a two-dimensional Fermi surface with negligible background density of states.** (**a, b**) de Haas-van Alphen oscillations in (**a**) magnetisation and (**b**) susceptibility of $YBCO_{6.55}$ (red curve) with the magnetic field inclined at an angle of 36° from the crystalline $\hat{c}$-axis. Contactless resistivity measured at a similar angle (green curve) is scaled to the torque data. Simulations assuming a zero background density of state ($g_{\mathrm{res}} = 0$, black curve) are found to agree well with the experimental data, while the simulations assuming a large background density of state ($g_{\mathrm{res}} = 25 \times g_{2\mathrm{D}}$, grey curve) showed a marked deviation. (**c, d**) de Haas-van Alphen oscillations in (**c**) magnetisation and (**d**) susceptibility of a GaAs heterostructure, a known two-dimensional system with an isolated Fermi pocket, from [115]. Similar features in the oscillation waveforms are found between $YBCO_{6.55}$ and GaAs heterostructure.

The observation of quantum oscillation signatures of an isolated Fermi pocket in the underdoped YBCO$_{6.55}$ is surprising. Given the starting paramagnetic band structure, the reconstructed Fermi surface is expected to consist of multiple fragmented sections spanning both nodal and antinodal regions as illustrated in Figure 6.12(a). The isolation of the observed Fermi pocket in momentum space indicates that the Fermi arcs are sharply truncated at their edges in momentum space with the antinodal density of states completely gapped, rather than rendered incoherent due to thermal or classical fluctuations. The Fermi arcs are connected by the biaxial CDW vectors in the presence of a magnetic field into an isolated electron pocket in the nodal region, as illustrated in Figure 6.12(b).

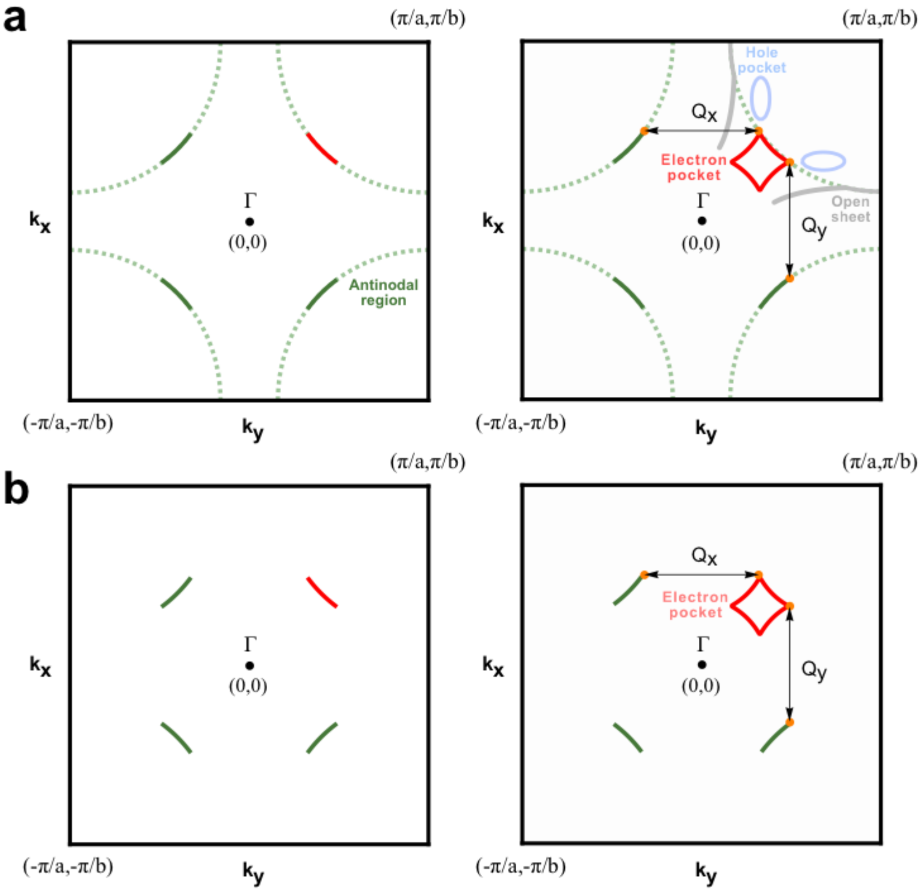

Figure 6.12: **Proposed pictures of Fermi surface in the pseudogap state of underdoped YBCO$_{6+x}$.** (**a**) In the first picture, the Fermi arcs are part of a large cylindrical Fermi surface with the antinodal density of states suppressed by thermal or classical fluctuations. In an applied magnetic field, the Fermi surface is translated by the biaxial CDW vectors, $\mathrm{Q_x}$ and $\mathrm{Q_y}$, and reconstruct into a nodal electron pocket, two antinodal hole pockets, and one-dimensional open sheets. (**b**) In the second picture, the Fermi arcs are isolated in the Brillouin zone with sharply truncated edges, with the antinodal density of states completely gapped. In an applied magnetic field, the Fermi arcs are connected by the same CDW vectors into a single nodal electron pocket.

Previously, the origin of the suppression of the antinodal density of states in the pseudogap regime at elevated temperatures was unclear [21]. The observation of the identifying signatures in quantum oscillation waveform indicates the small Fermi pocket in YBCO$_{6.55}$ is isolated in the Brillouin zone unaccompanied by other Fermi pockets or open sheets. The antinodal density of states at the Fermi energy in underdoped YBCO$_{6+x}$ is therefore shown to be completely gapped, given that complementary measurements have placed the small Fermi pocket in the nodal region of the Brillouin zone [80, 108]. An additional order parameter associated with the pseudogap is suggested to eliminate the antinodal density of states, which is likely a consequence of proximity to the antiferromagnetic Mott insulator.

6.3 Evidence of pairing correlations at high temperature

The field-resilient superconductivity in the underdoped YBCO$_{6+x}$ suggests a large energy scale for electron pairing, while its fragility against temperature and electrical current at low temperature suggests a frustrated pairing coherence. A wide temperature regime where the electrons exhibit pairing correlations without the phase coherence for long-range superconductivity is indicated. Here, by measuring in-plane resistivity over a broad range of doping, temperature, and magnetic field, we identified a characteristic temperature T_o, suggestive of the pairing correlations above $T_\mathrm{c}(0\ \mathrm{T})$ and a pairing energy scale of $\approx$ 100 meV.

6.3.1 Onset temperature of pairing correlations

Figure 6.13 shows the in-plane resistivity normalised at 170 K as a function of temperature in YBCO$_{6+x}$, measured using $I = 3$ mA in fixed magnetic fields applied perpendicular to the CuO$_2$ plane. Three regimes in the resistivity as a function of temperature can be identified. At high temperature, ρ_xx exhibits T-linear behaviour which can be fitted using $\rho_\mathrm{lin} = \rho_0 + aT$. At intermediate temperature, ρ_xx shows a downward departure from ρ_lin below an onset temperature T_o, identified using the criterion of $\rho_\mathrm{xx}/\rho_\mathrm{lin} < 0.99$, as illustrated in Figure 6.14. The sharpness of the resistivity reduction makes the uncertainty associated with T_o due to the choice of criterion minimal. A similar but slightly higher onset temperature is found by taking the first derivative of $\rho_\mathrm{xx}(T)$ with respect to T, as shown in Figure 6.15 for three dopings at zero magnetic field. At finite fields, this method leads to a larger uncertainty in determining the onset temperature, as limited by the noise performance. As temperature further decreases, the regime of reduced resistivity gives way to a zero-resistivity regime below the superconducting temperature T_c. At zero magnetic field, ρ_xx in overdoped samples with $p > 0.19$ shows an extended regime of linearity before the superconducting transition occurs abruptly at $T_\mathrm{c}(0\ \mathrm{T})$, whereas the reduction in resistivity becomes more gradual as p decreases and onsets at temperatures increasingly higher than $T_\mathrm{c}(0\ \mathrm{T})$.

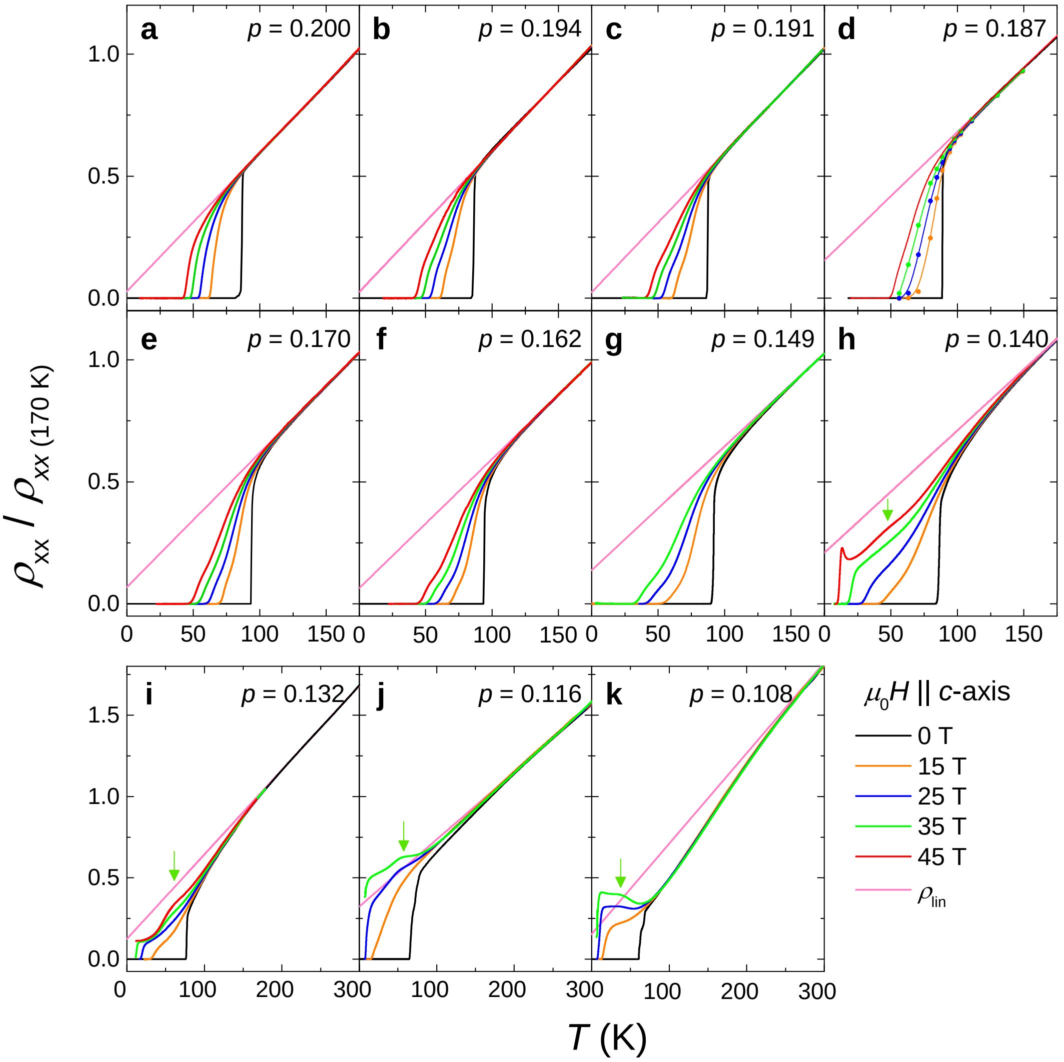

Figure 6.13: **In-plane resistivity normalised at 170 K as a function of temperature in YBCO$_{6+x}$. (a-k)** ρ_{xx} measured using $I = 3$ mA in fixed magnetic fields and hole dopings p as indicated. Pinks lines indicate the linear fits ($\rho_{\text{lin}} = \rho_0 + aT$) made to the high temperature regime where resistivity exhibits a T-linear dependence. Green arrows mark the broad maximum in ρ_{xx}, which we associated with the long range CDW order. The temperature below which the resistivity vanishes is defined as $T_{\text{c}}(\mu_0 H)$.

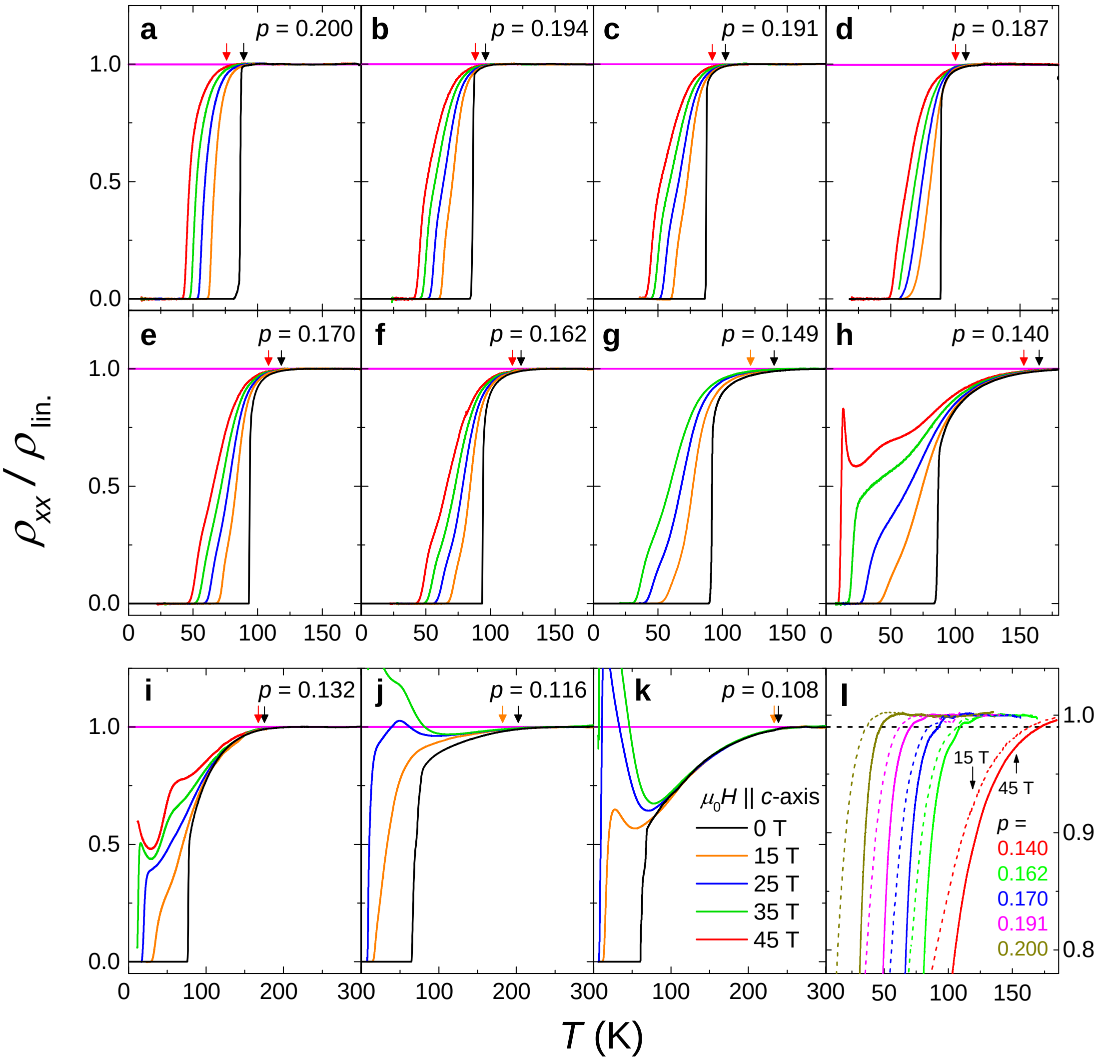

Figure 6.14: **Onset temperature T_o of reduced resistivity at fixed magnetic fields in YBCO$_{6+x}$.** (**a-k**) Deviation of resistivity from a T-linear behaviour revealed by plotting data shown in Figure 6.13 as ρ_{xx}/ρ_{lin}. Pink lines indicate the linear fits ρ_{lin}. Arrows indicate T_o at the magnetic fields of 45 T (red), 35 T (green), and 0 T (black). (**l**) The criterion used to extract T_o, defined as the temperature where $\rho_{xx}/\rho_{lin} < 0.99$. The uncertainty associated with T_o due to the choice of criterion is minimal owing to the sharpness of the resistivity reduction.

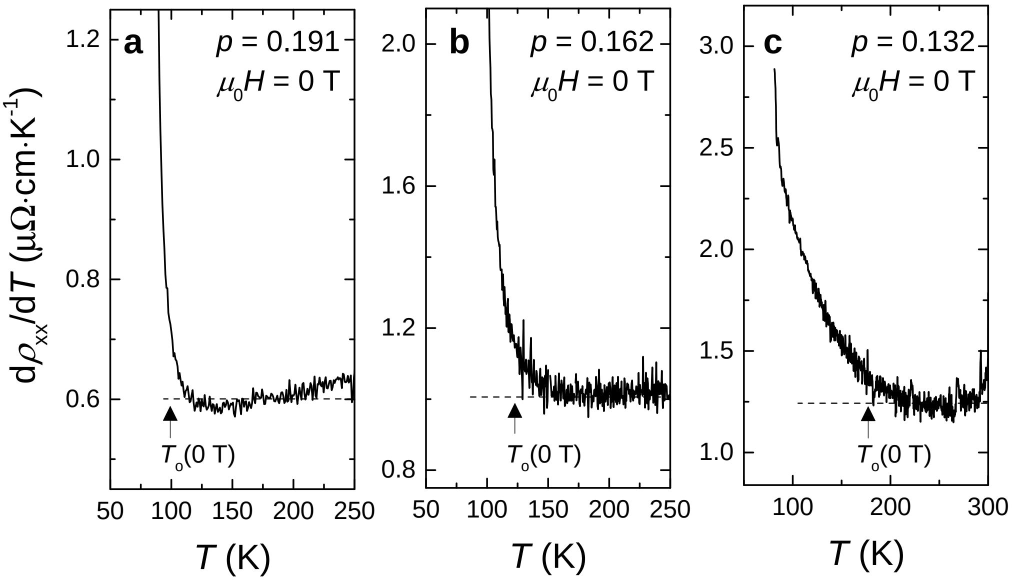

Figure 6.15: **Comparison of onset temperatures of deviation from T-linear resistivity obtained by different methods.** (**a-c**) $\mathrm{d}\rho_{\mathrm{xx}}/\mathrm{d}T$ for three hole dopings p as indicated at zero magnetic field. Horizontal dashed lines are guides to the eye for the regime of nearly-constant slope at high temperature. Arrows indicated the T_{o} extracted using the $\rho_{\mathrm{xx}}/\rho_{\mathrm{lin}} < 0.99$ criterion as illustrated in Figure 6.14.

An additional feature is present in the samples with $0.108 \leqslant p \leqslant 0.140$, where ρ_{xx} exhibits a broad peak at $T \approx 50$ K that becomes more pronounced with increasing magnetic field. We attributed this feature to the long-range CDW order observed in nuclear magnetic resonance measurements at similar temperature and doping range [117].

In the optimally and overdoped cuprates, the resistivity reduction occurring at T_{o} has been interpreted as superconducting fluctuations presiding the T_{c} [118, 119]. In the case of underdoped cuprates, the origin of the downward departure from the T-linear resistivity around the pseudogap temperature T^* has remained unclear. Here, we reviewed the experimental signatures of pairing correlations without phase coherence and found the intermediate temperature regime below T_{o} is consistent with such description. Within the conventional Ginzburg-Landau theories [120], the experimental signatures of superconducting fluctuations includes: (i) a downward departure in resistivity from the normal state behaviour at high temperature, (ii) a weakening of this suppression in electrical resistivity upon the application of a magnetic field, due to orbital pair-breaking effect such as vortex creation, and (iii) a marked anisotropy in the effect of applied magnetic fields, with a minimal effect when the magnetic field is applied parallel to the $\mathrm{CuO_2}$ plane, given the confinement of electronic orbital motions. Figure 6.16 shows the resistivity of four dopings with magnetic fields applied parallel to the $\mathrm{CuO_2}$ plane i.e. $\mathbf{H} \perp \hat{c}$-axis. Compared with the situation where $\mathbf{H} \parallel \hat{c}$-axis as shown in Figures 6.13 and 6.14, the increase in resistivity induced by magnetic field below $T_c(0\ \mathrm{T})$ is much suppressed in Figure 6.16. Taken together, our observations in high magnetic fields indicate the electron pairs evolve from a long-range superconducting state at low temperatures to local pairing correlations at intermediate temperature up to at least T_o.

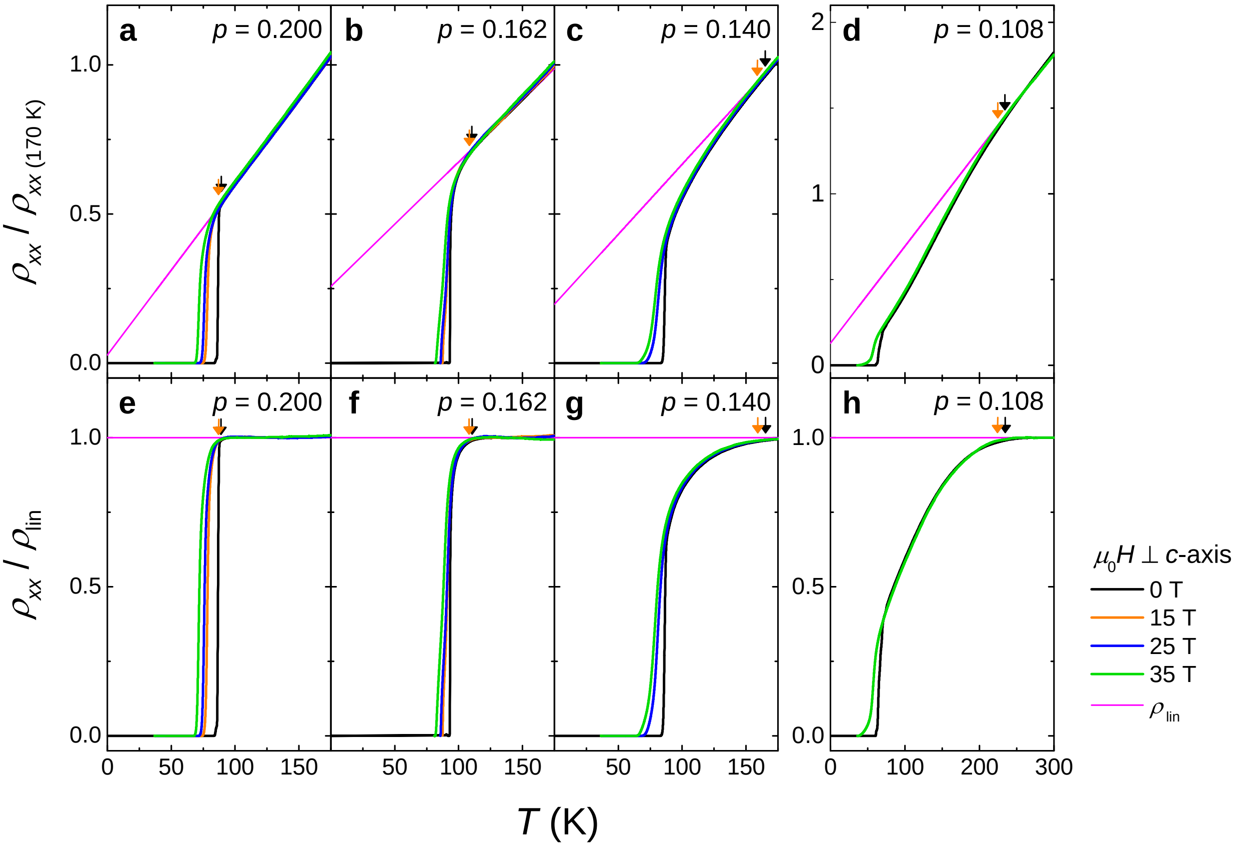

Figure 6.16: **In-plane resistivity as a function of temperature with magnetic field applied perpendicular to crystalline $\hat{c}$-axis in YBCO$_{6+x}$.** (**a-d**) Resistivity normalised at 170 K for different magnetic fields and multiple hole dopings p as indicated. Pink lines indicate the linear fits ($\rho_{\mathrm{lin}} = \rho_0 + aT$) made to the high-temperature regime. (**e-h**) Deviation of resistivity from the T-linear behaviour revealed by plotting data shown in (a-d) as $\rho_{\mathrm{xx}}/\rho_{\mathrm{lin}}$. Arrows indicate T_o at the magnetic fields of 35 T (orange) and 0 T (black) using the criterion of $\rho_{\mathrm{xx}}/\rho_{\mathrm{lin}} < 0.99$. The reduction of T_o with magnetic field is much suppressed compared the situation where $\mathbf{H} \parallel \hat{c}$-axis as shown in Figures 6.13 and 6.14.

A less sensitive measure of the local pairing correlations at intermediate temperature is the deviation of $\rho_{\mathrm{xx}}(\mu_0 H)$ from a H^2-dependence, expected for a conventional metallic state, at $T \gg T_{\mathrm{c}}(0\ \mathrm{T})$ [121]. Figure 6.17 shows the increase in ρ_{xx} due to magnetic field divided by the zero magnetic field value, $\Delta\rho/\rho_0$, as a function of $(\mu_0 H)^2$ in YBCO$_{6+x}$ at $p = 0.108$. Apparent deviation in $\Delta\rho/\rho_0$ from a H^2-dependence can be observed up to 120 K, while the deviation at $T > 130$ K is more subtle and persists to at least 180 K, the highest temperature measured, as shown in Figure 6.17(b). By analysing over the doping range $0.132 \leqslant p \leqslant 0.200$ as shown in Figure 6.18, we found the highest temperatures where a deviation from H^2-dependence is seen, T_{H}, to be similar to T_{o} (see Figure 6.23).

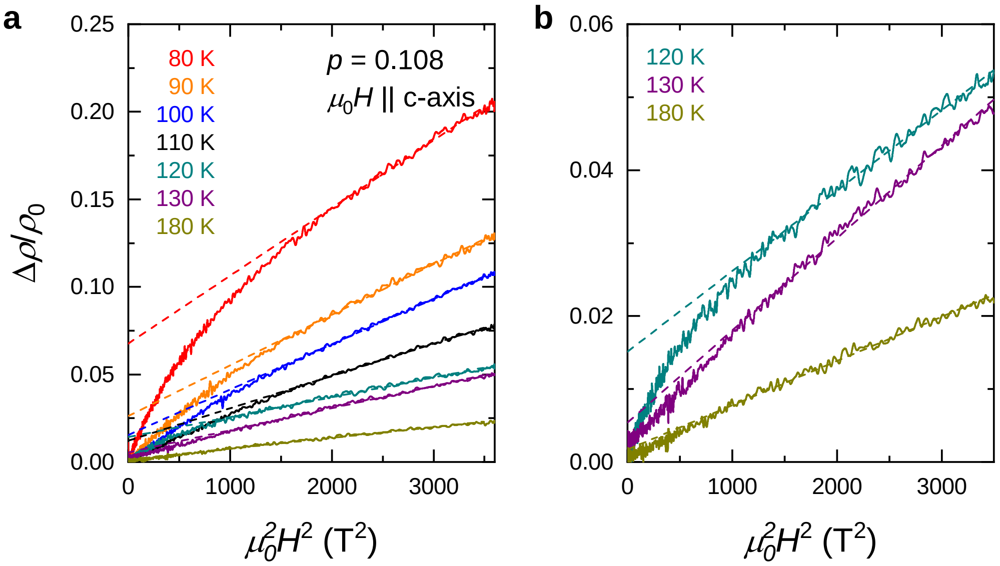

Figure 6.17: **Normalised increase in the in-plane resistivity due to magnetic field in YBCO$_{6.55}$.** (**a**) Field-induced resistivity divided by the zero field value, $(\Delta\rho = \rho(\mu_0 H) - \rho_0)/\rho_0$, as a function of the square of magnetic field at fixed temperatures as indicated. Dashed lines indicate linear fits to the high-field regime where $\Delta\rho$ exhibits a H^2-dependence. (**b**) An expanded view of the high temperature data reveals a subtle deviation from H^2-behaviour in $\Delta\rho/\rho_0$. A deviation from H^2-behaviour can be observed at 180 K, the highest temperature where the measurements were taken.

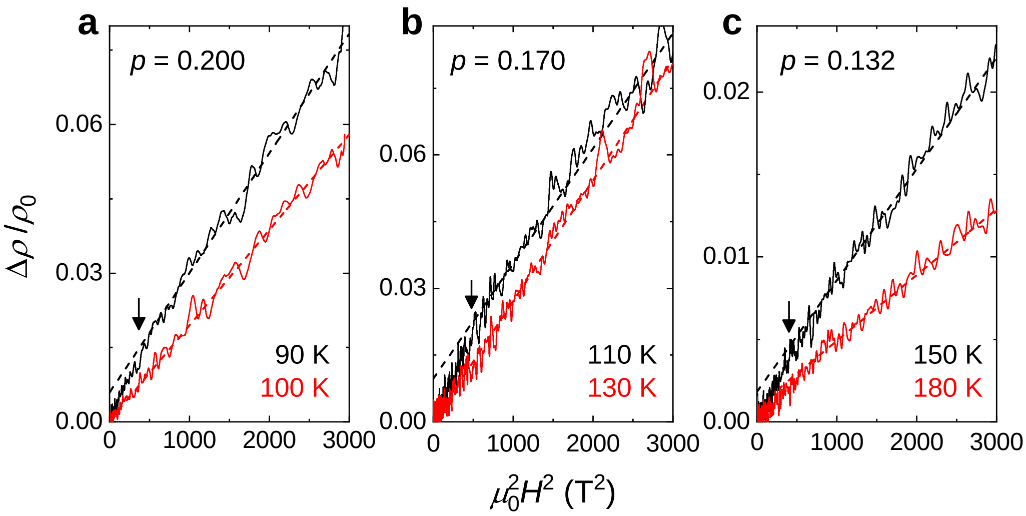

Figure 6.18: **Deviation of field-induced increase in in-plane resistivity from a H^2-dependence of in YBCO$_{6+x}$ over a broad doping range.** Normalised increase in the in-plane resistivity due to magnetic field observed in YBCO$_{6+x}$ with (**a**) $p = 0.20$, (**b**) 0.17, and (**c**) 0.132. Field sweeps taken at the highest temperatures where a deviation from a H^2-behaviour is seen (black) and the lowest temperatures where a H^2-behaviour is fully complied (red) are shown. Dashed lines are fits using $\Delta\rho/\rho_0 = aH^2$ down to the magnetic field where an apparent deviation from linearity is found, as marked by black arrows.

Recent study has reported an obedience of Kohler's rule in underdoped $HgBa_2CuO_{4+x}$ at $T \gg T_c$ in magnetic fields up to 30 T, suggesting a Fermi liquid-like magnetotransport behaviour in the pseudogap regime [122]. The Kohler's rule states the increase in isothermal resistivity due to applied magnetic field, $\Delta\rho$, can be described by a functional form

$$\Delta\rho/\rho_0 = F(\mu_0 H/\rho_0), \tag{6.3}$$

where ρ_0 is the zero-field resistivity that is proportional to the scattering rate $1/\tau$ [123]. For a Fermi liquid, $\Delta\rho \propto H^2$ and $\rho_0 \propto T^2$, hence the Kohler's rule is obeyed if a plot of $\Delta\rho/\rho_0$ versus $(\mu_0 H/\rho_0)^2$ collapse into a single, temperature-independent curve and the relation $\Delta\rho/\rho_0 \propto H^2T^{-4}$ holds. Figure 6.19 shows the Kohler plot for the same data shown in Figure 6.17. The curves measured at different temperatures do not collapse into a single curve and the transverse magnetoresistance coefficient $a_\perp \propto \Delta\rho/(\rho_0 H^2)$ exhibits a T^{-3}-dependence, rather than the T^4-dependence expected for a Fermi liquid. By extending the measurement field range to 60 T at $T \gg T_c$, we hereby find a violation of the Kohler's rule in $YBCO_{6.55}$.

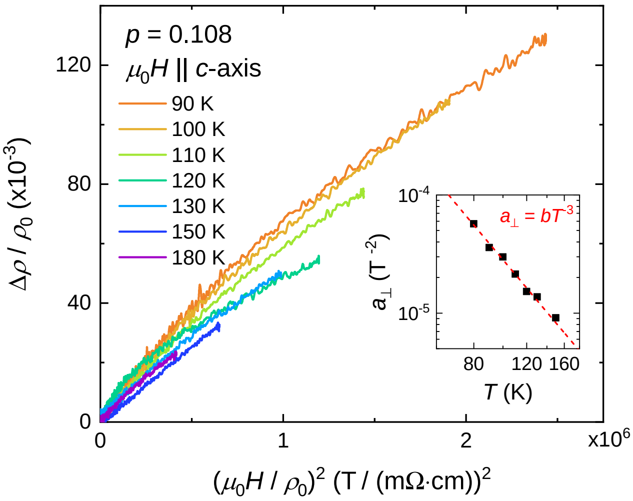

Figure 6.19: **Kohler plot of in-plane resistivity with out-of-plane magnetic field in $YBCO_{6.55}$.** Normalised increase in the in-plane resistivity versus $(\mu_0 H/\rho_0)^2$ using the same data shown in Figure 6.17. The curves measured at different temperature do not collapse into a single curve, which indicates a violation of the Kohler's rule. **Inset**: The magnetoresistance coefficient $a_\perp$, extracted by fitting the high-field regime where $\Delta\rho/\rho_0 = a_\perp(\mu_0 H)^2$, versus temperature in log-log scale. $a_\perp$ is found to follow a T^{-3}-dependence rather than T^{-4}-dependence expected for a Fermi liquid.

We examine the validity of a two-carrier model to account for the non-H^2 behaviour in $\Delta\rho$, which yields a T^2-behaviour in $\rho_{xx}(T)$ below 100 K in $YBa_2Cu_4O_8$, as suggested in [124]. A qualitative difference between the expectation from a two-carrier Fermi-liquid model and a superconducting fluctuation model is the curvature of $\rho_{\mathrm{xx}}(T)$: the former model would yield an upward curvature at high temperatures whereas the latter would yield a downward curvature [120]. Figure 6.20 shows ρ_{xx} as a function of magnetic field and temperature for a YBCO$_{6+x}$ crystal with $p = 0.140$, a doping level most similar to YBa$_2$Cu$_4$O$_8$. The zero-field resistivity below T_{c} is extracted by fitting the high-field regime of $\rho_{\mathrm{xx}}(\mu_0 H)$ using $\rho = \rho(H \to 0) + AH + BH^2$. At $T < T_{\mathrm{c}}$, the extracted $\rho(H \to 0)$ exhibits a seemingly T^2-behaviour that can be described by both the two-carrier Fermi-liquid and the superconducting fluctuation model; however, at $T > T_{\mathrm{c}}$, $\rho(H \to 0)$ diverges from the parabolic fit and exhibits a downward curvature at $T_{\mathrm{c}} < T < T_{\mathrm{o}} \approx 150$ K, which can only be reasonably fitted using a model of superconducting fluctuations [120]. The form of $\rho_{\mathrm{xx}}(T)$ with the signature downward curvature, observed in both zero and high magnetic fields (see Figure 6.13), points to a state of superconducting fluctuations as inferred from the T_{o} analysis. We thus conclude that the high-field transport behaviour in the underdoped YBCO$_{6+x}$ is most consistent with a state with broad regime of pairing correlations, rather than a conventional Fermi liquid-like metallic state.

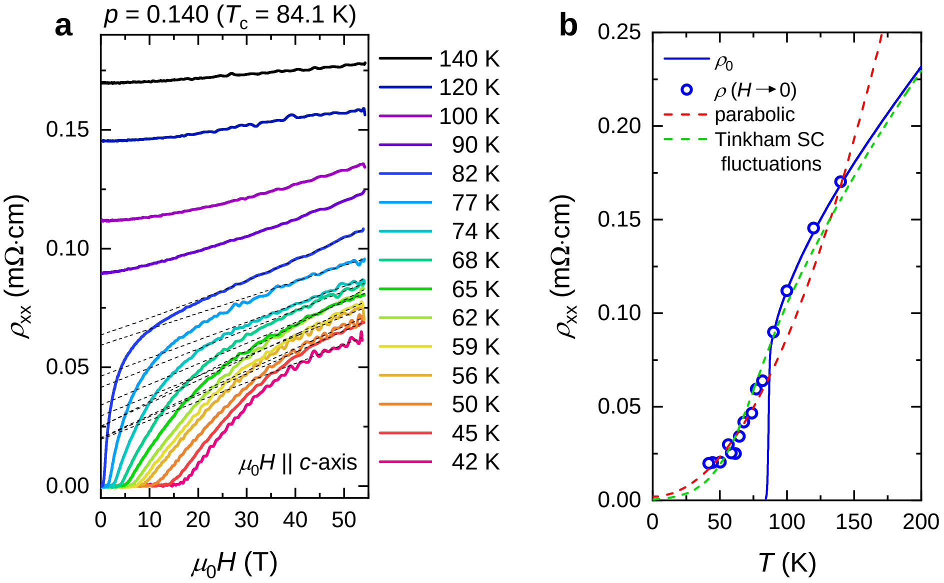

Figure 6.20: **Extraction of zero-field resistivity below T_{c}(0 T) in YBCO$_{6.84}$.** (**a**) ρ_{xx} as a function of magnetic field at temperatures as indicated. Dashed lines are fits to the high-field regime using $\rho = \rho(H \to 0) + AH + BH^2$. $T < 42$ K was not accessible for this sample due to a severe self-heating in pulsed fields. (**b**) Extracted $\rho(H \to 0)$ as a function of temperature. ρ_0 is measured at zero field. Red dashed curve is a parabolic fit made to the low-temperature data and green dashed curveis a fit using a model of superconducting fluctuations using a T-linear normal state resistivity [120]. $\rho(H \to 0)$ deviates from the parabolic fit above 80 K while its entire form can be described using the superconducting fluctuation model.

6.3.2 Estimation of pairing energy scale

The extent of local pairing correlations without phase coherence is illustrated by the colour plots of normalised resistivity $\rho_{\mathrm{xx}}/\rho_{\mathrm{lin}}$ as a function of magnetic field and temperature shown in Figure 6.21. In the overdoped regime, T_{o} is not significantly higher than $T_{\mathrm{c}}(0\ \mathrm{T})$, whereas the separation between the boundaries set by the zero resistivity superconductivity ($\mu_0 H_{\mathrm{r}}$) and the persistence of pairing correlations (T_{o}) widens as p decreases. T_{o} decreases only slightly as the magnetic field increases, indicating that the pairing correlations are remarkably resilient to magnetic field and associated with a large pairing energy scale. We estimate the magnetic field $H_{\mathrm{o}}(T_{\mathrm{o}} \to 0)$ by extrapolating the weak suppression of T_{o} under a magnetic field using

$$T_{\mathrm{o}}/T_{\mathrm{o}}(0\,\mathrm{T}) = 1 - (H/H_{\mathrm{o}})^2. \tag{6.4}$$

A rough estimate of the corresponding energy scale is obtained using [125]

$$\xi_0 = \sqrt{\Phi_0/2\pi\mu_0 H_{\mathrm{c2}}} = 2\hbar v_F/\pi E_{\mathrm{o}}, \tag{6.5}$$

where $\Phi = \hbar/2e$ is the magnetic flux quantum, H_{c2} is approximated by H_{o}, and $v_F \approx 2.5 \times 10^5$ ms^{-1} is the Fermi velocity of YBCO$_{6+x}$ [126]. A pairing energy scale $E_{\mathrm{o}} \approx 10^2$ meV is found as summarised in Table 6.1.

Table 6.1: Values of the oxygen composition x of measured YBCO$_{6+x}$ samples, hole doping p, critical temperature at zero magnetic field $T_{\mathrm{c}}(0\ \mathrm{T})$, critical temperature at 45 T in the limit of low applied current density $T_{\mathrm{c}}(45\ \mathrm{T})$, onset temperature of pairing correlations at zero field $T_{\mathrm{o}}(0\ \mathrm{T})$, onset temperature of pairing correlations at 45 T $T_{\mathrm{o}}(45\ \mathrm{T})$, extrapolated magnetic field corresponding to $T_{\mathrm{o}} = 0$ K $\mu_0 H_{\mathrm{o}}$, and pairing energy scale E_{o} (* represents values obtained at 35 T).

x	p	$T_{\mathrm{c}}^{(0\,\mathrm{T})}$ (K)	$T_{\mathrm{c}}^{(45\,\mathrm{T})}$ (K)	$T_{\mathrm{o}}^{(0\,\mathrm{T})}$ (K)	$T_{\mathrm{o}}^{(45\,\mathrm{T})}$ (K)	$\mu_0 H_{\mathrm{o}}$ (T)	E_{o} (meV)
0.55	0.108	61	0.04	237	235*	205(51)	82(8)
0.67	0.116	65.2	0.04	202	182*	112(28)	61(10)
0.75	0.132	75.8	0.3	175	167	175(44)	76(8)
0.84	0.14	84.1	4.8	165	154	170(43)	75(11)
0.87	0.149	89.5	30*	140	122*	94(24)	56(8)
0.92	0.162	93.8	43.1	123	116	205(51)	82(9)
0.97	0.17	93.2	45.5	118	108	167(42)	74(9)
2% Ca	0.187	88.2	48.5	108	100	145(36)	69(7)
3% Ca	0.191	86.5	40.2	102	92	143(36)	68(8)
4% Ca	0.194	84.7	40.6	96	88	150(38)	70(8)
5% Ca	0.20	81.5	42	89	76	109(27)	60(7)

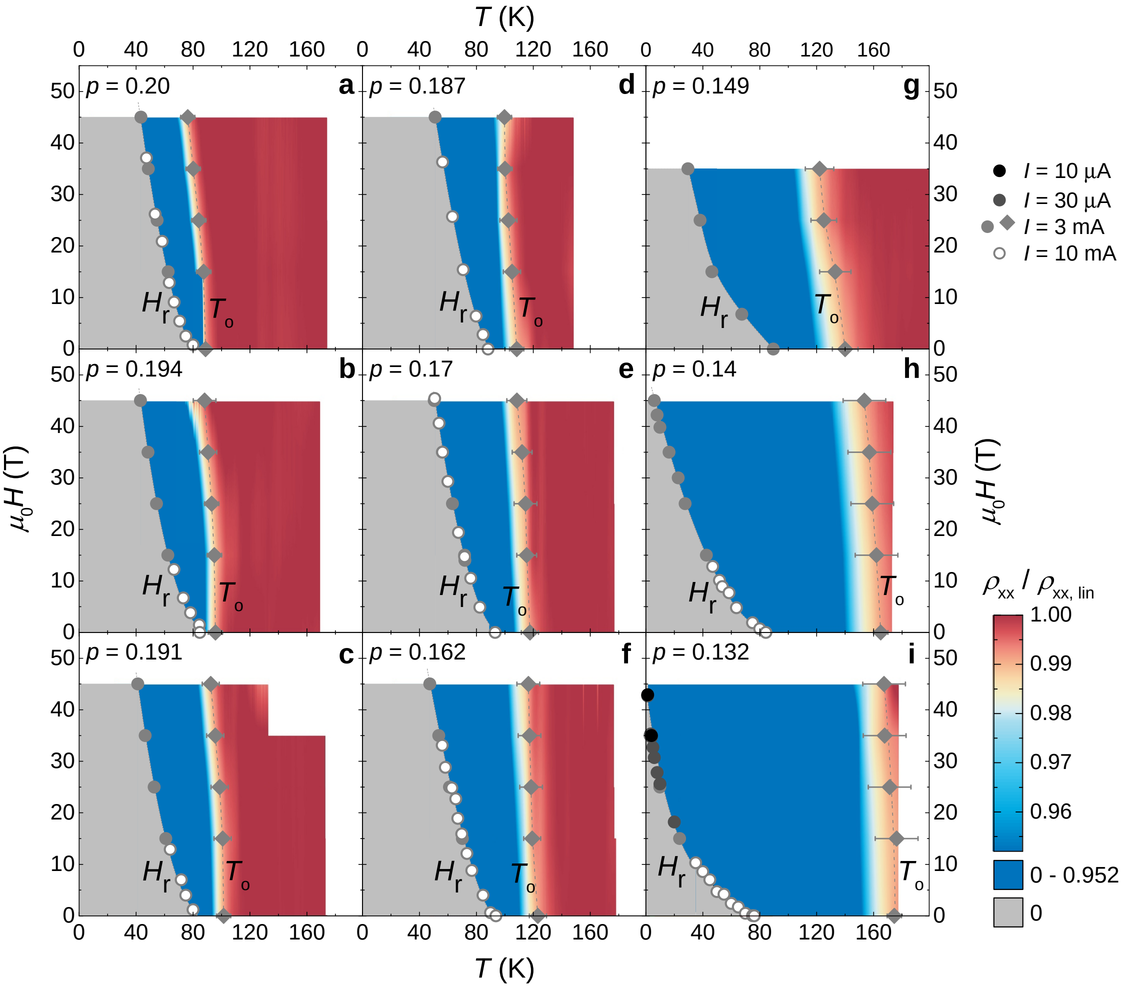

Figure 6.21: **Extent of pairing correlations and zero electrical resistivity superconductivity in YBCO$_{6+x}$. (a-i)** Magnetic field-temperature phase diagrams constructed from colour contours of the normalised in-plane resistivity ρ_{xx}/ρ_{lin} for several different hole dopings p as indicated. Red corresponds to the normal state with T-linear resistivity $\rho_{xx}/\rho_{lin} = 1$ while grey denotes the vortex solid state with zero resistivity $\rho_{xx} = 0$. The intervening region of superconducting fluctuations and pairing correlations appears in blue. Circles indicate the onset magnetic field of finite resistivity, $\mu_0 H_r$, extracted from Figure 6.13. Diamonds indicate the onset temperature of resistivity reduction, T_o, extracted from Figure 6.14.

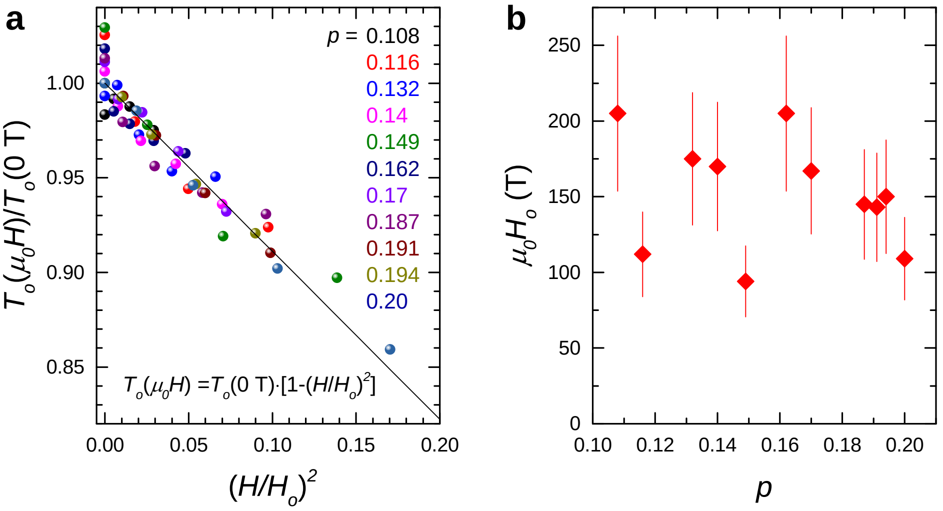

Figure 6.22: **Determination of $\mu_0 H_\text{o}$ from the magnetic field dependence of T_o.** (**a**) Symbols show T_o as a function of magnetic field. Solid line represents a fit of $T_\text{o}/T_\text{o}(0\text{ T}) = 1 - (H/H_\text{o})^2$ to the magnetic field dependence of T_o. $T_\text{o}(0\text{ T})$ refers to the value of T_o at zero magnetic field, $\mu_0 H_\text{o}$ refers to the magnetic field where T_o is suppressed to zero at $T = 0$ K. A fit is performed to obtain H_o for a doping of $p = 0.20$, where the variation of T_o is largest as a function of magnetic field. $\mu_0 H_\text{o}$ for the remaining dopings is obtained by scaling against the fitting curve, enabling independent estimates of $\mu_0 H_\text{o}$ to be obtained for each of the dopings. (**b**) $\mu_0 H_\text{o}$ obtained as in (a) for a range of doping.

6.4 Interplay between pseudogap and superconductivity

The ongoing debate of the correct description of the electronic ground state in the underdoped cuprates, even on the experimental level, has proven difficult to settle. We found that the electronic ground state in underdoped YBCO_{6+x} is characterised by an unusual coexistence of a Fermi surface with d-wave superconductivity at millikelvin temperature, with a very low critical temperature and critical current density in strong magnetic fields, which evolves to an extended regime of pairing correlations onset at temperatures up to the pseudogap temperature T^*. The onset of pairing correlations at a temperature much higher than T_c that only become coherent near T_c have also been suggested by complementary measurements such as Nernst effect [127], diamagnetism [128], and interlayer tunnelling [129].

The extreme sensitivity of the low-temperature superconductivity to thermal and electrical perturbations suggests some form of frustration is responsible for the suppression of superconductivity in the underdoped cuprates. Such frustration responsible for the suppression of long-range coherence of electron pairs may arise due to the large on-site repulsive energy scale of the Mott parent state or fluctuations of an additional order parameter, as suggested by various complementary measurements which observed a broken symmetries near T^* [34, 131, 132]. Various theoretical models have been proposed to describe the pseudogap regime as a result of local electron pairing correlations, including incoherent singlet pairs that effectively acquires a charge upon doping [1, 133], the BEC-BCS crossover [134], a regime of superconducting phase fluctuations [22], and others. Meanwhile, unconventional order parameters have also been considered to describe the pseudogap regime including a pair density wave state with finite superconducting order parameter and broken translational symmetry [135], an Amperean state with unconventional electron pairing [136], an association of topological order with discrete broken symmetries [137], and others.

Ultimately, it would be desirable to manipulate the pseudogap by suppressing or eliminating the frustration and enhance the critical temperature. A recent pump-probe spectroscopy experiment has demonstrated the signature of superconductivity persisting up to T^* [138], suggesting a transient near-room temperature superconductivity in underdoped YBCO_{6+x}. The radiation causes strong symmetry-selective distortion of the lattice, much higher than what can be achieved by realistic pressure, and suggests the important role played by the lattice configuration [139]. Architectural design to suppress the frustration and stabilise the transient superconductivity at T^* presents a possible route in the interfacial systems to pursue of an ever higher T_c [140, 141].

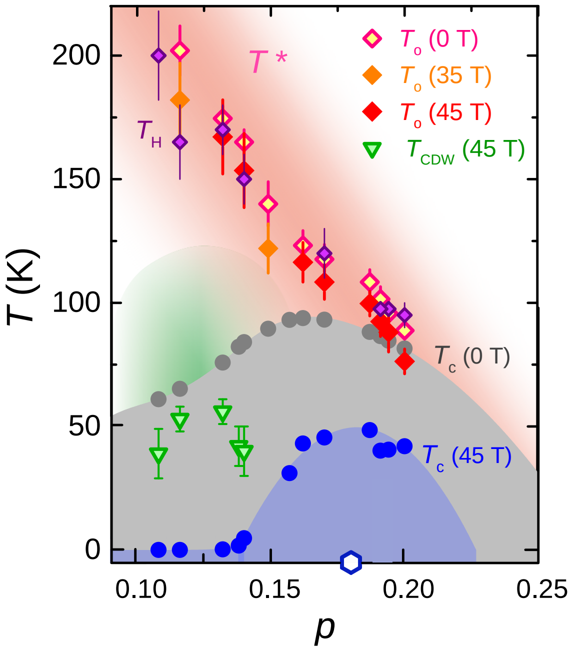

Figure 6.23: **Temperature-doping phase diagram of superconductivity, charge density wave order, and onset of pairing correlations in YBCO$_{6+x}$.** Diamonds denote the onset temperatures of pairing correlations. T_{H} is defined as the the highest temperature at which a deviation from a H^2-dependence is observed in $\Delta\rho = \rho(\mu_0 H) - \rho(0)$ as shown in Figure 6.17. Red shading denotes the pseudogap temperature T^* from various measurements. Circles denote the critical temperatures at zero magnetic field (grey) and 45 T (blue). The temperature axis has been offset by 5 K for clearer visibility of very low temperature superconductivity at low dopings. Green shading denotes short range charge density wave correlations observed from scattering experiments [33, 130] and downward triangles denote the long range charge order observed in Figure 6.13. Open hexagon denotes the position of a quantum critical point identified in quantum oscillation measurements [50].

Chapter 7

Concluding remarks

In the last chapter, I will review the motivating questions that initiated this work, summarise the main findings, and discuss some open questions regarding the Kondo insulator SmB_6 and high-T_c superconductor YBCO_{6+x}. The observation of unconventional Fermi surface in these strongly correlated materials suggests a new paradigm of Fermi surface in the absence of a conventional Fermi liquid.

7.1 SmB_6

Motivation

Can one observe a Fermi surface in the proposed topological Kondo insulator SmB_6*? If so, how does it differs from the weakly correlated topological insulators?*

Findings

De Haas-van Alphen oscillations are found to occur within the insulating state revealed by electrical transport. The observed Fermi surface has a three-dimensional geometry that is shared by the metallic rare-earth hexaborides and an absolute oscillation amplitude consistent with a bulk origin. The emergence of a neutral Fermi surface in SmB_6 is further supported by a sizeable linear specific heat coefficient and a significant field-enhancement of thermal conductivity at low temperatures, despite the extreme instance of Fermi liquid breakdown.

Outlook

In the quest to elucidate the origin of the low-temperature conducting channel in SmB_6, more questions have surfaced in light of the surprising discoveries. It has become clear that there is still much to be learnt about SmB_6 and, more generally, Kondo insulators. Some unaddressed questions that warrant further investigations are discussed below.

1. *Is the surface state topologically non-trivial?* As the observed quantum oscillations are not consistent with a surface origin, the topological conducting surface states, if they exist, are not observed in our measurements. Landau indexing, a method to identify the associated Berry phase (hence topological nature) of observed quantum oscillations [142], is not suited for SmB$_6$ since the oscillation frequencies are on the order of several hundred teslas. Other experimental probes are thus needed to conclusively address the topological nature of the surface conducting states.

2. *How can one observe quantum oscillations with a neutral Fermi surface?* An open question pertains to the observation of a neutral Fermi surface is that how can neutral quasiparticles exhibit quantum oscillations, which requires a coupling to the magnetic field for Landau quantisation. Among the existing theoretical proposals, the neutral Fermi surface arises from a composition or fractionalisation of quasiparticles. In the exciton model [96], the neutral exciton is a bound state of the electron and hole near the Fermi level, which exhibits quantum oscillations due to its constituents. In the spinon [94] and Majorana fermion models [99], the conventional quasiparticles fractionalise into chargeless spinons and Majorana fermions, which couple to the magnetic field via a non-vanishing coupling to the magnetic field above first order. In the composite exciton model [97], the neutral quasiparticle is a bound state of the unhybridised *d*-electron and fractionalised spinless holon. The gapped *d*-electrons remain coupled to the magnetic field and the gapless holons experience an effective magnetic field due to a strong coupling to the *d*-electrons. While these proposals provide explanations for our key observations, including the quantum oscillations and thermodynamic measurements, a quantitative comparison between theory and experiment remains outstanding. Other experimental predictions, such as a Meissner effect at low temperature and magnetic field [99] and a bulk thermal Hall effect [97] remain to be tested. An alternative possibility for a neutral Fermi surface is to consider a description beyond the convention of quasiparticles, such as topological and holographic models [143, 144].

3. *Is the neutral Fermi surface unique to SmB$_6$ or universal to Kondo insulators?* The striking observation of dHvA oscillations in a bulk insulating state calls for the investigation of similar systems. YbB$_{12}$, a Kondo insulator that shares key features with SmB$_6$ such as mixed Yb valency, bandgap size, and finite linear specific heat coefficient at low temperature [145, 146], is a promising candidate. Interestingly, it is also predicted to be a topological insulator [147], although the existence of surface conducting channels at low temperatures is not established. Other candidates includes SmS and Ce$_3$Bi$_4$Pt$_3$, which are Kondo insulators with finite linear specific heat coefficients at low temperature and near a insulator-metal transition tuned by pressure [148] and magnetic field [149] .

7.2 YBCO$_{6+x}$

Motivation

What is the correct description of the pseudogap ground state in underdoped YBCO$_{6+x}$ at low temperature?

Findings

A superconducting state that is resilient to magnetic field yet highly susceptible to thermal and electrical perturbations is revealed at millikelvin temperature. Quantum oscillations are found to occur deep within the vortex solid state, suggesting an unusual coexistence of nodal Fermi liquid quasiparticles with an antinodal superconducting gap. The long-range superconducting state at low temperature evolves into a state with short-range pairing correlations persisting up to the pseudogap temperature T^*, suggesting a form of frustration is responsible for the suppression of superconductivity in underdoped cuprates.

Outlook

The pseudogap ground state has proven to be more complex than a conventional metal plus a symmetry-breaking order parameter, despite the observation of seemingly Fermi liquid-like quantum oscillations. Although a complete description of the pseudogap state remains outstanding, progress has been made which led us much closer to the long-sought answer. Some open questions pertinent to the findings made in this work are discussed below.

1. *What determines the Fermi pocket size and quantum oscillations frequency in underdoped YBCO$_{6+x}$?* Among the various proposals for the Fermi surface reconstruction in underdoped cuprates [101, 150, 151], the one that invokes the charge order which leads to a nodal Fermi pocket is most consistent with our experimental observations [152]. In such a scenario, the Fermi pocket size is expected to be determined by the length of the Fermi arcs at zero magnetic field. It has been recently shown that a good correspondence can be found between the observed charge order vectors and quantum oscillation frequencies in the underdoped cuprates [153]. The onset magnetic field of quantum oscillations may therefore correspond to the magnetic field required to sufficiently suppress the nodal gap and reveal the full Fermi arcs for reconstruction, or for the charge order to become sufficiently long-range to reconstruct the Fermi surface.

2. *What breaks up the Fermi surface into Fermi arcs in the pseudogap regime?* The isolation of the nodal Fermi pocket in momentum space indicates the annihilation of density of states near the antinodal region, possibly due to an additional order parameter

and/or pairing correlations prior to the onset of charge order [136, 154]. Complementary measurements have reported signatures of various broken symmetries associated with the pseudogap, including rotational symmetry [131], time-reversal symmetry [132, 155], inversion symmetry [34], among others , which may relate to the additional order parameter. Experimental signatures of precursor superconductivity have also been reported up to T^* [127, 128, 129]. Some theoretical proposals have suggested the possibility of a state with intertwined order parameters that leads to a unconventional pair-density wave state [135, 156], among the various theoretical proposals that invoked pairing correlations as previously mentioned. The pseudogap phenomenology has been recently reproduced in Sr_2IrO_4, an analogue to the single layer cuprate La_2CuO_4, while superconductivity and charge density wave have not been observed in the accessed doping range [157, 158]. Further investigation into the formation of pseudogap in a system without superconductivity and charge order may provide new insights into understanding the formation of Fermi arcs.

3. *What is the nature of the frustration for the long-range superconductivity?* The fragility of the low-temperature superconductivity in the underdoped regime, despite a large pairing energy scale nearly independent of doping, suggests a form a frustration that is suppressing the long-range coherence of electron pairs. The possibilities of such frustration include a large on-site repulsive energy scale, due to the proximity of a Mott parent state with $J \approx 1000$ K, and fluctuations of a competing or intertwined order parameter as previously discussed. Geometric frustrations such as certain lattice configuration and low dimensionality may also be responsible. Identifying such a frustration factor will provide important clues for designing better superconductors, clues that may be found by investigating certain cuprates with similar crystal structure but very different critical temperatures [159].

— —

Quantum oscillations were first observed in 1930 in bismuth through the pioneering work of de Haas and van Alphen [160], soon after Landau published his paper on diamagnetism of metals in which he applied the newly developed quantum mechanics to free electrons and predicted the existence of discrete Landau levels [161]. However, Landau himself dismissed the possibility of observing the effect of Landau quantisation, as he thought the conditions are too stringent to be realised in experiment. Meanwhile, the concept of Fermi surface was only introduced in 1933 by Sommerfeld and Bethe as a property exclusive to metals [162]. For a long time, quantum oscillations were considered a mysterious and unique property of bismuth, until the same effect was observed in zinc in 1947 and soon in many other metals [163]. In the early 1950s, Onsager, Lifshitz, and Kosevich collectively formulated the theory for quantum oscillations [48, 164], which led to Pippard's much-celebrated mapping of the Fermi surface in copper in 1957 [165]. Fermiology has then become an established branch of solid state physics and the observation of quantum oscillations has been considered as the defining signature of the existence of quasiparticles within Landau's Fermi liquid framework [166]. Our surprising observation of quantum oscillations in insulating SmB_6 and superconducting $YBCO_{6+x}$ demonstrates a possible new paradigm of Fermi surfaces without a conventional Fermi liquid state. It remains to be seen whether an unconventional Fermi surface is a common characteristic of a broad family of strongly correlated materials and indicative of a new form of quantum matter. Once thought to be a phenomenon that can only be observed in metals and low temperatures, quantum oscillations have now been observed in gapped systems and above room temperature [167]. I have no doubt that there will be more fundamental breakthroughs to be made by this beautiful experimental technique that transforms theoretical concept into physical reality.

References

[1] Lee, P. A., Nagaosa, N. & Wen, X.-G. Doping a Mott insulator: Physics of high-temperature superconductivity. *Reviews of Modern Physics* **78**, 17 (2006).

[2] Dzero, M., Xia, J., Galitski, V. & Coleman, P. Topological Kondo Insulators. *Annual Review of Condensed Matter Physics* **7**, 80 (2016).

[3] de Boer, J. H. & Verwey, E. J. W. Semi-conductors with partially and with completely filled 3*d*-lattice bands. *Proceedings of the Physical Society* **49**, 59 (1937).

[4] Fukukawa, T., Miyazawa, K., Taniguchi, H., Kato, R. & Kanoda, K. Quantum criticality of Mott transition in organic materials. *Nature Physics* **11**, 221 (2015).

[5] Menth, A., Buchler, E. & Gelable, T. H. Magnetic and semiconducting properties of SmB_6. *Physical Review Letters* **22**, 295 (1969).

[6] Dzero, M., Sun, M., Galitski, V. & Coleman, P. Topological Kondo insulators. *Physical Review Letters* **104**, 106408 (2010).

[7] Hasan, M. Z. & Kane, C. L. *Colloquium*: Topological insulators. *Reviews of Modern Physics* **82**, 3045 (2010).

[8] Zhu, Z., Cheng, Y. & Schwingenschlögl, U. Band inversion mechanism in topological insulators: A guideline for materials design. *Physical Review B* **85**, 235401 (2012).

[9] Wolgast, W. *et al.* Low-temperature surface conduction in the Kondo insulator SmB_6. *Physical Review B* **88**, 180405 (2013).

[10] Kim, D. J., Xia, J. & Fisk, Z. Topological surface state in the Kondo insulator samarium hexaboride. *Nature Materials* **13**, 466 (2014).

[11] Kim, D. J. *et al.* Surface Hall effect and nonlocal transport in SmB_6: Evidence for surface conduction. *Scientific Reports* **3**, 3150 (2014).

[12] Denlinger, J. D. *et al.* SmB_6 photoemission: past and present. *JPS Conference Proceedings* **3**, 017038 (2014).

[13] Neupane, M., Alidoust, N., Xu, S. Y., Kondo, T. & Ishida, Y. Surface electronic structure of the topological Kondo-insulator candidate correlated electron system SmB_6. *Nature Communications* **4**, 2991 (2013).

[14] Wu, M. K. *et al.* Superconductivity at 93 K in a new mixed-phase Y-Ba-Cu-O compound system at ambient pressure. *Physical Review Letters* **58**, 908 (1987).

[15] Bednorz, J. G. & Müller, K. A. Possible high T_c superconductivity in the Ba-La-Cu-O system. *Zeitschrift für Physik B Condensed Matter* **64**, 189–193 (1986).

[16] Tranquada, J. M. *et al.* Antiferromagnetism in $YBa_2Cu_3O_{6+x}$. *Physical Review B* **38**, 2477 (1988).

[17] Liang, R., Bonn, D. A. & Hardy, W. N. Evaluation of CuO_2 plane hole doping in $YBa_2Cu_3O_{6+x}$. *Physical Review B* **73**, 180505 (2006).

[18] Vishik, I. *Low energy excitations in cuprate high temperature superconductors: angle-resolved photoemission spectroscopy studies.* Ph.D. thesis, Stanford University (2013).

[19] Homes, C. C. *et al.* A universal scaling relation in high-temperature superconductors. *Nature* **430**, 539 (2004).

[20] Božović, I., He, X., J., W. & Bollinger, A. T. Dependence of the critical temperature in overdoped copper oxides on superfluid density. *Nature* **536**, 309 (2016).

[21] Keimer, B., Kivelson, S. A., Norman, M. R., Uchida, S. & Zaanen, J. From quantum matter to high-temperature superconductivity in copper-oxides. *Nature* **518**, 179–186 (2015).

[22] Emery, V. J. & Kivelson, S. A. Importance of phase fluctuations in superconductors with small superfluid density. *Nature* **374**, 434–437 (1995).

[23] Takagi, H. *et al.* Systematic evolution of temperature-dependent resistivity in $La_{2-x}Sr_xCuO_4$. *Physical Review Letters* **69**, 2975 (1992).

[24] Hussey, N. E., Takenaka, K. & Takagi, H. Universality of the Mott-Ioffe-Regel limit in metals. *Philosophical Magazine* **84**, 2847–2864 (2004).

[25] Cooper, R. A. *et al.* Anomalous criticality in the electrical resistivity of $La_{2-x}Sr_xCuO_4$. *Science* **323**, 603–607 (2009).

[26] Doiron-Leyraud, N. *et al.* Correlation between linear resistivity and T_c in organic and pnictide superconductors. *arXiv preprints* **arXiv:0905.0964** (2009).

[27] Hashimoto, M., Vishik, I. M., He, R.-H., Devereaux, T. P. & Shen, Z.-X. Energy gaps in high-transition-temperature cuprate superconductors. *Nature Physics* **10**, 483 (2014).

[28] Monthoux, P., Pines, D. & Lonzarich, G. G. Superconductivity without phonons. *Nature* **450**, 1177–1183 (2007).

[29] Chang, J. *et al.* Direct observation of competition between superconductivity and charge density wave order in $YBa_2Cu_3O_{6.67}$. *Nature Physics* **8**, 871–876 (2012).

[30] Ghiringhelli, G. *et al.* Long-range incommensurate charge fluctuations in (Y, Nd)$Ba_2Cu_3O_{6+x}$. *Science* **337**, 821 (2012).

[31] Alireza, P. L. *et al.* Connecting high-field quantum oscillations to zero-field electron spectral functions in the underdoped cuprates. *Physical Review B* **95**, 100505(R) (2017).

[32] Tranquada, J. M., Sternlieb, B. J., Axe, J. D., Nakamura, Y. & Uchida, S. Evidence for stripe correlations of spins and holes in copper oxide superconductors. *Nature* **375**, 561 (1995).

[33] Blanco-Canosa, S. *et al.* Resonant x-ray scattering study of charge-density wave correlations in $YBa_2Cu_3O_{6+x}$. *Physical Review B* **90**, 054513 (2014).

[34] Zhao, L. *et al.* A global inversion-symmetry-broken phase inside the pseudogap region of $YBa_2Cu_3O_y$. *Nature Physics* **13**, 250–255 (2017).

[35] Hüfner, S., Hossain, M. A., Damascelli, A. & Sawatzky, G. A. Two gaps make a high-temperature superconductor? *Report on Progress in Physics* **71**, 062501 (2008).

[36] Norman, M. R., Pines, D. & Kallin, C. The pseudogap: friend or foe of high T_c? *Advances in Physics* **54**, 715–733 (2005).

[37] Tallon, J. L. & Loram, J. W. The doping dependence of T^* - what is the real high-T_c phase diagram? *Physica C: Superconductivity* **349**, 53–68 (2001).

[38] Sebastian, S. E. & Proust, C. Quantum oscillations in hole-doped cuprates. *Annual Review of Condensed Matter Physics* **6**, 30 (2015).

[39] Hossain, M. A. *et al.* *In situ* doping control of the surface of high-temperature superconductors. *Nature Physics* **4**, 527 (2008).

[40] Vignolle, B. *et al.* Quantum oscillations in an overdoped high-T_c superconductor. *Nature* **455**, 952 (2008).

[41] Doiron-Leyraud, N. *et al.* Quantum oscillations and the Fermi surface in an underdoped high-T_c superconductor. *Nature* **447**, 565–568 (2007).

[42] Mahan, G. D. *Many-particle physics* (Springer Science and Business Media, 2000).

[43] Luttinger, J. M. Fermi surface and some simple equilibrium properties of a system of interacting fermions. *Physical Review* **119**, 1153–1163 (1960).

[44] Anderson, P. W. How to have your Fermi surface without a Fermi liquid. *Journal of Physics and Chemistry of Solids* **52**, 1313–1317 (1991).

[45] Shoenberg, D. *Magnetic oscillations in metals* (Cambridge University Press, 1984).

[46] Watson, M. D. *et al.* Emergence of the nematic electronic state in FeSe. *Physical Review B* **91**, 155106 (2015).

[47] Bergemann, C., Mackenzie, A. P., Julian, S. R., Forsythe, D. & Ohmichi, E. Quasi-two-dimensional Fermi liquid properties of the unconventional superconductor Sr_2RuO_4. *Advances in Physics* **52**, 639–725 (2003).

[48] Lifshitz, I. M. & Kosevich, A. M. On the theory of magnetic susceptibility of metals at low temperatures. *Zh. Eksp. Teor. Fiz.* **29**, 730–742 (1955).

[49] Orbanic, F., Novak, M., Bacani, M. & Kokanovic, I. Quantum oscillations in a lead chalcogenide three-dimensional dirac system. *Physical Review B* **95**, 035208 (2017).

[50] Ramshaw, B. J. *et al.* Quasiparticle mass enhancement approaching the optimal doping in a high-T_c superconductor. *Science* **348**, 317–320 (2015).

[51] Ciomaga Hatnean, M., Lees, M. R., Paul, M. & Balakrishnan, G. Large, high quality single-crystals of the new Topological Kondo insulator, SmB_6. *Scientific Reports* **3**, 3071 (2013).

[52] Jacquet, P. A. *Metal Finishing* **47**, 62 (1949).

[53] Liang, R., Bonn, D. A. & Hardy, W. N. Growth of YBCO single crystals by the self-flux technique. *Philosophical Magazine* **92**, 3563–2581 (2012).

[54] Lin, C. T. & Kulakov, A. In situ observation of ferroelastic detwinning of YBCO single crystals by high temperature optical microscopy. *Physica C* **408**, 27–29 (2004).

[55] Erb, A., Walker, E. & Fluekiger, R. The use of $BaZrO_3$ crucibles in crystal growth of the high-T_c superconductors: Progress in crystal growth as well as in sample quality. *Physica C* **258**, 9–20 (1996).

[56] Erb, A., Traulsen, T. & Müller-Vogt, G. $YBa_2Cu_3O_{7-\delta}$-$BaCuO_2$-CuO: investigations on the phase diagram and growth of single crystals II. *Journal of Crystal Growth* **137**, 487–492 (1994).

[57] Lindemer, T. B. *et al.* Experimental and thermodynamic study of nonstoichiometry in $YBa_2Cu_3O_{7-x}$. *Journal of the American Ceramic Society* **72**, 1775–1788 (1989).

[58] Crank, J. *The Mathematics of Diffusion* (Oxford University Press, 1956).

[59] v. Zimmermann, M. *et al.* Oxygen-ordering superstructures in underdoped $YBa_2Cu_3O_{6+x}$ studied by hard x-ray diffraction. *Physical Review B* **68**, 104515 (2003).

[60] Herlach, F. & Miura, N. *High magnetic fields: science and technology*, vol. 1 (World Scientific Publishing Co. Pte. Ltd., 2003).

[61] Schneider-Muntau, H. J., Toth, J. & Weijers, H. W. Generation of the highest continuous magnetic fields. *IEEE Transactions on applied superconductivity* **14**, 1245–1252 (2004).

[62] Sebastian, S. E. *et al.* Quantum oscillations from nodal bilayer magnetic breakdown in the underdoped high temperature superconductor $YBa_2Cu_3O_{6+x}$. *Physical Review Letters* **108**, 196403 (2012).

[63] Altarawneh, M. M., Mielke, C. H. & Brooks, J. C. Proximity detector circuits: An alternative to tunnel diode oscillators for contactless measurements in pulsed magnetic field environments. *Review of Scientific Instruments* **80**, 066104 (2009).

[64] Wiegers, A. J. *et al.* A sensitive and versatile torque magnetometer for use in high magnetic fields. *Review of Scientific Instruments* **69**, 2369 (1998).

[65] Ohmichi, E. & Osada, T. Torque magnetometry in pulsed magnetic fields with use of a commercial microcantilever. *Review of Scientific Instruments* **73**, 3022–3026 (2002).

[66] Antonov, V. N., Shpak, A. P. & Yaresko, A. N. Electronic structure of mixed valent systems. *Condensed Matter Physics* **7**, 211–246 (2004).

[67] Phelan, W. A. *et al.* Correlation between bulk thermodynamic measurements and the low-temperature-resistance plateau in SmB_6. *Physical Review X* **4**, 031012 (2014).

[68] Allen, J. W., Batlogg, B. & Wachter, P. Large low-temperature hall effect and resistivity in mixed-valent SmB_6. *Physical Review B* **20**, 4807–4813 (1979).

[69] Cooley, J., Aronson, M., Fisk, Z. & Canfield, P. High pressure insulator-metal transition in SmB_6. *Physica B: Condensed Matter* **199**, 486–488 (1994).

[70] Wolgast, W. *et al.* Reduction of the low-temperature bulk gap in samarium hexaboride under high magnetic fields. *Physical Review B* **95**, 245112 (2017).

[71] Li, G. *et al.* Two-dimensional Fermi surfaces in Kondo insulator SmB_6. *Science* **346**, 1208–1211 (2014).

[72] Tan, B. S. *et al.* Unconventional Fermi surface in an insulating state. *Science* **349**, 287–290 (2015).

[73] Behler, S. & Winzer, K. De Haas-van Alphen effect in rare-earth hexaborides (RE = Pr, Nd, Gd). *Zeitschrift fuer Physik B Condensed Matter* **82**, 355 (1991).

[74] Stark, R. W. & Reifenberger. Quantitative theory for the quantum interference effect in the transverse magnetoresistance of pure magnesium. *Journal of Low Temperature Physics* **26**, 763–817 (1976).

[75] Harrison, N., Goodrich, R. G., Vuillemin, J. J., Fisk, Z. & Rickel, D. G. Quantum interference in LaB_6. *Physical Review Letters* **80**, 4498–4501 (1998).

[76] Ishizawa, Y., Tanaka, T., Bannai, E. & Kawai, S. de Haas-van Alphen effect and Fermi surface of LaB_6. *Journal of the Physical Society of Japan* **42**, 112–118 (1977).

[77] Harima, H., Sakai, O., Kasuya, T. & Yanase, A. A new interpretation of the de Haas-van Alphen signals of LaB_6. *Solid State Communications* **66**, 603–607 (1988).

[78] Ōnuki, T., Nishihara, M., Sato, M. & Komatsubara, T. Fermi surface and cyclotron mass of PrB_6. *Journal of Magnetism and Magnetic Materials* **52**, 317–319 (1985).

[79] Ōnuki, Y., Komatsubara, T., Reinders, P. H. P. & Springford, M. Fermi surface and cyclotron CeB_6. *Journal of the Physical Society of Japan* **58**, 3698–3704 (1989).

[80] Sebastian, S. E., Harrison, N. & Lonzarich, G. G. Towards resolution of the Fermi surface in underdoped high-T_c superconductors. *Reports on Progress in Physics* **75**, 102501 (2012).

[81] Taillefer, L. & Lonzarch, G. G. Heavy-fermion quasiparticles in UPt_3. *Physical Review Letters* **60**, 1570 (1988).

[82] Smith, H. G. *et al.* Experimental study of lattice dynamics in LaB_6 and YbB_6. *Solid State Communications* **53**, 15–19 (1985).

[83] Gabani, S. *et al.* Properties of the in-gap states in SmB_6. *Sold State Communications* **117**, 641–644 (2001).

[84] Biswas, P. K. *et al.* Low-temperature magnetic fluctuations in the Kondo insulator SmB_6. *Physical Review B* **89**, 161107 (2014).

[85] Hartstein, M. *et al.* Fermi surface in the absence of a Fermi liquid in the Kondo insulator SmB_6. *Nature Physics* **14**, 166 (2018).

[86] Harrison, N., Meeson, P., Probst, P.-A. & Springford, M. Quasiparticle and thermodynamic mass in the heavy-fermion system CeB_6. *Journal of Physics: Condensed Matter* **5**, 7435–7450 (1993).

[87] Sera, M., Kobayashi, S., Hiroi, M., Kobayashi, N. & Kunii, S. Thermal conductivity of RB_6 (R = Ce, Pr, Nd, Sm, Gd) single crystals. *Physical Review B* **54**, R5207–R5210 (1996).

[88] Nave, C. P. & Lee, P. A. Transport properties of a spinon Fermi surface coupled to a U(1) gauge field. *Physical Review B* **76**, 235124 (2007).

[89] Xu, Y. *et al.* Bulk Fermi surface of charge-neutral excitations in SmB_6 or not: A heat-transport study. *Physical Review Letters* **116**, 246403 (2016).

[90] Boulanger, M.-E. *et al.* Field-dependent heat transport in Kondo insulator SmB_6: phonons scattered by magnetic impurities. *arXiv preprints* **arXiv:1709.10456** (2018).

[91] Smith, M. F., Pauline, J., Walker, M. B. & Taillefer, L. Origin of anomalous low-temperature downturns in the thermal conductivity of cuprates. *Physical Review B* **71**, 014506 (2005).

[92] Yamashita, M. *et al.* Thermal-transport measurements in a quantum spin-liquid state of the frustrated triangular magnet κ-(BEDT-TTF)$_2$Cu$_2$(CN)$_3$. *Nature Physics* **5**, 44–47 (2009).

[93] Yamashita, M. *et al.* Highly mobile gapless excitations in a two-dimensional candidate quantum spin liquid. *Science* **348**, 1246 (2010).

[94] Motrunich, O. I. Orbital magnetic field effects in spin liquid with spinon Fermi sea: Possible application to κ-(ET)$_2$Cu$_2$(CN)$_3$. *Physical Review B* **73**, 155115 (2006).

[95] Knolle, J. & Cooper, N. R. Quantum oscillations without a fermi surface and the anomalous de haas-van alphen effect. *Physical Review Letters* **115**, 146401 (2015).

[96] Knolle, J. & Cooper, N. R. Excitons in topological Kondo insulator - theory of thermodynamic and transport anomalies in SmB_6. *Physical Review Letters* **118**, 096604 (2017).

[97] Chowdhury, D., Sodemann, I. & Senthil, T. Mixed-valence insulator with neutral Fermi surfaces. *arXiv preprints* **arXiv:1706.00418** (2017).

[98] Baskaran, G. Majorana Fermi sea in insulating SmB_6: A proposal and a theory of quantum oscillations in Kondo insulators. *arXiv preprints* **arXiv:1507.03477** (2015).

[99] Erten, O., Chang, P.-Y., Coleman, P. & Tsvelik, A. M. Skyrme insulators: insulators at the brink of superconductivity. *arXiv preprints* **arXiv:1701.06582** (2017).

[100] Anderson, P. W. Breaking the log-jam in many-body physics: Fermi surfaces without Fermi liquids. *Physica Scripta* **T42**, 11–16 (1992).

[101] Allais, A., Chowdhury, D. & Sachdev, S. Connecting high-field quantum oscillations to zero-field electron spectral functions in the underdoped cuprates. *Nature Communications* **5**, 5771 (2015).

[102] Grissonnanche, G. *et al.* Direct measurement of the upper critical field in cuprate superconductors. *Nature Communications* **5**, 3280 (2014).

[103] Yu, F. *et al.* Magnetic phase diagram of underdoped $YBa_2Cu_3O_y$ inferred from torque magnetization and thermal conductivity. *Proceedings of the National Academy of Sciences* **113**, 12667–12672 (2016).

[104] Bean, C. P. Magnetization of high-field superconductors. *Reviews of Modern Physics* **36**, 31 (1964).

[105] Higuchi, T., Yoo, S. I. & Murakami, M. Comparative study of critical current densities and flux pinning among a flux-grown $NdBa_2Cu_3Oy$ single crystal, melt-textured Nd-Ba-Cu-O, and Y-Ba-Cu-O bulks. *Physical Review B* **59**, 1514–1527 (1999).

[106] LeBoeuf, D. *et al.* Electron pockets in the Fermi surface of hole-doped high-T_c superconductors. *Nature* **450**, 533–536 (2007).

[107] Riggs, S. C. *et al.* Heat capacity through the magnetic-field-induced resistive transition in an underdoped high-temperature superconductor. *Nature Physics* **7**, 332 (2011).

[108] Sebastian, S. E. *et al.* Normal-state nodal electronic structure in underdoped high-T_c copper oxides. *Nature* **511**, 61–64 (2014).

[109] Sebastian, S. E. *et al.* A multi-component Fermi surface in the vortex state of an underdoped high-T_c superconductor. *Nature* **454**, 200–203 (2008).

[110] Sebastian, S. E. *et al.* Fermi-liquid behaviour in an underdoped high-T_c superconductor. *Physical Review B* **81**, 140505(R) (2010).

[111] Corcoran, R. *et al.* Quasiparticles in the vortex state of V_3Si. *Physical Review Letters* **72**, 701 (1994).

[112] Yasui, K. & Kita, T. Theory of the de haas-van alphen effect in type-ii superconductors. *Physical Review B* **66**, 184516 (2002).

[113] Maniv, T., Zhuravlev, V., Vagner, I. & Wyder, P. Vortex states and quantum magnetic oscillations in conventional type-II superconductors. *Reviews of Modern Physics* **73**, 867–911 (2001).

[114] Harrison, N. *et al.* Magnetotransport signatures of a single nodal electron pocket constructed from Fermi arcs. *Physical Review B* **54**, 9977 (1996).

[115] Potts, A. *et al.* Magnetization studies of Landau level broadening in two-dimensional electron systems. *Journal of Physics: Condense Matter* **8**, 5189–5207 (1996).

[116] Wilde, M. A. *et al.* Experimental evidence of the ideal de Haas-van Alphen effect in a two-dimensional system. *Physical Review B* **73**, 125325 (2006).

[117] Wu, T. *et al.* Magnetic-field-induced charge-stripe order in the high-temperature superconductor $YBa_2Cu_3O_y$. *Nature* **477**, 191–194 (2011).

[118] Oh, B. *et al.* Upper critical field, fluctuation conductivity, and dimensionality of $YBa_2Cu_3O_{7-x}$. *Physical Review B* **37**, 7861–7864 (1988).

[119] Carrington, A., Mackenzie, A. P., Sinclair, D. C. & Cooper, J. R. Field dependence of the resistive transition in $Tl_2Ba_2CuO_{6+\delta}$. *Physical Review B* **49**, 13243 (1994).

[120] Tinkham, M. Resistive transition of high-temperature superconductors. *Physical Review Letters* **61**, 1658–1661 (1988).

[121] Rullier-Albenque, F., Alloul, H. & Rikken, G. High-field studies of superconducting fluctuations in high-T_c cuprates: Evidence for a small gap distinct from the large pseudogap. *Physical Review B* **84**, 014522 (2011).

[122] Chan, M. K. *et al.* In-plane magnetoresistance obeys Kohler's rule in the pseudogap phase of cuprate superconductors. *Physical Review Letters* **113**, 177005 (2014).

[123] Pippard, A. P. *Magnetoresistance in Metals* (Cambridge University Press, 1993).

[124] Proust, C., Vignolle, B., Levallois, J., Adachi, S. & Hussey, N. E. Fermi liquid behaviour of the in-plane resistivity in the pseudogap state of $YBa_2Cu_4O_8$. *Proceedings of the National Academy of Sciences* **113**, 13654–13659 (2016).

[125] Waldram, J. R. *Superconductivity of Metals and Cuprates* (CRC Press, 1996).

[126] Borisenko, S. *et al.* Kinks, nodal bilayer splitting, and interband scattering in $YBa_2Cu_3O_{6+x}$. *Physical Review Letters* **96**, 117004 (2006).

[127] Xu, Z. A., Ong, N. P., Wang, Y., Kakeshita, T. & Uchida, S. Vortex-like excitations and the onset of superconducting phase fluctuation in underdoped $La_{2-x}Sr_xCuO_4$. *Nature* **406**, 486–488 (2000).

[128] Li, L. *et al.* Diamagnetism and Cooper pairing above T_c in cuprates. *Physical Review B* **81**, 054510 (2010).

[129] Dubroka, A. *et al.* Evidence of a precursor superconducting phase at temperatures as high as 180 k in $R\mathrm{Ba_2Cu_3O_{7-\delta}}(R = \mathrm{Y, Gd, Eu})$ superconducting crystals from infrared spectroscopy. *Physical Review Letters* **106**, 047006 (2011).

[130] Hücker, M. *et al.* Competing charge, spin, and superconducting orders in underdoped $YBa_2Cu_3O_y$. *Physical Review B* **90**, 054514 (2014).

[131] Sato, Y. *et al.* Thermodynamic evidence of a nematic phase transition at the onset of the pseudogap in $YBa_2Cu_3O_y$. *Nature Physics* doi:10.1038/nphys4205 (2017).

[132] Xia, J. *et al.* Polar Kerr-effect measurements of the high-temperature $YBa_2Cu_3O_{6+x}$ superconductor: Evidence for broken symmetry near the pseudogap temperature. *Physical Review Letters* **100**, 127002 (2008).

[133] Anderson, P. W. *et al.* The physics behind high-temperature superconducting cuprates: the plain vanilla version of RVB. *Journal of Physics: Condensed Matter* **16**, R755–R769 (2004).

[134] Randeria, M., Trivedi, N., Moreo, A. & Scalettar, R. T. Pairing and spin gap in the normal state of short coherence length superconductors. *Physical Review Letters* **69**, 2001–2004 (1992).

[135] Fradkin, E., Kivelson, S. A. & Tranquada, J. M. Colloquium: Theory of intertwined orders in high temperature superconductors. *Reviews of Modern Physics* **87**, 457–482 (2015).

[136] Lee, P. A. Amperean pairing and the pseudogap phase of cuprate superconductors. *Physical Review X* **4**, 031017 (2014).

[137] Chatterjee, S. & Sachdev, S. Insulators and metals with topological order and discrete symmetry breaking. *Physical Review B* **95**, 205133 (2017).

[138] Kaiser, S. *et al.* Optically induced coherent transport far above T_c in the underdoped $YBa_2Cu_3O_{6+\delta}$. *Physical Review B* **69**, 184516 (2014).

[139] Hu, W. *et al.* Optically enhanced coherent transport in $YBa_2Cu_3O_{6.5}$ by ultrafast redistribution of interlayer coupling. *Nature Materials* **13**, 705–711 (2014).

[140] Reyren, N. *et al.* Superconducting interfaces between insulating oxides. *Science* **317**, 1196–1199 (2007).

[141] Ge, J.-F. *et al.* Superconductivity above 100 K in single-layer FeSe films on doped $SiTiO_3$. *Nature Materials* **14**, 285–289 (2015).

[142] Ando, Y. Topological insulator materials. *Journal of the Physical Society of Japan* **82**, 102001 (2013).

[143] Wen, X.-G. Topological order: from long-range entangled quantum matter to a unified origin of light and electrons. *ISRN Condensed Matter Physics* **2013**, 198710 (2013).

[144] Zaanen, J., Liu, Y., Sun, Y.-W. & Schalm, K. *Holographic duality in condensed matter physics* (Cambridge University Press, 2015).

[145] Takeda, Y. *et al.* Temperature dependence of the electronic states of Kondo semiconductor YbB_{12}. *Physica B* **351**, 286–288 (2004).

[146] Iga, F. *et al.* Transport properties under high pressure of the dense Kondo compounds CePdSn and YbB_{12}. *Physica B* **186–188**, 419–421 (1993).

[147] Weng, H., Zhao, J., Wang, Z., Fang, Z. & Dai, X. Topological crystalline Kondo insulator in mixed valence ytterbium borides. *Physical Review Letters* **112**, 016403 (2014).

[148] Maple, M. & Wohlleben, D. Nonmagnetic $4f$ shell in the high-pressure phase of SmS. *Physical Review Letters* **27**, 511–515 (1971).

[149] Jaime, M. *et al.* Closing the spin gap in the Kondo insulator $Ce_3Bi_4Pt_3$ at high magnetic fields. *Nature* **405**, 160–163 (2000).

[150] Millis, A. J. & Norman, M. R. Antiphase stripe order as the origin of electron pockets observed in the 1/8-hole-doped cuprates. *Physical Review B* **76**, 220503(R) (2007).

[151] Yao, H., Lee, D.-H. & Kivelson, S. Fermi-surface reconstruction in a smectic phase of a high-temperature superconductor. *Physical Review B* **84**, 012507 (2011).

[152] Harrison, N. & Sebastian, S. E. Protected nodal electron pocket from multiple-Q ordering in underdoped high temperature superconductors. *Physical Review Letters* **106**, 226402 (2011).

[153] Harrison, N. Number of holes contained within the fermi surface volume in underdoped high-temperature superconductors. *Physical Review B* **94**, 085129 (2016).

[154] Efetov, K. B., Meier, H. & Pepin, C. Pseudogap state near a quantum critical point. *Nature Physics* **9**, 442–446 (2013).

[155] Fauque, B. *et al.* Magnetic order in the pseudogap phase of high-T_c superconductors. *Physical Review Letters* **96**, 197001 (2006).

[156] Wang, Y., Agterberg, D. F. & Chubukov, A. Coexistence of charge-density-wave and pair-density-wave orders in underdoped cuprates. *Physical Review Letters* **114**, 197001 (2015).

[157] Kim, Y. K. *et al.* Fermi arcs in a doped pseudospin-1/2 Hensenberg antiferromagnet. *Science* **345**, 6193 (2014).

[158] Battisti, I. *et al.* Universality of pseudogap and emergent order in lightly doped Mott insulators. *Nature Physics* **13**, 21–25 (2016).

[159] Zaanen, J. *et al.* Towards a complete theory of high T_c. *Nature Physics* **2**, 138–143 (2006).

[160] de Haas, W. J. & van Alphen, P. M. The dependence of the susceptibility of diamagnetic metals upon the field. *Proceedings of the Royal Netherlands Academy of Arts and Sciences* **33**, 1106–1118 (1930).

[161] Landau, L. D. Diamagnetismus der Metalle. *Zeitschrift für Physik* **64**, 639–637 (1930).

[162] Sommerfeld, A. & Bethe, H. Elektronetheorie der metal aufbau der zusammenhngenden materie. In *Handbuch der Physik*, vol. 24/2 (Springer Berlin, 1933).

[163] Marcus, J. A. The de Haas-van Alphen effect in a single crystal of zinc. *Physical Review* **71**, 559 (1947).

[164] Onsager, L. Interpretation of the de Haas-van Alphen effect. *Philosophical Magazine* **43**, 1006–1008 (1952).

[165] Pippard, A. B. An experimental determination of the Fermi surface in copper. *Philosophical Transactions of the Royal Society A* **250**, 325–357 (1957).

[166] Dugdale, S. B. Life on the edge: a beginner's guide to the Fermi surface. *Physica Scripta* **91**, 0531009 (2016).

[167] Kumar, R. K. *et al.* High-temperature quantum oscillations caused by recurring Bloch states in graphene superlattices. *Science* **357**, 181–184 (2017).

Appendix A

Fitting functions for ellipsoidal Fermi surface

Considering a parabolic energy band of free electrons, the general ellipsoidal surface of constant energy is determined by the energy dispersion

$$E(\mathbf{k}) = \frac{\hbar^2}{2m_\mathrm{e}} \sum \alpha_{ij} k_i k_j, \tag{A.1}$$

where the suffices denote 1, 2, 3 (or x, y, z) of the Cartesian coordinate axes, and α_{ij} is a symmetric matrix i.e. $\alpha_{ij} = \alpha_{ji}$. α_{ij} is determined by the the orientation of the ellipsoid with respect to the rectangular axes and its semi-principal axes ak_0, bk_0, ck_0 (referred as a-, b-, or c-axis herein). For a spherical surface, $\alpha_{ij} = \delta_{ij}$. If the magnetic field $\mathbf{H}$ has direction cosines (ν_1, ν_2, ν_3) with respect to the (k_x, k_y, k_z) axes, it can be shown [45] that the extremal cross-section of the ellipsoid by a plane normal to $\mathbf{H}$ has an area

$$S(E) = \frac{2\pi m_\mathrm{e} E}{\hbar^2 W^{1/2}}, \tag{A.2}$$

where W is given by

$$\begin{aligned} W = {} & \nu_1^2(\alpha_{22}\alpha_{23} - \alpha_{23}^2) + 2\nu_2\nu_3(\alpha_{12}\alpha_{13} - \alpha_{23}\alpha_{11}) \\ & + \nu_2^2(\alpha_{33}\alpha_{31} - \alpha_{31}^2) + 2\nu_3\nu_1(\alpha_{23}\alpha_{21} - \alpha_{31}\alpha_{22}) \\ & + \nu_3^2(\alpha_{11}\alpha_{12} - \alpha_{12}^2) + 2\nu_1\nu_2(\alpha_{31}\alpha_{32} - \alpha_{12}\alpha_{33}). \end{aligned}$$

The quantum oscillation frequency $F = \frac{\hbar c}{2\pi e} S(E_\mathrm{F})$ due to the ellipsoidal Fermi surface is thus given by

$$F = \frac{m_e c}{\hbar} \frac{1}{W^{1/2}}. \tag{A.3}$$

A.1 ρ-pocket

We model the ρ-branch of the Fermi surface in SmB$_6$ by twelve small ellipsoids with $a \approx b < c$, as shown in Figure A.1. The c-axes of the ρ-pockets are aligned along the $\langle 110 \rangle$ directions in reciprocal space. The quantum oscillation frequency corresponding to the ρ-pockets, when **H** rotates in the [100]-[110] plane at an angle θ with respect to [100], is given by

$$\rho_{1,2} : F^{\rho}_{\min} \frac{\sqrt{2}c}{\sqrt{2b^2\cos^2\theta + (a^2+c^2)\sin^2\theta}} \tag{A.4}$$

$$\rho_{3,4} : F^{\rho}_{\min} \frac{\sqrt{2}c}{\sqrt{(a^2+c^2)\cos^2\theta + 2b^2\sin^2\theta}} \tag{A.5}$$

$$\rho_{5} : F^{\rho}_{\min} \frac{\sqrt{2}c}{\sqrt{a^2+c^2-(c^2-a^2)\sin 2\theta}} \tag{A.6}$$

$$\rho_{6} : F^{\rho}_{\min} \frac{\sqrt{2}c}{\sqrt{a^2+c^2+(c^2-a^2)\sin 2\theta}}, \tag{A.7}$$

where $F^{\rho}_{\min}$ corresponds to the Fermi surface cross-section constructed by the a- and b-axes of the ellipsoids. The subscript corresponds to the labelled Fermi pocket shown in Figure A.1(a).

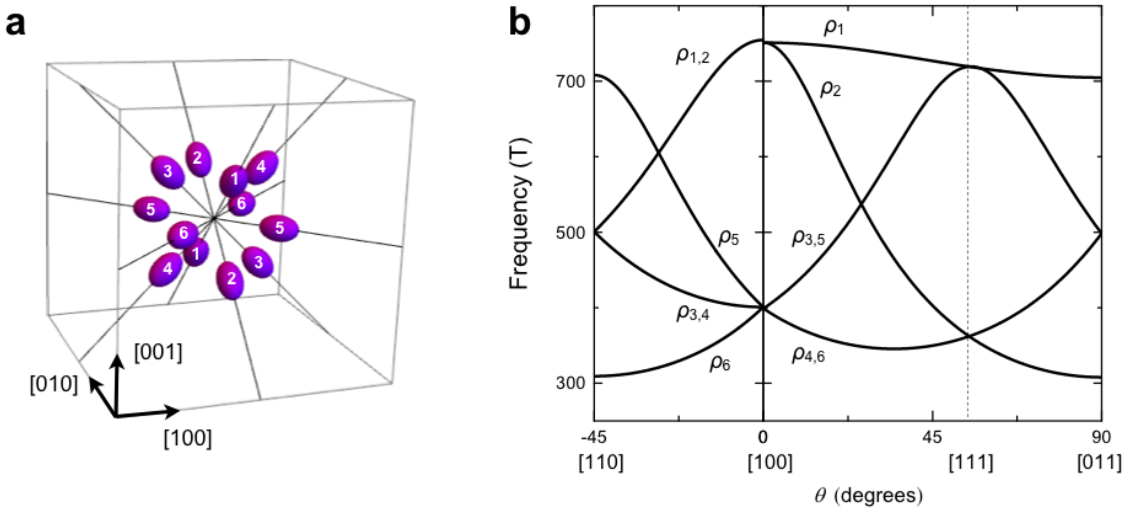

Figure A.1: **ρ-branch of Fermi surface model for SmB$_6$.** (**a**) ρ-pockets are twelve small ellipsoids with the relative ratios of the semi-principal axes $a \approx b < c$, oriented with the c-axes along the $\langle 110 \rangle$ directions. (**b**) Angular dependence of the quantum oscillation frequencies from ρ-pockets with magnetic field rotates along [100]-[111]-[011] and [100]-[110] planes. The branches are labelled by the corresponding pockets shown in (a). $F^{\rho}_{\min}$ of 309 T is used, as obtained by fitting to the experimental data.

When **H** rotates in the [100]-[111]-[011] plane at an angle θ with respect to [100], the quantum oscillation frequencies are given by

$$\rho_1 : F^{\rho}_{\min}\frac{c}{\sqrt{b^2\cos^2\theta + a^2\sin^2\theta}} \tag{A.8}$$

$$\rho_2 : F^{\rho}_{\min}\frac{c}{\sqrt{b^2\cos^2\theta + c^2\sin^2\theta}} \tag{A.9}$$

$$\rho_{3,5} : F^{\rho}_{\min}\frac{\sqrt{2}c}{\sqrt{3a^2+3c^2+2b^2+(a^2+c^2-2b^2)\cos 2\theta - 2\sqrt{2}(a^2-c^2)\sin 2\theta}} \tag{A.10}$$

$$\rho_{4,6} : F^{\rho}_{\min}\frac{\sqrt{2}c}{\sqrt{3a^2+3c^2+2b^2+(a^2+c^2-2b^2)\cos 2\theta + 2\sqrt{2}(a^2-c^2)\sin 2\theta}}. \tag{A.11}$$

The quantum oscillation frequency of the ρ-pockets as a function of θ is shown in Figure A.1(b), where four branches can be seen in both [100]-[111]-[011] and [100]-[110] rotation planes.

A.2 α-pocket

The α-branch of the Fermi surface in SmB$_6$ is modelled by six prolate spheroids with $a = b < c$, as shown in Figure A.2. The c-axes of the top and bottom spheroids (labeled 1) are aligned along the [001] direction, while the spheroids labeled 2 and 3 have c-axis aligned along [010] and [100] directions.

The quantum oscillation frequency corresponding to the α-pockets, when **H** rotates in the [100]-[110] plane at an angle θ with respect to [100], is given by

$$\alpha_1 : F^{\alpha}_{\min}\frac{c}{a} \tag{A.12}$$

$$\alpha_2 : F^{\alpha}_{\min}\frac{1}{\sqrt{\frac{a^2}{c^2}\cos^2\theta + \sin^2\theta}} \tag{A.13}$$

$$\alpha_3 : F^{\alpha}_{\min}\frac{1}{\sqrt{\cos^2\theta + \frac{a^2}{c^2}\sin^2\theta}}, \tag{A.14}$$

where $F^{\alpha}_{\min}$ corresponds to the Fermi surface cross-section constructed by the the circle of radius a. When **H** rotates in the [100]-[111]-[011] plane at an angle θ with respect to [100], the quantum oscillation frequencies are given by

$$\alpha_{1,2} : F^{\alpha}_{\min} \frac{c}{a} \frac{1}{\sqrt{\cos^2\theta + (\frac{1}{2} + \frac{c^2}{2a^2})\sin^2\theta}} \tag{A.15}$$

$$\alpha_3 : F^{\alpha}_{\min} \frac{1}{\sqrt{\cos^2\theta + \frac{a^2}{c^2}\sin^2\theta}} \tag{A.16}$$

The quantum oscillation frequency of the α-pockets as a function of angle θ is shown in Figure A.2. Two and three α-branches of the quantum oscillations frequency can be seen in the [100]-[111]-[011] and [100]-[110] rotation planes, respectively.

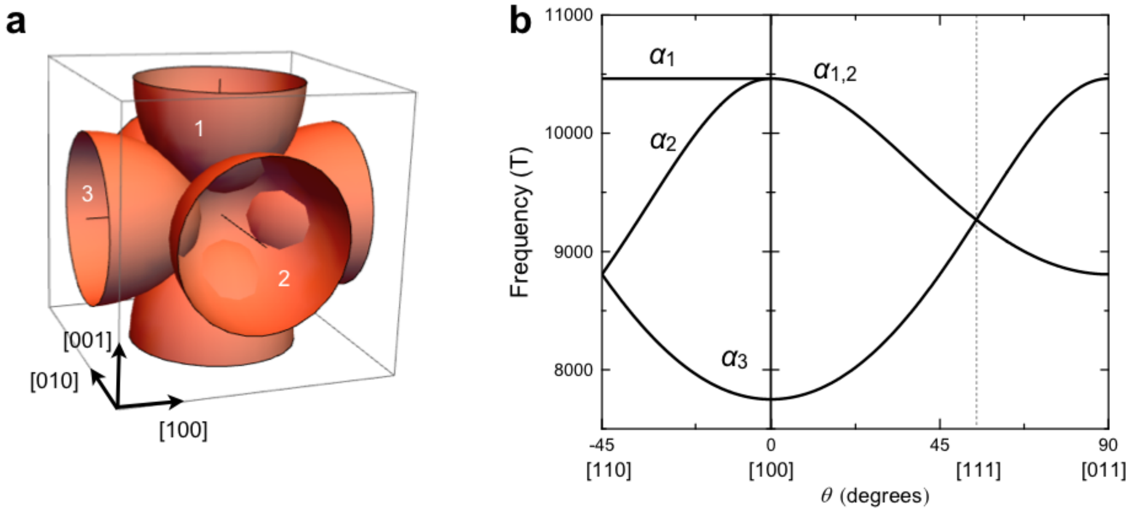

Figure A.2: **α-branch of Fermi surface model for SmB$_6$.** (**a**) α-pockets are six prolate spheroids with relative ratios of the semiprincipal axes $a = b < c$, oriented with the c-axes along the $\langle 100 \rangle$ directions. (**b**) Angular dependence of the quantum oscillation frequencies from α-pockets with magnetic field rotates along [100]-[111]-[011] and [100]-[110] planes. The branches are labelled by the corresponding pockets shown in (a). $F^{\alpha}_{\min}$ of 7 750 T is used, as obtained by fitting to the experimental data.